Fabrication and Mechanical Properties of Melt-Quenched Zeolitic Imidazolate Glasses

Stepniewska, Malwina

Publication date:
2019

Document Version
Publisher's PDF, also known as Version of record

FABRICATION AND MECHANICAL PROPERTIES OF MELT-QUENCHED ZEOLITIC IMIDAZOLATE GLASSES

BY
MALWINA STEPNIEWSKA

DISSERTATION SUBMITTED 2019

AALBORG UNIVERSITY
DENMARK

FABRICATION AND MECHANICAL PROPERTIES OF MELT-QUENCHED ZEOLITIC IMIDAZOLATE GLASSES

by

Malwina Stepniewska

AALBORG UNIVERSITY
DENMARK

Dissertation submitted in November 2019

Dissertation submitted:	November 2019
PhD supervisor:	Professor Yuanzheng Yue Aalborg University
PhD committee:	Associate Professor Casper Steinmann Svendsen (chair.) Aalborg University
	Associate Professor Satoshi Horike Kyoto University
	Professor Russell Hand University of Sheffield
PhD Series:	Faculty of Engineering and Science, Aalborg University
Department:	Department of Chemistry and Bioscience

ISSN (online): 2446-1636
ISBN (online): 978-87-7210-543-7

Published by:
Aalborg University Press
Langagervej 2
DK – 9220 Aalborg Ø
Phone: +45 99407140
aauf@forlag.aau.dk
forlag.aau.dk

Printed in Denmark by Rosendahls, 2020

ENGLISH SUMMARY

The recently discovered novel family of melt-quenched glasses, i.e., Metal-Organic Framework (MOF) glasses, has provided the researchers with the possibility to investigate a new, exciting group of materials. The most promising glass-forming candidates so far are a subset of MOFs, namely, Zeolitic Imidazolate Frameworks (ZIFs), which are three-dimensional networks with corner-shared tetrahedra constructed of metallic nodes connected by coordination bonds to the organic, imidazolate-derived ligands. However, along with the discovery of novel materials, new challenges come. These challenges need to be tackled before introducing the newly developed material into practical applications. The aim of this work is therefore to provide new insights into three of such challenges: (i) the influence of chemical composition on the glass-forming ability of ZIFs, (ii) the optimization of fabrication methods to enable production of a bulk ZIF glass, and (iii) the understanding of the mechanical properties of ZIF glasses.

Firstly, the influence of chemical composition on the glass-forming ability of ZIFs was discussed. Only a small number of ZIFs have so far been found to exhibit the melting ability upon heating, prior to their decomposition, and therefore, they can be transformed to glass by melt-quenching. The melting ability is the prerequisite for the glass-forming ability. Among the ZIFs with melting ability, ZIF-62 ($Zn(Im)_{2-x}(bIm)_x$, where Im is imidazolate, and bIm is benzimidazolate) was identified to be the best glass-former known until now. The influence of changing both the metallic nodes and the ligand ratios was thus investigated on ZIF-62. Cobalt nodes were successfully introduced into the structure by substitution of zinc nodes, with the final product (Co-ZIF-62) preserving the melting ability. Interestingly, the obtained Co-ZIF-62 phase differs from those reported in the literature, implying polymorphic transitions occur during the solvothermal synthesis of Co-ZIF-62. Furthermore, the ligand ratio changes in ZIF-62 did not affect its melting ability and glass-forming ability, although differences in characteristics such as glass transition temperature (T_g) and melting temperature (T_m) were observed.

Secondly, three methods were applied for fabricating bulk ZIF-62 glass samples, namely, ambient pressure melt-quenching in a tube furnace (MQ-AP), hot-pressing and Spark Plasma Sintering (SPS). All three techniques enabled the production of bulk samples, however, inhomogeneities in form of bubbles were observed in the glasses obtained via MQ-AP method, whereas the hot-pressing and SPS produced samples possess visible cracking. The sources of these defects were explored by using various characterization techniques. For these production methods, the possible routes for further optimization were found to reduce the extent of the inhomogeneities and cracking. Moreover, the application of pressure during the melting of the ZIF-62 in both the hot-pressing and the SPS techniques resulted in an increase of the density and decrease of the glass transition temperature (T_g) of the obtained glasses. These

phenomena were observed to be the most evident for the SPS-produced glass, where T_g was 565 K, and thus 35 K lower than T_g of MQ-AP glass. The possible structural origin of these phenomena was discussed.

Thirdly, the mechanical properties of the hot-pressed ZIF-62 glass were investigated via micro- and nanoindentation. The obtained hardness values (0.5 – 0.65 GPa, depending on the indentation load) of the ZIF-62 glasses were much smaller than those typically observed for oxide and metallic glasses. The fracture patterns with median and radial crack were revealed, analogous to that observed for the "normal" oxide glasses, such as window glass. Inside the indent impression, a step-like cracking pattern was observed. Two types of features were revealed there, namely, edge cracks and nano-scaled shear bands. The occurrence of the shear bands could be ascribed to the weak coordination bond between the metallic node and the organic ligands. The weak bond breaks easily under loading, enabling the movement of structural units along the slip lines. Subsequently, the reformation of the coordination bonds can occur. The local character of the plastic deformation by shear was further confirmed by the lack of observable pile-up along the indent edges. The influence of the chemical composition of ZIF-62 on its mechanical properties was studied but not conclusive due to the high degree of the scattering of the hardness values. The possible factors affecting the accuracy of the hardness data were identified and discussed.

DANSK RESUME

Den nyligt opdagede familie af smelteafkølede glasser, metalorganiske netværker (fra engelsk: *metal-organic frameworks*, forkortet MOF), har givet forskere muligheden for at undersøge en ny og spændende gruppe materialer. De mest lovende glasdannende kandidater er lige nu en undergruppe af MOF-glasser, nemlig ZIF-glasser (fra engelsk: *zeolitic imidazolate frameworks*), som er tredimensionelle netværker med tetraeder bestående af metalliske knudepunkter forbundet via koordinationsbindinger til organiske, immidazolat-deriverede ligander. Nye udfordringer opstår dog som følge af opdagelsen af nye materialer. Disse udfordringer skal tackles før de nyligt udviklede materialer kan finde anvendelse i praktiske applikationer. Målet med denne afhandling er derfor at skabe nyt indsigt inden for tre af de udfordringer: (i) indflydelse af kemisk sammensætning på glasdannelsesevnen af ZIF, (ii) optimering af fremstillingsmetoder til at muliggøre produktionen af bulk ZIF-glasser, og (iii) forståelse af de mekaniske egenskaber af ZIF-glasser.

Først, indflydelsen af den kemiske sammensætning på glasdannelsesevnen af ZIF-materiale var diskuteret. Kun et lille antal ZIF-materialer har indtil videre udvist evnen til at smelte under opvarmning før dekomponering og dermed være i stand til at overgå til en glastilstand ved smelteunderafkøling. Evnen til at smelte er et kriterie for glasdannelsesevnen. Iblandt ZIF-materialer med evnen til at smelte, ZIF-62 ($Zn(Im)_{2-x}(bIm)_x$ hvor Im er imidazolat og bIm er benzimidazolat) blev identificeret som den bedste kendte glasdanner. Cobalt-knudepunkter var succesfuldt introducerede i strukturen ved substitution med zink-knudepunkter, hvor den endelige produkt (Co-ZIF-62) bibeholdte evnen til at smelte. Interessant nok, den opnåede Co-ZIF-62 fase er forskellig fra de tidligere rapporterede faser, hvilket antyder at polymorfe faseovergange finder sted under den solvotermiske syntese af Co-ZIF-62. Derudover, ændringer i ligandratioen i ZIF-62 påvirkede ikke dets evne til at smelte eller glasdannelsesevnen, selvom forskelle i karakteristika som glasovergangstemperature og smeltetemperatur blev observerede.

Næst, tre metoder blev brugt til fremstilling af ZIF-62 glasprøver, nemlig smelteunderafkøling i en tubeovn (MQ-AP) ved atmosfærisk tryk, ”hot-pressing”, og Spark Plasma Sintring (SPS). Alle tre teknikker muliggjorde fremstillingen af bulkprøver, selvom inhomogeniteter i form af bobler blev observerede i glasserne fremstillede via MQ-AP metoden, hvorimod hot-pressing og SPS producerede prøver med synlig revnedannelse. Kilden til disse defekter blev undersøgt med forskellige karakteriseringsteknikker. For disse produktionsmetoder, mulige ruter til yderligere optimering blev fundet til at reducere udstrækningen af inhomogeniteter og revner. Derudover, applikationen af tryk under smeltning af ZIF-62 i både hot-pressing og SPS teknikker resulterede i en stigning i vægtfylde og et fald i glasovergangstemperatur (T_g) af de fremstillede glasser. Disse fænomener blev observerede mest fremtrædende fra SPS-fremstillede glasser, hvor T_g var 565 K, altså

35 K lavere end T_g af MQ-AP-fremstillet glas. Den mulige strukturel oprindelse af disse fænomener blev diskuteret.

Sidst, de mekaniske genskaber af hot-presset ZIF-62 glas blev undersøgt via mikro- og nano-indentering. Den målte hårdhedsværdi (0.5-65 GPa, afhængig af belastningen) af ZIF-62 glasser var meget mindre end hårdheden typisk registreret for oxidglasser og metalliske glasser. Revnemønster med medianrevne og radiale revner blev afsløret og konkluderet til at være analogt til et mønster typisk observeret i "normale" oxidglasser, som f.eks. vinduesglas. Inde i indtrykkene, en trinvis revnemønster blev observeret. To typer af deformationer blev afsløret, nemlig kantrevner og nanoskala forskydningsbånd. Forekomsten af forskydningsbåndene kunne tilskrives de svage koordinationsbindinger mellem de metalliske knudepunkter og organiske ligander. De svage bindinger bliver nemt brudt under en belastning, hvilket muliggør en bevægelse af strukturelle enheder langs sliplinjer. Dernæst, reformationen af koordinationsbindinger kan finde sted. Den lokale karakter af den plastiske deformation via forskydning var yderligere bekræftet ved en mangel af en observerbar ophobning af materialer langs kanterne af indtrykkene. Indflydelsen af den kemiske sammensætning af ZIF-62 på de mekaniske egenskaber blev studeret, men gav ingen endelig konklusion grundet høj spredning af hårdhedsværdierne. Mulige faktorer, der påvirkede nøjagtigheden af hårdhedsdata blev identificeret og diskuteret.

ACKNOWLEDGMENTS

This thesis has been submitted for assessment in partial fulfillment of the PhD degree. This thesis is based on scientific papers listed in Section 1.3. The work was performed from November 15th, 2016 to November 14th, 2019. The work was primarily performed at the Section of Chemistry of Department of Chemistry and Bioscience at Aalborg University, with external stays at State Key Laboratory of Silicate Materials for Architectures, Wuhan University of Technology in China (5 weeks), Institut des Sciences Chimiques de Rennes, Université de Rennes 1 in France (1 week) and two short-term visits to the Danish Technical University, Department of Mechanical Engineering. This study was a part of the "Glass Mechanical Properties: Structural Origins and Engineering" project funded by the VILUM FONDEN (research grant no. 13253.).

I would like to thank my supervisor, Professor Yuanzheng Yue, for all the guidance, help and support. Thank you for all the encouragement and time spend on valuable discussions. I appreciate all of the meetings and the discussions, which have helped me to become a better researcher.

Secondly, I would like to thank everyone from our VILLUM project, Professor Yuanzheng Yue, Professor MSO Morten M. Smedskjær, Professor Marcel A. J. Somers, Kacper, Saber, Thomas, Matteo, Ang, Theany. Our meetings have always provided great discussions and suggestions, which have proven especially helpful.

My thanks also go to my collaborators. My dearest thanks go to Professor Haizheng Tao, Ang Qiao, Zhitao Shan, Wen Chen from the Wuhan University of Technology. Thank you for making my stay in China one of the best adventures during my PhD work, for the long discussions and helping me organize the best trips. I would also like to thank Laurent Calvez and Professor Xianghua Zhang from Université de Rennes 1 for help during my short stay in France. The visit to Rennes last December has proven to be a great experience both for the experimental work and from the personal point of view – especially with the Christmas atmosphere in the city. Furthermore, I would like to thank Professor Grethe Winther from the Danish Technical University for facilitating the nanoindentation measurements and all the help. I would also like to thank Yongjian Yang and Professor John C. Mauro from Pennsylvania State University for the collaboration in finding the common ground between the experimental and simulation work on zinc/cobalt ZIFs.

The last three years in Aalborg would not be this amazing experience if not for my colleagues from the Department of Chemistry and Bioscience. I would therefore like

to thank all of you, highlighting Aamer, Ang, Anil, Anne-Sophie, Cejna, Chengwei, Esra, Hamid, Hao, Jiayan, Jonas, Martin, Mikkel, Nerea, Pengfei, Rasmus, Rasmus, René, Saurabh, Sheng, Sonja, Søren, Søren, Søren, Theany, Tobias, Usuma, Yang, Zhencai. Special thanks to Katie, Laura, Kamilla, and Nadieh – for taking good care of my social life, especially during the first, dark winter and Kasia – for all the support, conversations and the sea trips we had. Moreover, I would like to thank Chao for all the help – both work-related as well as personal. A particularly big thank you goes also to Kacper – thank you for helping me during all this time, starting even before I arrived in Denmark.

My greatest thanks goes to my family, especially my parents, Renata and Jacek, and my brother Szymon, for all the support they have given me during this time. It was not easy to move away from home, yet it never felt like home was far away with all the encouragement and assistance.

Finally, a special thanks goes to my boyfriend, Ferenc, for all the support, patience and believing in me during this demanding time.

TABLE OF CONTENTS

Chapter 1. Introduction 11

1.1. Background and Challenges 11

1.2. Objectives 13

1.3. Content 13

Chapter 2. Metal-Organic Frameworks – from Crystals to Glasses 15

2.1. Crystalline Zeolitic Imidazolate Frameworks 16

2.2. Melt-Quenched Zeolitic Imidazolate Framework Glasses 18

2.2.1. T_m-T_d Range Disparity between ZIF-4 and ZIF-62 19

2.2.2. From Crystals to Glass – Changes Observed in ZIF-4 and ZIF-62 22

2.2.3. Summary 23

Chapter 3. Modification of the Chemical Composition of ZIFs and its Effect on Glass-Forming Ability 25

3.1. Bimetallic ZIFs 25

3.1.1. Cobalt-Zinc Bimetallic Zeolitic Imidazolate Frameworks 26

3.1.2. Other Node-Exchange Trials in ZIF-62 33

3.2. Ligand Changes in ZIFs 36

3.2.1. Glass-Forming Ability of ZIFs with “Basic” Ligands (Imidazolate, Benzimidazolate) 39

3.2.2. Influence of Ligand Functionalization on Glass-Forming Ability 39

3.2.3. Changing Ligand Ratios in Mixed Ligand ZIFs 43

3.3. Summary 46

Chapter 4. Towards the Fabrication of Bulk ZIF-62 Glasses 47

4.1. Melt-Quenching in Inert Atmosphere Furnace 49

4.2. Hot-Pressing 51

4.3. Spark Plasma Sintering 54

4.4. Comparison of Described Fabrication Methods 58

Chapter 5. Mechanical Properties of ZIF Glasses 61
5.1. Overview of Terms in Materials Mechanics 61
5.2. Mechanical Behaviour of Crystalline ZIFs 68
5.3. Structure and Indentation Behaviour of More Conventional Glasses 71
5.4. Indentation Behaviour of ZIF-62 Glass 73
5.4.1. Hardness and Indentation Size Effect 74
5.4.2. Indentation Fracture 78
5.4.3. Indentation Deformation Mechanisms in ZIF-62 Glass 81
5.5. Indentation Behaviour of ZIF-62 Glasses with Changing Chemical Composition 84
5.5.1. Changing the Ligand Ratios in ZIF-62 85
5.5.2. Cobalt-Zinc Bimetallic ZIF-62 90
5.6. Summary 91
Chapter 6. Conclusions and Perspectives 93
Bibliography 97
List of Publications 107

CHAPTER 1. INTRODUCTION

The search for new materials has always been one of the greatest aspirations of materials science. Even in prehistoric times, the development of human society was closely linked to the discovery of new materials and understanding the nature of materials. Finding the original substances, with unique and unusual structures and properties, is therefore one of the most exciting parts of the materials research, from the beginning of times, up until recent times.

The recent discovery of metal-organic frameworks (MOF) has provided researchers with an exciting opportunity. The crystalline MOFs have been studied for the past 25 years. Their framework structure, with both organic and inorganic components, is characterized by fascinating features as high intrinsic porosity (*1–5*). They have therefore been named good candidates for a number of relevant applications, such as gas separation and storage (*6–9*), catalysis (*7*,*9–11*) and battery-related technologies (*7*,*12–14*).

However, crystalline MOFs show industrial limitations, such as their small size and low mechanical properties, which are highly limiting for their industrializations. A chance to tackle these problems came with the recent discovery of melt-quenched MOF glasses (*15*). This thesis focuses on this new material family, bordering between the novel MOF research and the well-established, yet still full of surprises, field of glass science.

1.1. BACKGROUND AND CHALLENGES

In 2015, a multidisciplinary research group, led by Thomas Bennett and Neville Greaves from the University of Cambridge and Yuanzheng Yue from Aalborg University, found that some MOFs can be first molten and then subsequently quenched to glass state (*15*). However, most of the MOFs decompose at a temperature much lower than their melting temperature. A search for MOFs with glass-forming ability has thus begun.

So far, zeolitic imidazolate frameworks (ZIFs), which are a particularly thermally and chemically stable subset of MOFs, show the promise in this novel field of glassy materials (*15–20*). ZIFs are the frameworks, in which metallic nodes together with imidazolate-derived ligands create structural tetrahedra (*16*,*17*,*22*). These corner-shared tetrahedra build a three-dimensional network, with two different types of bonds present – coordination bonds connecting the metallic node and the ligand, and the covalent bonds inside the bulky organic ligand. The melt-quenching of ZIFs leads to formation of glass with structural features similar to that of silica glass (*15–18*) – only with much larger [$ZnIm_4$] structural units instead of the four-fold [SiO_4] ones. Due to their special structure, ZIF glasses have exhibited a number of fascinating properties.

These include, for example, the ultrahigh glass-forming ability (T_g/T_m=0.84) and the high viscosity (10^5 Pa s) at the melting point, which are featured by ZIF-62 with the chemical structure of $Zn(Im)_{1.75}(bIm)_{0.25}$ (*16*). The investigations into physical and mechanical features of ZIF glasses in terms of the structural factors will provide a better understanding of the nature of glass in general. Based on the structure, ZIF glasses could also bridge the property gap observed between the non-organic (e.g. oxide and metallic) and polymeric glasses, in terms of, for example, mechanical properties. To be more explicit, ZIF-glasses should display higher mechanical properties than the soft, polymeric glasses, and the stronger oxide and metallic glasses. At the same time, melt-quenching of ZIFs allows the formation of bigger samples than the micrometric crystals, which is a new milestone in MOF research.

Nonetheless, with just a couple of years, the ZIF glass research is still at its infancy. Up until now, only a limited number of ZIFs have shown the melting ability prior to decomposition. This work provides some chemical and experimental information about the glass formation and fracture of ZIF glasses. However, the structural and topological features determining the glass-forming ability still need to be investigated.

A number of characterization techniques cannot be applied to measure the bulk physical properties of ZIFs due to the limited size of the samples. As one of the main advantages of ZIF glasses over their crystalline particles is that they can be prepared in the up-scaled bulk form, enabling different types of characterizations of the bulk properties.

The mechanical properties of ZIF glasses have been studied to a rather limited extent since these glasses have been discovered just recently. This project is devoted to providing some crucial experimental observations and analyses, benefiting both understanding of the chemistry-structure-property relationships of this novel family of materials. The results of this work are also useful for searching and design new glass-forming ZIF, even MOFs and for tailoring the properties of ZIF glasses.

The above-mentioned aspects, i.e., fabrication of ZIF glasses and their mechanical properties have been addressed in the current Ph.D. project.

1.2. OBJECTIVES

In summary, the presented work is addressing the following aspects:

1. The possible structural factors that improve the glass-forming ability of ZIFs;
2. The impact of the chemical composition on the glass-forming ability, as well as the properties of obtained ZIF crystals and glasses;
3. The development of a method enabling upscaling of the fabricated sample size;
4. The impact of various fabrication methods on the produced bulk ZIF glass;
5. The understanding of the mechanical properties of ZIF glass in terms of the structure-property relations;
6. The mechanism of deformation of ZIF glass under point loading;
7. The understanding of the indentation-induced fracture mechanism of ZIF glass.

1.3. CONTENT

After the comparison of a number of ZIFs, the author's opinion is that, for the current state of the art, ZIF-62 is the best candidate for experimental investigations of the objectives of this work. Due to this reason, all of the experimental work presented in this thesis was performed on this particular ZIF. However, a number of comparisons to other ZIFs, particularly ZIF-4 ($Zn(Im)_2$, the first-ever discovered glass-forming ZIF), are also included, based on literature or additional investigations performed by the author.

The thesis is divided into four parts. First, **Chapter 2**, provides the reader with a **comprehensive introduction into the field of ZIFs** in both crystalline and glassy states. Here, the melting and decomposition mechanisms are also described in detail, as they play an important role in the glass formation of ZIF glass. **Chapter 3** describes the influence of **the chemical composition of ZIFs on their glass-forming ability**. By coupling results obtained in this work with the data available in the literature, initial conclusions are here drawn as to structural factors that should be considered while on search for the new glass-forming ZIFs. After addressing the issue of the glass-forming ability of various ZIFs, **Chapter 4** focuses on **developing methods for the fabrication of a high-quality bulk sample of ZIF-62**. In the last part (**Chapter 5**), **the mechanical response of ZIF glass** is investigated with the use of micro- and nanoindentation coupled with additional analysis methods. Here, by sourcing from knowledge about structure-property relations in different families of glasses and the structure of ZIFs, the mechanism of indentation deformation and fracture are described.

The thesis is written in the form of an extended summary of findings from investigations performed throughout the duration of the project, including three papers submitted to peer-reviewed scientific papers. The knowledge presented in the papers is coupled with additional findings and literature review. The submitted papers are listed below and will be cited throughout the thesis by the roman numerals:

I. **Stepniewska M.,** Yang Y. J., Zhou C., Yue Y.Z., Mauro J. C., Determining the Phase Diagram, Structure and Properties of the Mixed Metallic ZIF-62 System via Experiments and Modelling, (Submitted).
II. **Stepniewska M.,** Januchta K., Zhou C., Qiao A., Smedskjær M. M., Yue Y. Z., Observation of Indentation Induced Nano-Shear Bands in a Metal-Organic Framework Glass, (Submitted).
III. **Stepniewska M.,** Østergaard M. B., Zhou C., Yue Y. Z., Towards Large-Sized Bulk ZIF-62 Glasses via Optimizing the Melting Conditions, *Journal of Non-Crystalline Solids* (In Press).

The author would like to note the novel character of this research, combining a number of diverse fields. Due to this multidisciplinary approach, the author included background information on both ZIFs and traditional glasses where relevant, in order to help the reader have a better understanding of these new areas of knowledge.

CHAPTER 2. METAL-ORGANIC FRAMEWORKS – FROM CRYSTALS TO GLASSES

Metal-Organic Frameworks (MOFs) are materials composed of organic and inorganic building units, where the metallic nodes are connected with organic ligands by coordination bonds. Their unique framework structures, characterized by tunable porosity and designable functionalization, leads to a number of potential applications covering a vast range of fields that are currently under high attention of many researchers. Those include catalysts, gas storage, and separation, energy storage in batteries, proton conductors and drug delivery.

Due to the high demand for the porous materials, great efforts have been made on the research of MOFs, indicated by the number of research outputs published in the past 15 years (Figure 2-1). Based on the observable trend, it is reasonable to conclude that MOFs materials will continuously attract more attention and play an important role in the applications mentioned above.

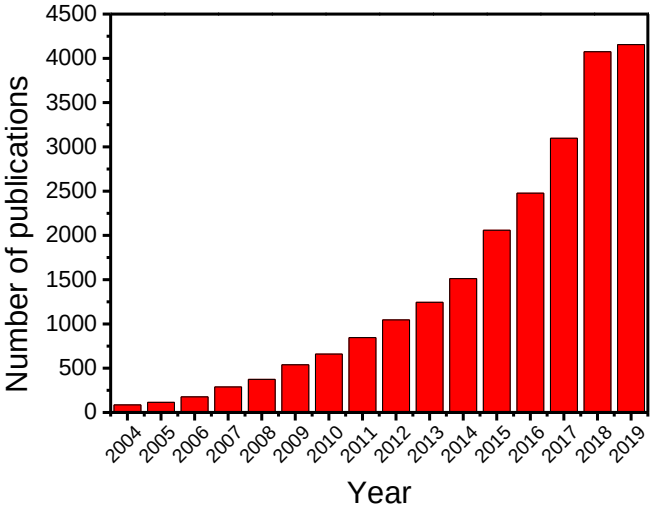

Figure 2-1 Number of scientific papers published on the subject of MOFs in years 2004 – 2019 (until November 2019). Source: ISI Web of Science. Articles were searched for by search on 7th November 2019 by search term of (("Metal Organic Framework") or ("Metal-organic Framework") or ("Metalorganic Framework")).

2.1. CRYSTALLINE ZEOLITIC IMIDAZOLATE FRAMEWORKS

Zeolitic Imidazolate Frameworks – ZIFs – are a subgroup of MOFs that possess relatively high chemical and thermal stability. For ZIFs, the organic ligands are imidazolate or its derivatives, which are connected to the central metallic node to form a tetrahedral unit (*16*,*17*,*22*). The three-dimensional framework is thus built of corner-shared structural tetrahedra of a general chemical formula of [Zn(Imidazolate derivative)$_4$]. When the tetrahedral units form a framework, the general chemical composition of ZIFs is Zn(Imidazolate derivative)$_2$. Different ZIFs are named ZIF-*X*, where *X* is a number referring to the given chemical composition and topology. Examples of ZIFs are: ZIF-4 (Zn(Im)$_2$, where Im stands for imidazolate, *cag* topology) (*17*,*23*), ZIF-8 (Zn(2-mIm)$_2$, where 2-mIm is 2-methylimidazolate, *sod* topology) (*15*,*24*) or ZIF-62 (Zn(Im)$_{1.75}$(bIm)$_{0.25}$, where bIm stands for benzimidazolate, *cag* topology) (16,*17*,*23*). As the numbers refer to the chronological order of discovery, they do not tell the reader much about the chemical composition of given ZIF. To check the chemical composition of a given ZIF, one must therefore refer to literature.

The name 'ZIF' is directly related to zeolites, as the ZIF structure is analogous to that of this well-known group of inorganic substances (Figure 2-2). However, we can see a number of differences between the two types of structure (ZIFs and zeolites), e.g.:

- Bond type: ZIFs have two types of bonds – covalent bonds between the atoms in the organic ligands and coordinative bonds connecting the nitrogen atoms of the ligand to the metal node. On the other hand, zeolites have only one, strong type of covalent bond present between silicon and oxygen atoms.
- Size of the tetrahedral units: Due to the size of the organic ligands in ZIFs, the distance between two neighboring metal nodes is significantly greater than that in the zeolites. It has been measured as about 6 Å between zincs in the Zn – Im – Zn unit (16,*17*, *22*), and about 3 Å between silicon atoms in Si – O – Si unit (*25*,*26*).
- Framework density: Due to the much larger size of the tetrahedral unit and lower molecular mass of the organic ligands, compared to those in zeolites, ZIFs have much lower density. The density of atoms per unit volume for ZIFs is typically in the range of 2-4 nm^{-3} (*23*,*27*), whereas for oxide zeolite this parameter is mainly in the range of 12-20 nm^{-3} (*23*,*27*).
- Structural flexibility: The framework, formed by organic ligands connected by coordinative bonds to the metal nodes, has a high degree of transitional and rotational freedom, in contrast to the rigid zeolite structure (*28*).
- 'Flexible' porosity in ZIFs: it is possible to accommodate molecules bigger than pore size suggests, by twisting and rotation of the ligands. For example, the 'breathing' phenomenon was observed in ZIF-8 and ZIF-4 (*29*,*30*), which exhibit a phase-to-phase transition under gas exposure, leading to the presence of larger pores in structure. Such a phenomenon is impossible in zeolites, where the structure is stiff.

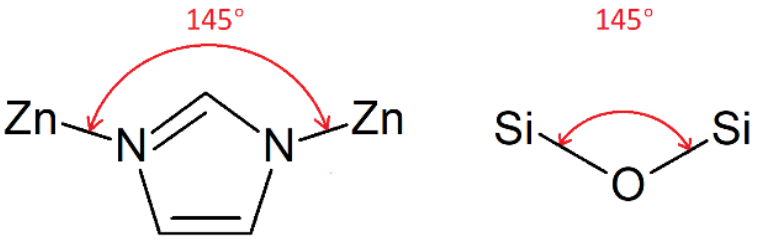

Figure 2-2 Examples of basic building units for ZIFs (on the left) and zeolites (on the right), as shown by Zn-Im-Zn and Si-O-Si units. Note the analogous positions of Zn and Si as well as Im and O in the presented structures.

The application fields of ZIFs cover a wide range of highly researched subjects. One of such fields is selective absorption of gas – for example, CO_2 from CO/CO_2 mixture by ZIF-68 or ZIF-70 (*31*) or CO_2 from CO_2/CH_4 mixture by ZIF-20 (*31*). Such a characteristic is especially important in light of the increasing importance of CO_2 separation and storage for green, environmentally friendly technologies. For these fields of applications, the flexibility of ZIFs and facile optimization of the porosity of MOFs through organic synthesis procedure is a great advantage over structurally rigid zeolites (*31*). The pore structure of the latter is difficult to change to fit the relevant applications.

Another interesting characteristic of ZIFs is photoluminescence. For ZIFs, the luminescence can be connected with either the linker or metal center emission or metal-to-ligand (or ligand-to-metal) charge transfer (*32*). An example of such a material is ZIF-8 with incorporated Cd^{2+} metal ions (*33*), and ZIF-62 with incorporated Co^{2+} metal nodes (*34*). Luminescent ZIFs could therefore be used in application fields such as photocatalysis, bioimaging or lasing (*35*).

The ZIF characteristics make them attractive candidates for many applications. However, a certain number of problems arise in their real-life applications. First of them is the difficult processability of the crystalline ZIF material. The as-synthesized ZIFs come in the form of small, brittle crystals, whereas industrial applications often require millimeter- or centimeter-scale products. It is, therefore, necessary to process the material to obtain bulk, monolithic samples. A typical approach for preparing a bulk ZIF sample is based on the addition of a binder substance, and subsequent sample processing (often involving pellet preparation under pressure) (*36*). However, such an approach can lead to the change of the porosity of the sample (as the binding substance often blocks the pores) (*37*) or changes of the structure due to the pressure (*38*). Furthermore, the produced monoliths are often characterized by low mechanical properties that might not be adequate for industrial use (*39*,*40*). Due to those reasons, fabrication of ZIF monoliths is an important issue – and melt-quenching to ZIF glass might provide a significant step in that direction.

2.2. MELT-QUENCHED ZEOLITIC IMIDAZOLATE FRAMEWORK GLASSES

It has recently been discovered that certain crystalline ZIFs can be melted and subsequently quenched to glasses (*15*,*17*). The structure of thee melt-quenched (MQ) ZIF glasses is found to be analogous to silica glass that can be described by the traditional continuous random network (CRN) model (*15–18*), i.e., both of them have fully polymerized structure, with basic building units of tetrahedra. The size of the short, intermediate and long-range structure is however different between those two systems, due to the larger size of ligands in ZIFs compared to the oxygen size in silica. In detail, ZIF glasses have short-range order (< 7 Å), intermediate (7 – 20 Å) and long (> 20 Å) range disorder (*16*,*22*,*41*). On the other hand, for silica, short-range refers to > 3 Å, the intermediate-range is 3-5 Å, and the long-range is over 5 Å distance (*42*,*43*).

So far, only a small number of crystalline ZIFs have been melt-quenched to glass. The first-ever MQ-ZIF was ZIF-4 - $Zn(Im)_2$ (a structural unit is presented in Figure 2-3) (*15*). Other reported melt-quenched ZIFs include ZIF-62 (*16*,*17*), ZIF-GIS (*17*), ZIF-76 (*44*), ZIF-76-mbIm (*44*) and TIF-4 (*17*). Considering the overall number of ZIF reaches over 180 (*45*), the number of known glass-formers is surprisingly small. This may be owing to the condition, that for a ZIF glass-former, its melting temperature T_m must be lower than decomposition temperature T_d, which does not occur for most of ZIFs. For most ZIF glass formers, T_m and T_d are just a couple of degrees apart (*17*,*22*,*44*), leading to partial decomposition of the material at the time of melting. Partial decomposition of organic ligands leads to foaming of, for example, ZIF-4 during melt-quenching and formation of many macroscopic bubbles in the final glass structure. So far, the most promising candidate for a bulk glass formation is ZIF-62. It exhibits the largest range of temperatures between T_m and T_d (around 100 K) (12) (Paper I, Paper II). The knowledge of the reasons for a large melting range for ZIF-62 might be crucial for understanding the characteristics of a good ZIF glass former.

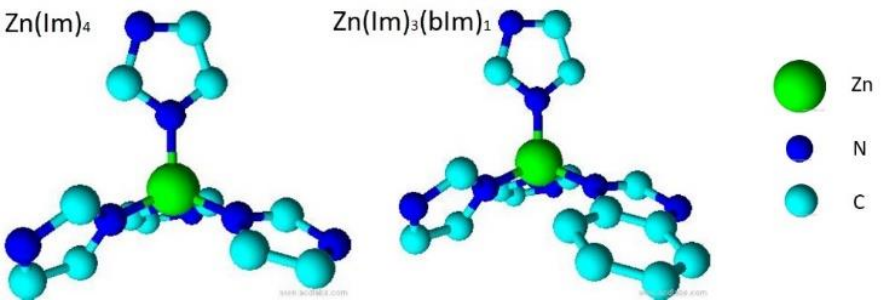

Figure 2-3 Structural tetrahedra present in ZIF-4 and ZIF-62. ZIF-4 is built of [ZnIm4] tetrahedral only, whereas the structure of ZIF-62 is constituted by two types of tetrahedra: [ZnIm4] and [ZnIm3bIm1]. Green represents zinc atoms, dark blue – nitrogen and light blue – carbon. Hydrogen atoms were omitted for clarity.

2.2.1. T_M-T_D RANGE DISPARITY BETWEEN ZIF-4 AND ZIF-62

To understand the disparity in the melting-to-decomposition range for ZIFs, we first need to compare the composition and structures of ZIF-4 (T_m-to-T_d range of just a couple of degrees) and ZIF-62 (T_m-to-T_d range of over 100 K). The framework of ZIF-4 is constructed by connecting zinc nodes by imidazolate (Im) ligand, and all the structural building units are [$ZnIm_4$] tetrahedra (*15*,*23*). In the case of ZIF-62, two ligands are present – imidazolate and benzimidazolate (bIm), where bIm ligand substitutes one of the Im ligands in part of the [$ZnIm_4$] tetrahedra, forming a mixed-ligand [$ZnIm_3bIm_1$] units (*23*,*46*). The typical chemical formula of ZIF-62 is $Zn(Im)_{1.75}(bIm)_{0.25}$, indicating that for every two tetradehra, seven of the ligands are imidazolates and one is benzimidazolate. It has been reported that a series of ZIF-62 phase materials are obtained with a range of imidazolate-to-benzimidazolate ratios, which could be denoted as $Zn(Im)_{2-x}(bIm)_x$ (*46*).

The presence of benzimidazolate ligands, which are larger than imidazolate ligands, means that a part of the structural tetrahedra in ZIF-62 is larger than those present in ZIF-4. In [$ZnIm_3bIm_1$] units two different Zn-N bonds are also present – Zn-N_{Im} and Zn-N_{bIm} (where N_{Im} is the nitrogen atom from imidazolate, and N_{bIm} is the nitrogen from benzimidazolate ligand respectively). In addition, the presence of the Zn-N_{bIm} bond may affect the three Zn-N_{Im} bonds present in the [$ZnIm_3bIm_1$] tetrahedra. The underlined structural differences and similarities will be considered below in the analysis of the melting and decomposition processes (Figure 2-4).

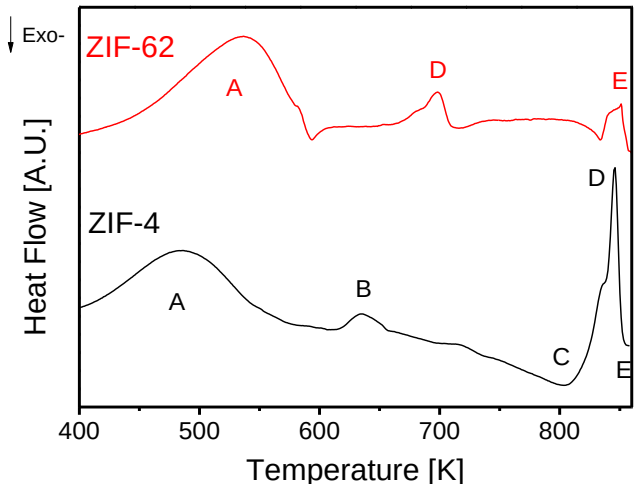

Figure 2-4 Thermal response of ZIF-62 (red line) and ZIF-4 (black line) samples upon heating in DSC. Characteristic phenomena are denoted with capital letters as follows: A – release of solvent, B – transformation to amorphous phase (only for ZIF-4), C – recrystallization to ZIF-zni (only for ZIF-4), D – melting, E – decomposition.

As shown in Figure 2-4, the thermal responses during the DSC upscan are very different for ZIF-4 and 62. For both crystals, the solvent molecules used in synthesis stay trapped in the internal porosity of the framework and are removed upon heating around 400-580 K (A in Figure 2-4). Subsequently, ZIF-4 crystals are transformed to amorphous phase around 600 K (B in Figure 2-4), due to a framework collapse, followed by recrystallization (C in Figure 2-4) to high-density ZIF-zni phase at around 800 K. The framework collapse and recrystallization is a characteristic of ZIF-4 and does not occur in ZIFs with other chemical compositions. Finally, ZIF-zni phase melts at around 840 K. In contrast, no phase transitions are observed prior to the melting of crystalline ZIF-62. This could be due to the larger size of benzimidazolate ligands stabilizing the crystal structure of ZIF-62 – thereby hindering the framework collapse and reformation prior to melting (*16*,*47*). The melting temperature of ZIF-4 and ZIF-62 differ by over 100 K, being respectively around 710 K for ZIF-4 and 845 K for ZIF-62 (D in Figure 2-4). Both crystals begin decomposing around the same temperature (~850 K, E in Figure 2-4). This means that the T_m-T_d range for ZIF-62 extends over 100 K, whereas for ZIF-4 – only a couple of degrees (under 10 K).

2.2.1.1 Melting Behavior Disparities between ZIF-62 and ZIF-4

The mechanisms of melting and decomposition of ZIF crystals will be described in this and the following sections in order to facilitate the explanation of the influence of the structure of T_m and T_d of ZIF-4 and ZIF-62. It is observed that the melting of ZIF crystals is governed by Zn-N bond breakage (*24*,*48*). After the bond breaks, a 'free' linker is formed and can move around to find and connect with another three-fold coordinated zinc (missing one ligand that broke away), reforming a new four-fold structural tetrahedron. It could happen in two ways: either the ligand breaks off from both zinc nodes it is connected to and moves freely until it connects to a new metal node, or only one coordinative bond is broken, and the tetrahedron flow is much more hindered, yet still present. This dynamic process of bond breakage and reformation occurs continuously in ZIF liquids. The bond breakage is shown to be a rare event (*24*). Therefore, it is likely to reach a state in which only one of the coordinative bond dissociates, enabling melting of ZIF to the liquid state (*24*). However, if more than one Zn-N bond breaks in a tetrahedral unit, the structure decomposes locally.

As described above, the melting of ZIFs is related to the dissociation of the first coordinative bond in a structural unit. This suggests the energy needed for dissociation of the first bond in ZIF-62 is much lower than that needed for ZIF-4. Two discrete reasons can be responsible for this difference. Firstly, the introduction of benzimidazolate into the ZIF-62 structure can change its bond structure. As only one of the ligands is exchanged per tetrahedral unit, it perturbs the Zn-N_{ligand} bonding symmetry around the metal node, which may lead to the decrease of the energy needed for a bond dissociation. For many traditional compounds, symmetrical molecules have higher melting points than their asymmetric counterparts (*49*,*50*), and a similar scenario might happen in the case of structural units of ZIFs.

The second factor to be considered is the phase transformation of ZIF-4 occurring prior to melting. Due to this phase transformation, the so-called T_m of ZIF-4 is actually T_m of ZIF-zni. The higher density ZIF-zni phase is the most energetically stable polymorph of ZIFs of $Zn(Im)_2$ chemical composition (*51–53*). Higher stability means more energy is needed to overcome the energy barrier for $Zn\text{-}N_{Im}$ bond dissociation during the melting of ZIF-zni. It means the process of bond dissociation in ZIF-zni is more energetically demanding than in the less energetically stable ZIF-4. In other words, the observed increase of T_m for ZIF-4 (as compared to ZIF-62) can be the result of phase transformation to a more energetically stable phase, and not fully connected to the bond structure difference between ZIF-4 and ZIF-62.

This approach seems to be further confirmed by the comparison of T_m values of ZIF-62 with ZIF-76-mbIm ($Zn(Im)_{1.5}(5\text{-mbIm})_{0.5}$, where 5-mbIm is 5-methyl-benzimidazolate) (*19*,*44*). All three ZIFs (ZIF-4, ZIF-62, and ZIF-76-mbIm) are characterized by the topology (*cag*). Although the structure of ZIF-76 is analogous to ZIF-62, ZIF-76 possesses larger 5-mbIm ligands (than bIm) in the framework. The T_m of ZIF-76-mbIm is around 30 K higher than that of ZIF-62 (*16*,*44*), indicating that the substitution of the ligands by bigger moieties leads to increase of T_m values. ZIF-4 is a clear outlier of this trend, implying the change of network topology (to *zni*) can be the main factor influencing the increase of T_m for ZIF-4, compared to other ZIF structures of the same topology.

2.2.1.2 Decomposition Behavior of ZIF-62 and ZIF-4

The decomposition of both ZIF-4 and ZIF-62 occurs in a similar temperature range (points E in Figure 2-4). It suggests the decomposition of the framework may be governed by the same mechanism in both cases. The decomposition of the framework occurs when more than one coordinative $Zn\text{-}N_{ligand}$ bond dissociates per structural tetrahedron. The similar T_d for ZIF-4 and ZIF-62 implies that this occurs at the same point for both $Zn\text{-}N_{Im}$ and $Zn\text{-}N_{bIm}$ coordinative bonds, which was further confirmed for ZIF-62 in Paper III. No changes can be observed in the ratio between imidazolate and benzimidazolate in ZIF-62 glasses decomposed to various extents, suggesting both ligands decompose at the same rate. This implies the bond dissociation energy for both $Zn\text{-}N_{Im}$ and $Zn\text{-}N_{bIm}$ is similar.

To summarize, based on the differences between melting and decomposition of ZIF-4 and ZIF-62, it can be implied, that the bond structure does not change to a great extent by introducing benzimidazolate to structural tetrahedra in ZIFs. However, it stabilizes the structure of the framework against framework collapse, which in turn stops the formation of a more energetically stable ZIF-zni phase (as the one observed for ZIF-4), which increases the melting temperature of ZIF-4. This, in turn, improves ZIFs glass-forming ability by extending the range between T_m and T_d, and therefore decreasing the probability of ligand decomposition in ZIF liquid.

2.2.2. FROM CRYSTALS TO GLASS – CHANGES OBSERVED IN ZIF-4 AND ZIF-62

For any family of materials, two main characteristics should be present to confirm glass has been formed: (i) no long-range order in atomic structure, (ii) glass transition temperature observable during heating of the material (*54*). In the following section, ZIF glasses will be described in terms of those two aspects. Subsequently, further structural data will be presented to describe structural changes happening over the medium- and short-range order during glass formation of ZIF glasses.

The loss of long-distance order during quenching is caused by the disordering of the atomic structure during fast cooling from the liquid state. On the laboratory scale, the easiest method for confirming the disordering of the atomic structure is X-ray diffraction (XRD). Figure 2-5 shows the X-ray patterns obtained for ZIF-4 and ZIF-62 crystals and melt-quenched glasses, confirming the quenched samples of both phases are 'X-ray amorphous'.

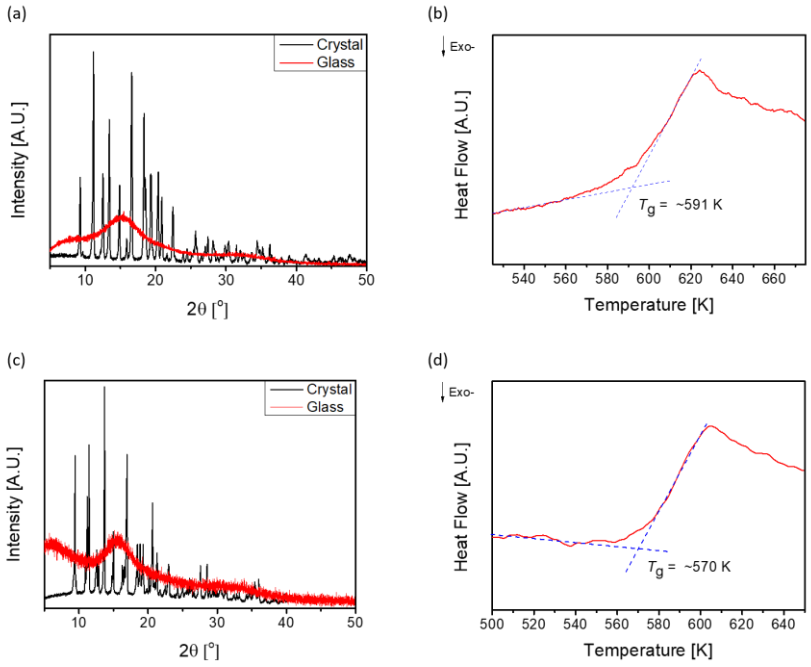

Figure 2-5 Glassy state characteristics confirmations for ZIF-62 and ZIF-4 glass. XRD patterns for crystals and a melt-quenched glass of (a) ZIF-62 and (c) ZIF-4; glass transition temperature as observed from upscan on DSC for (b) ZIF-62 glass and (d) ZIF-4 glass.

However, for a material to be called 'glass' a second condition must be met. Namely, a glass transition has to happen. Glass transition is usually taken to imply the freezing of a supercooled liquid to a non-equilibrium, non-crystalline state is understood (*54*). A glass is thus not at its deepest energy minimum (which refers to crystalline state), and tends to relaxation to equilibrium. Glass transition for ZIF-4 and ZIF-62 glass, obtained after quenching the material with cooling rate of 10 K/min, and subsequently measured with heating rate of 10 K/min in a differential scanning calorimeter (DSC), is shown in Figure 2-5 (b and d). Here it should be noted, that the measured T_g values for glass-forming ZIFs hold the same trend as for T_m values, namely, ZIF-62 and ZIF-76-mbIm possess higher T_g (for both materials, T_g is around 590 K) (*17*,*44*) than ZIF-4 (570 K) (*17*).

For the ZIFs with the glass-forming ability, structural differences between crystals and glasses were assessed. For both ZIF-4 and ZIF-62, X-ray total scattering functions show that on the short-range distance scale (< 7Å) the structure is ordered and the atomic distances in crystals and glasses are analogous, whereas the medium-(7–20 Å) and long-range (20 Å) is ordered in crystals, but highly disordered in glasses (*17*). X-ray photon spectroscopy (XPS), Raman and Fourier-Transform Infrared (FT-IR) spectroscopy analyses feature peaks at nearly the same positions, implying that on a local scale, the bond structure does not change significantly during quenching from ZIF-62 crystals to glasses, and local order is thus preserved (*16*). However, suggestions of local structural disorder for ZIF glasses may also be present. For example, a small exotherm was observed during the heating of ZIF-4 in a DSC (*22*). Such a peak would typically be associated with recrystallization of glass, yet in the case of ZIF-4 glass, no long-range order was restored (as confirmed by lack of crystalline peaks on X-ray diffraction pattern). The occurrence of this peak implies nonetheless that a kind of structural ordering takes place during heating of ZIF-4 glass. It is therefore likely that a certain degree of local disorder (i.e. orientational and rotational disorder inside the structural [$ZnIm_4$] tetrahedral) is present, and relaxes to a more ordered state upon heating. So far, no direct structural evidence has been obtained, however, this observation opens future exciting possibilities for ZIF glass investigations, as it could shed more light on the glass formation mechanism.

2.2.3. SUMMARY

In this section, the ZIF glass formation mechanism and structural characteristics were introduced. The possible explanations for the different range of temperatures between melting and decomposition processes were addressed. Comparing the thermal response of ZIF-4 and ZIF-62, a similar decomposition temperature is observed. However, their melting temperature differs by around 100 K, with ZIF-4 having a higher melting point. The author believes this is caused by the phase transformation from ZIF-4 to the high-density ZIF-zni phase, leading to an increase in thermal stability of the crystals. The presence of larger benzimidazolate moieties in the ZIF-62 structure hinders the phase transformation, however, the melting happens at a

lower temperature, leading to the extension of temperature range between T_m and T_d. The T_m value increases with ligand size, as shown for ZIF-62 and ZIF-76-mbIm, however, the decomposition temperature does not follow the same trend. At present, ZIF-62 is believed to be the glass-forming ZIF with the largest range between T_m and T_d values.

For the aforementioned reasons, the author chose to focus on ZIF-62 for the duration of this thesis. This ZIF phase refers to the $Zn(Im)_{2-x}(bIm)_x$ with *cag* topology, where the *x* value can be adjusted in a certain range (this will be addressed in more detail in section 2.3.2). It is characterized by viscosity of $10^{5.1}$ MPa·s at T_m (which is of similar range to that of silica being $10^{5.5}$ MPa·s at T_m) (*16*), fragility index of $m = 23$ (once again comparable to that of silica, being $m = 20$) and ultrahigh glass-forming ability calculated as T_g/T_m ratio (0.84). Its high structural stability upon heating was also confirmed (*41*). With this particular set of characteristics, ZIF-62 is the most promising candidate for producing large, homogenous samples of ZIF glass formers known so far.

CHAPTER 3. MODIFICATION OF THE CHEMICAL COMPOSITION OF ZIFS AND ITS EFFECT ON GLASS-FORMING ABILITY

One of the characteristics of ZIFs that has attracted a lot of attention from many researchers is the possibility of exchanging secondary building units in their structure. This can be performed by 2 different approaches: exchanging either the metal nodes or the ligands in their structures. As of the current state of literature, to the best of the author's knowledge, no review has been published on the subject of how the glass-forming ability is influenced by changing the chemical composition of the ZIF crystals.

In this chapter, the author decided therefore to assess crystal and glass-forming ability dependence on building blocks in various ZIFs. In chapter 3.1, the influence of substituting the zinc node with another metal source is discussed, based on introducing three other metal sources during the synthesis. Then, in chapter 3.2, the influence of changing the ligands on the crystal properties and glass-forming ability is described. It is hoped that this chapter sheds the light on the factors that can guide future ZIF glass investigators during their journey to the discovery of new glass-forming ZIFs.

3.1. BIMETALLIC ZIFS

Crystalline ZIFs can be composed of many different transition metal ions. The most common metallic nodes are zinc (e.g. ZIF 4, ZIF-8, ZIF-11, ZIF-62) (*23,46*) and cobalt (e.g. ZIF-12, ZIF-21, ZIF-65, ZIF-67) (*23*), but others, such as cadmium (*55*), copper (*56*, *57*) or indium (*58*), have also been investigated. One approach to obtain bimetallic ZIFs is to exchange a part of the nodes with another metal node, with the final obtained crystal being either one phase with 2 metallic nodes in the framework or a mixture of 2 phases. This approach was used for the following chapters of this work. ZIF-62 was chosen as the subject of the investigations due to its easy synthesis procedure, high yield of synthesis and high glass-forming ability. Three candidates for second metal sources (cobalt, cadmium, copper) were identified and introduced during solvothermal synthesis process (run according to synthesis procedure of ZIF-62 (*23,46*)). The crystals thus obtained were then characterized, and, in case of successful introduction of second metallic node, the glass-forming ability of the products was studied.

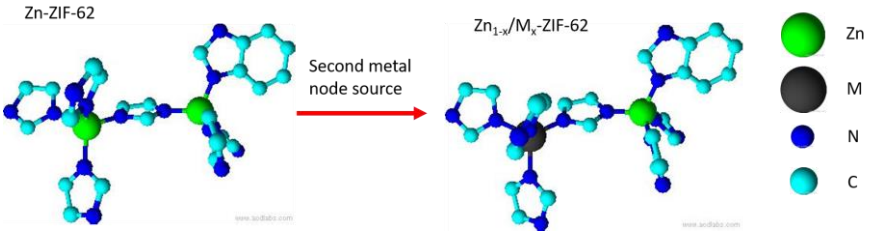

Figure 3-1 Schematic representation of introducing the second metallic node into the structure of ZIF-62.

3.1.1. COBALT-ZINC BIMETALLIC ZEOLITIC IMIDAZOLATE FRAMEWORKS

The substitution of zinc in ZIFs by cobalt has been widely studied, mostly based on the ZIF-8 ($Zn(2\text{-}mIm)_2$) and ZIF-67 ($Co(2\text{-}mIm)_2$) phases (*59–61*). Both phases have the same topology (*sod*). For this system, it was possible to mix two metal sources during synthesis and produce mixed-node samples. Surprisingly, the results are not analogous between studies, but differences can be easily spotted. For example, when describing the influence of the addition of cobalt source on obtained crystal size, Zareba et al. (*59*) showed an increase in crystal size with the cobalt addition when solution stirring synthesis method was used. However, in the case of the reaction-diffusion framework synthesis method (*61*), samples with both zinc and cobalt metal nodes were smaller than those produced with zinc (pure ZIF-8) or cobalt (pure ZIF-67) crystals, and their size decreased with increasing cobalt content. Discrepancies were also observed in terms of surface area changes observed with the introduction of cobalt nodes. And so, in Ref. (*59*), Brunauer-Emmett-Teller (BET) surface area was higher for the zinc-based ZIF-8 than for cobalt-based ZIF-67, whereas in (*60*), the same property showed the opposite relation. This illustrates the fact that synthesis parameters very strongly influence the outcome of the process. In this particular case, it is most likely linked with the synthesis method itself, yet it was shown that even in case of the same synthesis method, parameters such as solvent type (*62*), synthesis time (*51*) or pH of the environment (*63*) can influence the produced crystals and their properties. Such discrepancies are challenging, as they lead to difficulties in predicting the influence of chemical changes on properties of obtained crystals. This means extensive experimental work needs to be performed in order to describe this relationship, including the influence of synthesis parameters.

According to the literature, it is possible to synthesize ZIF-62 with both Zn and Co metallic nodes (*34*,*64*,*65*), where the obtained cobalt-containing phases have a structure analogous to ZIF-62. Obtaining a phase with Zn-ZIF-62-like structure after substitution of zinc with cobalt may be possible due to the small difference in ionic radii between Zn^{2+} (6 Å) and Co^{2+} (5.8 Å) (*34*). Such a small variation means that the substitution of Zn by Co will not lead to the creation of high stresses in the framework. For comparison of the cobalt-ZIF-62 phases obtained in this work and phases obtained

in other literature references (*34*,*64*,*65*), the phase obtained in Paper II will be designated as Co-ZIF-62$_{\text{Paper II}}$. In the case of referencing to one, specific reference, the 'Literature' subscript term will be exchanged to the reference number), e.g. Co-ZIF-62$_{(64)}$. The samples with zinc partially substituted by cobalt will be designated as $Zn_{1-x}Co_x$-ZIF-62, with analogous subscript designations.

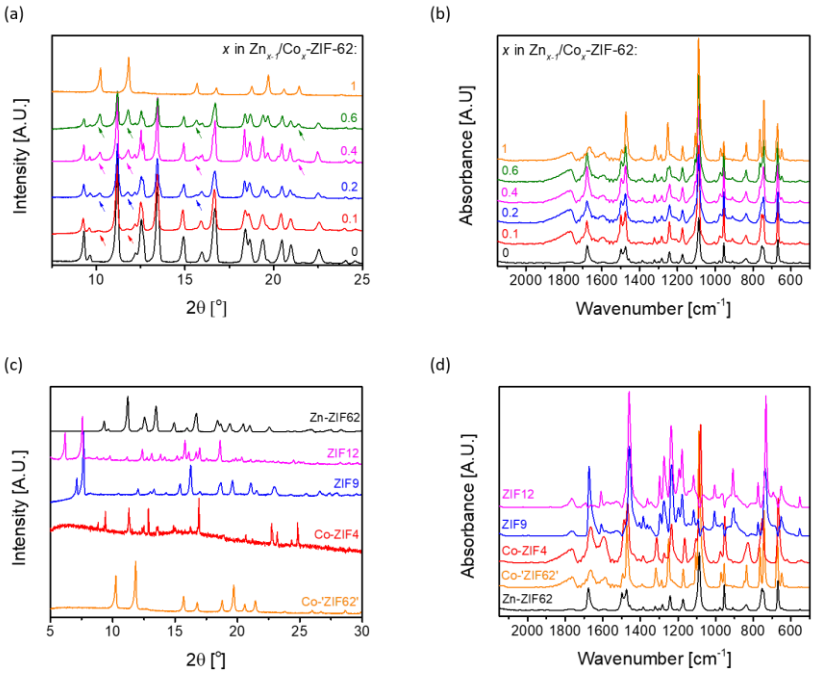

Figure 3-2 Structural characterizations of newly obtained Co-ZIF-62 phase. (a) XRD patterns for $Zn_{1-x}Co_x$-ZIF-62 with changing cobalt ratio (x value). Arrows indicate the positions of the newly present peaks appearing with the addition of cobalt. (b) FT-IR spectra of the $Zn_{1-x}Co_x$-ZIF-62 samples. (c) XRD patterns of Co-ZIF-62$_{\text{Paper II}}$ phase and three other known Co-ZIFs. (d) FT-IR spectra for Co-ZIF-62$_{\text{Paper II}}$ and three other known Co-ZIFs.

The introduction of cobalt source during the solvothermal synthesis of ZIF-62 leads to the formation of a new phase, as can be observed on powder XRD patterns (Figure 3-2 a) (Paper II). A secondary phase appears with the addition of cobalt nodes, and its peaks increase with increasing cobalt substitution. Comparing the XRD patterns, it is clearly visible that the Zn-ZIF-62 and the Co-ZIF-62$_{\text{Paper II}}$ phases have different structures. This new phase was not observed in investigations performed by other authors (*34*,*64*,*65*). A number of cobalt-based ZIF phases, with imidazolate and benzimidazolate ligands, were synthesized (namely, Co-ZIF-4, ZIF-9, and ZIF-12) and compared to the obtained phase. None of them display the XRD pattern (Figure 3-2 c) nor the FT-IR spectrum (Figure 3-2 d) analogous to the Co-ZIF-62$_{\text{Paper II}}$ phase. This indicates this Co-ZIF phase is a new, different phase, with a long-range order

different from those obtained in other works (*34*,*64*,*65*). This suggests the introduction of cobalt facilitated observation of polymorphic transitions in the Co-ZIF-62 phase.

Polymorphism in crystalline ZIFs has been described and investigated for, e.g., $Zn(Im)_2$ (*51*,*66*) and ZIF-8 (*67*). In both cases, changes in synthesis time led to the formation of denser crystals, according to the Ostwald's rule of stages. As one example, for $Zn(Im)_2$ composition, ZIF-zni was obtained with sufficient extension of synthesis time in both solvothermal (*66*) and solution mixing synthesis method (*51*). Accordingly, the Co-ZIF-$62_{\text{Paper II}}$ is most likely a less dense phase, formed prior to the formation of Co-ZIF-$62_{\text{Literature}}$ phase. Comparing the synthesis conditions used in this work with those used in literature, a difference in synthesis time can be noted. In paper II, the synthesis time was 3 days, whereas it was 5 days and 7 days in Ref. (*34*) and Ref. (*64*) respectively. These results accord well with suggested explanation – shorter synthesis time leading to the formation of a less dense phase of Co-ZIF-62. Further investigation into the polymorphic transitions in ZIF-62 needs to be performed in order to confirm and widen our understanding of the structural evolution of the ZIF-62 phase.

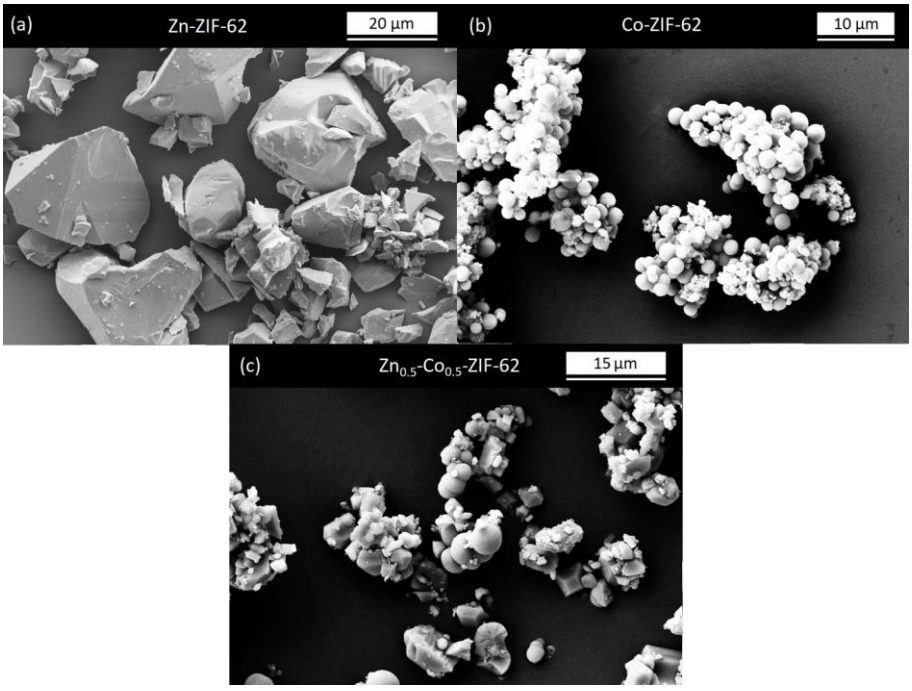

Figure 3-3 Scanning electron microscope images obtained for as-synthesized crystals of (a) Zn-ZIF-62, (b) Co-ZIF-62, (c) $Zn_{0.5}$-$Co_{0.5}$-ZIF-62.

Scanning electron microscope (SEM) images show changes in powder particle morphology with the addition of cobalt (Figure 3-3 a-c). Zn-ZIF-62 powder particles

have irregular shapes, with the size up to 30-40 µm. In contrast, Co-ZIF-62 crystals are spherical, with a much smaller size of about 1-2 µm. The mixed Zn/Co crystals, $Zn_{0.5}$-$Co_{0.5}$-ZIF-62 (Figure 3-3 c), feature a combination of the two morphologies that can be observed for the pure Zn and Co-based phases. The visible differences in crystal morphology agree with the phase separation observable in the XRD patterns (Figure 3-2 a). Energy dispersive X-ray Spectroscopy analysis confirms the mixed Zn/Co crystals contain both metal nodes (Figure 3-4 b).

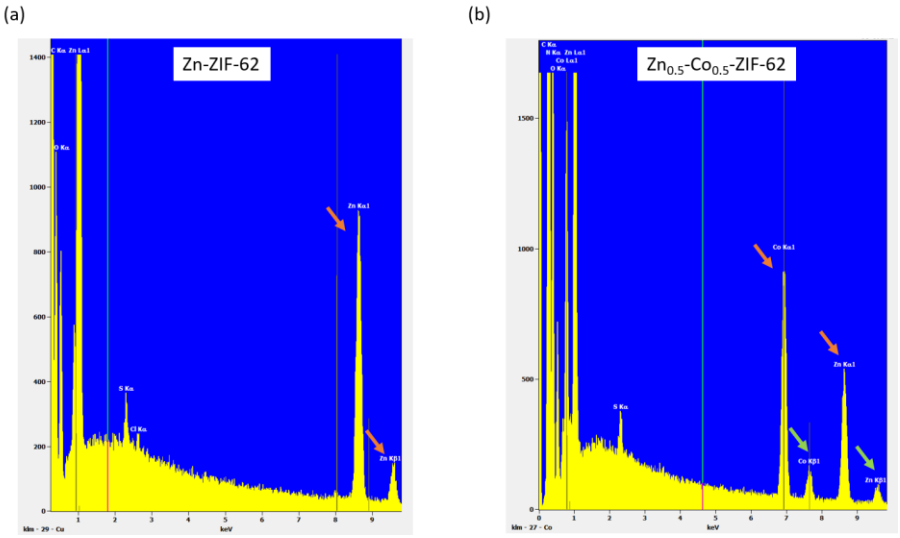

Figure 3-4 Examples of Energy Dispersive spectra obtained for (a) Zn-ZIF-62 and (b) $Zn_{0.5}$-$Co_{0.5}$-ZIF-62. The orange arrows point to peaks coming from zinc, whereas the green arrows point to peaks from cobalt.

Melting temperatures of $Zn_{1-x}Co_x$-ZIF-$62_{\text{Paper II}}$ were measured by differential scanning calorimetry (Figure 3-5 a). Measured T_m values are nearly the same (around 710 K) for Zn-ZIF-$62_{\text{Paper II}}$ and Co-ZIF-$62_{\text{Paper II}}$. This suggests the full substitution of zinc by cobalt does not affect the thermal stability of the obtained ZIF for the phase obtained during this work. However, comparting the T_m value of Co-ZIF-$62_{\text{Paper II}}$ with Co-ZIF-$62_{(64)}$, it is clearly visible that the Co-ZIF-$62_{(64)}$ has a slightly lower T_m of about 705 K. Samples with both zinc and cobalt exhibit lower T_m values than those with just zinc (Zn-ZIF-$62_{\text{Paper II}}$) and cobalt (Co-ZIF-$62_{\text{Paper II}}$) metal nodes. This suggests systems with two phases are less thermally stable than those with one metal node. The lowest T_m values (about 696-697 K) were obtained for samples with x of around 0.1-0.2. The binary phase diagram for Zn-ZIF-$62_{\text{Paper II}}$ and Co-ZIF-$62_{\text{Paper II}}$, constructed according to the obtained data for all of the Zn_{1-x}-Co_x-ZIF-$62_{\text{Paper II}}$ samples, is shown in Figure 3-5 a. As the DSC measurements were not performed in equilibrium conditions but with a heating rate of 10 K/min, the author notes that the values are overestimated. The (Zn-ZIF-$62_{\text{Paper II}}$)-(Co-ZIF-$62_{\text{Paper II}}$) binary diagram

(Figure 3-5 a) suggests two synthesized phases form an eutectic mixture around x = 0.1-0.2. In such mixtures, the surface atoms between the two phases interact with each other, which weakens the chemical bonding of the phases. This, in turn, leads to a decrease in the melting temperature, compared to melting points of pure phases.

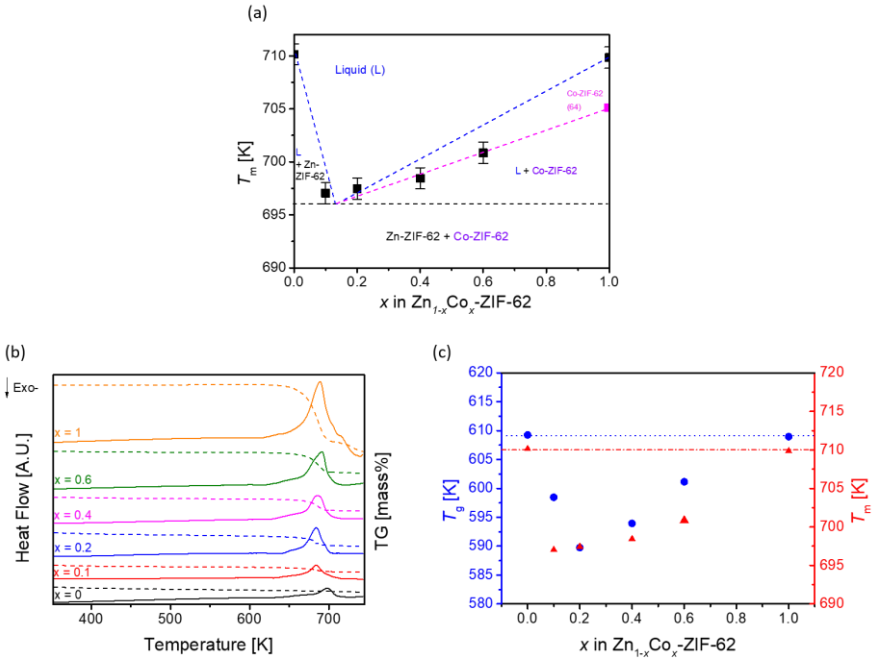

Figure 3-5 Thermal response of Zn_{1-x}-Co_x-ZIF-62 samples. (a) Melting points measured for samples with different cobalt content. Note that a reference point for Co-ZIF-62$_{(64)}$ was added (pink point). Dashed lines are added as a reference for eyes. The black dashed line represents the minimum of the melting points (solidus line). (b) Melting peaks observed during heating of Zn_{1-x}-Co_x-ZIF-62 samples (solid lines), together with the mass change measured with thermogravimetry (TG, dashed lines). Note the increase of the melting peaks' areas and the parallel increase of the mass change with an increase of the x values, (c) Comparison of the changes in glass transition temperature (blue points) and melting temperature (red points) with changing x values. Note that both parameters follow an analogous trend.

Another phenomenon worth mentioning is the melting peak shape and size changes with the introduction of cobalt nodes and a further increase of their content in Zn_{1-x}-Co_x-ZIF-62$_{\text{Paper II}}$ (Figure 3-5 b). The higher the x values, the bigger the peak area, which connects to higher enthalpy needed for melting to take place. The sample weight decrease with increasing x (measured by thermogravimetric measurement – TG, and shown by the dashed line for each composition) implies that two processes take place simultaneously: melting and partial decomposition of the Co-ZIF-62$_{\text{Paper II}}$ phase. The lower temperature of the beginning of the decomposition process in Co-ZIF-62 (as compared to Zn-ZIF-62) has also been noted in other works (*64*,*65*). In these reports, the substitution of zinc by cobalt had a limited impact on melting, but

much more significant one on the decomposition process of ZIF-62 phase. As described in section 2.2, melting happens when one metal-ligand bond breaks in one tetrahedral structural unit, whereas the decomposition occurs when more than one coordinative bond break. The decrease of range between the melting temperature and the decomposition temperature suggests the introduction of cobalt metallic nodes leads to increasing the probability of occurrence of the bond breakage event. The higher the probability of bond breakage, the higher the chance that two bonds break in one tetrahedral structural unit. The decomposition is also visible macroscopically – the glass samples with increasing cobalt content display an increase in bubble content, forming glass foam, analogous to those obtained for Zn-ZIF-4 after melt-quenching.

DSC upscans of samples after melt-quenching of $Zn_{1-x}Co_x$-ZIF-$62_{\text{Paper II}}$ confirm that all the samples feature a glass transition behavior upon heating. The measured glass transition temperature (T_g) follows the same trend as T_m values (Figure 3-5 c). The lowest T_g was observed at around $x = 0.2$ being around 590 K, whereas the T_g for Zn-ZIF-$62_{\text{Paper II}}$ and Co-ZIF-$62_{\text{Paper II}}$ were both around 610 K. The decrease of T_g for mixtures of phases forming eutectic mixtures occurs as the intermolecular interactions play an important role on T_g values (*68*). It is therefore not surprising that a deviation from ideal mixtures is observed not only for the melting point but also for the glass transition. In ref. (*64*), a decrease in T_g for Co-ZIF-$62_{(64)}$ sample was observed, compared to Zn-ZIF-$62_{(64)}$. For glass transition temperature, the change is around 30 K – and therefore much more significant than for the melting point (where the difference was about 5 K). This suggests that the partial decomposition noted during the melting of the samples could have led to further weakening of the bonds between two phases. However, further investigations of this phenomenon are needed for a deeper understanding of the structural reasons behind this observation.

Raman spectra of the obtained glasses (Figure 3-6) feature the appearance of an extra peak for samples containing cobalt. The wide peak is observed around 3200 cm^{-1}, which refers to –OH groups, indicating the presence of water in samples with cobalt nodes. This suggests that the introduction of cobalt changes ZIF-62 from hydrophobic to hydrophilic. Unfortunately, it was not possible to obtain spectra for crystalline samples, as they decomposed under the laser beam. The nature of interactions of water with different crystalline ZIFs has been discussed before in terms of their structures (*69*). A number of factors contributing to hydrophobic or hydrophilic behavior have been identified, including topology, linker functionalization or porosity change. As no linker functionalization changes were introduced in the present study, the topology of the initial crystal and porosity change are the most likely reasons for the possible change of glass behavior. The influence of modifying an initial phase of a ZIF with the same structural units has been studied only in the case of $Zn(Im)_2$ so far (*51,66*). During melt-quenching, two ZIFs with the same chemical composition but different topologies, ZIF-*nog* and ZIF-*zec* exhibited the same characteristic transitions (framework collapse, recrystallization, melting) but at different temperature points, whereas ZIF-zni melted at a slightly lower temperature than the other phases (*51*).

The glass transition temperature of all three phases happened however at very similar positions (in 3 K range) (*51*), which suggests only small structural changes occurred during melt-quenching from another initial crystal. On the other hand, the increase of synthesis time led to small, yet systematic changes in T_g values for glasses obtained from the same initial crystalline phase (*66*). This was attributed to the formation of more structural defects in the synthesized crystals, and thus in the vitrified glasses. It is nevertheless difficult to conclude how significant is the influence of the initial crystalline phase on the structure of glass, which somehow influences the hydrophobic or hydrophilic behavior change. The second probable reason is the change of porosity with the introduction of cobalt. The increase of porosity was observed for Co-ZIF-$62_{(64)}$ glass when measuring CO_2 gas absorption. As CO_2 absorption was shown to be correlated with the water absorption (*69*), it could be an indication that with the addition of cobalt, Co-ZIF-62 glass becomes more sensitive to water presence, and the increase of porosity is thus a probable reason for the change of water interactions for Co-ZIF-$62_{\text{Paper II}}$ phase.

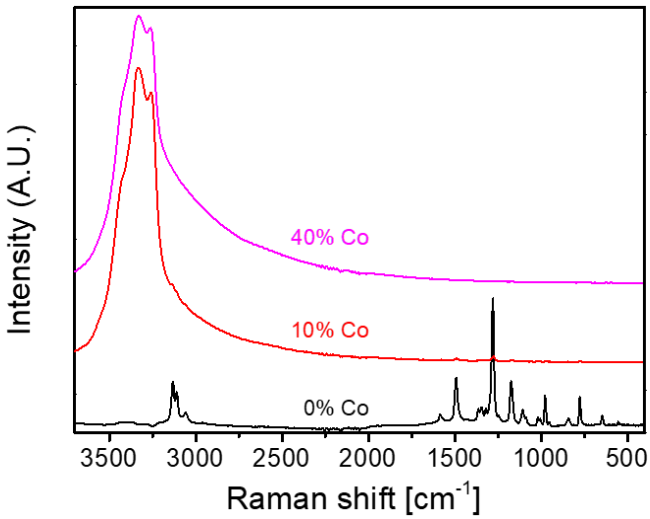

Figure 3-6 Raman spectra obtained for samples with x = 0 (black line), x=0.1 (red line) and x=0.4 (pink line).

To summarize section 2.3.1.1, after introducing a cobalt metal source during the solvothermal synthesis of ZIF-62, a new, cobalt-containing phase was obtained, which is characterized by a structure different from those of Co-ZIF-62 found in the literature. Melting temperature changes with cobalt content indicate that the formation of the eutectic mixture of Zn-ZIF-62 and Co-ZIF-62 phases. Melt-quenched glasses were obtained for all the compositions, and their glass transition temperatures follow the same eutectic trend as the melting temperatures.

3.1.2. OTHER NODE-EXCHANGE TRIALS IN ZIF-62

In order to assess the crystal forming ability of other bimetallic ZIFs, after reviewing literature, two more candidates were chosen to try to synthesize a Zn_{1-x}/M_x-ZIF-62 (where M is either Cu or Cd node). Cadmium forms a series of imidazolate frameworks with ligands such as 2-methylimidazolate, 2-ethylimidazolate or 2-nitroimidazolate (*55*). By adjusting the solvothermal and organic-based acid diffusion synthesis procedures, polymorphic phases were obtained for tested composition, with $Cd(2\text{-mIm})_2$ (where 2-mIm is 2-methylimidazolate) and $Cd(2\text{-eIm})_2$ (where 2-eIm is 2-ethylimidazolate) forming 4 polymorphs each (*55*). These Cd-based ZIFs were characterized by a low number of metal atoms per unit volume (1.85 – 3.51 nm^{-3}), large porosity (up to 3010 m^3g^{-1}) and high thermal stability against decomposition (to around 700 K). This may be linked with their greater structural unit sizes. Due to the greater size of cadmium atom (van der Waal's radius of 1.58 Å, compared to 1.36 Å for zinc, ionic radii: 0.78 Å for cadmium, 0.6 Å for zinc), the distance between two cadmium nodes was *ca*. 0.4 Å bigger than the distances between two Co or Zn atoms in analogous structures (*55*). The metal-ligand bond was also measured to be 0.2 Å longer than in the case of Co-N and Zn-N frameworks (*55*). Furthermore, CdIF-1 (cadmium-based ZIF of chemical composition $Cd(2\text{-mIm})_2$ and *sod* topology) is structurally analogous to zinc-based ZIF-8, which allowed to substitute part of zinc by cadmium nodes (*70*,*71*). The structural features (e.g. unit cell size or shifts in XRD peak positions) of the partially exchanged samples displayed systematic changes, which implies that facile fine-tuning of intermediate structures could be possible for Zn/Cd-ZIF-8 system (*70*).

Copper forms a number of both two- and three-dimensional polymorphs of various colors for $Cu(Im)_2$ composition (*56*,*72*). This series is especially important due to their potential practical application as catalysts (*56*). It has also been observed that imidazolates form an anticorrosive layer on copper metal (*56*). Moreover, three of the Cu-based polymorphs demonstrated a highly enhanced photocatalytic performance for reducing carbon dioxide with water into ethanol, demonstrating that Cu-based ZIFs could potentially be used as photocatalysts (*72*). Doping of ZIF-8 with Cu^{2+} has also been successfully performed in Ref. (*73*), where the x for $Zn_{1-x}Cu_x$-ZIF-8 was in the range between 0.1 and 0.25, and at $x = 0.5$, the only amorphous product was obtained. For synthesized crystals, an increase in copper content influenced the nucleation rate, i.e., with higher Cu content, fewer nucleates were formed, leading to the increase of particle size of obtained crystals (*73*). Moreover, as Cu^{2+} and Zn^{2+} have similar ionic radii (0.71 Å and 0.74 Å respectively), no significant framework distortions were observed after the introduction of Cu nodes (*73*). However, the presence of Cu in the framework did not increase the porosity of the framework, and all of the samples showed thermal stability up to around 700 K, based on the TGA measurements (*73*).

Both copper and cadmium are therefore potentially second metallic node candidates for incorporation into the framework structure. In this work, by adding x = 0, 0.1, 0.25, 0.5, 0.75 and 0.9 of second metal source into $Zn_{1-x}M_x$-ZIF-62 (M = Cu or Cd), a series of samples was synthesized by solvothermal method. The XRD patterns of obtained samples (Figure 3-7 a and b) display no significant changes with the addition of the second metal source, indicating that only the ZIF-62 phase was synthesized in all cases. In addition, energy dispersive X-ray spectroscopy analysis did not confirm the presence of Cd or Cu in the crystals, indicating that the second node did not get incorporated into ZIF-62 crystal (Figure 3-8 a and b). However, scanning electron microscope images (Figure 3-7 c) show that the crystal morphology changes with the addition of both copper and cadmium. In the case of cadmium addition, the increase of x value leads to a decrease in variability of crystal size and slight decrease in their mean size. The crystals become also similar in shape – only a small number of irregular crystals is observed for the $Zn_{0.1}Cd_{0.9}$-ZIF-62 sample. On the other hand, the addition of copper leads to an increase in the crystal size of the biggest crystals. Synthesized particles are also highly irregular in shape.

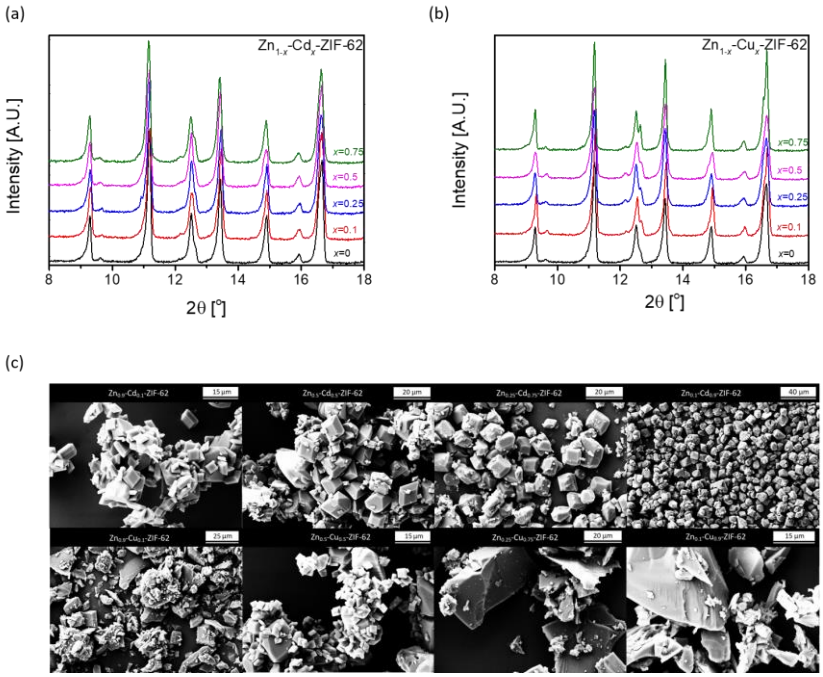

Figure 3-7 The effect of copper and cadmium substitution in ZIF-62. (a-b) XRD patterns of samples with (a) cadmium addition, (b) copper addition. Note lack of changes in the obtained patterns implying the ZIF-62 phase is synthesized in each of the cases. (c) SEM images of the samples obtained with second metallic node substitution. The top line shows samples with cadmium addition, the bottom line shows images obtained with copper substitution.

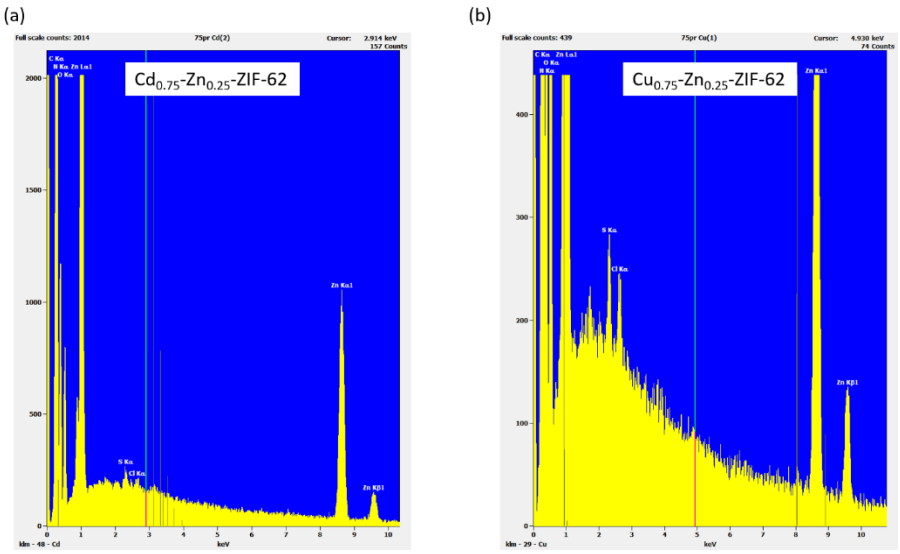

Figure 3-8 The effect of copper and cadmium substitution in ZIF-62. EDS spectra obtained for samples with x = 0.75 for (a) $Zn_{1-x}Cd_x$-ZIF62 and (b) $Zn_{1-x}Cu_x$-ZIF-62.

The abovementioned results show that the addition of the second metal source affects the crystal nucleation and growth processes of ZIFs, and the synthesized crystal size and its variability are related to the interplay between these two processes (*74*). In summary, the more nucleates form, the smaller the crystals obtained. In the case of the ZIF synthesis for Zn-Cd-ZIF-62 and Zn-Cu-ZIF-62 systems described above, two reasons might play a certain role in that.

Firstly, Cd^{2+} and Cu^{2+} ions may form intermediate clusters with imidazolates, hindering the formation of $Zn(Im/bIm)_2$ clusters and thus interfering with the formation of nucleates. This effect would decrease the size of crystals obtained for Zn-Cu systems, where the increase of copper content led to an increase of the crystal size, as a similar dependence was noted for Zn/Cu-ZIF-8 crystals (*73*).

On the other side, the decrease of the concentration of the primary metallic nodes (in this case, zinc) leads to an excess of ligands (comparative to metal nodes) in the solution. Assuming no strong interactions between the second metallic nodes and imidazolates, this should lead to the easier formation of $Zn(Im/bIm)_2$ clusters due to a higher probability of finding 4 ligands in the neighborhood of the zinc node. Such an influence would, in turn, lead to a higher nucleation rate – and thus, more crystals being formed, as was observed in case of Zn/Cd-ZIF-62. This might be related to the difference between zinc-ligand bond and cadmium-ligand bond. The significant differences in the bonds might lead to preferential formation of one of them, and thus hinder formation of the other phase – in this case Cd-ZIF-62. A similar phenomenon

was observed for ZIF-8, where changing metal to ligand ratio during synthesis led to a change of crystal size in an analogous manner (*75*).

Here, the results suggest that the influence of the addictive (in the cases, in which the second metallic node does not substitute zinc in a framework) depends on the strength of interactions of the second node with ligands in the solution. Hence, if strong interactions are present, the addition of the second metal source can lead to hindering the nucleation process, and thus the formation of bigger crystals. On the other hand, with no strong interactions, the addition of the second metal source leads to an increase of ligand to zinc ratio – and thus, increases the nucleation rate.

3.2. LIGAND CHANGES IN ZIFS

The most basic chemical composition of ZIFs is $Zn(Im)_2$. Examples of ZIFs with $Zn(Im)_2$ composition include ZIF-2, ZIF-3, ZIF-4, ZIF-10 and ZIF-64 (*23*). As can be seen, even with the basic chemical composition the number of ZIFs we can obtain is vast, depending on the used synthesis procedures. However, based on results obtained for $Zn(Im)_2$ (*17*,*51*) and $Zn(Im)_{2-x}(2\text{-mbIm})_x$ (*17*,*20*), it can be assumed that the initial ZIF topology (for ZIF crystals with the same ligands in structure) does not have a strong influence on glass-forming ability of ZIFs – although it does play important role in fine-tuning its properties. To further study the influence of ligand on glass formation of ZIF glasses, new ligands need to be introduced in place of the basic Im moieties.

The first type of structural change of the ligand is the addition of benzene ring to imidazolate structure. After such a change, benzimidazolate is obtained (Figure 3-9 b). Examples of ZIFs with benzimidazolate ligands include ZIF-11 (*23*,*27*,*76*,*77*) and ZIF-12 (*23*,*27*,*77*). In this chapter, the author will refer to Im and bIm ligands as the basic ligand forms. Another approach for obtaining a derivative of imidazolate is the substitution of one of the H atoms on the aromatic rings of the basic ligand with a functional group of +1 charge. Typical functional groups forming imidazolate derivatives forming ZIFs include, $-CH_3$, -Cl and $-C_2H_5$ units. In the case of the methyl group ($-CH_3$), depending on the location of the methyl group on the ring, a 2-methylimidazolate or 4-methylimidazolate can be obtained (see Figure 3-9 c and d). Analogously, for basic benzimidazolate moiety, 2-methylbenzimidazolate and 5- methylbenzimidazolate can be produced (Figure 3-9 e and f). This type of change of chemical composition of the ligand will be referred to as ligand functionalization in this work. Examples of ZIFs with functionalized ligands include ZIF-8 ($Zn(2\text{-mIm})_2$, where 2-mIm stands for 2-methylimidazolate) (*23*,*27*,*78*), ZIF-67 ($Co(2\text{-mIm})_2$) (*23*) or ZIF-71 ($Zn(dcIm)_2$, where dcIm is 4,5-dichloroimidazolate) (*23*). This type of structural change has proven especially important for many industrial applications, such as catalysis (*79*) or ligand-driven luminescence (*35*).

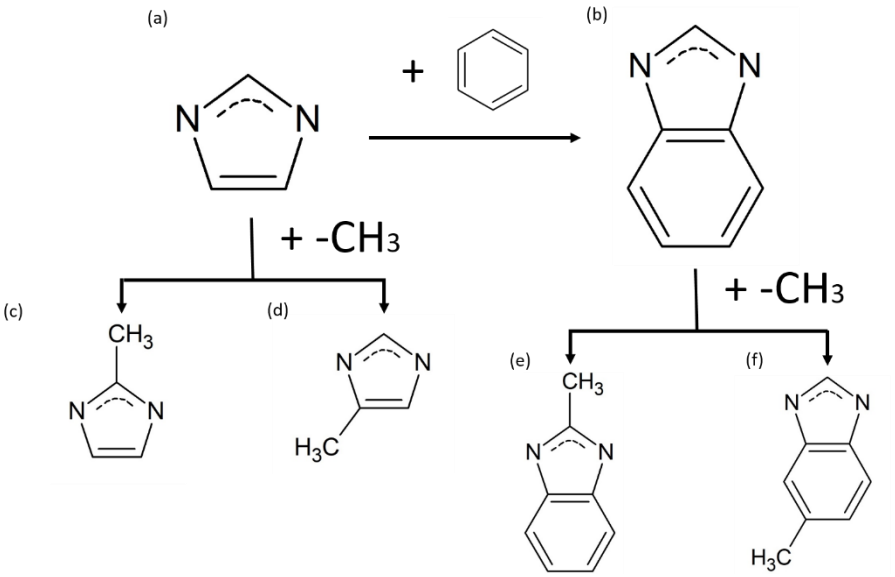

Figure 3-9 Graphical representation of structural ligand changes of imidazolate and its derivatives: (a) Basic imidazolate ligand; (b) Basic benzimidazolate ligand, as a moiety formed from addition of benzene ring to imidazolate structure; (c+d) functionalized imidazolate ligand by addition of methane group: (c) 2-methylimidazolate, (d) 4-methylimidazolate; (e+f) functionalized benzimidazolate ligand by addition of methane group: (e) 2-methyl-benzimidazolate, (f) 5-methylbenzimidazolate.

The last possibility to tune the chemical composition of ZIFs by changing the ligands that will be discussed in this work is using two types of ligands in one ZIF. Such ZIFs will be called mixed-ligand ZIFs. Examples of such materials include ZIF-60 ($Zn(Im)_{1.5}(mIm)_{0.5}$), ZIF-70 ($Zn(Im)_{1.13}(nIm)_{0.87}$) and ZIF-62 ($Zn(Im)_{1.75}(bIm)_{0.25}$). In these phases, the properties can be influenced not only by the introduction of the second ligand but also by varying ligand ratios. This enables further fine-tuning of their structures and/or properties.

Table 3-1 summarizes the described approaches to changing the chemical composition of ligands, chemical structures of imidazolates, and examples of ZIFs for given ligand groups.

Table 3-1. A summary of the ligand change approaches in ZIFs, as discussed in Section 2.3.2

ZIF type – ligand-based division	**Example of a ligand**	**Ligand structure**	**Examples of ZIFs**
'Basic' imidazolate ligand	Imidazolate		ZIF-2 (*23*), ZIF-4 (*23*), ZIF-10 (*23*)
	Benzimidazolate		ZIF-11 (*23*), ZIF-12 (*23*)
Functionalized ligand	2-methylimidazolate	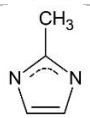	ZIF-8 (*23*), ZIF-67 (*23*)
	4,5-dichloroimidazolate	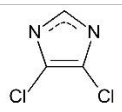	ZIF-71 (*23*), ZIF-72 (*23*)
	5-chlorobenzimidazolate		See: mixed ligand ZIFs
	5-methylbenzimidazolate	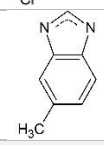	See: mixed ligand ZIFs
Mixed ligand ZIFs	Imidazolate + Benzimidazolate	See: individual ligands above	ZIF-62 (*23*)
	Benzimidazolate + 5-Chlorobenzimidazolate	See: individual ligands above	ZIF-76 (*20*)
	Benzimidazolate + 5-Methylbenzimidazolate	See: individual ligands above	ZIF-76-mbIm (*20*), TIF-4 (*81*)

Two main methods of introduction of ligands can be found in literature: introduction of the ligand during synthesis, and post-synthesis ligand exchange. The first method implies the addition of the desired ligand source during the synthesis process. The ligand gets incorporated into the ZIF structure during nucleation and crystal growth. This method enables the full exchange of ligand. The post-synthetic ligand exchange requires an extra step. First, a ZIF is synthesized with a basic ligand. Afterward, the synthesized crystal is treated in a solution of either another ligand source or functional groups. In the first case, the desired outcome is the exchange of the basic ligand to the more complex added ligand moieties. In the latter case, the H on aromatic rings of ligands are exchanged for functional groups – forming ZIF with functionalized ligands. For such a method, the exchange takes place firstly on the surface. With time, the process diffuses further in the crystal, which means, the full exchange of the ligands does not always happen, enabling the formation of crystals with different chemical compositions at their surface than in their core.

In this work, the author will focus on the first approach to describe the influence of ligands on the glass-forming ability of ZIFs.

3.2.1. GLASS-FORMING ABILITY OF ZIFS WITH "BASIC" LIGANDS (IMIDAZOLATE, BENZIMIDAZOLATE)

ZIF-4 and mixed-ligand ZIF-62 were one of the first discovered ZIFs with glass-forming ability. The melting and decomposition of ZIF-4 (or rather, ZIF-zni) and ZIF-62 were described in Section 2.2.1. The other systems based solely on the "basic ligand" are $M(bIm)_2$ ZIFs (where M stands for metallic node). To the best of author's knowledge, two of such ZIFs were tested before as a part of another Ph.D. work (*82*), namely, ZIF-7 ($Zn(bIm)_2$, *sod* topology) and ZIF-11 ($Zn(bIm)_2$, *rho* topology). Neither of them featured melting prior to decomposition upon heating, which has been ascribed to high steric hindrance of the bigger ligand moiety (*82*).

3.2.2. INFLUENCE OF LIGAND FUNCTIONALIZATION ON GLASS-FORMING ABILITY

The influence of introducing new ligands in ZIF crystals on their glass-forming ability is a wide subject that remains an open question and should be further researched. This section will summarize the published data considering the glass-forming ability of ZIFs with functionalized ligands, and compare them to 'basic ligand' systems.

To the best of author's knowledge, the ZIFs with functionalized ligands that can be molten prior to decomposition are ZIF-76 (*44*), ZIF-76-mbIm (*44*) and TIF-4 (*17*). To remind the reader, these systems have chemical formulas of: ZIF-76 - $Zn(Im)_{1.62}(5\text{-}ClbIm)_{0.38}$, *lta* topology; ZIF-76-mbIm - $Zn(Im)_{1.33}(5\text{-}mbIm)_{0.67}$, *lta* topology; and TIF-4: $Zn(Im)_{1.5}(5\text{-}mbIm)_{0.5}$, *cag* topology (*81*). On the other hand, one

of the most commonly researched ZIF crystals with a functionalized linker, ZIF-8 ($Zn(2\text{-}mIm)_2$, *sod* topology (*23*)) does not melt.

To explain the lack of melting of ZIF-8, the potential of mean force (PMF) between reaction coordinates was calculated by Gaillac *et al.* (*24*) for three systems: ZIF-4, ZIF-zni, and ZIF-8 ($Zn(2\text{-}mIm)_2$. For each system, PMF was calculated in two cases: where the reaction coordinates are Zn and N atom ($PMF_{Zn\text{-}N}$), and where the reaction coordinates are set at Zn atom and center of mass of the ligand ($PMF_{Zn\text{-}Im}$). This described the influence of the functional group, in the first case, on isolated Zn-N bond and, in the latter case, on Zn-N bond taking the whole 2-mIm ligand into consideration. Based on their results, the $PMF_{Zn\text{-}N}$ and $PMF_{Zn\text{-}Im}$ values for frameworks with the melting ability were similar, whereas a significant difference was observed for ZIF-8. In this case, the $PMF_{Zn\text{-}Im}$ value was significantly larger than $PMF_{Zn\text{-}N}$ value, meaning that the ligand environment plays an important role in strengthening the coordinative bond for ZIF-8.

Another non-meltable system is JUC-160, which is a mixed-ligand system of the chemical composition of $Zn(2\text{-}mbIm)_{0.75}(bIm)_{1.25}$ and *gis* topology (*82*). In this case, the methyl group is also substituted in the same position as in ZIF-8, suggesting $–CH_3$ group localized between the N atoms on the imidazolate ligand might be a limiting parameter for glass formation ability of the ZIFs.

Moreover, two ZIFs containing another benzimiodazolate-derived ligand with $–CH_3$ group, TIF-4, and ZIF-76-mbIm, were shown to melt upon heating (*17*,*20*). For this particular ligand, the methyl group is located on the benzene ligand – and thus further away from nitrogen atoms (see: Figure 3-9). Substitution of $–CH_3$ group by –Cl group on the benzene ring of benzimidazolate ligand, thus obtaining ZIF-76, did not affect its glass formation ability – ZIF-76 can also be melt-quenched to a glass (*20*). This observation accords with the theory that functional groups located further from N atoms of the ligand do not hinder the bond dissociation to the same extent as groups located in nitrogen's neighborhood (thus, closed to the coordination bond in ZIF structure). The lack of melting for ZIF-71 ($Zn(4,5\text{-}bcIm)_2$, *rho* topology) and TIF-5-Cl (Zn(Im)(4,5-dcbIm), *gis* topology) suggests that symmetrical substitution of H atoms on the aromatic rings of the ligands also has a disadvantageous influence on melting ability of ZIFs.

Table 3-2. Comparison of ZIFs tested for glass-forming ability. Mentioned ZIFs have been divided into two categories: ZIFs with glass-forming ability, and ZIFs without the glass-forming ability.

	ZIF Designation	**Chemical Composition**	**Topology**	**Reference**
ZIFs with glass-forming ability	ZIF-4	$Zn(Im)_2$	*cag*	(*17*,*23*)
	$Zn(Im)_2$ (gis)	$Zn(Im)_2$	*gis*	(*17*)
	$Zn(Im)_2$ (zec)	$Zn(Im)_2$	*zec*	(*51*)
	$Zn(Im)_2$ (nog)	$Zn(Im)_2$	*nog*	(*51*)
	$Zn(Im)_2$ (zni)	$Zn(Im)_2$	*zni*	(*51*)
	TIF-4	$Zn(Im)_{1.5}$ $(5\text{-mbIm})_{0.5}$	*cag*	(*17*,*81*)
	ZIF-62	$Zn(Im)_{1.75}$ $(bIm)_{0.25}$	*cag*	(*17*,*21*,*23*)
	ZIF-76	$Zn(Im)_{1.62}$ $(5\text{-ClbIm})_{0.38}$	*lta*	(*20*,*23*)
	ZIF-76-5-mbIm	$Zn(Im)_{1.33}$ $(5\text{-mbIm})_{0.67}$	*lta*	(*20*)
ZIFs without glass-forming ability	ZIF-7	$Zn(bIm)_2$	*sod*	(*82*)
	ZIF-8	$Zn(2\text{-mIm})_2$	*sod*	(*15*,*24*)
	ZIF-11	$Zn(bIm)_2$	*rho*	(*82*)
	ZIF-71	$Zn(4,5\text{-dcIm})_2$	*rho*	(*82*)
	TIF-5-Cl	Zn(Im) (4,5-dcbIm)	*gis*	(*82*)
	JUC-160	$Zn(2\text{-mbIm})_{0.75}$ $(bIm)_{1.25}$	*gis*	(*82*)

All of the discussed ZIFs in this section have been summarized in Table 3-2. The discussion presented in sections above leads the author to conclude, that two factors might increase the glass-forming ability of ZIF with functional groups:

i. The location of the functional group on the aromatic ring – by introducing a ligand close to N atoms on the aromatic ring, the degree of influence on the coordinative bond is prominent. This can, in turn, affect the melting ability of the ZIF, as shown for ZIF-8 and JUC-160. However, with functional groups introduced on the benzene ring in benzimidazolate ligand, TIF-4, ZIF-76 and ZIF-76-mbIm all featuring melting ability.
ii. Asymmetric ligands around the metal node – TIF-4, ZIF-76, and ZIF-76-mbIm all have asymmetric ligands.

The third factor with probable influence on the melting ability of ZIFs with functionalized groups is the electronegativity of the functional group. It is expected that ZIFs with ligands containing functional groups with higher electronegativity will have a smaller probability to melt than those with functional groups of lower electronegativity, provided the groups are located at analogous positions, due to bigger influence of the substitution on the electronic structure of the ligand.

Table 3-3. Comparison of melting temperature T_m and glass transition temperatures T_g for the ZIFs with glass-forming ability known in current literature.

ZIF Designation	T_m **[K]**	T_g **[K]**	T_g/T_m	**References**
ZIF-4	863	565	0.65	(*17*)
$Zn(Im)_2$ (*gis*)	857	565	0.66	(*17*)
$Zn(Im)_2$ (*zec*)	858	578	0.67	(*51*)
$Zn(Im)_2$ (*nog*)	853	575	0.67	(*51*)
$Zn(Im)_2$ (*zni*)	851	575	0.68	(*51*)
TIF-4	740	616	0.83	(*17*)
ZIF-62	710	591	0.83	(*17*)
ZIF-76	724	583	0.81	(*20*)
ZIF-76-5-mbIm	744	590	0.79	(*20*)

Finally, the glass-forming ability of the ZIFs was compared by the reduced glass transition temperature T_{rg}, i.e., the ratio of glass transition temperature to melting temperature (Table 3-3), analogously to calculations performed for ZIF-62 (*16*). For most traditional glass formers, the T_g/T_m ratio is close to 2/3. The higher the T_g/T_m ratio, the higher the glass-forming ability of a system. A larger T_{rg} is also connected to the high viscosity of the glass in the supercooled region or at T_m – which hinders any possible crystallization upon cooling, thus, facilitating glass formation.

The glasses produced from the initial crystal composition of $Zn(Im)_2$ all have the T_g/T_m ratio value of 2/3, as these crystals transform to the dense $Zn(Im)_2$ (*zni*) prior to melting during heating. The mixed-ligand ZIFs have higher glass-forming ability than those with just one ligand in its structure (Im). TIF-4 and ZIF-62 exhibit the highest glass-forming ability (T_g/T_m of ~0.83), suggesting that these glasses could be the best potential candidates for obtaining bulk samples.

3.2.3. CHANGING LIGAND RATIOS IN MIXED LIGAND ZIFS

Most of the mixed ligand ZIFs are characterized by one standard ligand ratio that is typically used by researchers, but fine-tuning of their chemical composition may involve adjusting one extra parameter: changing the ratios between the ligands. This is not a very common approach to address the optimization of crystalline ZIF properties. A number of literature reports can, however, be found concerning the changes in as-synthesized crystals obtained with changing ligand ratios. Such investigations were performed for example for $Zn(Im)_{2-x}(bIm)_x$ composition (*46*), $Zn(2\text{-}mIm)_{2-x}(2\text{-}CHOIm)_x$ (where 2-CHO Im is 2-imidazolatecarboxaldehyde) (*83*) or $Zn(2\text{-}nIm)_{2-x}(5\text{-}nbIm)_x$ (where 2-nIm is 2-nitroimidazolate, and 5-nbIm is 5-nitrobenzimidazolate) (*84*). Here, the author chose to address the ZIFs by their compositions rather than crystal phases, as with changes of ligand ratios, changes in the obtained crystal phase may follow. With the development of melt-quenched ZIF glasses, a number of researchers begun to study the influence of changing ligand ratios on the melt-quenching ability and final properties of obtained glasses (*16*,*65*,*85*). For both ZIF crystals and glasses, ZIF-62 is attracting the most attention so far.

For $Zn(Im)_{2-x}(bIm)_x$ composition, by adjusting the ratio between Im and bIm (thus, changing the x value), three different phases can be obtained after solvothermal synthesis, namely, ZIF-4, ZIF-62, and ZIF-7 (*46*). ZIF-4 was obtained only for $x = 0$, and any addition of bIm resulted in a change of the obtained phase. ZIF-7 phase was obtained for both mixed ligand samples and with pure bIm ligands, provided the x value was higher than ~0.5. For x values higher than 0 but lower than around 0.3, the obtained phase was ZIF-62. Tested x values between ~0.3 and 0.5 resulted in phase mixtures containing both ZIF-7 and ZIF-62. As described above, the ZIF-62 phase features the highest glass-forming ability so far. For this reason, this phase was chosen to study the influence of changing ligand ratios on obtained properties in both existing literature (*16*,*65*) and as a part of this work.

In the present work, by synthesizing crystals with varying *x* values, a varying amount of benzimidazolate was introduced (schematically shown in Figure 3-10 a). Selected XRD spectra are shown in Figure 3-10 b, confirming that all of the synthesized samples were ZIF-62. The *x* values (in $Zn(Im)_{2-x}(bIm)_x$) in synthesized samples were also quantified (denoted as measured *x*) and compared to ligand source ratios added for synthesis (denoted as added *x*) (Figure 3-10 c). The measured values were derived from the liquid NMR spectra of as-synthesized samples. For smaller additions of benzimidazolate, the measured *x* value is higher than the added *x* value. Interestingly, with increasing the bIm source added during synthesis, the deviation between the added and measured *x* values becomes smaller. This is in accordance with literature data (*16*). For both sets of results, added *x* is nearly equal to measured *x* for $ZnIm_{1.7}bIm_{0.3}$. Based on results reported in (*16*), it can be assumed that a further increase of benzimidazolate would lead to obtaining measured *x* values lower than added *x*.

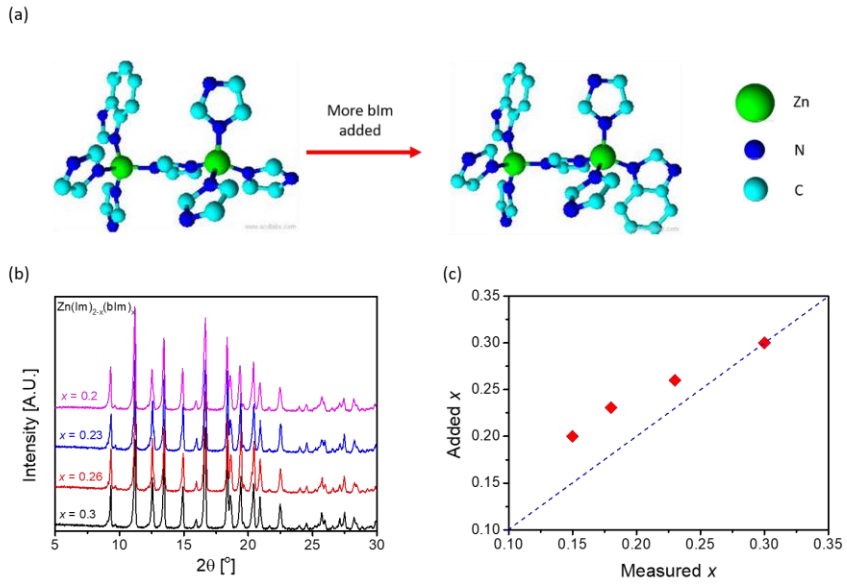

Figure 3-10 (a) Graphical representation of structural changes with the increase of benzimidazolate content. (b) XRD patterns obtained for samples with chosen x content for $Zn(Im)_{2-x}(bIm)_x$ system. (c) x values for $Zn(Im)_{2-x}(bIm)_x$ samples as added during synthesis (y-axis) and calculated based on liquid NMR measurements in as-synthesized samples. The blue line in the guide for an eye of y=x.

With an increase of benzimidazolate content, both melting temperature (T_m) and glass transition temperature (T_g) increase (Figure 3-11 a). Such a dependence is in agreement with experimental results reported elsewhere (*16*,*65*) and could be linked to the increase of steric hindrance with the increase of the content of the bigger size moieties in the structure. Exchange of the imidazolate moiety to the larger

benzimidazolate was shown to increase the constraint of atoms in $Zn(Im)_{2-x}(bIm)_x$ system (*85*). This leads to an increase in energy needed for changing the state of the material and is observed by an increase of both T_m and T_g values. As shown in Figure 3-11 b, the T_g/T_m ratio is nearly the same for all of the tested samples indicating that the increase of the ligand size has a similar influence on both melting and glass transition temperature changes.

A recent study concerning a model for glass transition temperature for ZIFs with imidazolate, benzimidazolate and 5-methylbenzimidazolate ligands (*85*) states that for $Zn(Im)_{2-x}(bIm)_x$ system glass transition temperature can be estimated by equation (3.1):

$$T_g(x) = \frac{154.4}{3-\frac{2+14(2-x)+(26-0.5)x}{11+4x}} \qquad (3.1)$$

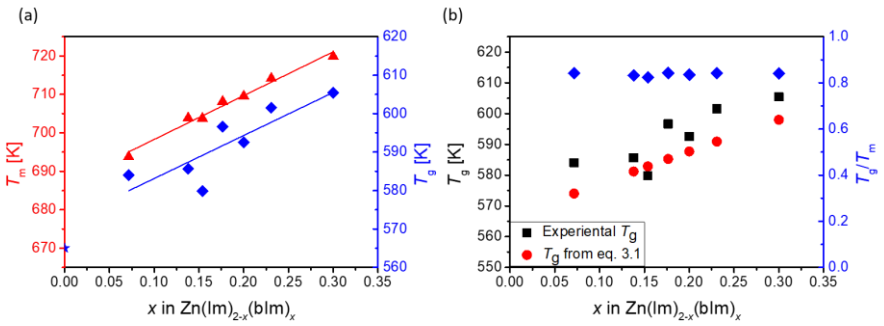

Figure 3-11 Thermal response of the $Zn(Im)_{2-x}(bIm)_x$ samples. (a) Melting temperature (T_m, red triangles) and glass transition temperature (T_g, blue diamonds). The solid lines are used as a guide for an eye. The blue star represents T_g for ZIF-4. (b) Comparison of the measured T_g values (black squares) with those calculated using equation 3.1 (85) (red circles) and T_g/T_m ratios (blue diamonds).

The T_g values calculated with the use of equation (3.1) were plotted together with experimental data points in Figure 3-11 b. The experimental trend seems to be slightly higher than the numerical model, yet the overall comparison presents a good agreement. Further developments of the model extended it to ternary $Zn(Im)_{2-x-y}(bIm)_x(5\text{-}mbIm)_y$ system (*85*). Such ternary glass-forming systems could be especially important in future research for better optimizations of properties of ZIF glasses and open a whole new chapter for tuning chemical compositions of ZIFs in terms of ligand substitution.

3.3. SUMMARY

Crystalline ZIFs have been attracting a lot of attention due to their unique features, such as high intrinsic porosity, which is advantageous in many industrial applications. However, due to their nature, producing a bulk sample without the addition of binding agents or usage of pressure is not possible. Melt-quenching, therefore, may prove to be a break-through solution that enables the up-scaling of ZIF elements to industrial scale. Unfortunately, not all ZIFs feature melting ability, due to their facile decomposition – for a crystalline ZIF to be melt-quenched to glass, melting must occur prior to decomposition upon heating. Only a small number of ZIFs with such characteristics have been found up until now.

In order to find new potential glass-forming ZIF candidates, the influence of the chemical composition of crystals was investigated in detail. Starting with changing the metallic node, the glass-forming ability of Co-ZIF-4 (*65*) and Co-ZIF-62 (*34*,*64*,*65*) indicates that these ZIFs keep their glass-forming ability after substitution of the metallic node. Initial trials to introduce other metallic nodes (such as cadmium or copper) into the ZIF-62 structure applying the same synthetic conditions were not successful, yet, a change in crystal morphology was observed. This observation suggests that cobalt might be the easiest node to substitute for zinc in solvothermal synthesis – to test the influence of other nodes, a change of synthesis conditions might be necessary.

Another approach to changing the chemical composition of crystalline ZIFs is the introduction of other ligands, and this has also been investigated herein. Three different subgroups of imidazolate ligands were specified (see: Table 3-1), namely, 'basic' imidazolate ligands, functionalized ligands, and mixed ligands. For 'basic' imidazolate ligand ZIFs, ZIFs with the chemical composition of $Zn(bIm)_2$ are the only ones that do not display the melting ability, which has been attributed to the high steric hindrance of the bIm groups. By comparing the chemical structure of all the zinc-based ZIFs that have been tested for the melting ability (to the best of the author's knowledge), three factors that could have an influence on melting ability were identified. Those are: the electronegativity of the functional group, the location of the functional group and the symmetricity of the ligand. To be more explicit, based on the author's observations, to increase the probability that the given ZIF will have the melting ability, functional groups should feature small electronegativity, be located further away from the metallic node-N_{ligand} coordination bond, and the ligands should be asymmetric. Finally, changing the ligand ratio is not observed to play a dominant role in the glass formation ability of given ZIF phase – provided that the crystal phases of the products do not change with changing the ligand ratio.

CHAPTER 4. TOWARDS THE FABRICATION OF BULK ZIF-62 GLASSES

As mentioned briefly at the end of Section 2.1, one of the biggest problems with the up-scaling of crystalline ZIFs is the fabrication of bulk samples. By melt-quenching promising candidates, it should be technically capable of obtaining bulk samples of ZIF glasses, which would be of great importance to the industrial applications of these materials.

However, the initial research into ZIF glasses has shown that a number of issues need to be tackled before a bulk, homogenous sample can be produced. The first of these issues is connected with the decomposition processes of ZIFs upon heating, as the temperature range between melting (T_m) and decomposition (T_d) is only a few degrees (as for ZIF-4, where the range is just around 10 K). Therefore, precise temperature control is a very important factor in producing ZIF samples. Most of the furnaces commonly used on laboratory and industrial-scale are characterized by temperature distribution. The temperature differences between different parts of the chamber might be bigger than the range of temperatures between T_m and T_d for many of the ZIFs with melting ability. Another possible problem with temperature control stems from temperature overshoot during heating. All of these issues should be considered when scaling up the fabrication of bulk ZIF glasses.

The second issue connected with the decomposition of ZIFs is facile oxidation at high temperatures. Due to this reason, the assurance of inert atmosphere (either inert gas atmosphere of vacuum) is especially important for bulk sample fabrication.

The high viscosity of ZIF melts is another aspect that should be considered. For instance, the viscosity of the melt-quenched ZIF-62 glass is $10^{5.1}$ Pa·s at melting temperature (*16*), which is close to the viscosity of silica at its T_m ($10^{5.5}$ Pa·s) (*86*). Such a high viscosity of the ZIF-62 melts hinders the homogenization of the glass melt, which leads to the formation of defects in the bulk samples, such as bubbles.

Most of the ZIF glass samples so far are prepared by melt-quenching ZIF crystals in a differential scanning calorimeter. Using a small DSC chamber for melt-quenching allows atmosphere control (minimization of oxygen reminder) and precise temperature control. The size of the sample (around 5 mm diameter) is not however efficient for many experimental characterizations of this novel material. Producing samples of various size and shape would also be an important step towards industrial applications of ZIF glasses.

In this chapter, three different methods were therefore utilized to fabricate bulk ZIF-62 samples. Namely, the samples were prepared using (i) inert atmosphere tube furnace, (ii) hot-press machine, (iii) spark plasma sintering (SPS) (see Figure 4-1). The methods will be described in the following sections, together with the characterization of the obtained materials. A comparison of samples produced will then follow, together with the author's opinions on the perspectives of the fabrication of bulk ZIF glasses.

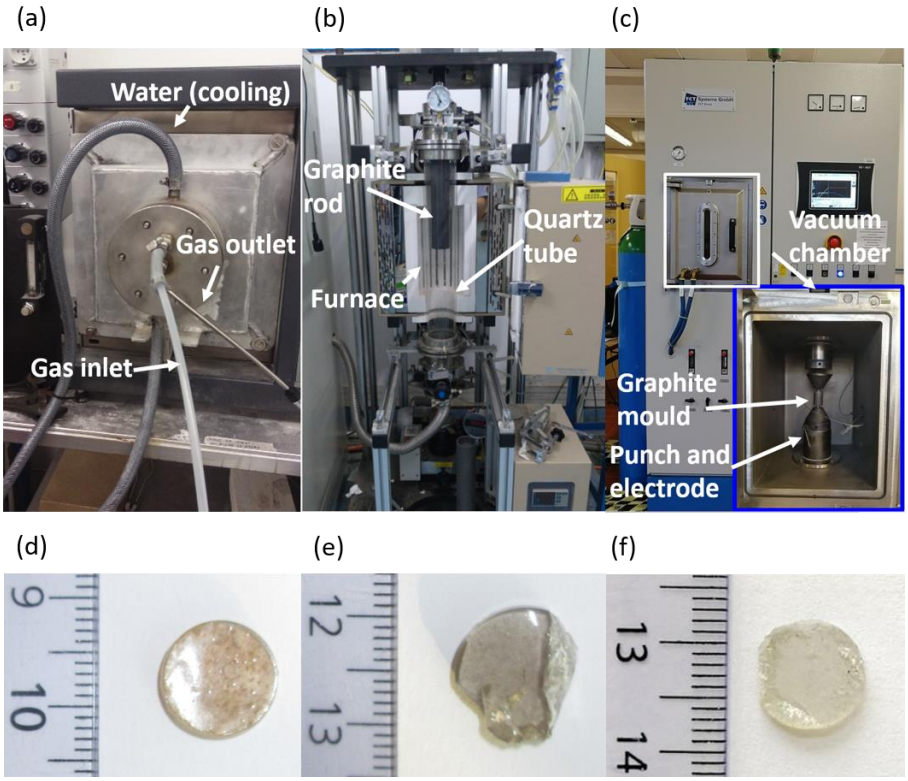

Figure 4-1 Three different methods used for the fabrication of bulk samples described in this section. (a-c) Photos of equipment utilized for each of the proposed methods for the preparation of bulk ZIF glass samples. (a) Inert atmosphere tube furnace; (b) Hot-press machine; (c) Spark Plasma Sintering (SPS) machine. (d-f) Macroscopic images of samples produced by the use of each of the methods. (d) An example of a sample produced in the inert gas furnace; (e) An example of a sample produced in the hot-press machine; (f) An example of a sample produced by SPS method.

4.1. MELT-QUENCHING IN INERT ATMOSPHERE FURNACE

Melt-quenching in an inert atmosphere furnace is relatively simple and quick in preparation. A short description of the sample fabrication method is as follows. Around 250 mg of crystalline ZIF-62 was pressed uniaxially with about 40 MPa pressure to form a pellet. The pellet was then placed and sealed in a tube furnace. A vacuum pump was utilized, and nitrogen gas was used to flush the chamber five consecutive times to remove oxygen from the furnace chamber. Subsequently, the samples were melt-quenched and cooled to room temperature, while a continuous nitrogen flow was applied. A macroscopic image of a produced sample is presented in Figure 4-1 d.

A number of advantages and disadvantages can be noted for this method. The first of the advantages is the facile production method. Lack of many complex steps leads to a simple procedure for glass fabrication, and no special steps need to be undertaken before the quenching process. Due to these reasons, samples can be produced in a timely manner.

Another advantage is the shape of the sample. After using a circular mould, a perfectly shaped cylindrical sample is obtained after melt-quenching, with shape analogous to that of the used pellet. A small shrinkage is observed due to the consolidation of the crystals during sintering and melting. Such a shrinkage could be easily accounted for, based on initial trials. On average, the produced pellets were 13 mm in diameter, whereas the melt-quenched samples were 11 mm in diameter. Glasses could therefore be produced in any shape, as long as a proper mould is available for the preparation of a pellet. Due to high the viscosity of its melt, the shape of the final sample should be analogous to the shape of the produced pellet.

The most prominent disadvantage of using inert atmosphere tube furnace is the existence of observable bubbles in the melt-quenched samples. In produced pellets, crystals are pressed close together, yet a certain level of free space remains between the particles due to shape and size differences. During the melt-quenching, only ambient pressure is present in the chamber and the viscosity of the melts is relatively high, the air bubbles formed from those free spaces cannot escape out of the melt. The bubbles are the biggest defects observed in the bulk samples formed after melt-quenching in the tube furnace.

As the optimization of melt parameters is expected to play a key role in assuring the high quality of obtained samples, the influence of the melting duration change was investigated in Paper III. The melting duration (t_m) refers to the time that a melt was held isothermally at 733 K. This step was introduced to enable homogenization of the ZIF-62 melt prior to the quenching.

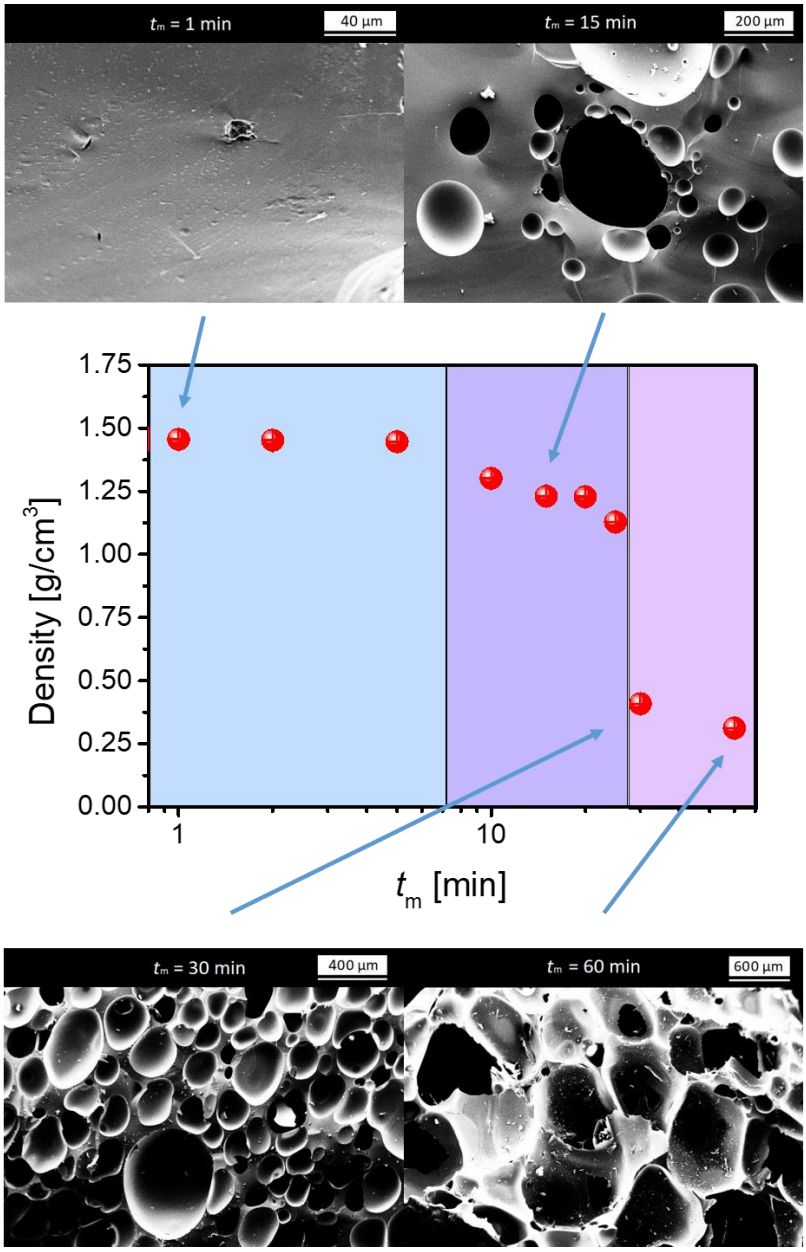

Figure 4-2 Density of the samples produced with varying melting durations. The three regions refer to different stages of the density changes: stable density for 0 <t_m< 6 min (blue background), a slow decrease of density with 6 min <t_m< 25 min (purple background), rapid decrease in density resulting in formation of MOF glass foam for t_m = (30, 60) min. Four SEM images placed above and under the diagram show sample cross-section and bubble structure of samples with t_m = (1, 15, 30, 60) min. Data taken from Paper III.

With the increase of melting duration t_m, a decrease of density accompanied by an increase of a number and size of bubbles inside the samples is observed from the cross-sectional images (as shown in Figure 4-2). For the longest melting durations (30 and 60 min), a drastic decrease in density, and thus an increase in porosity, is observed. As the bubbles become separated by thin walls of the glass, the two samples produced with the longest melting durations became glass foams.

The formation of bubbles and the decrease in porosity are most likely connected with the decomposition of organic ligands. With the decomposition of imidazolate moieties, gas molecules, such as H_2, CO_2, NH_3 could be formed and trapped inside the ZIF melt. With the increase of gas content, more and more bubbles are being formed, up until the late stage. At this time, the gas pressure inside the sample is high enough to cause foaming of the sample, leading to the formation of ZIF glass foams (samples with t_m = (30, 60) min).

These observations show that the decomposition should be taken into account. Even in an inert atmosphere, and at melting temperature much lower than decomposition temperature (T_d), the decomposition plays an important role in the up-scaling of bulk, ZIF glass sample fabrication.

As a certain duration is needed for the warming of the furnace chamber, and, more importantly, the whole sample to heat up to the desired temperature, a longer melting duration is expected to be more advantageous. The longest t_m before the decrease of density (and so, before detectable decomposition takes place) was 5 minutes, as presented in Figure 4-2. Therefore, a melting duration of 5 minutes seems to be the optimum and used in the further research (such as the comparison of the samples in Section 4.4).

4.2. HOT-PRESSING

The second of the used techniques was the hot-pressing technique. For this technique, a crystalline sample was placed between two dies and located in a vacuum furnace. The sample was then subjected to certain pressure (in case of the samples produced as the part of this thesis, the pressure was around 50 MPa) and the sample was subsequently heated to target temperature. Quenching of the sample was conducted after removing the load. The methodology is analogous to that presented in another published work (*87*) – the hot-pressed samples in both this work and in Ref. (*87*) have been produced on the same experimental setup. Surprisingly, another report considering the hot-pressing of ZIF-62 (*88*) concluded that this method did not allow the full melting of a sample with the pressure of 15 MPa and the melting temperature of 723 K (thus, nearly 15 K over the melting temperature of ZIF-62). Based on this observation, it is concluded that the assurance of the temperature distribution in a furnace chamber is as uniform as possible plays an essential role in this process.

However, by increasing the melting temperature, a fully molten glass sample can be obtained, as shown in Figure 4-1.

Certain advantages and disadvantages of using vacuum hot-press for bulk ZIF glass sample fabrication can be named. One of the main advantages is the lack of bubbles – easily observable with a naked eye. The presence of pressure during the melting of the crystalline ZIFs helps in the removal of the bubbles from the melt, in contrast to described before inert atmosphere melt, where no pressure was present. Obtained glasses do not exhibit other typical melt inhomogeneities such as striae, and the glass shows relatively low fluctuations in optical properties (*87*), which suggests that the obtained samples are microscopically homogenous.

The main disadvantage of using this method is that after removing from the metal dies, the samples do not remain intact. The breakage of the samples may be the result of various reasons. First of them might be a breakage during cooling. Even with the load removal prior to the quenching, the stresses in the brittle, vitrified samples can lead to sample breaking into pieces. Another possible explanation could be the adherence of the glass to the metallic die. In this case, sample breakage could occur during the extraction of the sample out of the dies.

Vacuum hot-pressing was performed on a series of samples with changing imidazolate to benzimidazolate ligand ratio. Analogously to designation used in section 3.2.3, the samples were synthesized with varying x value for $ZnIm_{2-x}bIm_x$ chemical composition. To measure the glass transition temperature of the vacuum hot-pressed samples, two upscans were performed in a DSC. The first upscan was performed in order to assure a known thermal history of the last quenching by cooling the sample from the supercooled liquid region with a cooling rate of 10 K/min. Two representative curves for x values of 0.18 and 0.43 are shown in Figure 4-3 a. Surprisingly, two distinct exothermal peaks can be observed – one with a local maximum around 500 K, another with a local maximum around 600 K. This suggests the unstable cooling rate might affect the structure of the glass, leading to the occurrence of a number of peaks during heating. Another explanation might be structural inhomogeneity coming from the high stress upon vitrification in the dies. To explain that phenomena, further structural investigations need to be conducted in the future.

Glass transition temperature was obtained from the second upscan of the samples (Figure 4-3 b). After cooling with a cooling rate of 10 K/min after the first upscan, one T_g peak is observed for the samples. Analogously to melt-quenched samples described in section 3.2.3, glass transition temperature increases with the increase of x. The values obtained for hot-pressed samples are however 15-20 K lower than those obtained for samples melt-quenched under ambient pressure. A more detailed discussion of such behavior will be included in section 4.4.

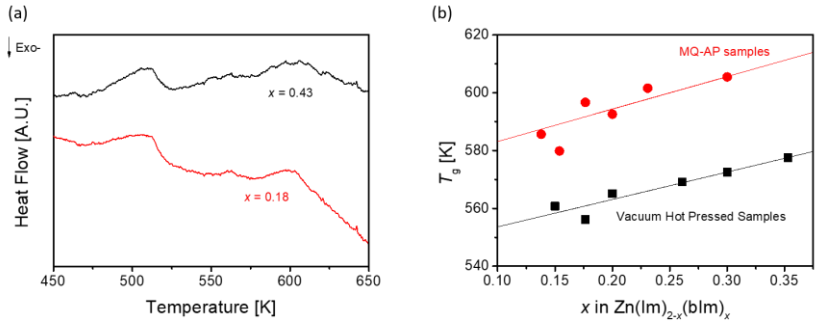

Figure 4-3 Thermal response of the vacuum hot-pressed samples. (a) Heat flow during the first upscan with the heating rate of 10 K/min. (b) Glass transition temperatures for the vacuum hot-pressed samples with varying x-values (black points). The values obtained by ambient pressure melt-quenching (MQ-AP) in the inert atmosphere tube furnace sample have been included for comparison (red circles). The straight lines have been included as a guide for the eyes.

One of the concerns connected with the application of pressure during the fabrication of bulk ZIF glass samples is the possible structural degradation due to the breakage of coordination bonds and the decomposition of ligands (Paper II). FT-IR spectra of hot-pressed and ambient pressure melt-quenching in the tube furnace (Chapter 4.1) samples do not show any differences, implying no significant changes in bond structure are caused by the usage of pressure (Figure 4-4 a). In order to assess possible changes in ligand ratios due to hot-pressing, liquid nuclear magnetic resonance spectroscopy was performed on as-synthesized ZIF-62 crystals and vacuum hot-pressed glass (Figure 4-4 b). Based on integrals of peaks corresponding to hydrogens labeled 1 and 3, ligand ratios were calculated, showing a small difference of around 0.03%.

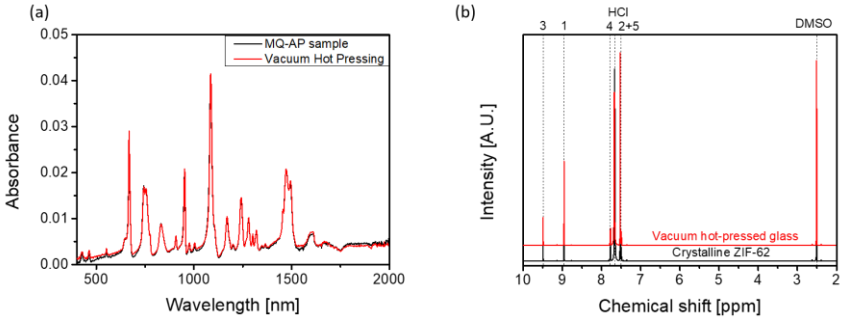

Figure 4-4 Structural characterizations of vacuum hot-pressed ZIF-62 glass as compared to other samples. (a) FT-IR spectra of vacuum hot-pressed sample compared to melt-quenching in ambient pressure (MQ-AP) in inert atmosphere tube furnace sample. (b)H^1 L-NMR spectra for crystalline ZIF-62 and vacuum hot-pressed glass sample. The data taken from Paper II.

To further improve the vacuum hot-pressing methodology, the author suggests addressing the issues connected with the breakage of the samples. One of the possible solutions could be to acquire more precise control of the pressure the sample is subjected to. By assuring that the sample is not loaded while solidifying, it could be feasible to obtain bulk samples with no cracks.

Another approach could be identifying an anti-adhesion agent for the metal dies that will not react with the sample. Such an action could hinder the adhesion of the sample to the dies and therefore prevent the occurrence of sample breakage to some extent.

Proper optimization of the hot-pressing process could lead to the facilitation of obtaining a bulk, glass sample, without any cracks. Such high-quality samples could be a great basis for further investigations, such as mechanical characterizations. As of the current moment, samples with chosen ligand ratios were investigated by indentation studies (see chapter 5.4).

4.3. SPARK PLASMA SINTERING

Spark plasma sintering (SPS) is characterized by short sintering times due to the application of electric current discharge during the process. This particular method is widely used in fields such as powder metallurgy (*89*,*90*), ceramics (*91*,*92*), chalcogenide glasses (*93*,*94*) or glass-ceramics (*94*,*95*).

To the best of the author's knowledge, only one article concerning the usage of the SPS technique for the fabrication of ZIF samples can be found (*39*). In the mentioned work, SPS has been used for the sintering of crystalline ZIF-4 samples. By changing the sintering temperature and pressure during the process, samples of three different phases (ZIF-4, amorphous ZIF-4, ZIF-zni) were obtained. The obtained monoliths were used for large-scale mechanical characterization. Namely, compression tests were performed, confirming that the up-scaled bulk samples could be used for broadening our knowledge about the mechanical response of ZIF materials.

For this production method, carbon paper was first placed in a graphite die to hinder possible adhesion of the sample to the equipment parts. On top of the carbon paper, aluminum foil was placed in order to hinder possible carbon diffusion into the sample during sintering. Powdered ZIF sample was subsequently placed into the die. The die with the sample was then placed in the chamber of an SPS machine. The sintering took place under vacuum, with a certain load applied to homogenize the ZIF melt. After reaching the target temperature, a current was applied to assist in sintering the powder particles.

One of the main advantages of the SPS technique is the homogenization of the fabricated samples (as shown in Figure 4-1 f). Analogous to the vacuum hot-pressed method, the pressure applied during the sintering process allowed the removal of

bubbles. Macroscopically, the samples do not exhibit any defects that could be a result of using the SPS technique. When extracted from the machine, the bulk samples were in the form of one, bulk piece. However, during the removal of the aluminum foil and carbon paper, chipping at the sides of the glass was observed, due to the high brittleness of the sample. The extent of such a phenomenon could probably be avoided with the improvement of the operational experience.

For the SPS work, two types of initial ZIF-62 powders were used: as-synthesized crystalline ZIF-62 (ZIF-62$_{crystalline}$) and ZIF-62 glass powder (ZIF-62$_{glass}$), obtained by grinding samples from the inert gas furnace into small powders. For the first series of produced samples, the load of 5 kN was applied for each trial. Two process parameters were varied for optimization of the sintering process for both ZIF-62$_{crystalline}$ and ZIF-62$_{glass}$ powders: the sintering time (t_s = (2, 5, 7, 10) minutes and sintering temperature (T_s).

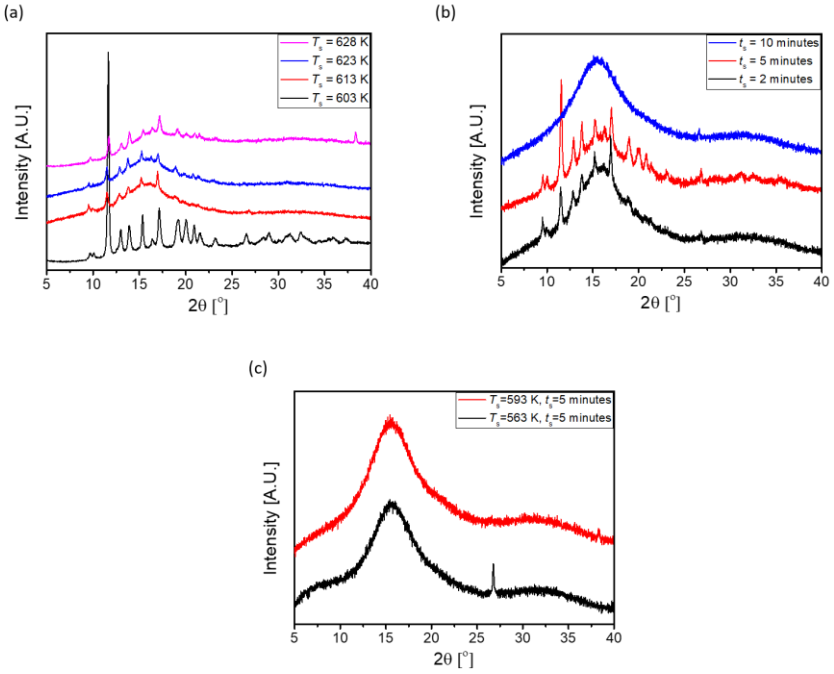

Figure 4-5 XRD spectra for the samples sintered with SPS technique. (a) Samples obtained from ZIF$_{crystalline}$ with sintering time of 2 minutes and varying sintering temperature T_s. (b) Samples obtained from ZIF$_{crystalline}$ with sintering temperature of 603 K and varying sintering time t_s. (c) Samples obtained from ZIF$_{glass}$ with sintering time of 5 minutes and sintering temperatures of 563 K and 593 K.

Sintering time for ZIF-62$_{crystalline}$ was varied between 603 and 628 K, whereas for ZIF-62$_{glass}$ the tested T_s was between 563 and 593 K. XRD patterns for selected

samples are shown in Figure 4-5. Figure 4-5 a presents patterns for samples produced with t_s = 2 minutes and varying sintering temperatures. All of the samples are partially crystalline, and the sample sintered with the T_s = 603 K is nearly fully crystalline. The only sample that is fully amorphous after the sintering of ZIF-62$_{crystalline}$ powders has been prepared with T_s = 613 K and t_s = 10 minutes (Figure 4-5 b). The results suggest SPS of crystalline ZIFs can be a good technique for preparing glass-crystal composites. However, for the fabrication of bulk glass samples, different routes should be explored. Sintering samples from glass powders lead to high-density, homogenous bulk samples. Figure 4-5 c presents the XRD patterns of samples obtained from ZIF-62$_{glass}$ powders with the lowest and highest T_s temperature, confirming no recrystallization occurred during sintering.

The sample produced with T_s = 593 K and t_s = 5 minutes was chosen for further characterizations. Upon the first upscan, the T_g of as-prepared glass was revealed to be 555 K (Figure 4-6 a), which is *ca.* 35 K lower than for glass that was melt-quenched under ambient pressure (MQ-AP glass). To get a better understanding of the decrease in T_g, the sample was then subjected to a number of heating-cooling cycles, with a stable heating and cooling rate of 10 K/min (Figure 4-6 a). 618 K was chosen for the maximum temperature during heating (i.e., 20 K higher than the T_g of the MQ-AP glass). Interestingly, with the increasing number of upscans, the T_g value increases slightly, indicating the structural relaxation taking place during heating.

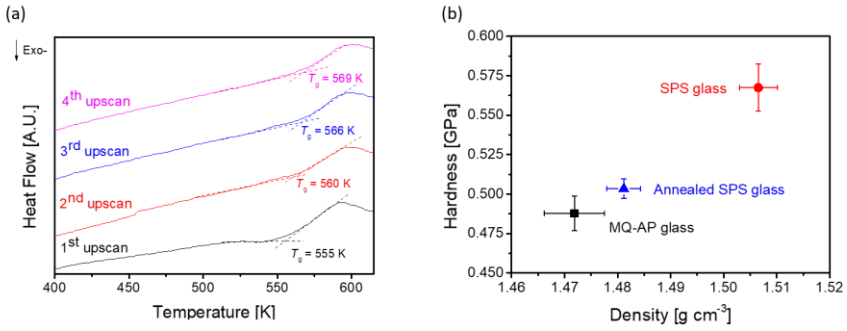

Figure 4-6 Relaxation of the glass as observed on (a) thermal response during heating and (b) density and hardness of the samples. (a) The influence of repeated heating on glass transition temperature values. Note the increase of T_g after each heating up to 618 K. (b) Hardness and density response to annealing of SPS produced bulk glass. The red circle represents SPS glass as prepared, blue triangle – SPS glass after annealing, black square – ambient pressure melt-quenched glass (MQ-AP glass).

The influence of the relaxation process is also observable on the density and hardness of the sample (Figure 4-6 b). The SPS glass features Vickers hardness (maximum load during measurement of 0.49 N) of around 15% higher than that of MQ-AP glass. The change was accompanied by around 2% increase in density. After annealing for 5 minutes in 618 K, a decrease in both hardness and density was observed. However,

the values were still higher than those obtained for glass melt-quenched under ambient pressure. Note that the density was measured using Archimedes' principle (measurements conducted in air and ethanol).

The results suggest that sintering the glass under applied pressure leads to a densification of the samples. The densification leads, in turn, to decrease of glass transition temperature and the increase of hardness. Upon heating, relaxation of the glass occurs which can be observed in an increase of T_g. The recovery is however partial, as the measured parameters do not reach the values observed for MQ-AP glass.

The following mechanism is proposed for the densification of the samples under the load application during sintering in the SPS process. The pressure the samples are subjected to, together with the flexibility of the organic ligands and the free volume of the framework, could lead to the redistribution of bonding angles and distances, and thus the increase of packing density. Another important factor could be the hindering of the bond reformation. As the building units are under pressure, the movement of the structural tetrahedra is hindered, which in turn leads to difficulties in finding another building unit for the reformation of the coordination bond. Such a phenomenon can result in the creation of structural defects, which could be reflected in a decrease of T_g and an increase of density.

Another difference between the SPS method and other fabrication methodologies is that no macroscopic melting happens during the sintering. The sintering process was controlled by diffusion processes occurring at the surface of powder particles (*91*). Hence, the building units inside the powder particles would not be affected by the sintering to such an extent as the ones located closer to the particle surface. In this case, the structure would be frozen upon cooling without being fully relaxed to a thermodynamical state (dynamic reason/cooling). The excess enthalpy would therefore be subsequently released during heating.

The application of the SPS method in sample fabrication allowed us to obtain bulk ZIF glasses of high homogeneity and quality (lack of bubbles). However, the problem of chipping during sample extraction should be addressed. Such an issue could be dealt with be either improving the method of extraction or gaining more experience in this manual task by the researchers. Here the author would like to note that this method is the newest one investigated in the duration of this thesis. It could therefore be possible to decrease the proportion of samples chipping after gaining more experience in working with these samples.

A better understanding of the influence of production parameters on the sample quality and properties should also be performed. This knowledge would also facilitate the optimization of the properties of the produced samples.

4.4. COMPARISON OF DESCRIBED FABRICATION METHODS

In order to compare the samples obtained with the usage of each of the three methods, one sample was chosen from each methodology. Macroscopically (Figure 4-1 d-f), a significant difference in the homogeneity of the ambient pressure melt-quenched sample can be noted, when compared to the other two samples. On the other hand, both the vacuum hot-pressed and the SPS samples break either during the fabrication process or extraction from the mold, whereas the ambient pressure melt-quenched sample maintains its shape.

The glass transition temperature (Figure 4-7 a) of the samples increases in order: MQ-AP glass (the lowest T_g value), vacuum hot-pressing, SPS (the highest T_g value). The decreasing glass transition correlates well with increasing density ρ (Figure 4-7 b), implying an inverse correlation between T_g and ρ. This agrees well with the classical glass formation theory, stating two glasses (with the same composition) with lower free volume (hence, higher density) feature lower T_g (*96*). In the case of the ZIF glasses, the mechanism behind this relationship is especially interesting. The reverse correlation may here be explained in terms of the influence of the different loads applied during sample fabrication on the structure of obtained glass. It is expected that the application of the load influences the structure of the final glass through a number of mechanisms.

Firstly, the application of load helps to remove bubbles from the melt, leading to obtaining a bulk sample with no macroscopic defects. Such a sample has a higher density, as the whole volume of the sample is occupied by ZIF glass and not by air bubbles.

If the applied pressure reaches a certain value, the flexible ZIF structure, characterized by a high number of internal pores, may also densify on a microscopic scale. The coordination bond between the ligand and the zinc node is highly flexible, thus enabling changes of angle and bond length. Under load, it enables limited movement of ligands and nodes without bond breakage, leading to more packed structure, with more structural building units per unit volume.

Another mechanism could be hindering bond reformation, as described in section 4.3 in terms of SPS. Here, it is assumed that the glass transition and the melting mechanisms are somewhat similar. The melting (and, most likely, the glass transition) occurs in ZIFs as parallel bond breakage and reformation. A bond breakage leads to the formation of a ‘free’ ligand, which then moves around trying to find a zinc tetrahedral with one bond’ missing’. After finding such an entity, the coordination bond between the ‘free’ linker and the three-fold coordinated zinc can be reformed. However, when a pressure is applied to the system, it densifies, leaving less free space for the ‘free’ linker and the three-fold coordinated zinc units to move around. The hindrance of the movement decreases the probability of the ‘free’ units to find

themselves and reform the broken bond. In turn, the probability of creation of defects in the form of three-fold coordinated zincs and 'free' ligands increases. If such defects are 'frozen' in the glass structure, the average number of constraints per building unit will decrease, which may lead to changes in physical properties, such as the decrease of T_g. This mechanism is expected to play an important role in the SPS samples.

The increase in density causes furthermore an increase of hardness (Figure 4-7 b). This suggests that the structural densification results from the hindrance of permanent deformation under point loading. Interestingly, combining this result with the defect introduction mechanism described in the last paragraph suggests, that even though T_g is highly influenced by the number of structural constraints per building unit, the hardness may be more dependent on the number of structural units per unit volume. For final confirmation of the suggested explanation, detailed structural studies need to be performed in the future.

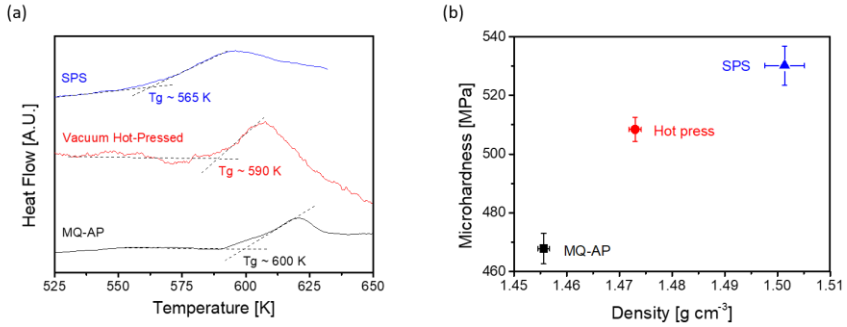

Figure 4-7 Comparison of properties of samples prepared using the three described methods: ambient pressure melt-quenching in a tube furnace (in black), vacuum hot-pressed glass (in red), spark plasma sintered bulk sample (from initial glass powder) (in blue). (a) Thermal response of the samples on the second upscan. The first heating and cooling cycle with the rate of 10 K/min has been performed in order to assure analogous thermal history. T_g values were evaluated as presented on the figure. (b) Microhardness – density relation for the tested bulk samples.

In summary, all of the presented methods show the potential for the fabrication of bulk ZIF glasses. Table 4-1 summarizes the information described in the following chapter. However, due to the decrease in the number of defects and better quality of the samples (less breakage than what was observed for vacuum hot-pressed samples), it is concluded that the SPS technique provides the most advantageous approach to the fabrication of samples for industrial use.

Table 4-1. Summary of the methods described in Chapter 2.

	Inert Atmosphere Tube Furnace	**Vacuum Hot-Pressing**	**Spark Plasma Sintering**
Advantages of the method	Facile and quick preparation method; Easy to obtain the desired shape of the sample.	No 'bubbles' inside the sample, sample macroscopically homogenous.	No 'bubbles' inside the sample, sample macroscopically homogenous.
Disadvantages of the method	Macroscopic 'bubbles' inside the samples.	Sample breakage.	Sample breakage.
Parameters tested as part of this work	Melting duration, t_m.	Ligand ratio in ZIF-62.	Time and temperature of sintering, T_s and t_s. Form of the initial powder (crystalline or glass).
Selected sample	t_m = 5 min		Glass powder, T_s = 593 K, t_s = 5 min.
T_g [K]	600	590	565
Density [g/cm^3]	1.46	1.47	1.50
Hardness [GPa]	0.470	0.508	0.530
Viscosity [s/K]	22	18	24

CHAPTER 5. MECHANICAL PROPERTIES OF ZIF GLASSES

Mechanical properties of any kind of material are one of the crucial factors affecting its industrial applications. If we do not understand the response of a material to any kind of loading, including its fracture behavior, we are not able to safely introduce the material for any application, bounded by the design and quality requirements. With an increasing number of potential ZIF glass application fields, sourcing from their unique properties, understanding the mechanical response is the next imperative step for industrialization of this novel material.

Motivated by the importance of understanding these properties of ZIF glasses, this chapter will focus on the subject of the mechanical response of materials. To introduce the reader to the field of mechanical properties, a number of definitions will be introduced for common mechanical properties (Chapter 5.1). Next, a short introduction to the up-to-date knowledge of the mechanical behavior of crystalline ZIFs follows (Chapter 5.2). As ZIFs are built by the connection of both organic and inorganic building units, their mechanical response features a unique combination of properties that should be observed for both ZIF crystals and glasses. The basics of the mechanical response of conventional families of glasses are also introduced (Chapter 5.3) in order to provide a comparison basis for the novel family of ZIF glasses. Afterward, the current state of knowledge on the subject of the mechanical response of ZIF glasses is addressed (Chapter 5.4). Finally, initial works performed on samples with the varying chemical composition (Chapter 5.5) are discussed.

5.1. OVERVIEW OF TERMS IN MATERIALS MECHANICS

In order to provide an introduction to the field of mechanics, a short overview of terms is used in the following section.

The main method of mechanical testing used both in this work and in the up-to-date studies of mechanical properties of ZIFs is indentation. In summary, indentation methods are all based on the same principle:

i. The sample surface is loaded through an indenter (e.g. Vicker's diamond pyramid) up to a certain load at a set loading rate;
ii. Then, the load may be kept constant for a certain time;
iii. Next, the load is removed with a set unloading rate;
iv. To quantify the hardness value, the remaining impression on the material's surface is measured and, subsequently, hardness can be calculated.

The schematic in Figure 5-1 presents the three stages of material indentation in a graphical form.

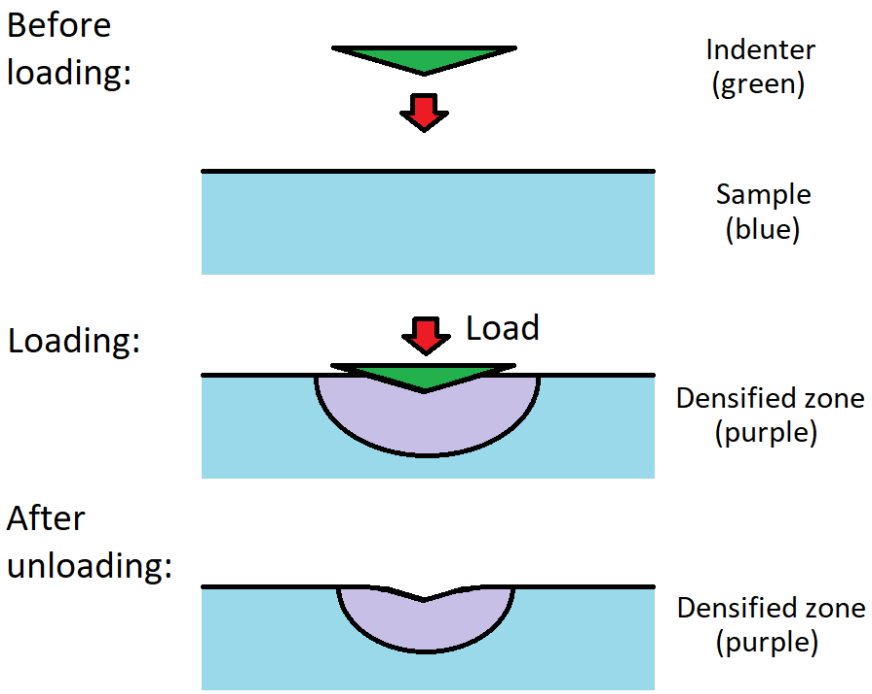

Figure 5-1 Visualization of the indentation of material. Three stages are included: the system before loading (top schematic), the system during the loading (middle schematic) and the surface of the sample after indentation (bottom schematic).

Depending on the loads used, indentation techniques can be divided into the macroscopic indentation, microindentation, and nanoindentation techniques. In this work, micro- and nanoindentation techniques were used. The former of them, microindentation, refers to loads in the range of 1 to 1000 gf (0.0098 N to 9.8 N). One of the typical indenter geometries is a diamond, four-sided pyramid, with the angle between the opposite faces equal to 136° (half-angle of 68°) - Vickers indenter. After removing the load, the top-view of the indent impression is then square-shaped, with two diagonals (d_1 and d_2) clearly visible (Figure 5-2 a). The diagonal lengths can then be used to calculate Vickers hardness, as:

$$\mathrm{HV} = 1854 \times \frac{L}{d^2} \qquad (5.1)$$

where: L – load in gf, d – an average of the length of the diagonals in μm. The numerical coefficient comes from the geometry of the indenter (2sin(68°)=1.854, where 68° is the half-angle of the Vickers indenter).

The latter method, nanoindentation, typically refers to indenting in a load range under 1 gf (9.8 mN). The typically used indenter geometry is Berkovich indenter. In this case, the tip geometry is a three-sided pyramid with a half-angle of 65.17°. The impression left after removing the load is, in this case, a triangle.

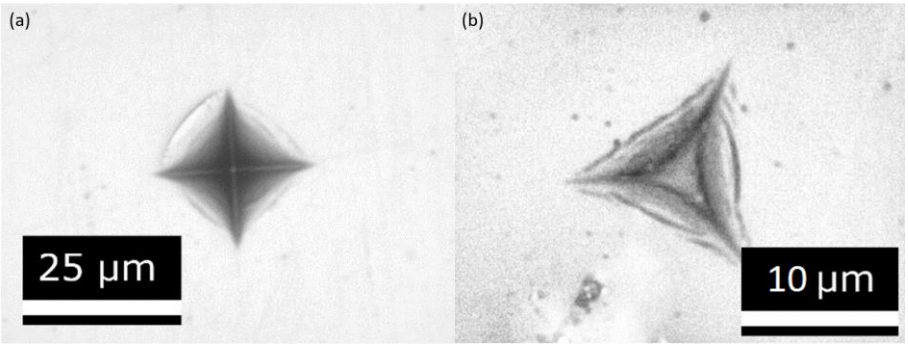

Figure 5-2 Examples of images of indent impressions obtained in (a) microindentation measurement, using a Vickers indenter, (b) nanoindentation measurement, using a Berkovich indenter. Both of the images are taken from the presented work.

The nanoindentation results are analyzed based on the load-displacement curves obtained during measurements. The Oliver-Pharr method is one of the methods used for such an analysis (*97*). Based on Sneddon's findings (*98*,*99*), this procedure is a comprehensive method of calculating both hardness and indentation modulus by an analysis of the load-displacement curve obtained during the nanoindentation measurement. The first step involves calculating the stiffness *S*, which is defined as the slope of the tangent to the load-displacement unloading curve at the maximum displacement. Next, the contact depths h_c is found, based on the maximum measured depth h_m and the depth of the displacement of the material surface at the indenter rim during loading (h_s):

$$h_c = h_m - h_s \tag{5.2}$$

The next step is to find the projected contact area function, which depends on the indenter tip shape. The functions can be found in the literature (*97*,*100*,*101*). Subsequently, the hardness *H* of the material can be calculated as:

$$H = \frac{F_m}{A_p} \tag{5.3}$$

Where the F_m stands for the maximum load.

The knowledge of the projected area A_p allows also calculations of the reduced modulus (E^*_{ind}):

$$E_{ind}^{*} = \frac{\sqrt{\pi}}{2}\frac{S}{\sqrt{A_p}} \quad (5.4)$$

Lastly, the indentation modulus E_{ind} can be calculated as shown in eq. 5.5

$$E_{ind} = \frac{(1-\nu^2)}{\frac{1}{E_{ind}^{*}} - \frac{(1-\nu_i^2)}{E_i}} \quad (5.5)$$

where: ν – Poisson's ratio of the sample, ν_i and E_i – indenter properties.

Three deformation mechanisms are commonly described in connection to the indentation studies. Those are, namely, reversible elastic deformation, and plastic: densification and shearing. The densification refers to the structural rearrangement leading to a more closely packed atomic arrangement that does not go back to the initial state after unloading. Glasses with a larger free volume exhibit therefore higher degree of densification. The densification is reversible, as this part of deformation can be recovered by annealing under the T_g (*102*,*103*). On the other hand, shearing of the material involves bond breakage and movement of the structural units and is therefore an irreversible process. For indentation, two discrete features can be noted as a result of shearing: shear banding and pile-up. Shear bands are formed because of a highly localized process of bond breakage and subsequent translational movement around slip planes. This movement leads to the creation of a nano- or microscaled step-like pattern on a sample's surface. In case of low free volume in a structure, the material is 'forced' to move outside under the indentation loading. The material flow leads to the creation of a pile-up in the vicinity of the indent (Figure 5-3, violet).

A pile-up is usually observed for materials characterized by low elastic-to-plastic deformation ratio, i.e., low elastic contribution. On the other end of the spectrum, for materials featuring high elastic contribution, a sink-in is observed under loading (Figure 5-3, red). By 'sink-in', a deformation inward the material under the loading is understood, on the contrary to the flow outward as in the case of a pile-up.

The term "hardness" refers to the ability of the material to withstand plastic deformation under point loading. The measurement of the diagonals for subsequent calculations is conducted on the impression left in the materials after unloading. Thus, it does not include the elastic deformation under the indenter. The mechanisms responsible for the formation of impressions visible after unloading are densification and shearing.

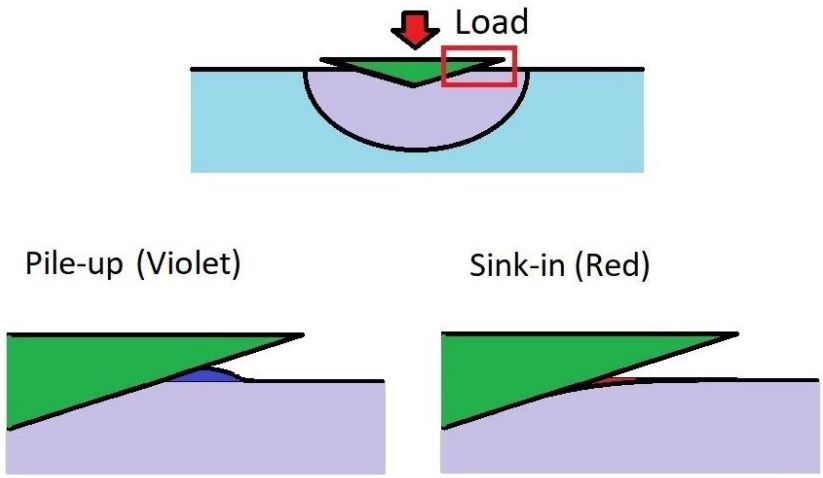

Figure 5-3 Two types of material's surface response to the point loading in the vicinity of the indenter's edges. The top image presents the material during the loading stage. The red frame shows the area zoomed in on the bottom schematics. The schematic on the left presents the formation of pile-up (in violet), whereas the schematic on the right shows the occurrence of sink-in (in red).

On the other hand, indentation modulus is measured during unloading, when it is assumed that only the elastic deformation plays a role. This means that, assuming little or none plasticity during unloading, the indentation modulus value is dependent on the elastic deformation of the sample. Elastic deformation is mostly caused by bond stretching or bending (but without bond breakage), and those bonds go back to their initial state after unloading. To summarize, the hardness value is dependent on the permanent deformation during point loading, whereas the modulus – on the elastic deformation.

The elastic-to-plastic deformation ratio can be determined based on the load-displacement curves obtained from the nanoindentation measurements (Figure 5-4). In this work, the elastic and plastic contributions will be quantified based on both displacement and work (area under the curve) values, according to the method presented below.

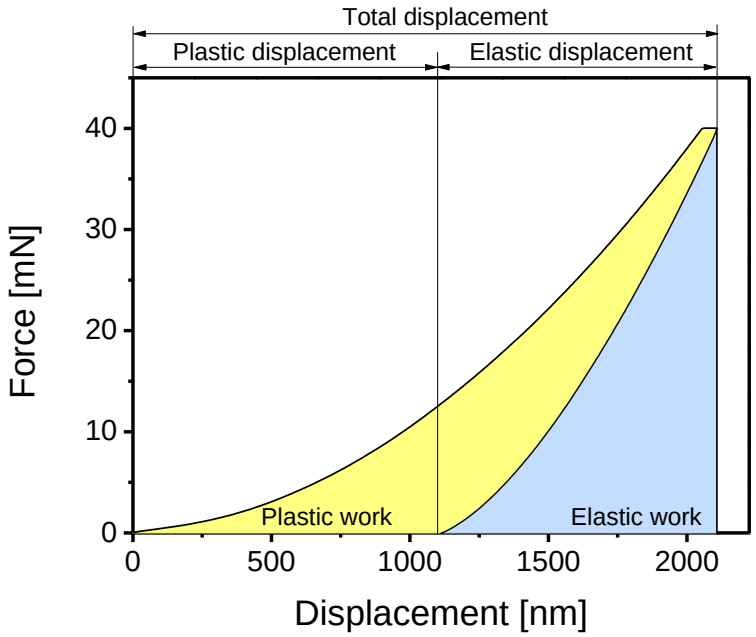

Figure 5-4 Nanoindentation curve obtained for loading with 40 mN force. The yellow area under the curve shows the plastic work, whereas the blue area refers to the elastic work performed during the measurement. The top designations show how the total, elastic and plastic displacements were calculated. The graphic is taken from Paper II.

Depending on the conditions of the indentation and the type of glass tested, four distinct crack systems can normally be obtained, namely: (i) cone, (ii) radial, (iii) median, (iv) Palmqvist and (v) lateral crack. For this work, the most focus will be directed towards cone and radial-median crack systems (see: Figure 5-5).

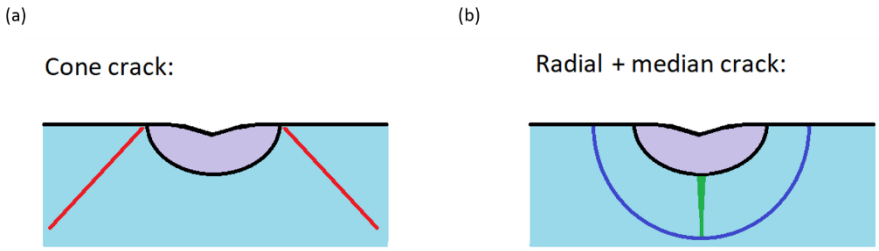

Figure 5-5 Two of the crack systems commonly found in glasses. (a) cone crack (in red) initiating on the surface, at the boundary between the highly deformed area under the indenter (purple) and undeformed glass (light blue). (b) radial (dark blue) and median (green) crack system. The median crack initiated at the boundary between the densified area (purple) and undeformed glass (light blue), whereas the radial crack initiates at the end of the median crack and propagates towards the surface.

Lastly, another parameter that can be analyzed based on indent impressions after Vickers microhardness measurements is the cracking resistivity (*CR*). The methodology was first introduced by Wada (*104*) and is based on measuring the probability of radial crack initiation during the indentation of material by Vickers indenter with a given force. As the maximal number of radial cracks that may be induced is four, this number is referred to as 100% probability. Analogously, one crack is 25%, two – 50% and three – 75%. By measuring the crack initiation probability on a number of indents induced with one load, an average probability is thus calculated in a range of loads. Subsequently, a crack initiation probability versus a load graph can be drawn, and a trend line can be added (typically S-shaped). The crack resistivity is then defined as the load value for which the probability of initiation of the radial crack is equal to 50%. The measurement is typically carried out for oxide glasses.

In material mechanics, three various moduli are used to describe properties of a material: Yong's modulus, shear modulus, and bulk modulus. The first one, Young's modulus *E*, is also known as elastic modulus. It describes the resistivity of the material to elastic deformation. Shear modulus *S* describes the resistance of the material to deformation by shear, whereas bulk modulus *B* is connected with resistance to isostatic compression. Together with Poisson's ratio *ν*, for isotropic material, these properties are linked by the following equations:

$$G = \frac{E}{2(1+\nu)} \tag{5.6}$$

$$K = \frac{E}{3(1-2\nu)} \tag{5.7}$$

The response of a material can be either isotropic or anisotropic. The term 'isotropy' means the measured properties are the same in every direction of measurement. *Au contraire*, anisotropy describes a phenomenon, at which significant changes in properties are noted when measuring material in different directions. Many crystalline materials feature anisotropic properties, due to the disordered structure of glasses, their properties are isotropic. In order to enable the facilitation of results analysis, calculating an 'average' value of such parameters is possible using a number of methods. One of them is the Voigt-Reuss-Hill averaging approximation equation (*105*). This equation is based on the elastic constant matrix values for an anisotropic material and can be found numerous literature sources (*106–108*). In this work, the anisotropy of mechanical properties is only mentioned in the case of crystalline ZIFs (Chapter 5.2).

5.2. MECHANICAL BEHAVIOUR OF CRYSTALLINE ZIFS

A number of studies have been published on the subject of the mechanical behavior of crystalline ZIFs. These studies include the simulation results (*107–111*), as well as a small number of experimental investigations (*111–114*). In this chapter, a short summary of both types of studies will be presented.

In most of the simulation studies, density functional theory (DFT) methods are utilized in order to obtain the elastic constants matrix (*107–112*). The parameters can then be used to calculate such characteristics as shear modulus, Young's modulus, and bulk modulus. Table 5-1 summarizes some of the results obtained for various, crystalline ZIFs. Here it should be noted that the values included in the table are average values, whereas all of the properties exhibit anisotropy.

Table 5-1. A summary of Voigt-Reuss-Hill averages for shear (G_{VRH}), Young's (E_{VRH}) and bulk (K_{VRH}) moduli, and Poisson's ratio (ν_{VRH}) values obtained by simulations of the crystalline ZIFs.

Material	G_{VRH} **[GPa]**	E_{VRH} **[GPa]**	K_{VRH} **[GPa]**	ν_{VRH}	**References**
ZIF-1	1.59	4.00	2.76	0.26	(*109*)
ZIF-2	1.25	3.44	4.88	0.38	(*109*)
ZIF-3	0.62	1.77	3.79	0.42	(*109*)
ZIF-4	1.11-1.55	2.69-3.82	1.54-2.41	0.21-0.24	(*107*,*109*,*110*)
ZIF-zni	2.23	6.37	15.63	0.44	(*110*)
ZIF-8	1.09	3.15	9.23	0.44	(*112*)
ZIF-62	1.33	3.24	1.92	0.22	(*107*)
ZIF-90	1.51	2.05	8.58	-	(*108*)
SALEM-2	1.44	1.99	8.04	-	(*108*)
TIF-4	1.83	4.79	4.20	0.31	(*107*)

Most of the experimental works for finding the mechanical properties of crystalline ZIFs were performed using nanoindentation studies (*111*,*113–115*). It should also be mentioned that in many of the nanoindentation studies, it is assumed that the indentation modulus could be used for the approximation of Young's modulus (*E*) value for ZIF crystals. This issue was mentioned in (*114*). The author of this work decided, however, to refer to the modulus obtained from indentation techniques as indentation modulus. Indentation modulus of ZIFs is in range of around 3-8 GPa and their hardness is mostly in the range of 0.2-1.2 GPa. The densest ZIF crystal known so far, ZIF-zni, features the highest values of both indentation modulus and hardness. When included in an Ashby plot of indentation modulus against hardness (*113*), the points place crystalline ZIFs in an area bordering the traditional groups of materials: ceramics, metals, and polymers.

By comparing various properties of crystalline ZIFs, Tan et al. established some possible relations between the mechanical properties and structural factors (*114*). According to their observations, the indentation modulus related to the physical density and showed an inverse relation with accessible void space. Interestingly, the relation between hardness and accessible void space obtained in the same work (*114*) did not seem as certain as the one concerning the indentation modulus. This could be explained in terms of the deformation mechanisms influencing the hardness and indentation modulus (*113*). The indentation modulus is solely dependent on the elastic response of the sample, whereas hardness, being a measure of permanent deformation under point loading, depends on both elastic and plastic components of the deformation. Plastic deformation is still not fully understood in framework structures such as ZIFs, as it is dependent on various factors. These numerous components lead to complex relations between structural factors and, in this case, hardness, resulting in higher data scatter in described hardness - accessible void space relation.

A small number of different experimental techniques were used to characterize other mechanical properties of crystalline ZIFs. Bulk moduli of ZIF-zni crystals were approximated from diamond anvil cell hydrostatic compression tests to be around 14 GPa (*116*). Brillouin scattering method was applied for measuring acoustic wave velocities of ZIF-8 (*112*). The measured values were then used to calculate the elastic modulus E (E_{VRH} = (3.145±0.013) GPa), bulk modulus K (K_{VRH} = (7.751±0.011) GPa), shear modulus G (G_{VRH} = (1.095 ± 0.005) GPa) and Poisson's ratio ν (ν_{VRH} = 0.43) of ZIF-8 crystal.

The change of mechanical properties with the chemical composition of ZIF crystals has also been considered in a number of studies, both experimentally and by simulation (*107*, *113*). The influence of the change of metallic node from zinc to cobalt has been assessed comparing the indentation modulus and hardness of ZIF-7 ($Zn(bIm)_2$, *sod* topology) and ZIF-9 ($Co(bIm)_2$, *sod* topology) (*113*). This structural change does not significantly affect neither density (ρ_{ZIF-7} = 1.24 g cm^{-3}, ρ_{ZIF-9} = 1.23 g cm^{-3}) nor the volume accessible to solvent (SAV_{ZIF-7} = 26.57%, SAV_{ZIF-9} = 26.78%)

(*113*). A very small influence of the node exchange is observed on indentation modulus ($E_{ind,\text{ZIF-7}}$ = 6.11 GPa, $E_{ind,\text{ZIF-9}}$ = 5.89 GPa) and the hardness ($H_{\text{ZIF-7}}$ = 0.64 GPa, $H_{\text{ZIF-9}}$ = 0.65 GPa) (*113*). This suggests that the rigidity of the framework structure is highly affected by the ligands and/or topology, and only to some extent affected by the coordination bond and the metallic node (*113*).

The above-stated argument agrees well with further studies of the influence of changing ligands on mechanical properties of ZIF crystals (*107*,*113*), for example, for ZIF-7 and ZIF-8 (*113*). Both of the crystals are zinc-based and have *sod* topology, however, ZIF-7 has a chemical composition of $Zn(bIm)_2$, whereas ZIF-8 is composed of $Zn(mIm)_2$ (for the ligand structures, refer back to Figure 3-9 and Table 3-1). The measured indentation modulus and hardness for ZIF-8 were $E_{ind,\text{ZIF-8}}$ = 3.32 GPa and $H_{\text{ZIF-8}}$ = 0.53 GPa. Comparing the values with those measured for ZIF-7 crystals ($E_{ind,\text{ZIF-7}}$ = 6.11 GPa, $H_{\text{ZIF-7}}$ = 0.64 GPa) a significant increase of both E_{ind} and H was observed with increase in ligand size. The relation between the size of the ligands and the mechanical properties was further confirmed by the simulation studies performed in (*107*). Comparing the *E*, *G* and *B* values obtained for ZIF-4, ZIF-62 and TIF-4, a clear increase of moduli was noted with the increase of the average ligand size (*107*).

The influence of ligand functionalization was investigated by simulation of SALEM-2 ($Zn(Im)_{1.7}(mIm)_{0.3}$, *sod* topology (*117*)) (*108*). By substituting the –H in unfunctionalized imidazolate in SALEM-2 by chromium, bromine and carboxyaldehyde groups, an increase in *E*, *G* and *B* values was observed in order: unfunctionalized SALEM-2 < -CHO group < -Cl < -Br. The results show that the functionalization of ZIFs could lead to an enhancement of the mechanical properties of the synthesized crystals.

Concerning the fracture mechanism of crystalline ZIFs, to the best of the author's knowledge, only one study performed on ZIF-8 can be found (*115*). In this work, an atomic force microscope (AFM) was equipped with the diamond cube-corner indenter tip for nanoindentation studies. Interestingly, the study has revealed four distinct failure modes of crystalline ZIF-8. Namely, it is proposed that failure of ZIFs occurs by: (i) grain boundary slippage, (ii) polycrystalline fracture, (iii) compaction of the material due to its high intrinsic porosity collapse, (iv) buckling of bonds. The proposed model implies the complexity of fracture of framework materials, due to a high number of distinct structural change mechanisms occurring under loading.

To summarize, the current state of knowledge concerning the mechanical properties of ZIF crystals is mostly based on DFT models and nanoindentation measurements. Initial studies applying Brillouin scattering and diamond anvil cell hydrostatic compression can also be found. However, based on the presented fracture study, complex relations between structure and mechanical properties are expected in further investigations of this family of framework materials.

5.3. STRUCTURE AND INDENTATION BEHAVIOUR OF MORE CONVENTIONAL GLASSES

One of the widely used mechanical characterization techniques for glasses is indentation. This is connected to the high brittleness of the glasses, which leads to fracture before any deformation can be observed under bigger-scale mechanical tests (*118*). On the other hand, the localized character of the indentation loading enables the occurrence of both elastic and plastic deformation, providing additional information about the mechanical response of glass. In this chapter, a short description concerning indentation behavior and other mechanical properties of oxide, chalcogenide, and metallic glasses will be introduced. These will then be used for comparison with the mechanical response of ZIF glasses.

The oxide glasses are probably the most studied family of glasses. Their structure is composed of metal (or half-metal) oxides. The metal cations are bridged by oxide anions, building up a random network structure. Depending on the type of oxides building the network, three different categories of building units can be named: network formers, network modifiers, and intermediates. The network formers are oxides such as SiO_2 or B_2O_3 constitute the basic network structure by forming a corner-sharing polyhedron connected to each other (*26*). The introduction of network modifiers leads to the creation of oxides connected to only one cation which disrupts the structure and causes depolymerization of the network (*26*). Such oxygen ions are called ‘non-bridging’ oxygen, as they are not bonded to two, separate cations. A number of oxides that can act as both network formers and network modifiers can also be found (e.g. Al_2O_3).

Based on the properties, indentation response and cross-sectional cracking patterns, oxide glasses can be divided into normal and anomalous mechanical response categories (*118*). The ‘normal glasses’ show a tendency to shear in terms of the preferred plastic deformation mechanism (*118*). With the modifiers partially depolymerizing the structure, shearing can initiate more easily. Under indentation, they exhibit median or radial cracking, initiating on shear displacement planes. The term ‘normal’ is related to the fact that most of typical, conventional oxide glasses exhibit this type of behavior. Examples of such glasses include soda-lime-silica (SLS) glasses. The name ‘anomalous glasses’ refers to glasses which under point loading exhibit a tendency to densify (*118*). With nearly fully polymerized structure, this mechanism of deformation is preferred over shearing. These glasses tend to exhibit cone crack in high tensile stress zone in the vicinity of the densified material area. The most common example of an anomalous glass is pure silica glass. It was shown that glasses with low Poisson’s ratio and E/H ratio values tend to display anomalous behavior (cone cracking) (*119*,*120*). The increase of both the Poisson’s ratio and the E/H ratio promotes the change of fracture mechanism to radial cracks, typical for the normal glasses (*119–121*).

The non-oxide chalcogenide glasses have structures somewhat analogous to those of oxide glasses. In this family of materials, the network formers are chalcogenides (sulfides, tellurides or selenides) of such compounds as silicon, germanium or antimony (*26*). Depending on the compounds building the network, the structure can range from structural polyhedra in form of corner-shared units, building up a covalently bonded three-dimensional network, to edge-shared units, covalently bonded in chain-like structure (*26*,*122*). For example, in Ge-Se systems (*122*), the two-fold selenium atoms build chalcogen chain structures which are then cross-linked by germanium atoms (which are four-fold). The Se-Ge crosslinks are strongly bonded in a covalent manner. However, the interactions between two chalcogen chains are weak, van der Waal's bonds, due to lone electron pairs on Se atoms. These structural differences have a direct influence on the mechanical properties of glasses. With an increase of four-fold germanium content, an increase in hardness, Young's modulus, and bulk modulus are observed due to the increase of the number of strong Ge-Se crosslinks (*122*). Interestingly, the increase of Ge content leads to a decrease of Poisson's ratio and the critical load to form radial/median cracks (*122*).

The metallic glasses differ significantly from the other non-organic glass families due to the presence of metallic bonds connecting the atoms, on contrary to the before-described covalent and ionic bonds. Their structure is often described as spherical atoms arranged randomly, which was specified in the dense cluster-packing model (*123*). According to this model, nearly-spherical solute-centered clusters are packed together, sharing some of the cluster atoms with neighboring units. Mechanically, metallic glasses (as compared to their crystalline counterparts) feature similar E values yet higher strength at room temperature, with localized plastic deformation by shear bands (*124*). Metallic glasses are characterized by high Poisson's ratio values and fracture energy compared to other families of glasses (*125*,*126*). The hardness of metallic glasses lies in a range similar to that of oxide glasses. Due to the facile shearing, a significant pile-up is observed in the vicinity of the indents.

The last family of conventional glasses is that of polymeric glasses. In general, polymers are built of organic chains connected together by van der Waal's forces. When a polymer is cooled to form a glass, the chains become intertwined in a random manner (*127*). Glassy polymers (below T_g) can exhibit hardness values up to 2-3 times higher than their crystalline counterparts (*128*). However, their hardness is much lower than that of inorganic glasses. In general, the hardness of polymeric glasses can be as high as 0.2 MPa (*128*). Typical values for Young's modulus of polymeric glasses lie in the range of 1-3 GPa (*127*). They are also characterized by high Poisson's ratio values, comparable to those of metallic glasses (*125*). During the indentation of polymeric glasses, viscoelasticity and viscoplasticity play a significant role (*129*), much bigger than in the case of the other groups of glasses. Due to this reason, special care must be taken when ensuring the loading and unloading conditions stay unchanged during indentation testing of this group of materials. The same phenomena of viscoplasticity and viscoelasticity lead to the high degree of recovery of the material

after unloading, leading to the high ratio of elastic deformation ($W_e/W_t > 0.5$, where W_e stands for elastic work, and W_t – total work. For more explanation: see section 5.1) (*130*).

To summarize, depending on the structure of the glasses, a different mechanical response of the material is observed. And thus, despite having hardness in a similar range of values, metallic and oxide glasses respond in a significantly different manner due to bond and topological differences. With the unique, organic-inorganic structure of ZIF glass, it is important to relate the structural factors to different responses, as they provide new insights into this novel group of materials.

5.4. INDENTATION BEHAVIOUR OF ZIF-62 GLASS

The mechanical properties of ZIF glasses have not been explored widely up until very recently. Only a small number of studies have been performed, covering mainly the nanoindentation of ZIF glasses (*16*,*17*,*88*). These studies have placed the nanohardness and indentation modulus of the glasses in the range of 0.7-0.9 GPa and 6-9 GPa, respectively (*17*). To the best of the author's knowledge, only one study investigated the response of the ZIF glasses using nanoindentation set-up further than just to find hardness and indentation modulus values, providing an initial overview to creep and scratching behavior (*88*). The study has shown a high strain-rate sensitivity of ZIF glasses (m = ~(0.6-0.8)). Compared to other groups of glasses, only glassy polymers, and chalcogenide, Se–rich glasses could reach this range of values. Moreover, for ZIF-62, Poisson's ratio was around 0.45, when measured by the Brillouin scattering (*16*). This value differs however significantly from the value obtained by measurement of the transitional and longitudinal wave velocity, which was calculated to be 0.35 (Paper II). The origin of such a high discrepancy is still under investigation. Both values are nonetheless higher than that of the Poisson's ratio value of crystalline ZIF-62 (ν = 0.15) (*16*). Such a significant difference between the Poisson's ratio of glass and its crystalline counterpart is highly unusual, and it suggests that crystalline ZIF-62 is more brittle than the glass. This observation implies that investigations of the mechanical properties of ZIF glasses will feature relations between properties that might have not been observed before.

In this chapter, the micro- and nanoindentation techniques were used for further investigations of the indentation response of hot-pressed ZIF-62 glass. Hardness, indentation fracture, and the response mechanisms are studied and the results are described in the following sections.

5.4.1. HARDNESS AND INDENTATION SIZE EFFECT

The measurement of Vickers hardness of ZIF-62 glass was conducted in a range of loadings from 0.1 N to 1.96 N as shown in Figure 5-6. The microhardness values range from around 0.65 GPa for the smallest load to around 0.5 GPa for the highest. The values are one order of magnitude lower than those observed for typical, non-organic glasses. The sample is characterized by hardness values significantly higher than the soft, polymeric glasses. Nevertheless, when comparing the values with those obtained for non-organic glasses, it can be argued that ZIF glasses belong to the softer part of the hardness spectrum.

As mentioned before, ZIF-62 and silica share an analogous topology, although their mechanical properties differ significantly (as will be pointed out in this chapter). Considering the structural differences, four factors may explain the softness of ZIF glass in comparison to that of silica (Paper II).

The first factor is the weak coordinative bond between the Zn node and the ligand. This weak bond leads to comparatively easy breakage, facilitating the permanent plastic deformation. As hardness is defined as the resistance of the material to permanent deformation, the low bond energy translated into lowering of the hardness with respect to other non-organic glasses. For comparison, the energy barrier that is needed to break the bond between zinc and imidazolate in ZIF-4 is equal to 76 kJ mol^{-1} (*48*), whereas the Si-O bond, like the ones in silica glass, has ionic bond strength of 443 kJ mol^{-1} (*131*). It is therefore clear that the bond strength in silica is nearly six times higher than that of a coordinative bond in ZIFs. Such a significant difference surely has an influence on the onset of plastic deformation during indentation. The author notes that the bond energy in ZIF-4 is not the same as the one in ZIF-62, however, due to the structural similarities, although it is assumed that the values should be of similar magnitude.

The second factor is the number of constraints per unit of volume in ZIF glass. Based on the relationship between the density of constrains and hardness (*132*), the size of a singular structural $[Zn(Im/bIm)_4]$ tetrahedral would lead to the small number of Zn-ligand constrains per unit volume, comparing to silica glass. The Zn-Im-Zn distance in the ZIF structure is around 6 Å (*16*,*17*,*41*), whereas the Si-O-Si distance in silica glass is around 3 Å (*25*,*26*). Assuming the geometrical similarity of both the structural tetrahedra (ZIF and silica), the around two times longer Zn-Im-Zn distance will then translate to around eight times bigger volume of a single tetrahedron. The size difference will therefore lead to a decrease of constrains per unit volume, and thus, decrease in hardness.

The third factor is the rotational and orientation freedom of organic ligands in the ZIF structure. Comparing to the analogous oxygen atoms in silica, the big, organic moieties, built of a number of atoms, are characterized by the easiness of rotational

changes, which, under pressure, are assumed of being able to change their shape to accommodate the strain. This leads to further facilitation of the deformation under loading, especially when compared to rigid structural units.

The fourth factor is the larger degree of free volume in ZIF glass than in silica glass. The big size of the structural tetrahedral and the large size of the organic ligands scale up the glass structure (compared to, for example, silica glass). The upscaling results also in upscaling of the free volume present in the structure. With the increase of voids volume, deformation can be initiated easier. Namely, with more free volume, more densification can be accommodated. Such behavior has been observed in studies concerning conventional glasses (*120*,*133–136*) and is assumed to also be true for ZIF glasses.

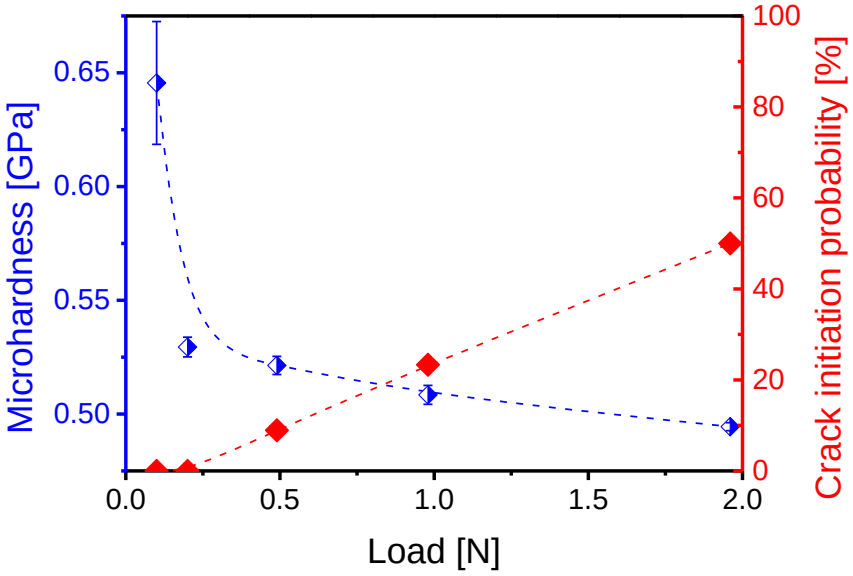

Figure 5-6 Vicker's microhardness values measured for ZIF-62 glass for a range of loads (shown by blue points). In red: crack initiation probability measured for various loads. Data taken from Paper II.

Comparing the hardness values obtained for the various loads, a significant influence of the load on hardness can be noted. That is, the hardness decreases with increasing load. Such a phenomenon is in accordance with the indentation scale effect (ISE), observed in many traditional materials, including oxide glasses (*137–139*), metallic glasses (*140*,*141*) and polymeric glasses (*142*,*143*). Generally, the indentation size effect is considered to be a result of the varying elastic deformation contribution with changing loading. More explicitly, the ratio between the indentation surface and indentation volume increases with decreasing load. The bigger the surface/volume

ratio, the more significant elastic response is, meaning a larger contribution of elastic deformation on lower loads tested (*144*,*145*). As hardness values are inversely dependent on the plastic deformation during indentation, the decrease of load, accompanied by the increase of elastic contribution, leads to an increase of hardness.

In order to quantify the extent of the ISE in ZIF-62 glass, the method first suggested by Bernhardt was used (*146*). According to this method, the dependence between the indentation load (P) and the indent diagonal (l) can be written as follows:

$$\frac{P}{l} = a_1 + a_2 \times l \qquad (5.8)$$

Equation (5.8) includes two constants, a_1 and a_2, where a_1 is directly related to the indentation size effect extent, and a_2 is a load-independent constant. The estimations of those constants can be read from $\frac{P}{l}$ (l) graphs, like the one shown in Figure 5-7, where a_1 is the intercept, and a_2 – the gradient of the linear fit. The obtained value of a_1 parameter for ZIF-62 glass is small (a_1 = 0.02 kgf/mm) compared to the values found in the literature for a range of oxide glasses, exhibiting the a_1 of being an order of magnitude higher (*139*). Such a difference is likely linked with the 'easiness' of the plastic deformation in ZIF glasses, described by the four factors mentioned before.

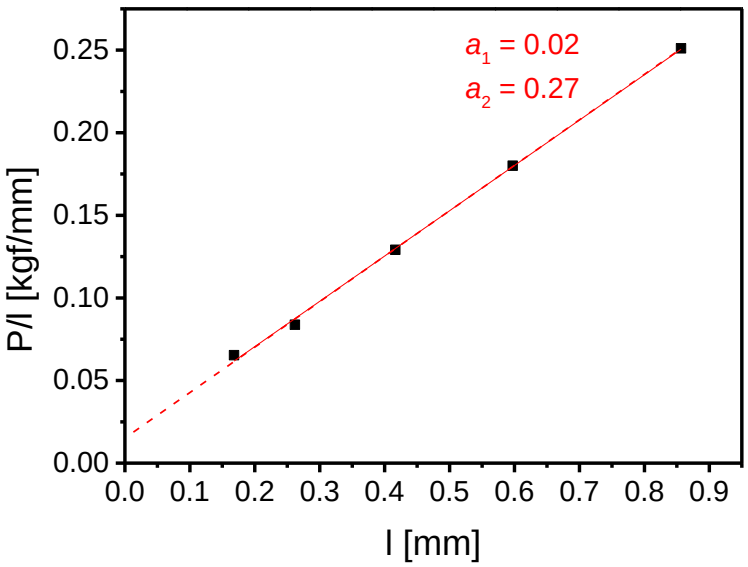

Figure 5-7 The ratio between the load and diagonal length (P/l) versus diagonal length (l) dependence used for approximation of indentation size effect coefficients (a_1 and a_2) according to the method proposed by Bernhardt (146).

Looking at the shape of the hardness-load curve (Figure 5-6), a strong decrease of the hardness with the load can be noted in the first section of the graph, i.e. the sharp hardness falls between the two points with the lowest loads (0.1-0.2 N). The deviation from the rest of the points for the lowest load can also be observed on the figure used for estimation of the extent of the indentation size effect. This creates a two-regime dependence, with abrupt changes of hardness in the low-load segment, and more stable relationships in the high-load segment (loads over 0.2 N).

A number of structural factors could lead to the change of extent of the indentation size effect. In metallic glasses, the indentation size effect has been connected to the shear banding process (*140*). In this work, the ISE was divided into two categories: "strong effect" observed for lower loads, and "weak effect" observed for higher loads. For the "strong ISE" range, a rapid decrease of hardness is observed with the smallest load changes. The effect becomes less observable with the increase of the load ("weak" effect), reaching a stable hardness regime at a certain load point. For the lower loads, "distributed shear banding" is observed, meaning a number of relatively small bands are formed after reaching local stress value high enough to overcome the energy barrier of shear band formation (*140*). At this stage, even a small load increase

leads to the formation of many new shear bands, facilitating plastic deformation, and thus leading to big hardness drop. With the increase of load, bigger "localized shear bands" are formed (*140*). In other words, the energy needed to initiate the shear banding is reached easily at the higher load, and they can accommodate the plastic deformation easily. As, in this higher load regime, the small increase of the load does not result in the formation of a much higher number of shear bands, and thus, the ISE becomes weaker. This mechanism, observed in metallic glass, is somewhat analogous to the dislocation-controlled indentation size effect, described for crystalline materials (*147*).

Interestingly, the hardness – load relation obtained for ZIF-62 glass seems to feature a similar, two-stage ISE, like the one described for metallic glasses (*140*). One of the proposed factors is the collapse of the voids in the structure of the glass. Such a structural change could explain the rapid decrease of hardness in the low load section. The similarities of the shape of the curve for ZIF-62 glass to that observed for metallic glasses also means that the change between the two regimes could be related to reaching the critical load needed to initiate the plastic deformation mechanism (such as shear banding).

Moreover, an interesting structural mechanism for an explanation of ISE has also been suggested for amorphous polymers (*142*). For these materials, a strong relationship between the extent of the ISE and the size of the more rigid parts of the chain has been found. Namely, the ISE in polymers with short or no rigid parts (e.g. PE, PTFE) is small. This suggests that plastic deformation in polymers is governed by the rigid parts of the structure. More explicitly, higher energy (i.e. higher load) is needed to initiate

plastic deformation mechanisms in polymers with longer rigid sections. This suggests that the elastic-to-plastic deformation contribution ratio is not necessarily governed by small structural features (such as dislocations in crystals or shear bands in metallic glasses), but also depends on the motion of much bigger structural units.

For the ZIF glasses, an analogy between the structural rigid and flexible parts in polymeric chains and the "rigid" structure of the organic ligands in ZIF glasses (compared to the coordinative bond between the metallic node and the ligand, which would represent the "softer" region) could also be extended. It is therefore worth investigating the extent of the indentation size effect in ZIF glasses with varying ligand sizes.

5.4.2. INDENTATION FRACTURE

Another feature that can be observed on indent impressions is a fracture of the samples during point loading. For ZIF-62 glass, two distinct fracture features are observed on indents obtained after loading with various loads (Figure 5-8).

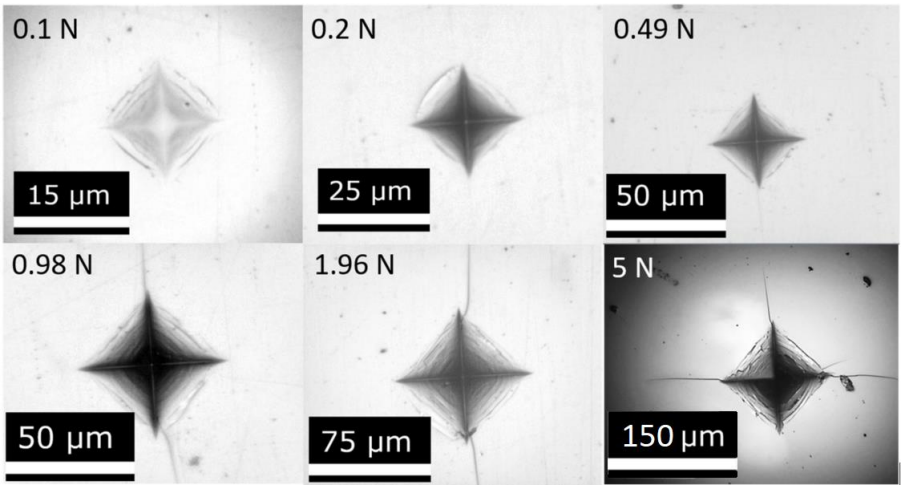

Figure 5-8 Indent impressions left after indentation with varying loads. The applied loads are noted in the top-right corner of each image. Data taken from Paper II.

For all indents, step-like cracks located inside the indent impression are visible under the optical microscope. The cracks are roughly parallel to the indent edges. The step-like indent cracking pattern has been observed before e.g. in chalcogenide glasses (*122*) and soda-lime glasses (*148,149*). In ref. (*122*), shear banding was deduced to be responsible for the development of this step-like structure. In the case of silicate glasses (*148,149*), the edge cracking was a result of tensile stress developed on the surface in the vicinity of the indenter's edge due to the sink-in on the material surface under point loading. This means that the edge cracks are developed during the loading

cycle of indentation. In the case of ZIF-62 glass, both mechanisms (edge cracking and shear banding) seem to be responsible for the occurrence of this pattern.

The other type of fracture, developing at higher loads, is the radial crack. Based on the radial crack initiation points, it is clear that these features are secondary cracks, formed after the edge features are formed. Namely, the radial cracks do not initiate from indent corners, but from the firstly-developed edge cracks. This suggests they are formed in the unloading part of the indentation cycle, in accordance with what was observed for silicate glasses (*149*). Based on the number of radial cracks formed after indentation with various loads, it was possible to estimate crack resistance (*CR*) of ZIF-62 glass (Figure 5-6, red curve). Counting the number of radial cracks formed in the vicinity of the indent corner shows that the 50% crack formation probability occurs at 2 N of load, i.e. $CR_{ZIF\text{-}62}$ = ~2 N. This value is rather low, compared to most oxide glasses, for which crack resistance spans typically up to around 30 N (*102*). Together with the formation of edge cracks at very small loads, the low *CR* value suggests that ZIF-62 glass is characterized by low resistance to crack initiation. This could be linked with the weak coordination bond between zinc and organic ligands in the ZIF framework structure. The presence of such easily breakable bonds leads to both facile initiation of the fracture and the creation of paths by which the crack may easily propagate. Here it should be noted that the *CR* for ZIF-62 was only measured up to load of 1.96 N, as the crack became too extensive and the indent size was too large to conduct a number of indentations high enough to provide a proper statistical analysis of the data. The 5 N indent in Figure 5-8 was obtained on another piece of the cracked glass that was used to obtain a cross-sectional image of the indent (Figure 5-9).

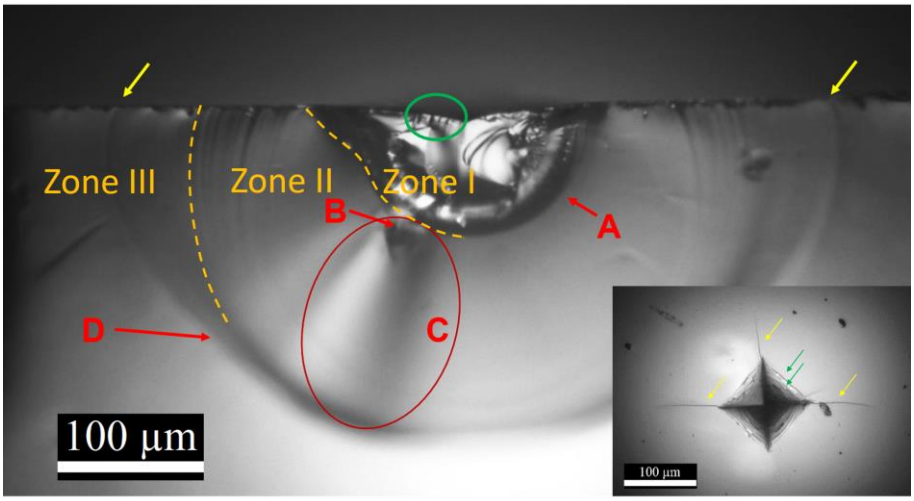

Figure 5-9 Cross-sectional image of an indent on ZIF-62 glass. Three distinct deformation zones are observed: Zone I – zone of high plastic deformation, the border is designated by A, Zone II – radial crack section (D) with visible median crack (initiation at B, propagation – C), Zone III – undeformed material. Data taken from Paper II.

The cross-sectional image of the indent along one of the indent diagonals is presented in Figure 5-9. Three zones can be clearly observed, namely, the highly deformed zone underneath the indenter (Zone I), the radial crack section (Zone II) with visible median crack (initiation point – B, propagation path – C) and the non-deformed material (Zone III).

Zone I represents the densified material volume. It should be noted that its depth is quite big, suggesting a high contribution of densification to the overall indentation deformation mechanism in ZIF-62. In this section, initiating at the surface, a number of micro-cracks can be observed, corresponding to the "step-like" features inside the indents. Zone II presents the section bordered by radial crack. Inside the sample, another crack can be observed, i.e., median crack. The median crack initiated at the border of the densified zone, as a result of changing stress (from compressive inside the densified zone to tensile at the outside boundary (*150*). The median crack propagates to the edge of the tensile stress zone, where a radial crack is formed. On the outside border of the radial crack, un-deformed material is located (Zone III). A number of extra cracks parallel to the radial crack can here be observed. It is assumed that these cracks have been created during the bending of the sample, which occurred during the sample preparation for the cross-sectional analysis.

The described fracture behavior of ZIF-62 glass accords well with the fracture patterns typically obtained for the "normal" glasses with high Poisson's ratio and E/H ratio (*118–121*). Based on the measurements of wave velocities (longitudinal and transverse), the Poisson's ratio of the investigated glass was calculated to be 0.35, which is placed in the 'high Poisson's ratio' group. Nanoindentation measurements with loads of 10 mN, 20 mN and 40 mN place the E_{ind}/H ratio value at around 8 (Paper II). Although this value is not particularly high, it is still high enough to promote median cracking according to the indentation cracking driving-force map (*119*).

The obtained fracture patterns are therefore analogous to typical cracking patterns of the other glasses with similar mechanical properties. At the same time, it features, however, a certain anomaly. Referring once more to the silica glass, which is the most commonly known example of an "anomalous glass", a significant discrepancy in behavior between silica and ZIF-62 glasses is observed. (*118*). This discrepancy in the mechanical properties is interesting, as there are significant similarities between the ZIF and silica glasses in terms of such thermodynamic properties as viscosity at T_m or the fragility index m. The indentation behavior of ZIF-62 glass implies that the similar network structure between ZIF and silica glasses plays a less important role than the structural differences (e.g. the number of constraints per unit volume) in terms of mechanical response. Using this approach, ZIF-62 glasses do not exhibit analogous properties to either anomalous or normal glasses, but a combination of them.

5.4.3. INDENTATION DEFORMATION MECHANISMS IN ZIF-62 GLASS

The indentation fracture study has provided initial insights into the deformation mechanism of ZIF-62 under indentation. In order to study it further, nanoindentation measurements were conducted using three loads: 10 mN, 20 mN, and 40 mN.

Examples of the obtained indent impressions are shown in Figure 5-10. Surprisingly, the "step-like" pattern inside the indent is observed also for these small loads. This reflects the low resistance of ZIF-62 glass to fracture.

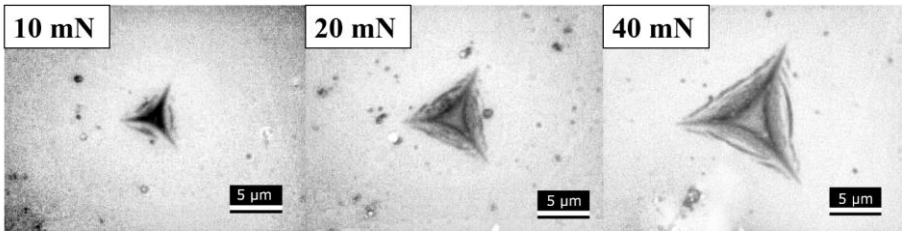

Figure 5-10 Examples of images of indent impressions after nanoindentation with various loads (loads are noted in the top-left corner of the images). Data taken from Paper II.

The indent shape, namely, the lack of pronounced indent edges, suggests that under loading sink-in occurs, reflecting a high contribution of elastic deformation into the deformation mechanism of ZIF-62. The elastic deformation contribution has been quantified based on the nanoindentation curves. Both the percentage contribution of elastic work and elastic displacement were calculated and presented in Table 5-2. The values of these parameters are about 50%, confirming that the reversible, elastic deformation plays an important role in the deformation of ZIF-62 glass.

Table 5-2. The contribution of elastic work and elastic displacement to the deformation under nanoindentation with various loads, in [%]. Data taken from Paper II.

Load [mN]	**Elastic displacement [%]**	**Elastic work [%]**
10	48.7±0.80	53.9±2.0
20	48.4±0.5	52.4±0.8
40	48.3±0.4	51.7±0.2

The next step was using the obtained results, from both the nano- and microindentation measurements, to characterize the extent of the plastic deformation mechanisms. The first of the mechanisms was isochoric shear flow. By applying

atomic force microscopy (AFM) for a three-dimensional indent shape analysis (Figure 5-11), the pile-up was assessed. A very slight pile-up was observed, indicating that this mechanism did not contribute significantly to the plastic deformation of ZIF-62 glass under the indenter. This observation is in accordance with the lack of visible edge and the high contribution of elastic deformation.

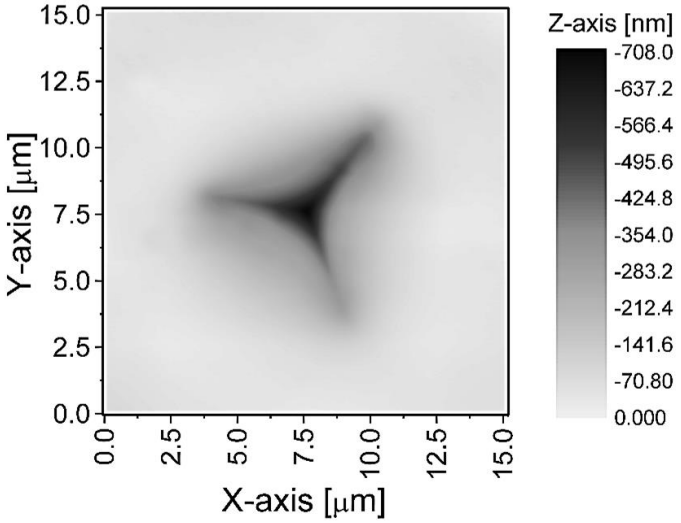

Figure 5-11 An example of a height profile of an indent and the neighboring area used for calculations of the pile-up contributions to the overall plastic deformation of ZIF-62 glass under point loading with 10 mN load. Data taken from Paper II.

As the pile-up investigations did not provide much insight into describing the plastic deformation of ZIF-62 glass under indenter, further studies of the layered fracture pattern were conducted. Figure 5-12 a presents one of the Vicker's indents, where two distinct kinds of features are observed inside the indents. One of them (shown by orange arrows) is a clearly visible dark feature, resembling the median cracks observed outside the indents (blue arrows). The other one (green arrows) is of much lighter, grey color. Further AFM analysis was conducted of a small section of the inner indent, capturing both features (Figure 5-12 b). Here, the distinct difference between the two features can be observed more clearly. The darker element (marked as A) looks like a structural discontinuity (i.e. open crack), whereas the lighter element (marked as B) looks more like a 'step' on the indent face.

The "step-like" character of the second feature was confirmed with an AFM line scan (Figure 5-12 c), which featured a visible, significant change of the sample surface level at the line. The observation confirms that shear banding takes place under the point loading of ZIF-62 glass.

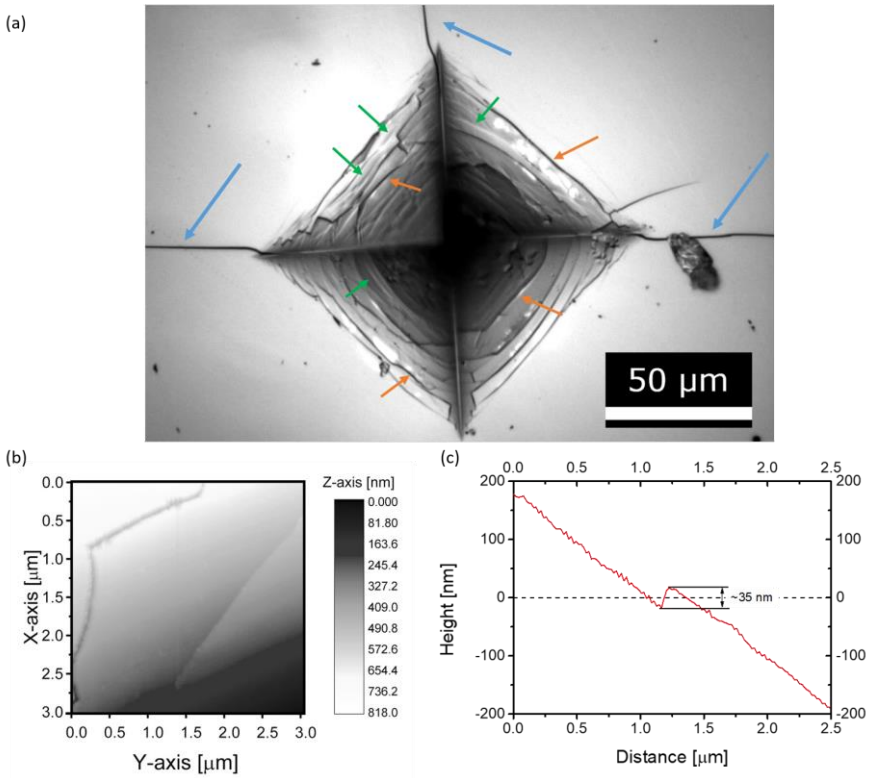

Figure 5-12 Observations of the features around the indents. (a) An indent image (5 N load) showing median cracking outside the impression (blue arrows), edge cracks (orange arrows) and shear bands (green arrows). (b) AFM scan of an area inside the indent with both the edge crack (A) and shear bands (B). (c) An AFM line scan of the shear band featuring the change in the height profile. Data taken from Paper II.

On the atomic level, shear bands are formed in a three-step process (*151*). The bonds between the structural units firstly break under the stress from the indentation. This enables the subsequent translational motion of the units. Finally, the bond reformation takes place between the structural units after their movements. This three-step process leads to highly localized plastic deformation, visible on the sample surface in a form of step-like features.

Shear bands have been widely studied in metallic glasses (*140,141*), some oxide glasses (*152–155*) and chalcogenide glasses (*122*). The shear band formation in metallic glasses initiates with the formation of STZs – shear transformation zones (*124,156*). These point defects are formed by the atomic rearrangement of a group of atoms on a local scale under shear loading. However, due to its small size (average of 1 nm (*156*)), it is difficult to observe STZs experimentally. Subsequently, a shear band is formed from a group of STZs located close by. The exact mechanism of this is still not known, however, some theories are stated in literature (*156*). These cover, for

example, initiation of shear banding by percolation of STZs or activation of STZs by stress concentrators (such as another point defect in the form of e.g. microvoids) (*156*). In oxide glasses, shear bands were observed in depolymerized structures with network modifiers present. In these cases, the existence of weaker bonds in the glass structure leads to promoting of bond breakage and reformation (*152–155*). The results obtained for some oxide glasses also suggest that some of the edge cracks are created from shear bands, which will later lead to separation of the material and, thus, develop into cracks. On the other hand, no shear band has ever been observed in silica glass. This is linked with silica's structure built of corner-shared tetrahedra, with no significantly 'weaker' bonds, which hinders the formation of shear bands under loading. For Germanium–Selenium chalcogenide glasses (*122*), shear bands are observed for samples with higher Se content. These glasses have Van der Waal's bonds between the chains structures, which act as the 'weaker' bonds in the structure, decreasing the glasses' resistance to permanent deformation.

The observation of shear bands in ZIF-62 glass in an unexpected, anomalous phenomenon, because of the polymerized network of this glass analogous to that of silica. However, the difference in bond strength between the coordination bond (Zn-ligand bond) and that of the stronger covalent bonds inside the organic ligands may promote the shear band formation. The mechanism behind this phenomenon is proposed as follows. The weakest bond in the ZIF-62 glass structure, the coordination bond, breaks under loading. The shearing stress leads to the translational movement of the material along the slip direction by a number of structural units (shear offset). After reaching an equilibrium position, the bonds reform in new locations (Paper II).

The plastic deformation under indentation can occur by shearing (observed in a form of a pile-up or shear bands) and densification. Typically, in the case of oxide glasses, densification is the main contributor to the plastic deformation of anomalous glasses, whereas the normal glasses promote deformation by shearing. In the case of the ZIF-62 glass, the presence of shear bands together with the significant depth of the densified zone suggests an intermediate mechanism of plastic response. Namely, both shearing and densification play a significant role in indentation deformation. Further investigations of the densification will be performed in the near future in order to quantitatively describe the deformation mechanisms of ZIF-62 glass.

5.5. INDENTATION BEHAVIOUR OF ZIF-62 GLASSES WITH CHANGING CHEMICAL COMPOSITION

As shown in Chapter 3, ZIF-62 crystals are characterized by facile changes of the building units both in terms of tuning the imidazolate-to-benzimidazolate ligand ratio and exchanging the zinc metal nodes by cobalt ones. As the obtained crystals display glass-forming ability, initial studies have been conducted on assessing how the chemical compositions of ZIF-62 affect the mechanical properties (i.e., hardness and indentation modulus). The results of these studies are presented in this chapter. Firstly,

the ligand ratio changes are assessed. Secondly, the results obtained for samples with cobalt nodes are presented.

5.5.1. CHANGING THE LIGAND RATIOS IN ZIF-62

The ligand ratio changes have shown to have a significant influence on the thermal properties of the ZIFs. Namely, the increase of the steric hindrance of the system with the content increase of the bulkier benzimidazolate has resulted in an increase of melting point and glass transition temperatures. In this chapter, the indentation investigations of the samples with varying ligands ratios produced by the hot-pressing method are presented.

5.5.1.1 Reproducibility and Repeatability Study

Due to the significant differences between results obtained by the author and a collaborator at Wuhan University of Technology (WUT) in hardness values of the hot-pressed samples with the same chemical composition (the same x values in $Zn(Im)_{2-x}(bIm)_x$) (Figure 5-13), a short study concerning the repeatability and reproducibility of the samples was conducted.

The first step was defining all the variable parameters between the two sets of data. As mentioned above, the results were obtained by two observers, on two separate machines, and on two separate samples, leading to observer error, equipment variance and sample-related variance influencing results. The first one (observer error) is connected to the result variance created by the differences in the measurement procedure of two researchers. During hardness measurement, the diagonals of an indent are measured by the researcher. Such a measurement is based solely on their individual impression of the indent (colloquially saying, how they see the indent and its edges). This phenomenon brings a high observer bias into the measurement. Another important error source is the machine. Each machine has its individual stiffness, the used indenter tips might be degraded to different extend (worn out) and accuracy and repeatability of the loading could differ. The last group of factors that may have affected the spread of the data is the sample itself. Both researchers measured samples hot-pressed in WUT, however, the samples were synthesized separately, at Aalborg University (AAU) and at WUT. The synthesized ZIF-62 crystals could differ slightly, leading to differences in obtained glasses.

A higher number of factors influencing the hardness measurements can be named (*157*), however, in this project, the author chose to focus on the factors described above.

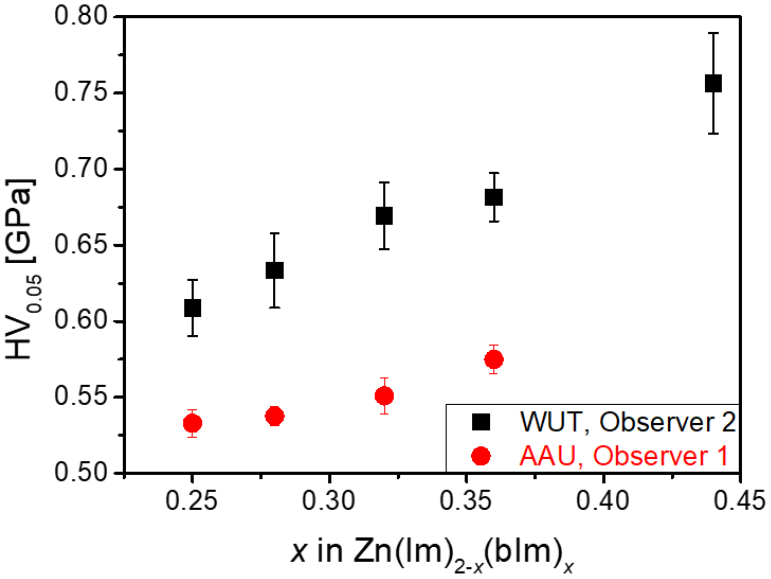

Figure 5-13 Vickers microhardness of ZIF-62 glass samples with varying imidazolate-to-benzimidazolate ratio ($ZnIm_{2-x}bIm_x$), as measured by two observed at two institutions. Red points are the values measured by the author at Aalborg University (AUU), the black points – values measured by a collaborator at Wuhan University of Technology (WUT).

Ïn order to minimize the significant experimental variations seen in Figure 5-13, a number of measures were introduced. The first step of the investigation was a discussion with the observer 2 to define the measurement procedure applied to the hardness measurement. As described in the earlier sections (Chapter 5.4.3), indent impressions obtained after indentation of ZIF glasses are characterized by not clearly visible edges and diagonal ends, due to the high degree of elastic deformation. It was therefore especially important to discuss the common view on the diagonal measurements. As one of the author's external stays took place at WUT, it was also possible to use the same equipment for measurements to limit the influence of equipment variability. Lastly, the sample variability was addressed by measuring the same samples by both observers. The environmental factors were controlled by running the measurements on the same day. The corrected measurements are presented in Figure 5-14.

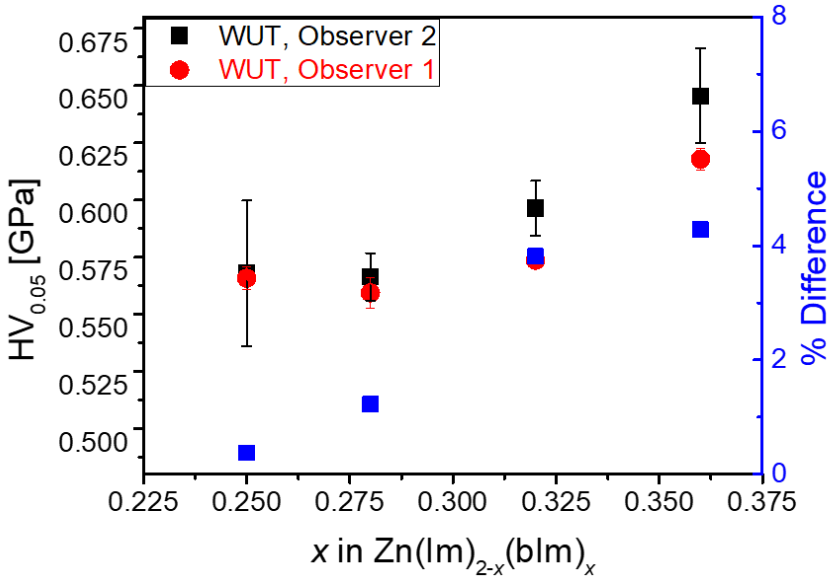

Figure 5-14 Vickers microhardness of ZIF-62 glass samples with varying imidazolate-to-benzimidazolate ratio ($ZnIm_{2-x}bIm_x$), as measured by two observed at one institution (Wuhan University of Technology). Red points are the values measured by the author, the black points – values measured by a collaborator. Blue squares represent the percentage difference in obtained values.

The results in Figure 5-14 display clear improvement in terms of data variability. However, an increasing difference between the measured hardness results can be observed with increasing benzimidazolate content (x in $Zn(Im)_{2-x}(bIm)_x$). These results indicate the observer variation plays an important role in measuring the hardness of ZIF glasses, especially with the high content of the bigger moieties. Such a dependence suggests there might be an increase of elastic response with an increase of benzimidazolate content, leading to a decrease of visibility of the indent edges, which in turn perturbs measurements of the indent diagonals.

To quantify the influence of the observer on obtained hardness results, a further study has been conducted at AAU. For this study, a sample with $x = 0.32$ was chosen (as the difference between the observer 1 and 2 at WUT became significant for this x value). Three AAU researchers (observers 3, 4 and 5) were asked to measure the same indents produced by the AAU equipment. Each of the researchers was experienced in the indentation method. The hardness results measured by them, as well as the author (observer 1) are shown in Table 5-3. The results obtained at WUT are included for further comparison. A significant difference in hardness values can be observed between each of the observers, revealing that the reproducibility of the hardness measurement is somewhat low. However, the standard deviation value stays low for each of the observers, signifying the repeatability of the results is high.

Table 5-3. Vickers microhardness values obtained on the same sample by five different observers. Note that the observers 1 and 2 in the first two rows measured the indents at the Wuhan University of Technology (WUT), whereas the rest of the results were obtained at Aalborg University (AAU). H_{min} value was taken as 0.5214 GPa, and the difference was calculated to assess the influence of different factors (i.e., place and observer influence).

Observer	**Place**	**Hardness [GPa]**	**% Difference to H_{min}**
1	WUT	0.5963±0.0036	14.37
2	WUT	0.5736±0.0120	10.01
1	AAU	0.5214±0.0003	-
3	AAU	0.5872±0.0011	12.62
4	AAU	0.5771±0.0012	10.68
5	AAU	0.5675±0.011	8.84

To summarize, this short study concludes that the reproducibility problem has high importance for ZIF glasses. Even though this problem is well known in hardness measurements, it should be underlined that in the case of these novel glasses, this issue seems to be much more significant. Due to this reason, it should be assured that only one observer measures the hardness of the tested samples series.

5.5.1.2 Is There an Influence of Changing the Ligand Ratio on the Hardness of ZIF-62 Glasses?

With the increase of benzimidazolate content, a certain increase in hardness values can be observed. However, as was described in chapter 5.5.1.1, this increase is accompanied by an increase in measurement uncertainty due to observer error. In this chapter, the author will try to answer the question stated by the title: is there an actual influence of changing the ligand ratio on hardness? Or is the visible trend simply the result of the increasing difficulties in conducting a certain measurement?

For measuring hardness without the observer error, the nanoindentation technique was applied to four samples with changing composition. Surprisingly, both the hardness and indentation modulus (Figure 5-15 a and b, respectively) decrease with the increase of benzimidazolate in the structure. However, the hardness values feature a higher uncertainty of the results, and the sample with x = ~ 0.255 is a clear outlier from the trend. This suggests the exchange of the ligand might not have as pronounced of

influence of the obtained results as implied on the initial microhardness results. Namely, the uncertainty of the obtained values might have an effect much more significant than that of ligands exchange in the tested range in this work. On the other hand, the indentation moduli suggest a clearer decrease with increasing benzimidazolate content.

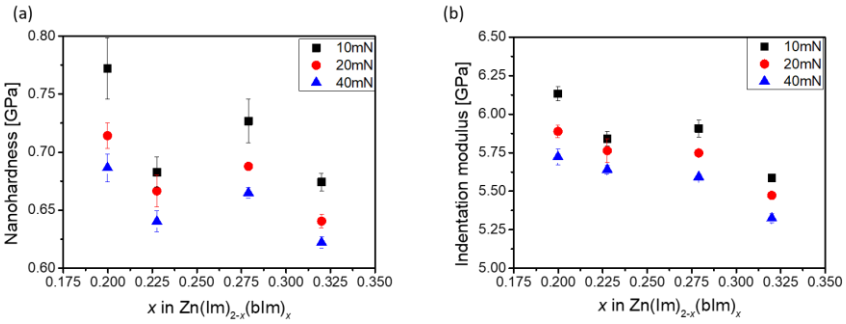

Figure 5-15 Nanohardness and indentation modulus as measured by nanoindentation technique with loads of 10 mN (black points), 20 mN (red points) and 40 mN (blue points) for ZIF-62 samples with varying imidazolate-to-benzimidazolate ratio ($ZnIm_{2-x}bIm_x$).

Three possible explanations to the decreasing hardness and indentation moduli with increasing benzimidazolate content are proposed, compared to the increasing values for microindentation measurements.

Firstly, the hardness values represent the resistance of the material to plastic deformation. This means the elastic component is not considered. With the increase of elastic response, the hardness values would increase. However, this explanation does not cover the slightly decreasing indentation moduli values. At the same time, the indentation moduli for loads of 10 mN and 20 mN are of relatively similar values for the three samples with lower benzimidazolate content, which may suggest little-if-any modulus changes with changing ligand ratio.

Another explanation could be the inhomogeneity of the ZIF glasses. Due to the small size of the sample pieces obtained from the hot-press, it was not possible to test the indentation on the same area of the sample. It is therefore suggested that for future studies at least three different areas of the glass should be tested. As an initial study, four selected areas were tested for both nano- and microindentation study and similar results were obtained. However, this initial investigation has not provided enough data to evaluate possible small trends. A systematic study should therefore be performed before the final conclusions can be drawn.

Lastly, it is possible that changing benzimidazolate content leads to the extent of the indentation size effect. As the extent of changes in hardness values could vary between samples with changing chemical composition, a possible artifact in the obtained

relations might be created. As the influence of shear banding has a pronounced effect on the hardness changes in the low-load range in metallic glasses (*140*), it is possible that a similar effect might be observed in ZIF glasses. In this case, an energy barrier needed for shear band formation might have an influence on the measured results and leads to a change of the trend between the hardness and ligand ratio in different loading ranges.

All of these explanations might lead to the difference in hardness values obtained with various loads and on different samples, creating a fictitious trend. The possible factors affecting the trends between the ligand ratio and mechanical properties should therefore be investigated further in order to quantify the influence of each and every one of them. For the first factor, a closer study of the indentation response mechanism for samples with changing ligand ratios is suggested. This would give a clear overview of how the various responses affect the obtained hardness and modulus values in ZIF glass with changing chemical composition. The author also suggests mapping the hardness and indentation modulus on samples produced with the SPS technique. Considering the samples do not break into as many pieces as the hot-pressed samples, this might enable a quantification of the possible inhomogeneity of the sample. Lastly, a systematic study of the indentation size effect should be performed. Together with other data, this would provide a new point of view on the chemical composition's influence on hardness and indentation modulus.

5.5.2. COBALT-ZINC BIMETALLIC ZIF-62

As described before (Chapter 3.1.1), partially cobalt-substituted ZIF-62 samples were melt-quenched. In order to check the influence of the node exchange on the mechanical properties, hardness and indentation moduli were measured using nanoindentation technique for samples with cobalt content up to $x < 0.6$ (Figure 5-16 a). It was impossible to carry out measurements on the Co-ZIF-62 sample due to the high bubble content. For the same reason, the Vickers microhardness measurements were not suitable for mechanical characterizations of samples with varying Co content. Instead, nanohardness measurements were conducted on the Co-ZIF-62 samples. As shown in Figure 5-16a, nanohardness values seem not to be influenced by the addition of cobalt in a significant manner, as the values do not display any systematic change with increase of cobalt content.

However, indentation modulus exhibits a minimum at $x = 0.4$ for two of the tested maximum loads (20 – 40 mN), as can be observed in Figure 5-16 b. The tendency is somewhat similar to what was observed for T_g and T_m values, which also featured minima when tested with changing cobalt content. Here it should be noted, that the increase of E_{ind} with x values observed for the $x = 0.6$ is a strong indication that the value fluctuations are not solely caused by the increase of bubble content of the samples. In that case, a decrease in values would be expected for all the samples with increasing cobalt content. Interestingly, the x value at the minimum value differs

between the indentation modulus and the T_g and T_m measurements, suggesting different structural factors may influence the changes in different parameters.

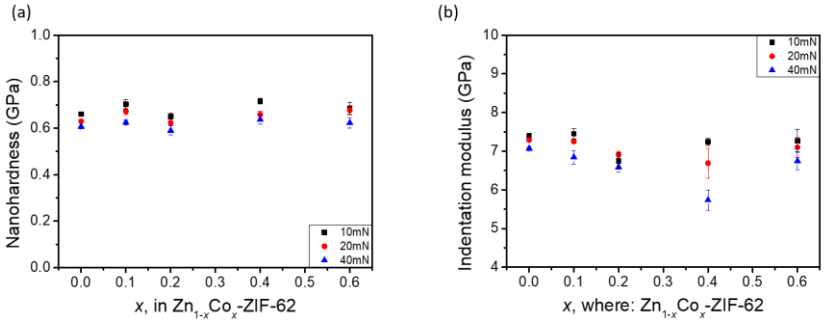

Figure 5-16 Nanohardness and indentation modulus as measured by nanoindentation technique with loads of 10 mN (black points), 20 mN (red points) and 40 mN (blue points) for ZIF-62 samples with cobalt substitution ($Zn_{1-x}Co_x$-ZIF-62).

The fluctuation of the results for 10 mN series might be caused by the roughness of the surface that was not fully removed by polishing with a 0.25 μm polishing medium. One of the reasons for that could be the presence of bubbles, as material chipping during the polishing could scratch the sample's surface. With higher loads, the indentation depth is much larger than the layer which is significantly affected by the surface roughness. The nanoindentation measurement results thus suggest that the introduction of the second metallic node affects the elastic deformation (indentation modulus) on a bigger scale than the permanent deformation. It can therefore be implied that the introduction of the second metal node influences the reversible bond rearrangement to a higher extent than the permanent atomic rearrangement (densification) and bond breakage enabling the shearing. However, deeper investigations should be performed in order to provide better understanding of these trends.

5.6. SUMMARY

The indentation behavior of hot-pressed ZIF-62 glass has been characterized by the use of micro- and nanoindentation techniques and further analyses with other methods (such as AFM). The low hardness of the ZIF glass (comparing to oxide and metallic glasses) has been explained in terms of structural factors.

The fracture patterns display the presence of radial-median cracks outside the highly deformed zone. This observation accords well with the high Poisson's ratio measured for ZIF-62 glass, yet it is anomalous for the low E/H ratio materials. Inside the indent impression, a system of step-like cracks is noted. With further AFM analysis, the features inside the impressions are identified as edge cracks and shear bands. The following mechanism for shear band formation is suggested: (i) the coordinative bond

between Zn and the ligand breaks, providing more freedom of translational movement, (ii) under the indentation stress, the building units on two sides of the broken bond move along the slip plane, (iii) after the movement, the building units reform coordination bond in the new location. Interestingly, the two-stage hardness drop observed with load increase (Figure 5-6) could be linked with shear banding process. Further investigations should, however, be performed to confirm this theory. By analyzing nanoindentation load-displacement curves, the elastic contribution to the deformation mechanism of ZIF-62 glass was shown to be around 50%. This high value accords well with the indent shape (the occurrence of sink in). Interestingly, a significant pile-up was not observed in the vicinity of the indent. Together with the observed shear bands, the plastic deformation in ZIF-62 glass by shearing occurs on a small, local scale only. Unfortunately, it is technically difficult to quantify the densification in this novel glass. Due to the high free volume in the framework structure, this particular mechanism should also play an important role in deformation induced by indentation. The investigation is this mechanism is still ongoing.

Lastly, initial trials were performed to characterize the influence of chemical composition on the mechanical response of ZIF-62 glass. Unfortunately, the results for both changing the ligand ratio and partial substitution of zinc in the framework structure do not display any undoubtable trends. For the samples with varying ligand ratios, the trend changes between microindentation and nanoindentation measurements. Three possible reasons for this phenomenon have been presented in Chapter 5.5.1.2. The metallic node substitution seems to result in a visible minimum of indentation modulus for Co content of around 40%. The hardness values do not exhibit any significant trends. However, it should be noted that the samples for this study were obtained by melt-quenching (in contrary to the hot-pressed samples with varying ligand ratios). The sample fabrication technique might affect the homogeneity of the samples, and thus, result in the lack of visible trends. Interestingly, for both cases (ligand and metallic node exchange) indentation modulus values feature smaller result variations, suggesting this parameter is influenced by uncontrollable parameters to a smaller extent.

CHAPTER 6. CONCLUSIONS AND PERSPECTIVES

This thesis focuses on three main areas of interest: (i) the relations between the chemical composition of ZIF and their glass-forming ability, (ii) the fabrication of bulk ZIF glass samples and (iii) the exploration of mechanical properties of ZIF glasses. Based on the information presented in this thesis, the following conclusions are drawn and future investigations are proposed.

The influence of the chemical composition of ZIFs on their glass-forming ability

After conducting a comprehensive literature review of ZIFs reported as the glass formers and the substances with no melting ability, two regions of chemical composition changes were addressed. Starting with the change of metallic node, the substitution of zinc by cobalt did not seem to affect the ability of both ZIF-4 and ZIF-62 to melt. For now, this conclusion has not been extended to other types of metallic nodes, as no other metallic nodes have been successfully incorporated into the ZIF structure via solvothermal synthesis. Furthermore, the obtained results indicate that Co-ZIF-62 forms polymorph crystals. The Co-ZIF-62 polymorph forms an eutectic mixture with Zn-ZIF-62, which was observed for both T_m and T_g values.

Secondly, the effect of the ligand change was assessed. Initially, the differences in the melting abilities (or lack of thereof) of ZIFs with basic ligands (imidazolate, benzimidazolate) were discussed. Furthermore, three factors concerning the structure of the ligands with functional groups that may affect the glass-forming ability of ZIFs were identified, i.e.: the location of the functional group on the aromatic rings, the electronegativity of the functional group, and the asymmetry of the ligand. Moreover, the ratio differences between different ligands in mixed-ligand ZIFs do not affect their melting ability. In the case of ZIF-62, the changes in the ligand ratio led to an increase of both T_m and T_g with the increase of benzimidazolate content.

The next steps in the search for new ZIF glass-formers are proposed as follows. Firstly, the three proposed factors concerning the ligand structure favoring the glass-forming ability of ZIFs should be tested experimentally. This should lead to defining certain structural characteristics determining the glass-forming ability of ZIF glasses. Furthermore, the search for other nodes that can substitute zinc should be continued, possibly with extension to different synthesis methods. This could be particularly helpful in finding application fields for ZIF glasses, as the mixed-metals ZIFs have shown, e.g., unique catalytic properties (*56*, *72*).

The fabrication of bulk ZIF glass samples

The second area of interest covered the development of methods for the fabrication of bulk ZIF glass samples. Here, three methods (melt-quenching under ambient pressure MQ-AP, hot-pressing and spark plasma sintering – SPS) were conducted and various process parameters were optimized. Both the hot-press and SPS methods provide glass samples with good quality (assessed on lack of bubbles inside the sample). On the other hand, the facile MQ-AP process produced bulk samples with small bubbles, yet the shape of the sample was preserved after the melt-quenching. This is in contrast to the cracking and chipping observed on the glasses obtained via both hot-pressing and SPS techniques. The influence of the pressure applied during the fabrication process was also studied, namely, a decrease of T_g by around 35 K and an increase of a density of around 3% of the produced samples. This phenomenon was observed in SPS samples to the highest extent. Namely, it was explained in terms of possible structural induced by the pressure applied, i.e., the structural densification and distortion, since the pressure could affect the diffusive process during sintering (on the contrary to the melting process taking place in both MQ-AP and hot-pressing).

With regard to the optimization of the processes, a special focus is to be turned towards eliminating the chipping and cracking of the samples produced by hot-pressing and SPS methods. If these artifacts were eliminated, both of the methods could produce high-quality bulk samples that could be used for further examinations and applications. This would be especially helpful in the field of mechanical properties, where the possibility of fabrication of a bulk sample will open the doors to the characterization methods such as tensile, compression or bending tests.

Indentation behavior of ZIF-62 glass

Lastly, a detailed investigation into the indentation behavior of ZIF-62 glass was performed. The hardness of ZIF-62 glass (0.5-0.65 GPa, depending on load used during indentation) fits between the values typically obtained for stronger, inorganic glasses and softer, polymeric glasses. The relatively low hardness of ZIF glass (when compared to another traditional glass of structure analogous to ZIF glass – silica glass) was explained in terms of four structural factors, i.e., the bond strength (weak coordination bond in ZIFs), the number of constraints per unit volume, the rotational and orientational freedom of the building units (organic ligands) and the degree of free volume. The Poisson's ratio was measured to be 0.35, which is surprisingly higher than that of ZIF-62 crystal (ν = 0.15) (*16*).

Furthermore, the fracture pattern of ZIF glasses was studied. A step-like pattern was discovered inside the indent impressions, where both the edge cracks and shear bands were found. Out of the indent area, a median-radial crack system was observed. This

crack pattern is anomalous when comparing to that of silica glass, indicating the analogous structure of the glasses is not the dominating factor affecting the fracture behavior. Instead, the observed behavior of ZIF-62 correlates well with the high Poisson's ratio glasses shown on the indentation driving-force map (*119*).

Moreover, the investigations into the deformation mechanism have shown that ZIF glasses exhibit a high contribution of elastic deformation under indentation conditions. The cross-sectional image of the indent also suggests a high degree of densification. For shearing mechanism, no pile-up has been detected (in accordance with the sink-in due to the high elastic deformation), however, nano-metric shear banding was observed. This latter observation is especially important, considering the polymerized structure of ZIF glasses. Shear-bands were never observed before in network glasses with such structure. Here, the mechanism for shear bands formation was proposed, which is based on the breakage of the weak coordination bond present in ZIF glass and their subsequent recreation after translational movement along slip lines.

Future work should be focused on the investigation of the shear bands. Those should include the step-size distribution studies under various loadings and the initiation mechanism of shear bands. The latter could be an interesting subject, as the two-stage indentation size effect might be linked to the shear banding process (as was shown in the case of metallic glasses (*140*)). Moreover, the densification under point loading should be investigated to provide a comprehensive overview of all of the deformation mechanisms.

Unfortunately, no certain trends could be obtained regarding the influence of the chemical composition on the mechanical properties of the tested samples. This was most likely linked to the higher fluctuations of the measured values than the differences among the parameters themselves. Here, it is proposed that firstly, a more detailed study of the external factors affecting the mechanical properties of samples should be undertaken. Based on the current results, it is clear to see the observer's influence has a great impact on the results, which suggests other factors could be as important. These could include, e.g., different mechanical property values in different sections of one sample or variability between samples fabricated with the same parameters. Further investigations should be conducted into these factors before definite conclusions can be drawn.

BIBLIOGRAPHY

1. O. M. Yaghi, H. Li, C. Davis, D. Richardson, T. L. Groy, Synthetic Strategies, Structure Patterns, and Emerging Properties in the Chemistry of Modular Porous Solids. *Acc. Chem. Res.* **31**, 474–484 (1998).
2. S. L. James, Metal-organic frameworks. *Chem. Soc. Rev.* **32**, 276–288 (2003).
3. O. M. Yaghi *et al.*, Reticular synthesis and the design of new materials. *Nature*. **423**, 705–714 (2003).
4. S. Horike, S. Shimomura, S. Kitagawa, Soft porous crystals. *Nat. Chem.* **1**, 695–704 (2009).
5. S. Horike, S. S. Nagarkar, O. Tomohiro, S. Kitagawa, New Dimension of Coordination Polymers and Metal–Organic Frameworks toward Functional Glasses and Liquids. *Angew. Chemie Int. Ed.*, Accepted Article, 2019, doi:10.1002/anie.201911384.
6. D. Alezi *et al.*, MOF Crystal Chemistry Paving the Way to Gas Storage Needs: Aluminum-Based soc -MOF for CH_4, O_2, and CO_2 Storage. *J. Am. Chem. Soc.* **137**, 13308–13318 (2015).
7. H. Furukawa, K. E. Cordova, M. O'Keeffe, O. M. Yaghi, The chemistry and applications of metal-organic frameworks. *Science* **341**, 1230444 (2013).
8. G. Xu *et al.*, Exploring metal organic frameworks for energy storage in batteries and supercapacitors. *Mater. Today*. **20**, 191–209 (2017).
9. S. Hasegawa *et al.*, Three-dimensional porous coordination polymer functionalized with amide groups based on tridentate ligand: Selective sorption and catalysis. *J. Am. Chem. Soc.* **129**, 2607–2614 (2007).
10. J. Lee *et al.*, Metal-organic framework materials as catalysts. *Chem. Soc. Rev.* **38**, 1450–1459 (2009).
11. S. Horike, M. Dincă, K. Tamaki, J. R. Long, Size-selective Lewis acid catalysis in a microporous metal-organic framework with exposed Mn2+ coordination sites. *J. Am. Chem. Soc.* **130**, 5854–5855 (2008).
12. P. Ramaswamy, N. E. Wong, G. K. H. Shimizu, MOFs as proton conductors-challenges and opportunities. *Chem. Soc. Rev.* **43**, 5913–5932 (2014).
13. S. S. Han, J. L. Mendoza-Cortés, W. A. Goddard, Recent advances on simulation and theory of hydrogen storage in metal-organic frameworks and covalent organic frameworks. *Chem. Soc. Rev.* **38**, 1460–1476 (2009).
14. S. Horike, D. Umeyama, S. Kitagawa, Ion conductivity and transport by porous coordination polymers and metal-organic frameworks. *Acc. Chem. Res.* **46**, 2376–2384 (2013).
15. T. D. Bennett *et al.*, Hybrid glasses from strong and fragile metal-organic framework liquids. *Nat. Commun.* **6**, 8079 (2015).
16. A. Qiao *et al.*, A metal-organic framework with ultrahigh glass-forming ability. *Sci. Adv.* **4**, eaao6827 (2018).
17. T. D. Bennett *et al.*, Melt-Quenched Glasses of Metal-Organic Frameworks. *J. Am. Chem. Soc.* **138**, 3484–3492 (2016).

18. H. Z. Tao, T. D. Bennett, Y. Z. Yue, Melt-Quenched Hybrid Glasses from Metal–Organic Frameworks. *Adv. Mater.* **29**, 1601705 (2017).
19. T. D. Bennett, S. Horike, Liquid, glass and amorphous solid states of coordination polymers and metal–organic frameworks. *Nat. Rev. Mater.* **3**, 431–440 (2018).
20. C. Zhou *et al.*, Metal-organic framework glasses with permanent accessible porosity. *Nat. Commun.* **9**, 1–9 (2018).
21. A. Qiao *et al.*, A metal-organic framework with ultrahigh glass-forming ability. *Sci. Adv.* **4**, eaao6827 (2018).
22. J. Y. Zhang *et al.*, Structural Evolution in a Melt-Quenched Zeolitic Imidazolate Framework Glass during Heat-treatment. *Chem. Commun.* **55**, 2521–2524 (2019).
23. R. Banerjee *et al.*, High-throughput synthesis of zeolitic imidazolate frameworks and application to CO_2 capture. *Science* **319**, 939–943 (2008).
24. R. Gaillac *et al.*, Liquid metal–organic frameworks. *Nat. Mater.* **16**, 1149 (2017).
25. P. A. V. Johnson, A. C. Wright, R. N. Sinclair, Neutron scattering from vitreous silica II. Twin-axis diffraction experiments. *J. Non. Cryst. Solids*. **58**, 109–130 (1983).
26. G. N. Greaves, S. Sen, Inorganic glasses, glass-forming liquids and amorphizing solids. *Adv. Phys.* **56**, 1–166 (2007).
27. K. S. Park *et al.*, Exceptional chemical and thermal stability of zeolitic imidazolate frameworks. *Proc. Natl. Acad. Sci. U. S. A.* **103**, 10186–10191 (2006).
28. D. Peralta *et al.*, Comparison of the behavior of metal-organic frameworks and zeolites for hydrocarbon separations. *J. Am. Chem. Soc.* **134**, 8115–8126 (2012).
29. S. A. Moggach, M. T. Wharmby, P. A. Wright, S. Parsons, Opening the Gate : Framework Flexibility in ZIF-8 Explored by Experiments and Simulations. *J. Am. Chem. Soc.* **133**, 8900–8902 (2011).
30. Y. Q. Cheng, A. J. Ramirez-cuesta, I. Ravikovitch, New insights into the breathing phenomenon in ZIF-4. *J. Mater. Chem. A.* **7**, 14552–14558 (2019).
31. J. R. Li, R. J. Kuppler, H. C. Zhou, Selective gas adsorption and separation in metal-organic frameworks. *Chem. Soc. Rev.* **38**, 1477–1504 (2009).
32. S. Yuan *et al.*, Luminescent sensors based on metal-organic frameworks. *Coord. Chem. Rev.* **354**, 28–45 (2017).
33. S. Liu, Z. Xiang, Z. Hu, X. Zheng, D. Cao, Zeolitic imidazolate framework-8 as a luminescent material for the sensing of metal ions and small molecules. *J. Mater. Chem.* **21**, 6649 (2011).
34. M. A. Ali *et al.*, Broad Mid-Infrared Luminescence in a Metal − Organic Framework Glass. *ACS Omega*. **4**, 12081–12087 (2019).

35. T. N. Nguyen, F. M. Ebrahim, K. C. Stylianou, Photoluminescent, upconversion luminescent and nonlinear optical metal-organic frameworks: From fundamental photophysics to potential applications. *Coord. Chem. Rev.* **377**, 259–306 (2018).
36. B. Valizadeh, T. N. Nguyen, K. C. Stylianou, Shape engineering of metal – organic frameworks. *Polyhedron*. **145**, 1–15 (2018).
37. T. Tian, J. Velazquez-Garcia, T. D. Bennett, D. Fairen-Jimenez, Mechanically and chemically robust ZIF-8 monoliths with high volumetric adsorption capacity. *J. Mater. Chem. A*. **3**, 2999–3005 (2015).
38. D. Bazer-bachi, L. Assié, V. Lecocq, B. Harbuzaru, V. Falk, Towards industrial use of metal-organic aframework : Impact of shaping on the MOF properties. *Powder Technol.* **255**, 52–59 (2014).
39. R. N. Widmer *et al.*, Manufacturing Macroporous Monoliths of Microporous Metal − Organic Frameworks. *ACS Appl. Nano Mater.* **1**, 497–500 (2018).
40. D. Bazer-bachi, L. Assié, V. Lecocq, B. Harbuzaru, V. Falk, Towards industrial use of metal-organic framework: Impact of shaping on the MOF properties. *Powder Technol.* **255**, 52–59 (2014).
41. C. Zhou *et al.*, Thermodynamic features and enthalpy relaxation in a metal–organic framework glass. *Phys. Chem. Chem. Phys.* **20**, 18291–18296 (2018).
42. S. R. Elliott, in *Encyclopedia of Materials: Science and Technology (Second Edition)*, J. Buschow et al., Eds. (Elsevier, 2nd ed, 2001), pp. 215–219.
43. S. L. Webb, in *Mineral behaviour at extreme conditions*, R. Miletich, Ed. (Eötvös University Press, Budapest, 2005), pp. 65–94.
44. C. Zhou *et al.*, Metal-organic framework glasses with permanent accessible porosity. *Nat. Commun.* **9**, 5042 (2018).
45. D. W. Lewis *et al.*, Zeolitic imidazole frameworks: Structural and energetics trends compared with their zeolite analogues. *CrystEngComm*. **11**, 2272–2276 (2009).
46. M. Gustafsson, X. Zou, Crystal formation and size control of zeolitic imidazolate frameworks with mixed imidazolate linkers. *J. Porous Mater.* **20**, 55–63 (2013).
47. R. N. Widmer *et al.*, Pressure promoted low-temperature melting of metal–organic frameworks. *Nat. Mater.* **18**, 370–376 (2019).
48. R. Gaillac, P. Pullumbi, F.-X. Courdet, *J. Phys. Chem. C*, **112**, 6730-6736 (2018).
49. R. Pinal, Effect of molecular symmetry on melting temperature and solubility. *Org. Biomol. Chem.* **2**, 2692–2699 (2004).
50. A. Gavezzotti, C. Strutturale, U. Milano, Molecular symmetry, melting temperatures and melting enthalpies of substituted benzenes and naphthalenes. *J. Chem. Soc. Perkin Trans. 2*. **2**, 1399–1404 (1995).
51. C. Zhou *et al.*, Polymorph formation for a zeolitic imidazolate framework composition - $Zn(Im)_2$. *Microporous Mesoporous Mater.* **265**, 57–62 (2018).
52. R. N. Widmer *et al.*, Rich Polymorphism of a Metal-Organic Framework in Pressure-Temperature Space. *J. Am. Chem. Soc.* **141**, 9330–9337 (2019).

53. L. Bouëssel Du Bourg, A. U. Ortiz, A. Boutin, F. X. Coudert, Thermal and mechanical stability of zeolitic imidazolate frameworks polymorphs. *APL Mater.* **2**, 124110 (2014).
54. Q. Zheng, Y. Zhang, M. Montazerian, O. Gulbiten, J. C. Mauro, Y. Z. Yue, Understanding Glass through Differential Scanning Calorimetry. *Chem. Rev.*, 1–270 (2018).
55. Y. Q. Tian *et al.*, Cadmium imidazolate frameworks with polymorphism, high thermal stability, and a large surface area. *Chem. - A Eur. J.* **16**, 1137–1141 (2010).
56. N. Masciocchi *et al.*, Extended polymorphism in copper(II) imidazolate polymers: A spectroscopic and XRPD structural study. *Inorg. Chem.* **40**, 5897–5905 (2001).
57. Z. Wang *et al.*, Fe, Cu-Coordinated ZIF-Derived Carbon Framework for Efficient Oxygen Reduction Reaction and Zinc–Air Batteries. *Adv. Funct. Mater.* **28**, 1–8 (2018).
58. M. E. Schweinefuß *et al.*, Indium imidazolate frameworks with differently distorted ReO3-type structures: Syntheses, structures, phase transitions, and crystallization studies. *Cryst. Growth Des.* **14**, 4664–4673 (2014).
59. J. K. Zareba, M. Nyk, M. Samoć, Co/ZIF-8 Heterometallic Nanoparticles: Control of Nanocrystal Size and Properties by a Mixed-Metal Approach. *Cryst. Growth Des.* **16**, 6419–6425 (2016).
60. K. Zhou *et al.*, Characterization and properties of Zn/Co zeolitic imidazolate frameworks vs. ZIF-8 and ZIF-67. *J. Mater. Chem. A.* **5**, 952–957 (2017).
61. D. Saliba, M. Ammar, M. Rammal, M. Al-Ghoul, M. Hmadeh, Crystal Growth of ZIF-8, ZIF-67, and Their Mixed-Metal Derivatives. *J. Am. Chem. Soc.* **140**, 1812–1823 (2018).
62. A. Phan *et al.*, Synthesis, structure, and carbon dioxide capture properties of zeolitic imidazolate frameworks. *Acc Chem Res*. **43**, 58–67 (2010).
63. M. Jian, B. Liu, G. Zhang, R. Liu, X. Zhang, Adsorptive removal of arsenic from aqueous solution by zeolitic imidazolate framework-8 (ZIF-8) nanoparticles. *Colloids Surfaces A Physicochem. Eng. Asp.* **465**, 67–76 (2015).
64. H. Moldenhauer *et al.*, Porous purple glass – a cobalt imidazolate glass with accessible porosity from a meltable cobalt imidazolate framework. *J. Mater. Chem. A*. **7**, 985–990 (2018).
65. L. Frentzel-beyme, M. Kloß, P. Kolodzeiski, R. Pallach, S. Henke, Meltable Mixed-Linker Zeolitic Imidazolate Frameworks and Their Microporous Glasses: From Melting Point Engineering to Selective Hydrocarbon Sorption. *J. Am. Chem. Soc.* **141**, 12362–12371 (2019).
66. J. Y. Zhang, A. Qiao, H. Z. Tao, Y. Z. Yue, Synthesis, phase transitions and vitrification of the zeolitic imidazolate framework: ZIF-4. *J. Non. Cryst. Solids*. **525**, 119665 (2019).

67. A. D. Katsenis *et al.*, In situ X-ray diffraction monitoring of a mechanochemical reaction reveals a unique topology metal-organic framework. *Nat. Commun.* **6**, 6662 (2015).
68. W. Tu *et al.*, Glass transition and mixing thermodynamics of a binary eutectic system. *Phys. Chem. Chem. Phys.* **16**, 3586–3592 (2014).
69. A. U. Ortiz, A. P. Freitas, A. Boutin, A. H. Fuchs, F. X. Coudert, What makes zeolitic imidazolate frameworks hydrophobic or hydrophilic? The impact of geometry and functionalization on water adsorption. *Phys. Chem. Chem. Phys.* **16**, 9940–9949 (2014).
70. J. Sun *et al.*, Facile synthesis of Cd-substituted zeolitic-imidazolate framework Cd-ZIF-8 and mixed-metal CdZn-ZIF-8. *Microporous Mesoporous Mater.* **264**, 35–42 (2018).
71. P. Krokidas, S. Moncho, E. N. Brothers, M. Castier, I. G. Economou, Tailoring the gas separation efficiency of metal organic framework ZIF-8 through metal substitution: a computational study. *Phys. Chem. Chem. Phys.* **20**, 4879–4892 (2018).
72. J. Li *et al.*, Copper (II) imidazolate frameworks as highly efficient photocatalysts for reduction of CO2 into methanol under visible light irradiation. *J. Solid State Chem.* **203**, 154–159 (2013).
73. A. Schejn *et al.*, Cu^{2+}-doped zeolitic imidazolate frameworks (ZIF-8): efficient and stable catalysts for cycloadditions and condensation reactions. *Catal. Sci. Technol.* **5**, 1829–1839 (2015).
74. A. S. Myerson, R. Ginde, in *Handbook of Industrial Crystallization*, A. S. Myerson, Ed. (Elsevier Science & Technology, Oxford, ed. 2, 2019), pp. 33–66.
75. N. Stock, S. Biswas, Synthesis of metal-organic frameworks (MOFs): Routes to various MOF topologies, morphologies, and composites. *Chem. Rev.* **112**, 933–969 (2012).
76. B. Seoane, J. M. Zamaro, C. Tellez, J. Coronas, Sonocrystallization of zeolitic imidazolate frameworks (ZIF-7, ZIF-8, ZIF-11 and ZIF-20). *CrystEngComm*. **14**, 3103–3107 (2012).
77. M. He, J. Yao, Q. Liu, Z. Zhong, H. Wang, Toluene-assisted synthesis of RHO-type zeolitic imidazolate frameworks: synthesis and formation mechanism of ZIF-11 and ZIF-12. *Dalt. Trans.* **2**, 16608–16613 (2013).
78. Y. R. Lee *et al.*, ZIF-8: A comparison of synthesis methods. *Chem. Eng. J.* **271**, 276–280 (2015).
79. J. Wan *et al.*, Strategies to improve metal organic frameworks photocatalyst's performance for degradation of organic pollutants. *Coord. Chem. Rev.* **376**, 449–466 (2018).
80. C. Zhou *et al.*, Metal-organic framework glasses with permanent accessible porosity. *Nat. Commun.* **9**, 5042 (2018).
81. T. Wu, X. Bu, J. Zhang, P. Feng, New zeolitic imidazolate frameworks: From unprecedented assembly of cubic clusters to ordered cooperative organization of complementary ligands. *Chem. Mater.* **20**, 7377–7382 (2008).

82. C. Zhou, Ph.D. thesis, Aalborg University (2018).
83. Y. Te Liao *et al.*, Synthesis of Mixed-Ligand Zeolitic Imidazolate Framework (ZIF-8-90) for CO_2 Adsorption. *J. Inorg. Organomet. Polym. Mater.* **25**, 251–258 (2015).
84. Y. Ban, Y. Li, X. Liu, Y. Peng, W. Yang, Solvothermal synthesis of mixed-ligand metal-organic framework ZIF-78 with controllable size and morphology. *Microporous Mesoporous Mater.* **173**, 29–36 (2013).
85. Y. Yang *et al.*, Prediction of the Glass Transition Temperatures of Zeolitic Imidazolate Glasses through Topological Constraint Theory. *J. Phys. Chem. Lett.* **9**, 6985–6990 (2018).
86. J. C. Mauro, Y. Z. Yue, A. J. Ellison, P. K. Gupta, D. C. Allan, Viscosity of glass-forming liquids. *Proc. Natl. Acad. Sci. U. S. A.* **106**, 19780–19784 (2009).
87. A. Qiao *et al.*, Optical properties of a melt-quenched metal–organic framework glass. *Opt. Lett.* **44**, 1623 (2019).
88. S. Li *et al.*, Mechanical Properties and Processing Techniques of Bulk Metal-Organic Framework Glasses. *J. Am. Chem. Soc.* **141**, 1027–1034 (2019).
89. V. Mamedov, Spark plasma sintering as advanced PM sintering method. *Powder Metall.* **45**, 322–328 (2002).
90. X. Song, X. Liu, J. Zhang, Neck Formation and Self-Adjusting Mechanism of Neck Growth of Conducting Powders in Spark Plasma Sintering. *J. Am. Ceram. Soc.* **89**, 494–500 (2006).
91. R. Chaim, Densification mechanisms in spark plasma sintering of nanocrystalline ceramics. *Mater. Sci. Eng. A.* **443**, 25–32 (2007).
92. D. Sciti, A. Bellosi, Fast Densification of Ultra-High-Temperature Ceramics by Spark Plasma Sintering. *Int. J. Appl. Glas. Sci.* **3**, 32–40 (2006).
93. J. Adam, L. Calvez, J. Trol, V. Nazabal, Chalcogenide Glasses for Infrared Photonics. *Int. J. Appl. Glas. Sci.* **6**, 287–294 (2015).
94. L. Calvez, Comptes Rendus Physique Chalcogenide glasses and glass-ceramics : Transparent materials in the infrared for dual applications. *Comptes Rendus Phys.* **18**, 314–322 (2017).
95. B. Xue *et al.*, Mechanical milling and SPS used to obtain GeS 2 - β GeS 2 infrared glass-ceramic. *J. Non. Cryst. Solids*. **377**, 240–244 (2013).
96. P. G. Debenedetti, F. H. Stillinger, Supercooled liquids and the glass transition. *Nature*. **410**, 259 (2001).
97. W. C. Oliver, G. M. Pharr, An improved technique for determining hardness and elastic modulus using load and displacement sensing indentation experiments. *J. Mater. Res.* **7**, 1564–1583 (1992).
98. I. N. Sneddon, The relation between load and penetration in the axisymmetric boussinesq problem for a punch of arbitrary profile. *Int. J. Eng. Sci.* **3**, 47–57 (1965).
99. J. W. Harding, I. N. Sneddon, The elastic stresses produced by the indentation of the plane surface of a semi-infinite elastic solid by a rigid punch. *Proc. Camb. Philol. Soc.* **41**, 16 (1945).

100. D. Chicot *et al.*, A contact area function for Berkovich nanoindentation: Application to hardness determination of a TiHfCN thin film. *Thin Solid Films*. **558**, 259–266 (2014).
101. A. C. Fischer-Cripps, *Nanoindentation*, Springer, (2011), ISBN 978-1-4419-9871-2.
102. K. Januchta, M. M. Smedskjaer, Indentation deformation in oxide glasses: Quantification, structural changes, and relation to cracking. *J. Non-Crystalline Solids X*. **1**, 100007 (2019).
103. S. Yoshida, J. C. Sanglebœuf, T. Rouxel, Quantitative evaluation of indentation-induced densification in glass. *J. Mater. Res.* **20**, 3404–3412 (2005).
104. M. Wada, Crack resistance of glass on Vickers indentation. *Proc. 10th Int. Congr. Glas.* **11**, 39 (1974).
105. R. Hill, The Elastic Behaviour of a Crystalline Aggregate. *Proc. Phys. Soc. A*. **65**, 349–354 (1952).
106. C. S. Man, M. Huang, A simple explicit formula for the Voigt-Reuss-Hill average of elastic polycrystals with arbitrary crystal and texture symmetries. *J. Elast.* **105**, 29–48 (2011).
107. M. Xiong, N. Li, N. Greaves, Y. Z. Yue, *arXiv Prepr.*, ArXiv ID 1712.07372 (2017).
108. B. Zheng *et al.*, Theoretical prediction of the mechanical properties of zeolitic imidazolate frameworks (ZIFs). *RSC Adv.* **7**, 41499–41503 (2017).
109. M. R. Ryder, J.-C. Tan, Explaining the mechanical mechanisms of zeolitic metal–organic frameworks: revealing auxeticity and anomalous elasticity. *Dalt. Trans.* **45**, 4154–4161 (2016).
110. J. Tan, B. Civalleri, A. Erba, E. Albanese, Quantum mechanical predictions to elucidate the anisotropic elastic properties of zeolitic imidazolate frameworks: ZIF-4 vs. ZIF-zni. *CrystEngComm*. **17**, 375–382 (2015).
111. M. Kosa, J. Tan, C. A. Merrill, M. Krack, A. K. Cheetham, Probing the Mechanical Properties of Hybrid Inorganic – Organic Frameworks: A Computational and Experimental Study. *ChemPhysChem*. **11**, 2332–2336 (2010).
112. J. C. Tan *et al.*, Exceptionally low shear modulus in a prototypical imidazole-based metal-organic framework. *Phys. Rev. Lett.* **108**, 095502 (2012).
113. J. Tan, T. D. Bennett, A. K. Cheetham, Chemical structure, network topology, and porosity effects on the mechanical properties of Zeolitic Imidazolate Frameworks. *Proc. Natl. Acad. Sci. U. S. A.* **107**, 9938–9943 (2010).
114. J. C. Tan, A. K. Cheetham, Mechanical properties of hybrid inorganic–organic framework materials: establishing fundamental structure–property relationships. *Chem. Soc. Rev.* **40**, 1059 (2011).
115. Z. Zeng, J. C. Tan, AFM Nanoindentation to Quantify Mechanical Properties of Nano- and Micron-Sized Crystals of a Metal-Organic Framework Material. *ACS Appl. Mater. Interfaces*. **9**, 39839–39854 (2017).

116. E. C. Spencer, R. J. Angel, N. L. Ross, B. E. Hanson, J. A. K. Howard, Pressure-Induced Cooperative Bond Rearrangement in a Zinc Imidazolate Framework : A High-Pressure Single-Crystal X-Ray Diffraction Study. *J. Am. Chem. Soc.* **131**, 4022–4026 (2009).
117. O. Karagiaridi *et al.*, Opening ZIF-8: A catalytically active zeolitic imidazolate framework of sodalite topology with unsubstituted linkers. *J. Am. Chem. Soc.* **134**, 18790–18796 (2012).
118. A. Arora, D. B. Marshall, B. R. Lawn, M. V. Swain, Indentation deformation/fracture of normal and anomalous glasses. *J. Non. Cryst. Solids*. **31**, 415–428 (1979).
119. T. Rouxel, Driving force for indentation cracking in glass: composition, pressure and temperature dependence. *Philos. Trans. R. Soc. A Math. Phys. Eng. Sci.* **373**, 20140140 (2015).
120. P. Sellappan *et al.*, Composition dependence of indentation deformation and indentation cracking in glass. *Acta Mater.* **61**, 5949–5965 (2013).
121. B. R. Whittle, R. J. Hand, Morphology of Vickers Indent Flaws in Soda-Lime-Silica Glass. *J. Am. Ceram. Soc.* **84**, 2361–2365 (2004).
122. J. Guin, T. Rouxel, J. Sanglebœuf, I. Melscooet, J. Lucas, Hardness, Toughness, and Scratchability of Germanium–Selenium Chalcogenide Glasses. *J. Am. Ceram. Soc.* **85**, 1545–1552 (2002).
123. D. B. Miracle, A structural model for metallic glasses. *Nat. Mater.* **3**, 697–702 (2004).
124. M. M. Trexler, N. N. Thadhani, Mechanical properties of bulk metallic glasses. *Prog. Mater. Sci.* **55**, 759–839 (2010).
125. M. B. Østergaard *et al.*, Revisiting the Dependence of Poisson ' s Ratio on Oxide Glasses. *Materials (Basel).* **12**, 2439 (2019).
126. G. N. Greaves, A. L. Greer, R. S. Lakes, T. Rouxel, Poisson's ratio and modern materials. *Nat. Mater.* **10**, 823–837 (2011).
127. A. H. Windle, in *Encyclopedia of Materials: Science and Technology*, K. H. J. Buschow et al., Eds. (Pergamon, Second., 2001), pp. 3551–3552.
128. A. Flores, F. Ania, F. J. Baltá-Calleja, From the glassy state to ordered polymer structures: A microhardness study. *Polymer (Guildf).* **50**, 729–746 (2009).
129. P. E. Mazeran, M. Beyaoui, M. Bigerelle, M. Guigon, Determination of mechanical properties by nanoindentation in the case of viscous materials. *Int. J. Mater. Res.* **103**, 715–722 (2012).
130. M. Rodríguez, J. M. Molina-Aldareguía, C. González, J. Llorca, Determination of the mechanical properties of amorphous materials through instrumented nanoindentation. *Acta Mater.* **60**, 3953–3964 (2012).
131. D. C. Clupper, L. L. Hench, Crystallization kinetics of tape cast bioactive glass 45S5. *J. Non. Cryst. Solids*. **318**, 43–48 (2003).
132. Q. Zheng, Y. Z. Yue, J. C. Mauro, Density of topological constraints as a metric for predicting glass hardness. *Appl. Phys. Lett.* **111**, 011907 (2017).

133. T. Rouxel, Elastic properties of glasses: a multiscale approach. *Comptes Rendus - Mécanique*. **334**, 743–753 (2006).
134. L. Wondraczek *et al.*, Towards Ultrastrong Glasses. *Adv. Mater.* **23**, 4578–4586 (2011).
135. K. W. Park, J. il Jang, M. Wakeda, Y. Shibutani, J. C. Lee, Atomic packing density and its influence on the properties of Cu-Zr amorphous alloys. *Scr. Mater.* **57**, 805–808 (2007).
136. Y. Q. Cheng, E. Ma, Atomic-level structure and structure-property relationship in metallic glasses. *Prog. Mater. Sci.* **56**, 379–473 (2011).
137. K. G. Aakermann *et al.*, Indentation deformation mechanism of isostatically compressed mixed alkali aluminosilicate glasses. *J. Non. Cryst. Solids*. **426**, 175–183 (2015).
138. T. M. Gross, M. Tomozawa, Fictive temperature-independent density and minimum indentation size effect in calcium aluminosilicate glass. *J. Appl. Phys.* **104**, 063529 (2008).
139. M. M. Smedskjaer, Indentation size effect and the plastic compressibility of glass. *Appl. Phys. Lett.* **104**, 24–27 (2014).
140. Y. M. Lu *et al.*, Shear-banding Induced Indentation Size Effect in Metallic Glasses. *Sci. Rep.* **6**, 28523 (2016).
141. S. Nachum, A. L. Greer, Indentation size effect in metallic glasses: Mean pressure at the initiation of plastic flow. *J. Alloys Compd.* **615**, S98–S101 (2015).
142. C.-S. Han, S. Nikolov, Indentation size effects in polymers and related rotation. *J. Mater. Res.* **22**, 1662–1672 (2007).
143. G. Z. Voyiadjis, L. Malekmotiei, A. Samadi-Dooki, Indentation size effect in amorphous polymers based on shear transformation mediated plasticity. *Polymer (Guildf).* **137**, 72–81 (2018).
144. H. Li, R. C. Bradt, The microhardness indentation load/size effect in rutile and cassiterite single crystals. *J. Mater. Sci.* **28**, 917–926 (1993).
145. T. Kavetskyy, J. Borcc, K. Sangwal, V. Tsmots, Indentation size effect and Vickers microhardness measurement of metal-modified arsenic chalcogenide glasses. *J. Optoelectron. Adv. Mater.* **12**, 2082–2091 (2010).
146. E. O. Bernhardt, On Microhardness of Solids at the Limit of Kick's Similarity Law. *Z. Met.* **33**, 135 (1941).
147. I. Manika, J. Maniks, Size effects in micro- and nanoscale indentation. *Acta Mater.* **54**, 2049–2056 (2006).
148. S. Yoshida *et al.*, Evaluation of Sinking-In and Cracking Behavior of Soda-Lime Glass under Varying Angle of Trigonal Pyramid Indenter. *Front. Mater.* **3**, 54 (2016).
149. S. Yoshida *et al.*, Direct observation of indentation deformation and cracking of silicate glasses. *J. Mater. Res.* **30**, 2291–2299 (2015).
150. S. Yoshida, Indentation deformation and cracking in oxide glass – toward understanding of crack nucleation. *J. Non-Crystalline Solids X*. **1**, 100009 (2019).

151. F. M. Ernsberger, Mechanical properties of glass. *J. Non. Cryst. Solids*. **25**, 293–321 (1977).
152. R. Chakraborty, A. Dey, A. K. Mukhopadhyay, Loading Rate Effect on Nanohardness of Soda-Lime-Silica. *Metall. Mater. Trans. A*. **41**, 1301–1312 (2010).
153. J. T. Hagan, Shear deformation under pyramidal indentations in soda-lime glass. *J. Mater. Sci.* **15**, 1417–1424 (1980).
154. K. W. Peter, Densification and Flow Phenomena of Glass in indentation experiments. *J. Non. Cryst. Solids*. **5**, 103–115 (1970).
155. T. M. Gross, J. Wu, D. E. Baker, J. J. Price, R. Yongsunthon, Crack-resistant glass with high shear band density. *J. Non. Cryst. Solids*. **494**, 13–20 (2018).
156. A. L. Greer, Y. Q. Cheng, E. Ma, Shear bands in metallic glasses. *Mater. Sci. Eng. R Reports*. **74**, 71–132 (2013).
157. Struers, Hardness Testing (2019), (available at https://www.struers.com/en/Knowledge/Hardness-testing#hardness-testing-how-to, accessed: 11.11.2019).

LIST OF PUBLICATIONS

PUBLICATIONS IN PEER REVIEWED JOURNALS

1) Zhou C., **Stepniewska M.,** Sørensen J. M., Scarpa L., Magnacca G., Boffa V., Bennett T. D., Yue Y. Z., Polymorph formation for a zeolitic imidazolate framework composition - $Zn(Im)_2$. *Microporous and Mesoporous Materials*, 265, 57-62 (2018).
2) Zhou C., **Stepniewska M.,** Longley L., Ashling C. W., Chater P. A., Keen D. A., Bennett T. D., Yue Y. Z., Thermodynamic Features and Enthalpy Relaxation in a Metal-Organic Framework Glass. *Physical Chemistry Chemical Physics*, 20, 18291-18296 (2018).
3) Januchta K., **Stepniewska M.,** Jensen L. R., Zhang Y., Somers M. A. J., Bauchy M., Yue Y. Z., Smedskjaer M. M., Breaking the Limit of Micro-Ductility in Oxide Glasses, *Advanced Science*, 6, 9, 1901281 (2019).
4) **Stepniewska M.,** Yang Y. J., Zhou C., Yue Y. Z., Mauro J. C., Determining the Phase Diagram, Structure and Properties of the Mixed Metallic ZIF-62 System via Experiments and Modelling, (Submitted).
5) **Stepniewska M.,** Østergaard M. B., Zhou C., Yue Y. Z., Towards Large-Sized Bulk ZIF-62 Glasses via Optimizing the Melting Conditions, *Journal of the Non-Crystalline Solids* (In Press).
6) **Stepniewska M.,** Januchta K., Zhou C., Qiao A., Smedskjær M. M., Yue Y. Z., Anomalous Cracking in a Metal-Organic Framework Glass, (Submitted).
7) Sørensen S. S., Østergaard M. B., **Stepniewska M.,** Johra H., Yue Y. Z., Smedskjær M. M., Metal-Organic Framework Glasses possess Higher Thermal Conductivity than their Crystalline Counterparts, (Under Review).

ORAL AND POSTER PRESENTASTIONS AT CONFERENCES

1) **Stepniewska M.,** Zhou C., Yue Y. Z., Mechanical Properties of Melt-Quenched MOF Glasses and Their Relation to Microstructure –Will the Neutron Scattering be the Key Tool? **Poster:** Materials for Energy Applications through Neutron and X-Ray Eyes workshop, Chalmers University of Technology, Goteborg, Sweden (2017).
2) **Stepniewska M.,** Zhou C., Yue Y. Z., Fracture and Deformation Behavior of Melt-Quenched ZIF Glasses. **Oral:** 7th International Workshop on Flow and Fracture of Advanced Glasses, Aalborg, Denmark (2017)
3) **Stepniewska M.,** Zhou C., Yue Y. Z., Synthesis and Glass Forming Ability of Several Dual-Metallic Zeolitic Imidazolate Frameworks. **Poster**: 2nd European Conference on Metal Organic Frameworks and Porous Polymers (2nd EuroMOF), Delft, Netherlands (2017)
4) **Stepniewska M.,** Østergaard M. B., Zhou C., Yue Y. Z., Producing bulk ZIF-62 glasses by optimizing melting process. **Poster** (2nd award for best poster presentation): 15th International Conference on Physics of Non-Crystalline Solids & 14th European Society of Glass Conference, Saint Malo, France (2018).
5) **Stepniewska M.,** Zhou C., Qiao A., Yue Y. Z., Glass formation and mechanical properties of melt-quenched glasses of mixed metal node Zn/Co ZIF-62. **Oral**: 15th International Conference on Physics of Non-Crystalline Solids & 14th European Society of Glass Conference, Saint Malo, France (2018).
6) **Stepniewska M.,** Januchta K., Zhou C., Winther G., Smedskjær M. M., Yue Y. Z., Indentation of a Melt-Quenched Zeolitic Imidazolate Framework Glass. **Oral**: ICG Annual Meeting 2018, 59th Meeting on the Glass and Photonic Materials & 14th Symposium of the Glass Industry Conference of Japan, Yokohama, Japan (2018).
7) **Stepniewska M.,** Januchta K., Zhou C., Qiao A., Winther G., Smedskjær M. M., Yue Y. Z., Mechanical Response of Melt-Quenched Zeolitic Imidazolate Framework Glass to Sharp Contact Loading. **Oral:** 25th International Congress on Glass, Boston, USA (2019).
8) **Stepniewska M.,** Qiao A., Østergaard M. B., Zhou C., Calves L., Zhang X. H., Yue Y. Z., An Approach towards High Quality Bulk Zeolitic Imidazolate Framework Glasses. **Poster:** 25th International Congress on Glass, Boston, USA (2019).

PAPER I

Determining the phase diagram, structure and properties of the mixed metallic ZIF-62 system via experiments and modeling

Malwina Stepniewska[1,‡], Yongjian Yang[2,‡], Chao Zhou[1], Yuanzheng Yue[1,], John C. Mauro[2,*]*

[1]Department of Chemistry and Bioscience, Aalborg University, DK-9220 Aalborg, Denmark

[2]Department of Materials Science and Engineering, The Pennsylvania State University, University Park, Pennsylvania 16802, United States

Corresponding Authors

* yy@bio.aau.dk (Yuanzheng Yue) and jcm426@psu.edu (John C. Mauro)

ABSTRACT. A series of bimetallic zeolitic imidazolate framework (ZIF-62 series) with Co and Zn atoms were synthesized using a solvothermal procedure. We discovered a Co-ZIF-62 crystal with unique long-range order compared to the standard crystal structure. The phase diagram of the bimetallic ZIF-62 system was established with respect to the melting point (T_m). T_m is lowest (i.e., eutectic point) when the molar ratio of [Co]/([Co]+[Zn]) is in the range of 0.1-0.2. To account for the structural mismatch effect on T_m, a model summing contributions from different structural units in the material is proposed, demonstrating good agreement with experiment. Density functional theory calculations and molecular dynamics simulations show that when Zn is partially substituted by Co, both unit cell volume and internal energy decrease with Co content, consistent with current experimental results and the reported data. We demonstrate that optimal properties such as the minimum T_m of ZIF-62 can be achieved by tuning both the organic ligands and also the metallic nodes.

TOC GRAPHICS

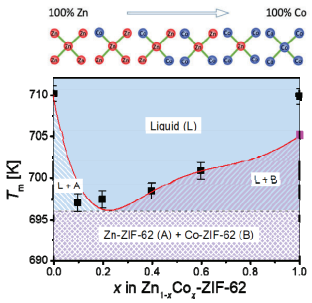

KEYWORDS: Zeolitic Imidazole Frameworks; Mixed Metallic Nodes; Phase Diagram; Density Functional Theory; Molecular Dynamics

Zeolitic Imidazole Frameworks (ZIFs), which consist of metallic nodes interconnected by organic ligands, have received considerable attention[1–4] due to their vast range of potential

applications, including catalysis,[2,5] gas storage,[6,7] gas separation[2,3,7] and chemical sensing.[2,8] Introduction of second metallic nodes/organic linkers to ZIFs has been used to fine tune their properties.[9–15] Such approach has mainly focused on ZIF-8 (a framework built of zinc ions linked by 2-methylimidazole, mIm) and ZIF-67 (the cobalt counterpart of ZIF-8). By adjusting the metal sources during synthesis, intermediate structures with various ratios of metallic nodes can be synthesized, for which interesting features have been observed. For example, an increase in CO_2 and H_2 uptake has been achieved in Zn/Co bimetallic $Zn_xCo_{1-x}(mIm)_2$ compared to Zn-ZIFs.[13,16,17] Such an approach can also lead to improved size control and tailoring of the physicochemical properties.[12,15] Bimetallic ZIFs have been demonstrated to be effective precursors in nanoporous carbon synthesis.[14] Very recently, Zn/Co bimetallic ZIF-62 was found to exhibit super-broadband mid-infrared (Mid-IR) luminescence,[18] which may be used to find new photonic applications of bulk MOF glasses, such as Mid-IR lasers. The first microporous cobalt ZIF-62 glass was obtained by Frentzel-Beyme et al., having the potential to be applied in gas separation, energy storage and catalysis.[19] However, difficulties in obtaining stable ZIFs with a single-phase bimetallic structure have been encountered, as one-pot synthesis regularly leads to production of multiple phases.[15,20] According to recent studies,[21] the mixed-ligand ZIF-62 system ($Zn(Im)_{1.75}(bIm)_{0.25}$, Im: imidazolate; bIm: benzimidazolate) exhibits ultrahigh glass forming ability (T_g/T_m) and intriguing properties such as high viscosity (about 10^5 Pa s) at its liquidus temperature and high resistance to crystallization. Its glassy state shows high light transmittance (90%) in visible range,[22] luminescence and anomalous fracture behavior.[23] To understand the chemical origin of these properties of the ZIF materials, we investigate the structure and properties of ZIF-62 by altering the ratios between zinc and cobalt from both experiments and theoretical calculations. To do so, we apply techniques including powder X-ray diffraction (P-XRD), X-ray photoelectron spectroscopy (XPS), infrared spectroscopy (FT-IR), ^1H liquid state nuclear

magnetic resonance (L-NMR), and differential scanning calorimetry (DSC). Recently, computational modeling of ZIFs (and MOFs)[24,25] using density functional theory (DFT)[26–29] and molecular dynamics (MD)[29–36] have been used to further the understanding of ZIF structures including the node[3737] and linker effects.[38] To obtain the theoretical trend of the properties, we also conduct DFT and classical MD calculations on the crystalline phase of the bimetallic ZIF-62 systems. The experimental data and modeling results are combined to shed light on the structural features and tailorable properties of bimetallic ZIFs.

Macroscopic observations of six obtained ZIF-62 samples with two metallic nodes ($Zn_{1-x}Co_x$) show a clear relationship between the sample color and the amount of cobalt added during synthesis (Figure S1). The color changes from white (Zn-ZIF-62) to deep purple (Co-ZIF-62). The structures of the ZIF-62 samples were first characterized by P-XRD and L-NMR. P-XRD patterns (Figure 1a) show new peaks appearing for samples with mixed metallic nodes compared with that of Zn-ZIF-62. Moreover, the relative intensity of the strongest new peak ($2\theta = 11.2°$) increases with increasing the amount of Co in the framework, whereas the peak positions for ZIF-62 phase of mixed Zn/Co node samples remain unchanged. The XRD pattern of Co-ZIF-62 shows significantly different peak positions and intensities compared to Zn-ZIF-62, indicating that the long-range structures are different between them. The XRD pattern of the Co-ZIF-62 crystals that we obtained has not been seen in literature to our best knowledge.

The Pawley refinement performed via Topas3 software (Figure S3) also indicates that the structure of Co-ZIF-62 obtained in this work differs greatly from that of Co-ZIF-62 phase reported in a recent study by Henke group.[19] The Co-ZIF-62 phase obtained by this group is nearly the same as that of Zn-ZIF-62 regarding the XRD pattern. By comparing the synthesis procedures used in both our work and theirs[19], we can see some differences (e.g., in synthesis time or reaction container volume), which might affect the obtained structures. The Henke

group synthesized the samples for longer time and smaller reaction container than we did. Thus, the crystal that we synthesized is not the standard Co-ZIF-62 crystal. Rather, it is a unique new form of Co-ZIF-62 having a structure with a different long-range order. To be more explicit, the difference in XRD patterns of Henke group and the present authors implies that there are likely polymorphic transitions in Co-ZIF-62, i.e., transitions from one type of crystal to another, depending on the synthesis conditions. The effect of the synthesis time on the structures of other ZIF crystals, e.g., ZIF-4 and ZIF-8 has been studied by solution mixing method[39] and mechanochemical reaction[40], respectively. These studies showed the extension of synthesis time led to a denser crystal phase as the final product, according to the Oswald rule. We can therefore infer that our Co-ZIF-62 sample is a less dense phase of the Co-ZIF-62. A recent study[41] also shows that a sufficient extension of reaction time for ZIF-4 crystal synthesis can cause formation of ZIF-zni, instead of ZIF-4, suggesting that optimization of the synthesis condition plays a crucial role in getting the targeted crystal phase. Thus, we discovered a new form of Co-ZIF-62 crystal.

As an initial attempt to characterize the structure of the new type of Co-ZIF-62, we performed FT-IR measurements as shown in Figure S2b. The results show similar peak positions for all samples with any Co content. ^{1}H NMR spectra exhibit two peaks between 5.7 and 6.8 ppm in the Co-containing samples, the intensities of which increase with increasing the cobalt content. These peaks cannot be assigned to the local structure of either imidazole or benzimidazole. Based on the ^{1}H L-NMR data (Figure 1b and Figure S2a), the ligand ratio between Im and bIm remains nearly constant with increasing the cobalt content, up to the highest cobalt content sample: $Zn_{0.4}Co_{0.6}$-ZIF-62 (based on the peak characteristics for Im and bIm compound designated as peaks 1 and 3 in Figure 1b). For comparison, three additional kinds of the cobalt-containing ZIFs (i.e., Co-ZIF-4, ZIF-9 and ZIF-12) were synthesized (see Supporting Information (SI)). No strong correlations in peak positions of the

XRD, NMR or FT-IR spectra between the three new samples and the Co-ZIF-62 sample were observed, indicating that the Co-ZIF-62 obtained in this work is not the same crystal as one of the above-mentioned ZIFs. However, the detailed structure of Co-ZIF-62 still needs to be clarified.

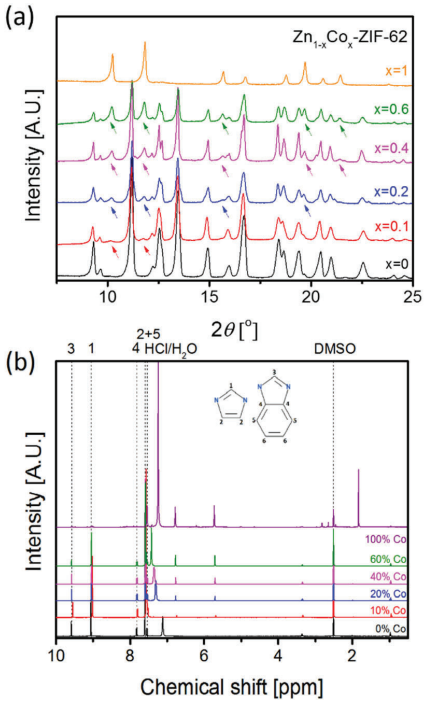

Figure 1. Structural data obtained for synthesized samples of $Zn_{1-x}Co_x$-ZIF-62 with changing chemical composition: (a) PXRD pattern (arrows pointing to the new peaks appearing with addition of Co during the synthesis); (b) ^{1}H-LNMR spectra (dashed lines showing the location of typical peaks from imidazole and benzimidazole structures, with numbers referring to specific to specific H atoms in the structure)

Dried samples were subjected to two DSC upscans. The first upscan was used for solvent dissolution (Figure S5a), and the second one was used for assessing the thermodynamic

values for melting, such as melting point (T_m) (i.e., the liquidus temperature) and melting enthalpy. Figure 2a shows the binary phase diagram for a node-mixed ZIF system concerning T_m, which was determined via DSC, viz., the T_m trend of with the [Co]/[Co+Zn] ratio, for $Zn_{1-x}Co_x$-ZIF-62 systems. T_m is here defined as the offset temperature of the melting peak. Here it should be mentioned that the T_m defined here was not determined under equilibrium conditions, but instead during a DSC upscan at 10 K/min. This means that a kinetic effect was involved in T_m determination, and thus, the T_m values are slightly overestimated.[42] However, the trend of the change of T_m with the [Co]/[Co+Zn] ratio was not influenced. Moreover, the T_m of the standard Co-ZIF-62 is also shown in Figure 2a for comparison. It is seen in Figure 2a that T_m drastically decreases from 711 K to the lowest value, i.e., the eutectic point (about 696-698 K) when substituting 10~20% cobalt for zinc, and then increases with a further increase of the cobalt content. Note that the accurate T_m value cannot be definitively given in this work since the error range and the limited dataset. In other words, Figure 2a suggests only approximate locations of both the liquidus line and the eutectic point. As shown by the solid curve in Figure 2a, the measured T_m trend is in a good agreement with that described by a proposed model which sums contributions from different structural units in the material. The rationale for the model is provided in the following paragraphs. In Figure 2a, four phase domains are marked, which are the solid mixture of Zn-ZIF-62 (A) and Co-ZIF-62 (B), liquid (L), the mixture of L and phase A and the mixture of L and phase B. These domains are distinguished using the solidus line (dashed line extrapolated from the eutectic point) and the liquidus line (solid line).

The existence of the eutectic point indicates that the least thermal energy is needed for melting the ZIF with the ratio of x=0.1~0.2, and this is a typical feature of a binary eutectic phase diagram. This means that all three of the phases present on the investigated phase diagram (liquid, Zn-ZIF-62 and Co-ZIF-62) are in equilibrium at T_m for this particular phase

composition. When cobalt partially substitutes zinc or vice versa, the structural instability of two-phased material due to the structural mismatch effect will increase, and consequently the atomic vibration becomes enhanced and thus more easily reaches Lindemann's melting criterion.[43] The observation of the eutectic point also implies that the Zn-ZIF-62 and Co-ZIF-62 most effectively interact with each other, leading to a decrease of T_m, as compared to pure Zn-ZIF-62 and Co-ZIF-62 phase. At the eutectic point, the atoms on the surface of the particles of either phases weaken the chemical bonds of the two phases in the most efficient way (compared with other phase compositions), i.e., the thermodynamic driving force is the largest for both melting and solidification at the eutectic point. The T_m values of Zn-ZIF-62 and Co-ZIF-62 samples are nearly the same (about 710 K), indicating similar structural stability of with a single type of metallic node. Here it should be mentioned that T_m of the standard Co-ZIF-62 crystal obtained by Henke group[19] is slightly lower (705 K) than that of our sample (710 K), confirming that they have different long-range order structure (see XRD patterns in Fig. 1a). The T_m of the standard Co-ZIF-62 crystal is included in Fig. 2a to illustrate its difference to that of the Co-ZIF-62 derived in this work.

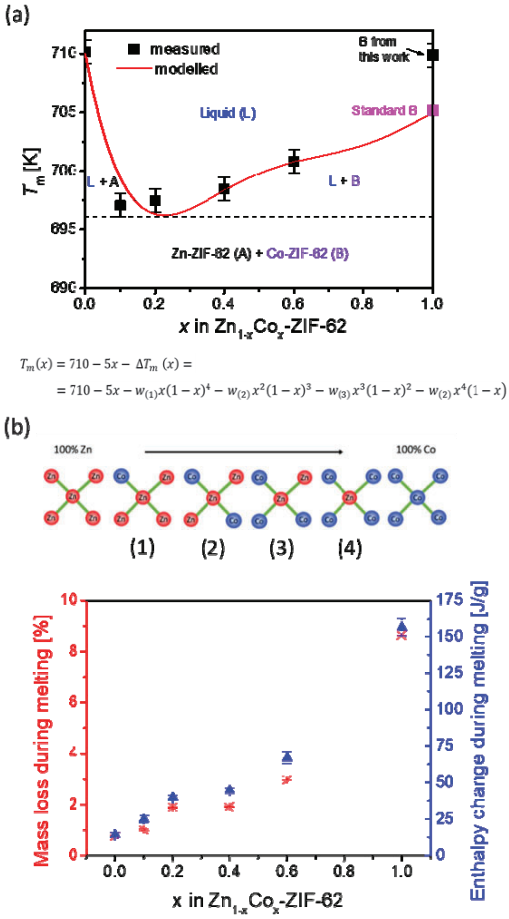

Figure 2. $Zn_{1-x}Co_x$-ZIF-62 samples: (a) The phase diagram of the bimetallic ZIF-62 frameworks, i.e., $Zn_{1-x}Co_x$-ZIF-62 regarding the melting point (T_m), obtained by experiments (black points) and modeling (red curve). Dashed line: the extrapolated line from the eutectic point. The model for T_m is presented by the equation below Figure 2a, where 710 K is the T_m for both Zn-ZIF-62 and Co-ZIF-62, w(i) is a weighting factor accounting for the disorder/instability effect of each type of Zn structural unit, and the term after each w(i) stands for the probability of i^{th} Zn structural unit as shown in Figure 2b. (b) Zn structural units that may appear in $Zn_{1-x}Co_x$-ZIF-62. In random mixing, Zn atoms with higher Co coordination increases with x. The green bar between the cation atoms stand for the organic

ligand; (c) mass loss during first upscan (red data points) and enthalpy change during melting (blue data points). Note the small values of the error bars shown on the graph.

Because it is challenging to measure the compositions of the liquid phase and solid phase in equilibrium with each other at every x, a phenomenological model for the composition dependence of the melting point ($\Delta T_m(x)$) is constructed by considering a random mixture of different Zn-Co coordination environments, as shown in Figure 2b. The model relies on two assumptions: (1) both Zn and Co are 4-fold coordinated according to the chemical stoichiometry; (2) ΔT_m is controlled by the structural disorder/instability of each type of Zn-Co configuration (a linear dependence is assumed). The model for T_m is presented in form of an equation (shown below Figure 2a). The formula contains a linear term, 710-5x, so that it passes through the melting temperatures of pure Zn (710 K) and pure Co phases (705 K). Quadratic interpolations have been carried out to generate more data points between the six experimental data and improve the fitting. Note that, we use the T_m value of the standard Co-ZIF-62 sample for fitting, since that of the standard Zn-ZIF-62 crystal is also used, which is synthesized in this work. The fitting curve plotted in Figure 2a shows a eutectic point around x = 0.2 and has a root-mean-square error of 2.6 K in good agreement with the experiments. The obtained $w_{(i)}$ values are $w_{(1)}$=155.9 K, $w_{(2)}$=-28.5 K, $w_{(3)}$=98.6 K and $w_{(4)}$=20.9, suggesting that type (1) and (3) configurations are less stable than type (2) and (4). We note here that one can improve the model by considering the configurational entropy change at different x, however, because the eutectic point is strongly biased toward small x values, its effect seems less important than the structural instability due to different Zn-Co coordination environments.

The enthalpy change (Figure 2c) during melting integrated from the melting peak area of the DSC scans shows an increase of values with increasing cobalt content. The increase of mass loss with Co content during melting indicates that part of the sample has decomposed during the melting process (Fig. 2c), leading to the increase of energy needed for melting to

occur. This is also reflected in the change of (high asymmetry and much higher peak) the shape of the endothermic peak obtained during second upscan for Co-ZIF-62 sample (Figure S5b). Compared to the Zn-ZIF-62 and Zn/Co samples, a sharp decline in the DSC curve for Co-ZIF-62 can be noticed right after the melting peak. A similar feature has been observed for the ZIF-4 phase,[44] right before foaming caused by the decomposition. This implies a much lower thermal stability of cobalt ZIF structures at higher temperature compared to the zinc samples. However, it is worth noting that even for the Co-ZIF-62 sample, mass decrease during second upscan does not exceed 10% (Figure S5c).

XPS spectra of the samples are shown on Figure S6a. For cobalt 2p, the main peaks at binding energies around 781 eV for $2p_{3/2}$ and 797 eV for $2p_{1/2}$ are assigned in all samples to cobalt.[45] Two satellite shake-ups (denoted on Figure S6b as sat.) are also observed. Peak position differs slightly among samples. However, in case of Zn2p peaks, there is a small difference in peak position between the Zn-ZIF-62 sample and the cobalt-containing samples (Figure S6c). Specifically, the $Zn2p_{3/2}$ peak shifts from 1022 eV for the zinc-containing sample to around 1021.5 eV for the cobalt-containing samples. The 0.5 eV shift is also observed for $Zn2p_{1/2}$ (from around 1045 to 1044.5 eV). A similar shift is also observed for N1s binding energy (Figure S6d), i.e., the peak position shifts from around 399 eV for pure zinc nodes to 398.6 eV for pure cobalt nodes. The same Co2p peak position for the cobalt-containing samples implies that adding the second metallic node (i.e., Co) has a larger impact on electronic structure of zinc and nitrogen than on electronic structure of cobalt.

As mentioned above, addition of the second metallic node (Co) to Zn-ZIF-62 induced formation of a second phase, which is challenging for molecular simulations without knowledge of the exact atomic configurations. Therefore, DFT and MD calculations are only attempted using the Zn-ZIF-62 structure as a starting point. Figure 3a shows the simulation

results for Zn-ZIF-62 concerning the unit cell volume, the internal energy, the bulk modulus and Young's modulus. Densities of crystalline Zn-ZIF-62 phase determined from DFT and MD methods are close to the published density data[46] and the values obtained from the present experiment (Table S2). As shown in Figure 3b, the unit cell volumes from both DFT and MD calculations differ by ~0.5%, and the volume of the Co-substituted sample decreases up to 1% with the substitution of Co for Zn atoms up to 62.5%. This can be partially attributed to the shorter Co-N bond compared to Zn-N bond according to the DFT calculation by Krokidas et al.[17,47] The differences in the above-mentioned values among the cobalt-containing samples can also be observed between Zn-ZIF-4 and Co-ZIF-4,[48] although the differences are much larger for ZIF-62 samples (see Table S1) due to their different phases.

Figure 3c shows that internal energy obtained from DFT calculations decreases with increasing cobalt content. This is expected because the Co-N bond is stronger than the Zn-N bond.[49] This is also consistent with the increasing enthalpy in the melting process in Figure 2c. For the powder samples (see Figure S1), it is a challenge to measure the mechanical properties experimentally, and thus, only theoretical determination of bulk modulus and Young's modulus are reported here to show the effect of cobalt on the Zn-ZIF-4 configuration. The bulk and elastic moduli of the crystalline ZIF-62 are shown in Figure 3d. DFT and MD calculations yield an average bulk modulus of 3.8 ± 0.2 GPa and 4.7 ± 0.2 GPa for all samples. With increasing cobalt content, there is a moderate increase in the bulk modulus. Young's modulus has a different trend with increasing cobalt content, depending on the crystal orientation, i.e., it increases in the [100] direction, decreases in the [001] direction, and remains roughly the same in the [010] direction.

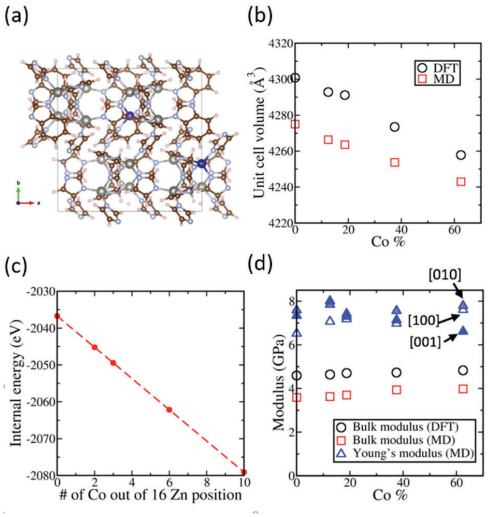

Figure 3. (a) Crystal structure of $Zn_{1-x}Co_x$-ZIF-62 with x = 0.125. The blue atoms are Co, and the large grey atoms are Zn. (b) Unit cell volume of crystalline ZIF-62 versus Co concentration (c) Internal energy calculated by DFT for increasing Co content (d) Moduli of crystalline ZIF-62 as a function of Co concentration. The three orientations are marked for Young's modulus.

In this work, we synthesized bimetallic zinc-cobalt ZIFs with the same organic ligand as ZIF-62 ($M(Im)_{1.75}(bIm)_{0.25}$) using the solvothermal method. We obtained a unique Co-ZIF-62 crystal having a long-range order different from that of the standard crystal. This new crystal has a similar T_m value as Zn-ZIF-62, yet greater mass loss and a visible endothermic signal right after melting due to partial sample decomposition. An initial phase diagram of the bimetallic ZIF-62 system was established with respect to the melting point (T_m) via both DSC measurements and modeling. Thermal stability decreases in the bimetallic frameworks compared to that of the Zn-ZIF-62 and Co-ZIF-62, as evidenced by the minimum in T_m. A model considering all types of configurations in the bimetallic ZIFs was built to account for

the effects of structural mismatch on T_m. DFT and MD calculations show that, with increasing cobalt content, both the unit cell volume and internal energy tend to decrease, consistent with results from both the current experiments and literature. From both experiments and modeling, we demonstrate that the properties of ZIF systems can be tailored via substitution of the metallic node in combination with the use of different organic ligands.

EXPERIMENTAL METHODS AND COMPUTATIONAL METHODS

Preparation of Zn/Co-ZIF-62 and other Co-ZIFs. Solvothermal synthesis was used to obtain crystalline products characterized in this work. 0.6 M zinc nitrate hexahydrate ($Zn(NO_3)_2 \cdot 6H_2O$) and cobalt nitrate hexahydrate ($Co(NO_3)_2 \cdot 6H_2O$), 0.5 M benzimidazole ($C_7H_6N_2$) and 4 M imidazole ($C_3H_4N_2$) solutions in N,N-dimethylformamide (DMF) were used for synthesis. By altering the amount of added metal sources, six Zn_{1-x}/Co_x-ZIF-62 samples were obtained, with x = 0, 0.1, 0.2, 0.4, 0.6 and 1 by volume of cobalt nitrate added as metal salt. Precalculated volumes of each of the solutions (as stated in Table 1) were stirred for 30 minutes using a magnetic stirrer, and then placed in a furnace at 120 °C for 48 hours. Obtained crystals were then washed three times with DMF and once with dichloromethane and dried in the fume hood at room temperature overnight.

Table 1. Volumes of solutions used during synthesis of samples.*

	$Zn(NO_3)_2 \cdot 6H_2O$ 0.6M [ml]	$Co(NO_3)_2 \cdot 6H_2O$ 0.6M [ml]	$C_3H_4N_2$ (Im) 4M [ml]	$C_7H_6N_2$ (bIm) 0.5M [ml]	C_3H_7NO (DMF) [ml]
Zn-ZIF-62	17.45	-	33.82	21.82	1.91
$Zn_{0.9}Co_{0.1}$-ZIF-62	15.71	1.75	33.82	21.82	1.91
$Zn_{0.8}Co_{0.2}$-ZIF-62	13.96	3.49	33.82	21.82	1.91
$Zn_{0.6}Co_{0.4}$-ZIF-62	10.47	6.98	33.82	21.82	1.91

$Zn_{0.4}Co_{0.6}$-ZIF-62	6.98	10.47	33.82	21.82	1.91
Co-ZIF-62	-	17.45	33.82	21.82	1.91

*Extra DMF was used in order to set a constant volume of solution at 75 ml.

For Co-ZIF-4 synthesis, solvothermal method has also been used. For this process, 291 mg cobalt nitrate hexahydrate ($Co(NO_3)_2 \cdot 6H_2O$) and 136 mg of imidazole ($C_3H_4N_2$) was dissolved in 60 ml of DMF and stirred for 30 minutes using a magnetic stirrer, followed by heating in a furnace at 130 °C for 48 hours. Synthesized crystals were then washed three times with DMF and once with ethanol. After each washing step, samples were centrifuged for 5 minutes to separate crystals from solvents.

ZIF-9 ($Co(bIm)_2$, SOD topology) has been synthesized by dissolving 291 mg cobalt nitrate hexahydrate ($Co(NO_3)_2 \cdot 6H2O$) and 276 mg of benzimidazole ($C_7H_6N_2$) in 60 ml of DMF. Solution was then stirred for 30 minutes using a magnetic stirrer and placed for 48 hours in a furnace heated up to 130 °C. Sample was then washed using a procedure analogous to the one used for Co-ZIF-4, only using methanol instead for ethanol for the last wash.

ZIF-12 ($Co(bIm)_2$, RHO topology) was obtained by dissolving 120 mg of benzimidazole in mixture of 6.06 ml of methanol, 66.67 ml of 35% aqueous NH3 and 5.287 ml toluene, and then addition of 125 mg of cobalt acetate tetrahydrate, according to procedure proposed elsewhere.[50] Then, the mixture was stirred for 3 hours at room temperature. The product was then washed with methanol, using centrifugation for separation of crystals from solvents.

Characterization of Co-ZIF-62 (XRD, DSC, XPS, FT-IR). Liquid NMR measurements were performed, using a Bruker Avance III 500 MHz spectrometer at 298 K. Before the measurements, samples were digested in DCl/D_2O/DMSO-d6 solution

Part of the crystalline samples were dried in 120 °C for 2 hours to remove the solvent from the framework. X-ray diffraction measurements were carried out using PANalytical empyream XRD Cu $K_{\alpha 1}$ radiation (λ = 1.54098 Å). Data were collected with a step size of 0.013° in the range of 5-50°.

Thermal properties were characterized with differential scanning calorimetry (DSC) with parallel thermogravimetry, using Netzsch STA 404C. All measurements were performed in argon at both heating and cooling rate of 10 K/min. Two upscans were performed by heating: (1) up to 330 °C, in order to remove the solvent left in the framework after synthesis and washing processes, and (2) up to 500 °C, in order to assess the melting of crystals.

X-ray photoelectron spectroscopy (XPS) measurements were conducted on ESCALAB 250Xi X-ray photoelectron spectrometer. Spectra were measured in ranges in the energy range of 0-1300 eV. Calibration was done referring to carbon peak at 284.6 eV.

Fourier-transform infrared spectroscopy (FT-IR) measurements were performed on Bruker Tensor II equipped with platinum ATR. Spectra were measured in a wavenumber range 4000-400 cm^{-1} in absorbance mode.

DFT calculation of crystalline Co-ZIF-62. Atomic configuration for crystalline Zn-ZIF-62 was obtained from the Cambridge Structural Database (CSD, CCDC number 671070). The original structure does not contain Co atoms. To create the $Zn_{1-x}Co_x$-ZIF-62, different numbers of Zn atoms were substituted by Co atoms. Because the distance between the nodes (Zn/Co atoms) in ZIF-62 is relatively large (>6 Å) with direct substitution of Zn atoms with Co atoms, interaction between Co sites can be ignored. The crystal Zn-ZIF-62 structure was then relaxed using the projector augmented-wave PAW method as implemented in the Vienna ab initio simulation package (VASP). An energy cutoff of 650 eV was applied for the plane wave basis set. Perdewe-Burkee-Ernzerh (PBE) functional was used to evaluate the

electronic exchange and correlation with a D3 van der Waals correction by Grimme.[51] The Brillouin zone was sampled at the Γ-point which is considered sufficient for the ZIF-62 unit cell dimension of 296 atoms. For the structural relaxation, we set the EDIFF to be 10-3~10-4 eV. The ionic relaxation stops when all forces are converged to less than 0.005 eV Å-1. In order to calculate the bulk modulus, the ZIF-62 structures of different Co concentrations had been relaxed with a series of volume changes from -4 % to 2 %. Birch–Murnaghan equation of state[52] was used to extract the bulk modulus from the energy curve at different volume.

Molecular simulation of crystalline $Zn_{1-x}Co_x$-ZIF-62. In the molecular dynamics simulations, the bimetallic $Zn_{1-x}Co_x$-ZIF-62 structures from the above DFT calculations are first subjected to energy minimization using LAMMPS.[53] The energy tolerance and the force tolerance for the minimization are 4.3×10^{-17} eV and 7×10^{-16} nN, respectively. The conjugate gradient algorithm is used as implemented in LAMMPS. To measure bulk modulus, the ZIF-62 structural is relaxed with a series of volumes changes from -3% to 3% around the equilibrium volume. The bulk modulus is obtained by fitting the equation of state using a Birch-Murnaghan equation.[52] To measure the Young's modulus, the ZIF-62 sample is stretched or compressed in one direction up to ~5% while the external pressure in other two directions are kept around zero. Elastic modulus at 0 K is extracted from the stress-strain curve. For the interaction between atoms, UFF4MOF force field extended for MOFs[54,55] has been used. UFF4MOF is based on the Universal Force Field[56] and contains transition metals including Zn and Co commonly found in ZIFs. It has been shown that UFF4MOF force field can reproduce very accurately the structural characteristics and the bulk modulus for many different type of MOFs that have been well studied in experiments.[31,55,57]

ASSOCIATED CONTENT

Supporting Information.

The following files are available free of charge on the ACS Publications webpage:

- Supporting experimental and modelling results: macroscopic image of $Zn_{1-x}Co_x$-ZIF-62 samples, supporting structural information of $Zn_{1-x}Co_x$-ZIF-62 samples, Topas3 refinement for Co-ZIF-62, supporting structural information for other Co-based ZIFs, further thermal response data for $Zn_{1-x}Co_x$-ZIF-62 samples, XPS spectra obtained for $Zn_{1-x}Co_x$-ZIF-62 samples, experimental and simulated (DFT and MD) densities of Zn-ZIF-62 (PDF).

AUTHOR INFORMATION

Notes

‡These authors contributed equally.

The authors declare no competing financial interests.

ACKNOWLEDGMENT

MS and YZY would like to acknowledge financial support from VILLUM FONDEN through research grant no. 13253. YJY and JCM acknowledge the Institute for CyberScience Advanced CyberInfrastructure (ICS-ACI) at The Pennsylvania State University for providing computing resources. The authors would also like to thank Thomas D. Bennett of University of Cambridge and Ang Qiao and Haizheng Tao of Wuhan University of Technology for helpful discussions

REFERENCES

(1) Park, K. S.; Ni, Z.; Côté, A. P.; Choi, J. Y.; Huang, R.; Uribe-Romo, F. J.; Chae, H. K.; O'Keeffe, M.; Yaghi, O. M. Exceptional Chemical and Thermal Stability of Zeolitic

Imidazolate Frameworks. *Proc. Natl. Acad. Sci. U. S. A.* **2006**, *103*, 10186–10191, DOI: 10.1073/pnas.0602439103.

(2) Chen, B.; Yang, Z.; Zhu, Y.; Xia, Y. Zeolitic Imidazolate Framework Materials: Recent Progress in Synthesis and Applications. *J. Mater. Chem. A* **2014**, *2*, 16811–16831, DOI: 10.1039/C4TA02984D.

(3) Pimentel, B. R.; Parulkar, A.; Zhou, E.; Brunelli, N. A.; Lively, R. P. Zeolitic Imidazolate Frameworks: Next-Generation Materials for Energy-Efficient Gas Separations. *ChemSusChem* **2014**, *7*, 3202–3240, DOI: 10.1002/cssc.201402647.

(4) Bennett, T. D.; Horike, S. Liquid, Glass and Amorphous Solid States of Coordination Polymers and Metal–organic Frameworks. *Nat. Rev. Mater.* **2018**, *3*, 431–440, DOI: 10.1038/s41578-018-0054-3.

(5) Zhu, M.; Srinivas, D.; Bhogeswararao, S.; Ratnasamy, P.; Carreon, M. A. Catalytic Activity of ZIF-8 in the Synthesis of Styrene Carbonate from CO2 and Styrene Oxide. *Catal. Commun.* **2013**, *32*, 36–40, DOI: 10.1016/j.catcom.2012.12.003.

(6) Banerjee, R.; Phan, A.; Wang, B.; Knobler, C.; Furukawa, H.; O'Keeffe, M.; Yaghi, O. M. High-Throughput Synthesis of Zeolitic Imidazolate Frameworks and Application to CO2 Capture. *Science (80-.).* **2008**, *319*, 939–943, DOI: 10.1126/science.1152516.

(7) Ban, Y.; Li, Y.; Peng, Y.; Jin, H.; Jiao, W.; Liu, X.; Yang, W. Metal-Substituted Zeolitic Imidazolate Framework ZIF-108: Gas-Sorption and Membrane-Separation Properties. *Chem. - A Eur. J.* **2014**, *20*, 11402–11409, DOI: 10.1002/chem.201402287.

(8) Lu, G.; Hupp, J. T. Metal - Organic Frameworks as Sensors : A ZIF-8 Based Fabry - Perot Device as a Selective Sensor for Chemical Vapors and Gases. *J. Am. Chem. Soc.* **2010**, *132*, 7832–7833, DOI: 10.1021/ja101415b.

(9) Thompson, J. A.; Blad, C. R.; Brunelli, N. A.; Lydon, M. E.; Lively, R. P.; Jones, C. W.; Nair, S. Hybrid Zeolitic Imidazolate Frameworks: Controlling Framework Porosity and

Functionality by Mixed-Linker Synthesis. *Chem. Mater.* **2012**, *24*, 1930–1936, DOI: 10.1021/cm3006953.

(10) Thompson, J. A.; Vaughn, J. T.; Brunelli, N. A.; Koros, W. J.; Jones, C. W. Mixed-Linker Zeolitic Imidazolate Framework Mixed-Matrix Membranes for Aggressive CO 2 Separation from Natural Gas. *Microporous Mesoporous Mater.* **2014**, *192*, 43–51, DOI: 10.1016/j.micromeso.2013.06.036.

(11) Gustafsson, M.; Zou, X. Crystal Formation and Size Control of Zeolitic Imidazolate Frameworks with Mixed Imidazolate Linkers. *J. Porous Mater.* **2013**, *20*, 55–63, DOI: 10.1007/s10934-012-9574-1.

(12) Zareba, J. K.; Nyk, M.; Samoć, M. Co/ZIF-8 Heterometallic Nanoparticles: Control of Nanocrystal Size and Properties by a Mixed-Metal Approach. *Cryst. Growth Des.* **2016**, *16*, 6419–6425, DOI: 10.1021/acs.cgd.6b01090.

(13) Kaur, G.; Rai, R. K.; Tyagi, D.; Yao, X.; Li, P.-Z.; Yang, X.-C.; Zhao, Y.; Xu, Q.; Singh, S. K. Room-Temperature Synthesis of Bimetallic Co–Zn Based Zeolitic Imidazolate Frameworks in Water for Enhanced CO 2 and H 2 Uptakes. *J. Mater. Chem. A* **2016**, *4*, 14932–14938, DOI: 10.1039/C6TA04342A.

(14) Tang, J.; Salunkhe, R. R.; Zhang, H.; Malgras, V.; Ahamad, T.; Alshehri, S. M.; Kobayashi, N.; Tominaka, S.; Ide, Y.; Kim, J. H.; et al. Bimetallic Metal-Organic Frameworks for Controlled Catalytic Graphitization of Nanoporous Carbons. *Sci. Rep.* **2016**, *6*, 3–4, DOI: 10.1038/srep30295.

(15) Zhou, K.; Mousavi, B.; Luo, Z.; Phatanasri, S.; Chaemchuen, S.; Verpoort, F. Characterization and Properties of Zn/Co Zeolitic Imidazolate Frameworks vs. ZIF-8 and ZIF-67. *J. Mater. Chem. A* **2017**, *5*, 952–957, DOI: 10.1039/C6TA07860E.

(16) Kuruppathparambil, R. R.; Babu, R.; Jeong, H. M.; Hwang, G.-Y.; Jeong, G. S.; Kim, M.-I.; Kim, D.-W.; Park, D.-W. A Solid Solution Zeolitic Imidazolate Framework as a

Room Temperature Efficient Catalyst for the Chemical Fixation of CO_2. *Green Chem.* **2016**, *18*, 6349–6356, DOI: 10.1039/C6GC01614F.

(17) Krokidas, P.; Moncho, S.; Brothers, E. N.; Castier, M.; Economou, I. G. Tailoring the Gas Separation Efficiency of Metal Organic Framework ZIF-8 through Metal Substitution: A Computational Study. *Phys. Chem. Chem. Phys.* **2018**, *20*, 4879–4892, DOI: 10.1039/C7CP08456K.

(18) Ali, M. A.; Ren, J.; Liu, X.; Hua, Y.; Yue, Y.; Jianrong, Q. Discovery of Superbroad Mid-Infrared Luminescent Metal-Organic Framework Glass. *ChemRxiv Prepr.* **2019**, 7635746.v1, DOI: 10.26434/chemrxiv.7635746.v1.

(19) Moldenhauer, H.; Henke, S.; Pallach, R.; Kloß, M.; Debus, J.; Wende, H.; Salamon, S.; Landers, J.; Frentzel-Beyme, L. Porous Purple Glass – a Cobalt Imidazolate Glass with Accessible Porosity from a Meltable Cobalt Imidazolate Framework. *J. Mater. Chem. A* **2018**, *7*, 985–990, DOI: 10.1039/c8ta08016j.

(20) Saliba, D.; Ammar, M.; Rammal, M.; Al-Ghoul, M.; Hmadeh, M. Crystal Growth of ZIF-8, ZIF-67, and Their Mixed-Metal Derivatives. *J. Am. Chem. Soc.* **2018**, *140*, 1812–1823, DOI: 10.1021/jacs.7b11589.

(21) Qiao, A.; Bennett, T. D.; Tao, H.; Krajnc, A.; Mali, G.; Doherty, C. M.; Thornton, A. W.; Mauro, J. C.; Greaves, G. N.; Yue, Y. A Metal-Organic Framework with Ultrahigh Glass-Forming Ability. *Sci. Adv.* **2018**, *4*, eaao6827, DOI: 10.1126/sciadv.aao6827.

(22) Qiao, A.; Tao, H.; Carson, M.; Aldrich, S.; Thirion, L.; Bennett, T.; Mauro, J.; Yue, Y. Optical Properties of a Melt-Quenched Metal-Organic Framework Glass. *Opt. Lett.* **2019**, *44*, 1623–1625, DOI: 10.1364/OL.99.099999.

(23) Stepniewska, M.; Januchta, K.; Zhou, C.; Qiao, A.; Smedskjaer, M. M.; Yue, Y. Anomalous Cracking in a Metal-Organic Framework Glass. *ChemRxiv Prepr.* **2019**, 7844720.v1, DOI: 10.26434/chemrxiv.7844720.v1.

(24) Coudert, F.-X.; Fuchs, A. H. Computational Characterization and Prediction of Metal–organic Framework Properties. *Coord. Chem. Rev.* **2016**, *307*, 211–236, DOI: 10.1016/j.ccr.2015.08.001.

(25) Getman, R. B.; Bae, Y.-S.; Wilmer, C. E.; Snurr, R. Q. Review and Analysis of Molecular Simulations of Methane, Hydrogen, and Acetylene Storage in Metal–organic Frameworks. *Chem. Rev.* **2011**, *112*, 703–723, DOI: 10.1021/cr200217c.

(26) Tan, J. C.; Civalleri, B.; Lin, C. C.; Valenzano, L.; Galvelis, R.; Chen, P. F.; Bennett, T. D.; Mellot-Draznieks, C.; Zicovich-Wilson, C. M.; Cheetham, A. K. Exceptionally Low Shear Modulus in a Prototypical Imidazole-Based Metal-Organic Framework. *Phys. Rev. Lett.* **2012**, *108*, 095502, DOI: 10.1103/PhysRevLett.108.095502.

(27) Ortiz, A. U.; Boutin, A.; Fuchs, A. H.; Coudert, F.-X. Anisotropic Elastic Properties of Flexible Metal-Organic Frameworks: How Soft Are Soft Porous Crystals? *Phys. Rev. Lett.* **2012**, *109*, 195502, DOI: 10.1103/PhysRevLett.109.195502.

(28) Tan, J.; Bennett, T. D.; Cheetham, A. K. Chemical Structure, Network Topology, and Porosity Effects on the Mechanical Properties of Zeolitic Imidazolate Frameworks. *Proc. Natl. Acad. Sci. U. S. A.* **2010**, *107*, 9938–9943, DOI: 10.1073/pnas.1003205107.

(29) Walker, A. M.; Civalleri, B.; Slater, B.; Mellot-Draznieks, C.; Corà, F.; Zicovich-Wilson, C. M.; Román-Pérez, G.; Soler, J. M.; Gale, J. D. Flexibility in a Metal–Organic Framework Material Controlled by Weak Dispersion Forces: The Bistability of MIL-53 (Al). *Angew. Chemie Int. Ed.* **2010**, *49*, 7501–7503, DOI: 10.1002/anie.201002413.

(30) Gao, M.; Misquitta, A. J.; Rimmer, L. H.; Dove, M. T. Molecular Dynamics Simulation Study of Various Zeolitic Imidazolate Framework Structures. *Dalt. Trans.* **2016**, *45*, 4289–4302, DOI: 10.1039/C5DT03508B.

(31) Boyd, P. G.; Moosavi, S. M.; Witman, M.; Smit, B. Force-Field Prediction of Materials Properties in Metal-Organic Frameworks. *J. Phys. Chem. Lett.* **2017**, *8*, 357–363, DOI:

10.1021/acs.jpclett.6b02532.

(32) Gaillac, R.; Pullumbi, P.; Beyer, K. A.; Chapman, K. W.; Keen, D. A.; Bennett, T. D.; Coudert, F.-X. Liquid Metal–organic Frameworks. *Nat. Mater.* **2017**, *16*, 1149, DOI: 10.1038/nmat4998.

(33) Zhang, L.; Hu, Z.; Jiang, J. Sorption-Induced Structural Transition of Zeolitic Imidazolate Framework-8: A Hybrid Molecular Simulation Study. *J. Am. Chem. Soc.* **2013**, *135*, 3722–3728, DOI: 10.1021/ja401129h.

(34) Hu, Z.; Chen, Y.; Jiang, J. Zeolitic Imidazolate Framework-8 as a Reverse Osmosis Membrane for Water Desalination: Insight from Molecular Simulation. *J. Chem. Phys.* **2011**, *134*, 134705, DOI: 10.1063/1.3573902.

(35) Yang, Y.; Shin, Y. K.; Li, S.; Bennett, T. D.; van Duin, A. C.; Mauro, J. C. Enabling Computational Design of ZIFs Using ReaxFF. *J. Phys. Chem. B* **2018**, *122*, 9616–9624, DOI: 10.1021/acs.jpcb.8b08094.

(36) Yang, Y.; Wilkinson, C. J.; Lee, K.-H.; Doss, K.; Bennett, T. D.; Shin, Y. K.; van Duin, A. C.; Mauro, J. C. Prediction of the Glass Transition Temperatures of Zeolitic Imidazolate Glasses through Topological Constraint Theory. *J. Phys. Chem. Lett.* **2018**, *9*, 6985–6990, DOI: 10.1021/acs.jpclett.8b03348.

(37) Dubbeldam, D.; Walton, K. S.; Ellis, D. E.; Snurr, R. Q. Exceptional Negative Thermal Expansion in Isoreticular Metal–organic Frameworks. *Angew. Chemie* **2007**, *119*, 4580–4583, DOI: 10.1002/anie.200700218.

(38) Xiong, M.; Li, N.; Greaves, N.; Yue, Y. Quantum Chemical Calculations to Elucidate the Electronic and Elastic Properties of Topologically Equivalent Metal Organic Frameworks. *arXiv Prepr.* **2017**, 1712.07372.

(39) Zhou, C.; Stepniewska, M.; Sørenses, J. M.; Scarpa, L.; Magnacca, G.; Boffa, V.; Bennett, T. D.; Yue, Y. Polymorph Formation for a Zeolitic Imidazolate Framework

Composition - Zn(Im)2. *Microporous Mesoporous Mater.* **2018**, *265*, 57–62, DOI: 10.1016/j.micromeso.2018.01.038.

(40) Katsenis, A. D.; Puškarić, A.; Štrukil, V.; Mottillo, C.; Julien, P. A.; Užarević, K.; Pham, M. H.; Do, T. O.; Kimber, S. A. J.; Lazić, P.; et al. In Situ X-Ray Diffraction Monitoring of a Mechanochemical Reaction Reveals a Unique Topology Metal-Organic Framework. *Nat. Commun.* **2015**, *6*, DOI: 10.1038/ncomms7662.

(41) Zhang, J.; Qiao, A.; Tao, H.; Yue, Y. Synthesis, Phase Transitions and Vitrification of the Zeolitic Imidazolate Framework: ZIF-4. *J. Non. Cryst. Solids* **2019**, *Under revi*.

(42) Zheng, Q.; Zhang, Y.; Montazerian, M.; Gulbiten, O. Understanding Glass through Differential Scanning Calorimetry. *Chem. Rev.* **2018**, 1–270, DOI: 10.1021/acs.chemrev.8b00510.

(43) Lindemann, F. The Calculation of Molecular Natural Frequencies. *Phys. Zeitschrift* **1910**, *11*, 609–611.

(44) Tao, H.; Bennett, T. D.; Yue, Y. Melt-Quenched Hybrid Glasses from Metal–Organic Frameworks. *Adv. Mater.* **2017**, *29*, 1601705, DOI: 10.1002/adma.201601705.

(45) Moulder, J. F.; Stickle, W. F.; Sobol, P. E.; Bomben, K. D. *Handbook of X-Ray Photoelectron Spectroscopy: A Reference Book of Standard Spectra for Identification and Interpretation of XPS Data*; Chastain, J., Ed.; Perkin-Elmer Corporation, Physical Electronics Division: Eden Prairie, Minnesota, USA, 1992, DOI: 10.1002/sia.740030412.

(46) Bennett, T. D.; Yue, Y.; Li, P.; Qiao, A.; Tao, H.; Greaves, N. G.; Richards, T.; Lampronti, G. I.; Redfern, S. A. T.; Blanc, F.; et al. Melt-Quenched Glasses of Metal-Organic Frameworks. *J. Am. Chem. Soc.* **2016**, *138*, 3484–3492, DOI: 10.1021/jacs.5b13220.

(47) Krokidas, P.; Castier, M.; Moncho, S.; Brothers, E.; Economou, I. G. Molecular

Simulation Studies of the Diffusion of Methane, Ethane, Propane, and Propylene in ZIF-8. *J. Phys. Chem. C* **2015**, *119*, 27028–27037, DOI: 10.1021/acs.jpcc.5b08554.

(48) Henke, S.; Wharmby, M. T.; Kieslich, G.; Hante, I.; Schneemann, A.; Wu, Y.; Daisenberger, D.; Cheetham, A. K. Pore Closure in Zeolitic Imidazolate Frameworks under Mechanical Pressure. *Chem. Sci.* **2018**, *9*, 1654–1660, DOI: 10.1039/C7SC04952H.

(49) Krokidas, P.; Castier, M.; Moncho, S.; Sredojevic, D. N.; Brothers, E. N.; Kwon, H. T.; Jeong, H.-K.; Lee, J. S.; Economou, I. G. ZIF-67 Framework: A Promising New Candidate for Propylene/Propane Separation. Experimental Data and Molecular Simulations. *J. Phys. Chem. C* **2016**, *120*, 8116–8124, DOI: 10.1021/acs.jpcc.6b00305.

(50) He, M.; Yao, J.; Liu, Q.; Zhong, Z.; Wang, H. Toluene-Assisted Synthesis of RHO-Type Zeolitic Imidazolate Frameworks: Synthesis and Formation Mechanism of ZIF-11 and ZIF-12. *Dalt. Trans.* **2013**, *2*, 16608–16613, DOI: 10.1039/c3dt52103f.

(51) Grimme, S.; Antony, J.; Ehrlich, S.; Krieg, H. A Consistent and Accurate Ab Initio Parametrization of Density Functional Dispersion Correction (DFT-D) for the 94 Elements H-Pu. *J. Chem. Phys.* **2010**, *132*, 154104, DOI: 10.1063/1.3382344.

(52) Birch, F. Finite Elastic Strain of Cubic Crystals. *Phys. Rev.* **1947**, *71*, 809, DOI: 10.1103/PhysRev.71.809.

(53) Plimpton, S. Fast Parallel Algorithms for Short-Range Molecular Dynamics. *J. Comput. Phys.* **1995**, *117*, 1–19, DOI: 10.1006/jcph.1995.1039.

(54) Addicoat, M. A.; Vankova, N.; Akter, I. F.; Heine, T. Extension of the Universal Force Field to Metal–organic Frameworks. *J. Chem. Theory Comput.* **2014**, *10*, 880–891, DOI: 10.1021/ct400952t.

(55) Coupry, D. E.; Addicoat, M. A.; Heine, T. Extension of the Universal Force Field for Metal–organic Frameworks. *J. Chem. Theory Comput.* **2016**, *12*, 5215–5225, DOI:

10.1021/acs.jctc.6b00664.

(56) Rappé, A. K.; Casewit, C. J.; Colwell, K.; Goddard Iii, W.; Skiff, W. UFF, a Full Periodic Table Force Field for Molecular Mechanics and Molecular Dynamics Simulations. *J. Am. Chem. Soc.* **1992**, *114*, 10024–10035, DOI: 10.1021/ja00051a040.

(57) Vanduyfhuys, L.; Vandenbrande, S.; Wieme, J.; Waroquier, M.; Verstraelen, T.; Van Speybroeck, V. Extension of the QuickFF Force Field Protocol for an Improved Accuracy of Structural, Vibrational, Mechanical and Thermal Properties of Metal–organic Frameworks. *J. Comput. Chem.* **2018**, *39*, 999–1011, DOI: 10.1002/jcc.25173.

Supporting Information

Determining the phase diagram, structure and properties of the mixed metallic ZIF-62 system via experiments and modeling

Malwina Stepniewska[1,‡], *Yongjian Yang*[2,‡], *Chao Zhou*[1], *Yuanzheng Yue*[1,*], *John C. Mauro*[2,*]

[1]Department of Chemistry and Bioscience, Aalborg University, DK-9220 Aalborg, Denmark

[2]Department of Materials Science and Engineering, The Pennsylvania State University, University Park, Pennsylvania 16802, USA

‡ These authors contributed equally.

*** Corresponding Authors:** yy@bio.aau.dk (Yuanzheng Yue) and jcm426@psu.edu (John C. Mauro)

Supporting results

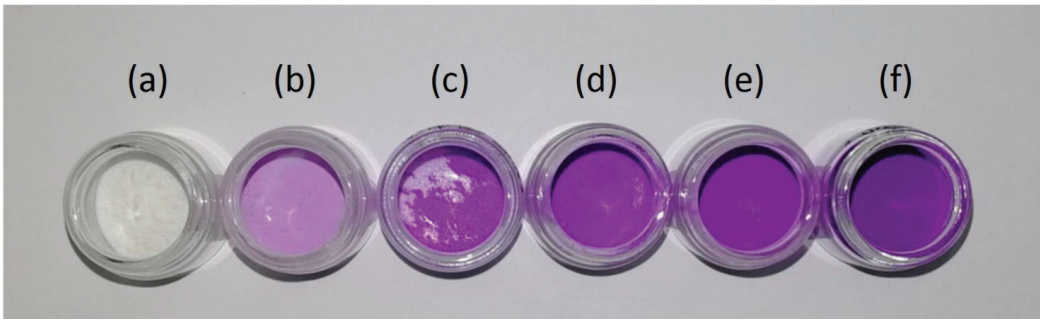

Figure S1. Macroscopic image of 6 obtained samples of $Zn_{1-x}Co_x$-ZIF-62, with increasing cobalt content from (a) Zn-ZIF-62 to (f) Co-ZIF-62

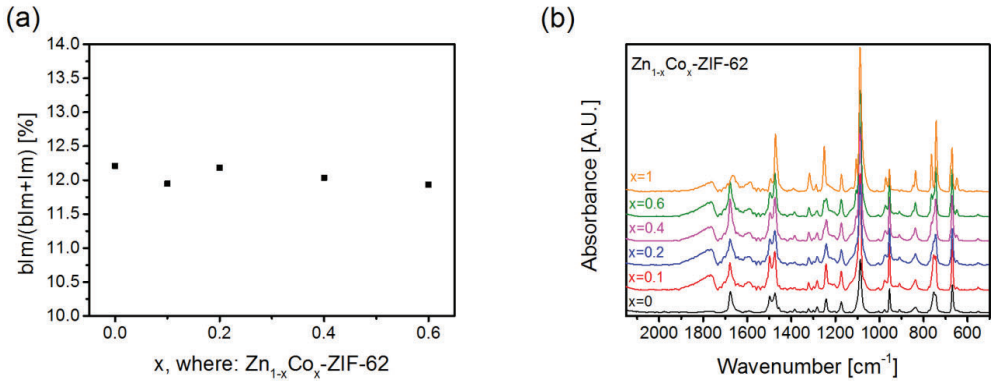

Figure S2. Supplementary structural information for synthesised $Zn_{1-x}Co_x$-ZIF-62 samples: (a) Ligand ratio obtained in synthesised samples, calculated using 1H-LNMR spectra; (b) FT-IR measurements for samples with changing cobalt content.

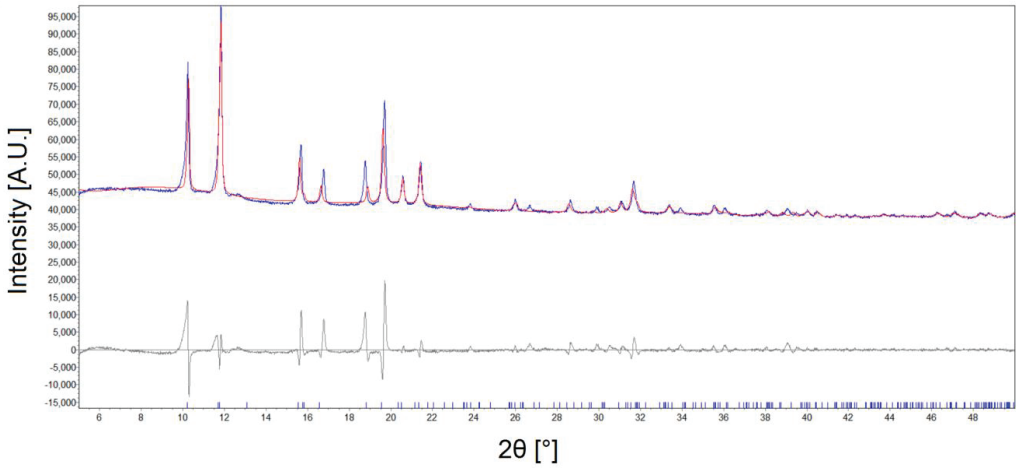

Figure S3. Topas3 refinement of obtained powder XRD pattern of pure cobalt $Zn_{1-x}Co_x$-ZIF-62 phase refined as *Pbca* space group.

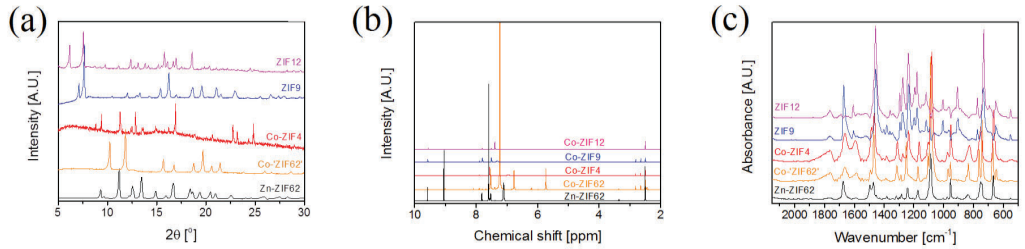

Figure S4. Results of measurements performed on samples with one metallic node, including those performed on Co-ZIF4, ZIF-9 and ZIF-12: (a) P-XRD spectra; (b) H1-LNMR spectra; (c) FT-IR spectra.

For the Co-ZIF-62 sample, the NMR spectrum differs greatly, with peaks coming from 1 and 3 hydrogen hardly visible. For obtaining further data that could be helpful in analysis of Co-ZIF-62 phase, extra XRD and NMR measurements were performed on phases constructed of Co nodes and pure either benzimidazole or imidazole as ligand, namely ZIF-4, ZIF-9 and ZIF-12 (Figure S4). Comparing obtained XRD and H1 L-NMR (Figure S4a and S4b) results with those obtained for synthesised sample, it can be noted that the phase synthesised with 100% Co and both imidazole and benzimidazole sample differs from those synthesized with only one ligand. FT-IR measurements also show significant differences in peak positions between spectra obtained for mixed ligand samples (Zn-ZIF-62 and Co-ZIF-62), and samples with only 1 organic ligand (Co-ZIF-4, ZIF-9 and ZIF-12), as can be noted on figure S4. These differences include an appearance of extra peaks for ZIF-9 and ZIF-12 mostly around 1400-800 wavenumber region. We also note similarities between the Co-ZIF-4 and ZIF-62 spectra, and their resemblance of the spectrum obtained for the new phase.

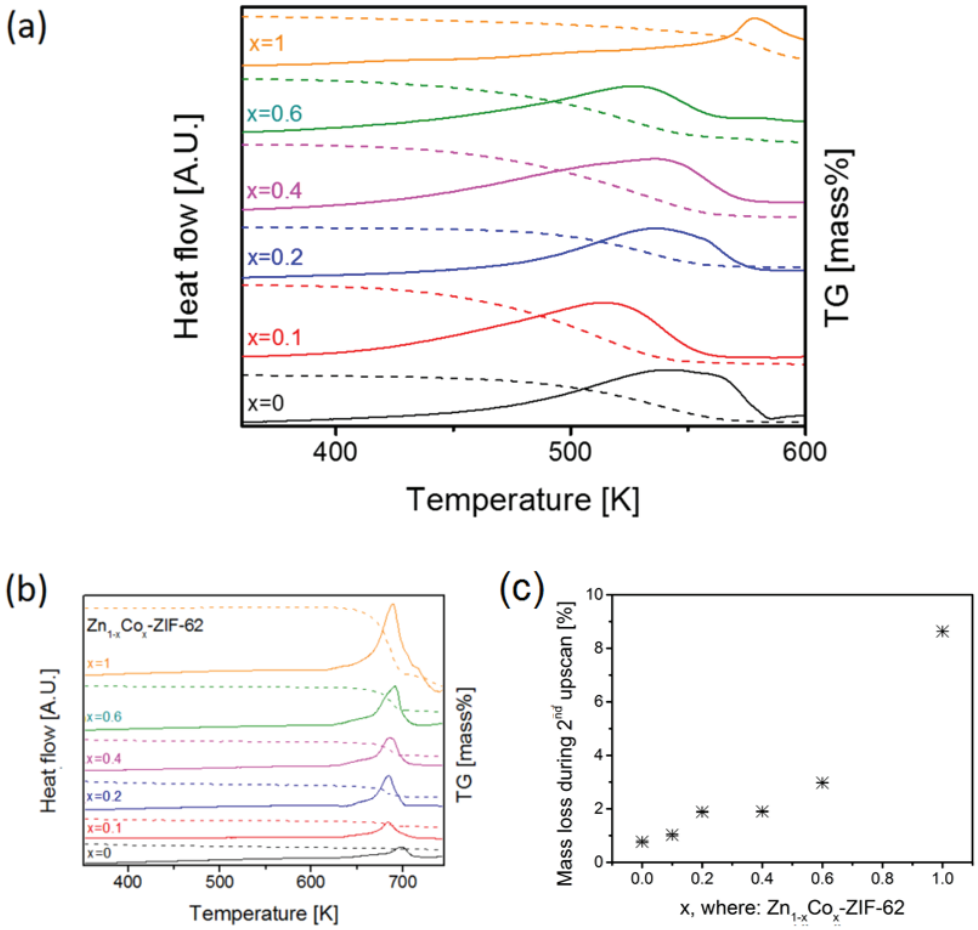

Figure S5. Further thermal response data for $Zn_{1-x}Co_x$-ZIF-62 samples obtained by DSC analysis:(a) DSC and TG curves obtained during the first upscan (solvent dissolution). *x* is cobalt content as in $Zn_{1-x}Co_x$-ZIF-62; (b) and (c): Characteristics obtained during the second upscan (melting): (b) DSC and TG curves obtained; (c) mass loss.

Mass loss during solvent dissolution does not show any dependence on the amount of cobalt added during synthesis (figure S5B), with the loss values ranging from around 6.5% to around 12.5%. The upscan curves (figure S5C) obtained for Co-ZIF-62 shifts to higher temperatures, implying more energy is needed to remove solvent for the sample with Co-ZIF-62.

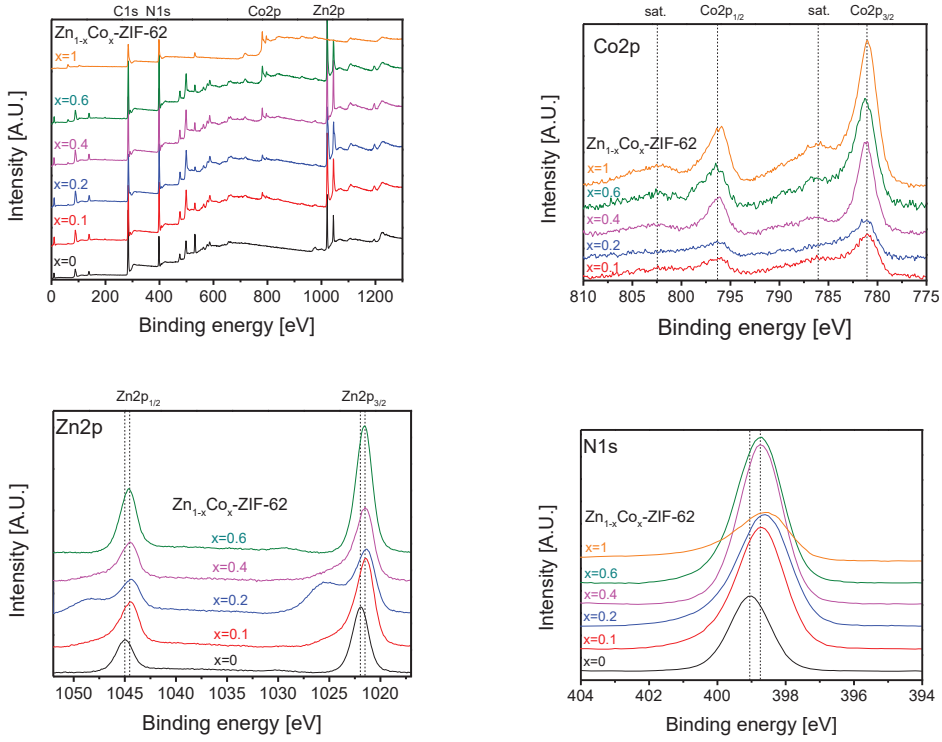

Figure S6. XPS spectra obtained for synthesised samples: (a) full range; (b) Co2p; (c) Zn2p; (d)N1s.

Table S1. Densities of Zn-ZIF-62 from experiments and DFT and MD calculations. Solvent content taken from[1] has been added in the calculation of density for both DFT and MD results.

	Zn-ZIF-62 crystal
Exp[1]	1.494
Current Exp	1.467
DFT (PBE-D3)	1.537
MD	1.546

REFERENCES:

(1) Bennett, T. D.; Yue, Y.; Li, P.; Qiao, A.; Tao, H.; Greaves, N. G.; Richards, T.; Lampronti, G. I.; Redfern, S. A. T.; Blanc, F.; et al. Melt-Quenched Glasses of Metal-Organic Frameworks. *J. Am. Chem. Soc.* **2016**, *138*, 3484–3492, DOI: 10.1021/jacs.5b13220.

PAPER II

Observation of Indentation Induced Nano-Shear Bands in a Metal-Organic Framework Glass

Malwina Stepniewska,[†] Kacper Januchta,[†] Chao Zhou,[†] Ang Qiao,[†,‡] Morten M. Smedskjaer[†] and Yuanzheng Yue [†,‡,§,]*

[†] Department of Chemistry and Bioscience, Aalborg University, DK-9220 Aalborg, Denmark

[‡] State Key Laboratory of Silicate Materials for Architectures, Wuhan University of Technology, Wuhan 430070, China

[§] School of Materials Science and Engineering, Qilu University of Technology, Jinan 250353, China

KEYWORDS. *Metal-Organic Framework Glasses, Zeolitic Imidazolate Framework Glasses, Mechanical Properties, Nano-Shearing*

ABSTRACT: Metal-organic framework (MOF) glasses are a newly emerged family of melt-quenched glasses. Recently, several intriguing features, such as ultrahigh glass-forming ability and low liquid fragility, have been discovered in a number of zeolitic imidazolate frameworks (ZIFs) that are a subset of MOFs. However, the fracture behavior of ZIF glasses remains elusive. Here,

we report the first observation of both cracking patterns and nano-shear bands induced by micro- and nanoindentation in a representative melt-quenched ZIF glass, i.e., ZIF-62 glass ($ZnIm_{1,68}bIm_{0.32}$). The shear banding in the ZIF glass is in strong contrast to the cracking behavior of other types of fully polymerized glasses, which do not exhibit any shear bands under indentation. We attribute this anomalous cracking behavior to the easy breakage of the coordinative bonds (Zn-N) in ZIF glasses, since these bonds are much weaker than the ionic, covalent, and metallic ones in network glasses.

Metal-organic frameworks (MOFs) are composed of metal nodes and organic linkers. An important subset of MOFs is the zeolitic imidazolate frameworks (ZIFs), which exhibit higher thermal and chemical stability than other subsets.[1,2] Like silica or zeolites, ZIFs have a three-dimensional network structure, which is constituted by interconnected metal-ligand tetrahedra. The tetrahedron consists of one central transition metal and four imidazolate ligands.[3–6] Recently, it was discovered that some ZIFs can be melted and subsequently quenched to the glassy state prior to thermal decomposition.[7–12] This new family of melt-quenched glasses is structurally and chemically distinct from other traditional glass families such as metallic, organic, and inorganic ones.

Despite progress in understanding the structure and properties of ZIF glasses,[12–17] their mechanical properties have been studied to a very limited extent, in particular, their cracking behavior has not been reported so far. However, to understand the nature of ZIF glasses and to find their application fields, it is necessary to study their fracture and deformation behavior. Therefore, in the present work, we investigated the mechanical properties of ZIF glasses by using

ZIF-62 glass as a representative object of our study. We chose ZIF-62 glass because it can be made to relatively large, homogeneous bulk samples for mechanical testing, and also because it has already been studied regarding its structure[10] and various material properties.[11,15,16]

ZIF-62 ($Zn(Im)_{2-x}(bIm)_x$) is an excellent glass former, in which the central Zn node is connected by two types of ligands: imidazolate (Im) and benzimidazolate (bIm).[2,17,18] ZIF-62 exhibits higher thermal and structural stability in the liquid state compared to other ZIFs, e.g., a broader temperature range (about 100 K) exists between melting and decomposition (Figure S1).[8,10] ZIF-62 glasses were found to have the ultrahigh glass-forming ability (T_g/T_m=0.84, where T_g is glass transition temperature and T_m is melting point) and high viscosity (~10^5 Pa s) at T_m,[10] as well as structural stability upon heating.[11] The structural difference between ZIF-62 crystal and glass has recently been revealed by X-ray total scattering and X-ray photoelectron spectroscopy analyses.[10] In terms of pair distribution functions, ZIF-62 crystal features high degree of short (< about 7 Å), intermediate (about 7-20 Å) and long range (>20 Å) order, whereas ZIF-62 glass is characterized by high degree of intermediate and long range disorder.[10] A certain degree of local structural disorder (i.e., orientational and rotational disorder) in ZIF glasses is also present.[14] Evidence for the local structural has also been obtained by performing thermal treatment on ZIF-4 glass.[14] When heating this glass in a differential scanning calorimeter to the temperature of ZIF-zni formation, an exotherm occurred around the similar temperature, while a Bragg peak was not observed, i.e., long-range order did not appear. Thus, the exotherm must be associated with the decrease in the degree of the local structural disorder.

In previous works, the indentation modulus of ZIF-62 glass was determined to be about 6 GPa by means of nanoindentation,[8] while its Poisson's ratio was found by Brillouin scattering to be 0.45.[10] Usually, glasses with higher Poisson's ratio exhibit higher ductility than those with

lower ratio.[19] However, the ZIF-glass displays an anomalous behavior, i.e., it features easy crack nucleation despite its high Poisson's ratio. The reason for this anomalous behavior, as well as the detailed fracture mechanism of ZIF glasses, have not been explored so far. To the best of our knowledge, there is only one report on the creep and scratch behaviors of ZIF-62 glass.[15] In the present study, we perform micro- and nanoindentation on ZIF-62 glass to study its deformation and crack initiation behavior and fracture patterns during sharp contact loading. We compare the hardness values of ZIF-62 glass with those of metallic and oxide glasses, explain the structural origin of their difference, and attempt to clarify its sub-surface cracking and deformation mechanism on both micro- and nanoscale.

Figure 1a shows the obtained Vickers indent impressions, suggesting the occurrence of sink-in in the ZIF glass, i.e., deformation downward with respect to the sample surface. A change in the cracking pattern with increasing load is observed, i.e., the crack density increases with increasing load, with radial cracks initiating at the highest loads (0.5 N). The crack resistance, as determined from the load at 50% probability of initiation of radial cracks,[20] is estimated to be around 2 N (Figure 1b, red points). The micro-indentation data are also used to calculate Vickers hardness. As shown in Figure 1b, the hardness first decreases drastically from 0.65 to 0.53 GPa with increasing load from 0.1 to 0.2 N, and then gradually decreases from 0.53 to 0.50 GPa for higher indentation loads. This two-step trend is in contrast to the trend for other types of materials, where the indentation size effect typically leads to a continuous non-linear hardness drop.[21] The first stage of the hardness drop for ZIF-62 glass could be ascribed to a drastic decrease in the free volume of the glass network when the load is slightly increased, since the coordinative Zn-N bonds are more easily broken compared to other types of bonds such as metallic, covalent, ionic ones.[21] The second stage could be associated with the indentation size

effect,[22,23] i.e., an increased ratio between indentation surface and deformation volume with decreasing load. This means that the elastic contribution to the total deformation caused by indentation becomes larger at a lower load.[24,25] The similar two-stage hardness drop with the load increase was also observed in metallic glasses, where the transition from the drastic drop to the slight drop was related to shear band formation.[26] In those metallic glasses, the drastic drop of hardness with load was related to delocalized shear banding, whereas the slight drop was associated with the localized shear banding. This explanation could apply to the case for ZIF-62 glass, where the two-stage hardness drop is striking. The shear banding in ZIF-62 glass will be shown in the later parts.

From Figure 1b, the hardness of bulk ZIF-62 glass lies in the range of 0.5-0.65 GPa, thus is much softer than inorganic network glasses, e.g., oxide glasses that possess a range of the hardness of 3-9 GPa.[27] The much lower hardness of ZIF glasses could be attributed to the following four aspects.

First, the three-dimensional ZIF network is constructed through the coordinative bonds between the metal nodes and the N atoms of imidazolate and benzimidazolate ligands. Such bonds are much weaker than, e.g., the Si-O bonds in inorganic network glasses. For instance, to break the coordinative bonds of ZIF-4, which is a glass with similar bond structure to ZIF-62, an energy barrier of 81 kJ/mol needs to be overcome.[28] In contrast, 443 kJ/mol is required to break the Si-O bonds.[29] Consequently, the resistance of the ZIF glasses to plastic deformation is significantly lower than that of the oxide glasses.

Second, the density of the topological bond constraints, i.e., the number of bond stretching and bond bending constraints per unit of volume, in ZIF glasses is much lower than

that in oxide glasses. This is because the volume of the tetrahedral unit $Zn(Im/bIm)_4$ of ZIF-62 is considerably larger (about 6 Å distance for Zn-Im-Zn[8,10,11,14]) than that of oxide glasses (e.g., 3 Å distance for Si-O-Si[30,31]) for the same number of linear and angular constraints. It is known that the glass hardness decreases with decreasing volumetric constraint density.[32] Thus, the ZIF glasses are softer than the oxide glasses. The detailed calculation of the constraint density will be conducted in a separate work.

Third, ZIF glasses possess a large fraction of organic ligand molecules, which have a higher degree of rotational and translational freedom, e.g., compared to the rigid oxide network consisting of four-fold $[SiO_4]$ units.[33] Therefore, ZIF glasses are more deformable than oxide glasses upon indentation, as demonstrated in Figure 2.

Fourth, ZIF materials feature a large amount of free volume, i.e., voids. Despite the collapse and disordering of those voids during vitrification, the free volume is still much larger than that of oxide glasses. The larger fraction of voids leads to a lowering of the deformation resistance.[34–38]

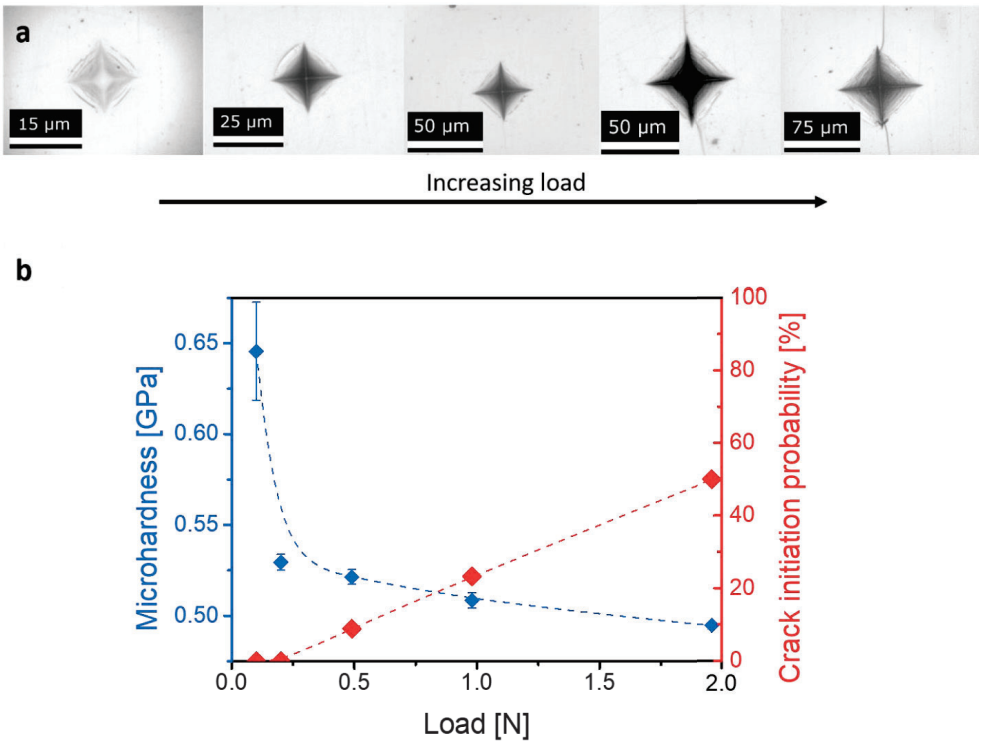

Figure 1. Indentation behavior and Vickers microhardness for ZIF-62 glass in the load range of 0.1 to 1.96 N. (a) Indent images (note the different scale) for increasing load as shown by the arrow. (b) Microhardness (blue points) and crack initiation probability (red points) as a function of applied load. The dashed lines are guides for the eyes.

Figure 2a shows the optical images of the cross-section of an indent along one horizontal crack (see inset) generated under the maximum load of 5 N for the ZIF-62 glass. The sub-surface area can be divided into three main zones, as marked in Figure 2a, in order to study the crack initiation and material deformation mechanisms.[39] Zone I refers to the process zone (i.e., densified region or plastic contact zone), which is located below the visible indent and

constitutes a strongly deformed plastic contact zone with a clear hemispherical boundary (denoted as A). In Zone I, we also observe micro-cracks originated at the surface (see green ellipse). The micro-cracks will be further illustrated in Figure 3. Zone II is the nearly spherical elastic zone,[26,41] which lies between Zone I and the un-deformed glass matrix. In this zone, both median and radial cracks can be observed. The median crack initiates at point B and then propagates further as indicated by C (see the red circles in Figure 2a). The radial cracks occur as a semi-circle (indicated by D). Zone III is the semi-spherical domain, which is situated outside Zone II and is bordered by the glass matrix that is not subjected to deformation during indentation. Here we should note that the extra cracks in this zone might have been created during the bending fracture of the sample for cross-sectional observations. The occurrence of the three zones is a typical feature of most silicate glasses,[39,42] which are topologically similar, despite the difference in bond strength, to the present ZIF-62 glass due to the tetrahedral O-Si-O and Im-Zn-bIm building units in the former and latter, respectively. As shown in Figure 2b, the standard soda lime silica (SLS) window glass, included for comparison, exhibits a similar fracture pattern as the ZIF-62 glass. The occurrence of radial cracks correlates well with the relatively high Poisson's ratio of ZIF glasses,[43] yet not with the low elastoplastic E/H ratio which usually promotes ring cracking instead of radial cracking.[36,43,44] However, the occurrence of the median crack in ZIF glass is an abnormal behavior since it is a high Poisson's ratio system.[43] This behavior could be related to the coordinative bonds in the ZIF glass, which are weaker than the ionic, covalent, and metallic ones in network glasses.

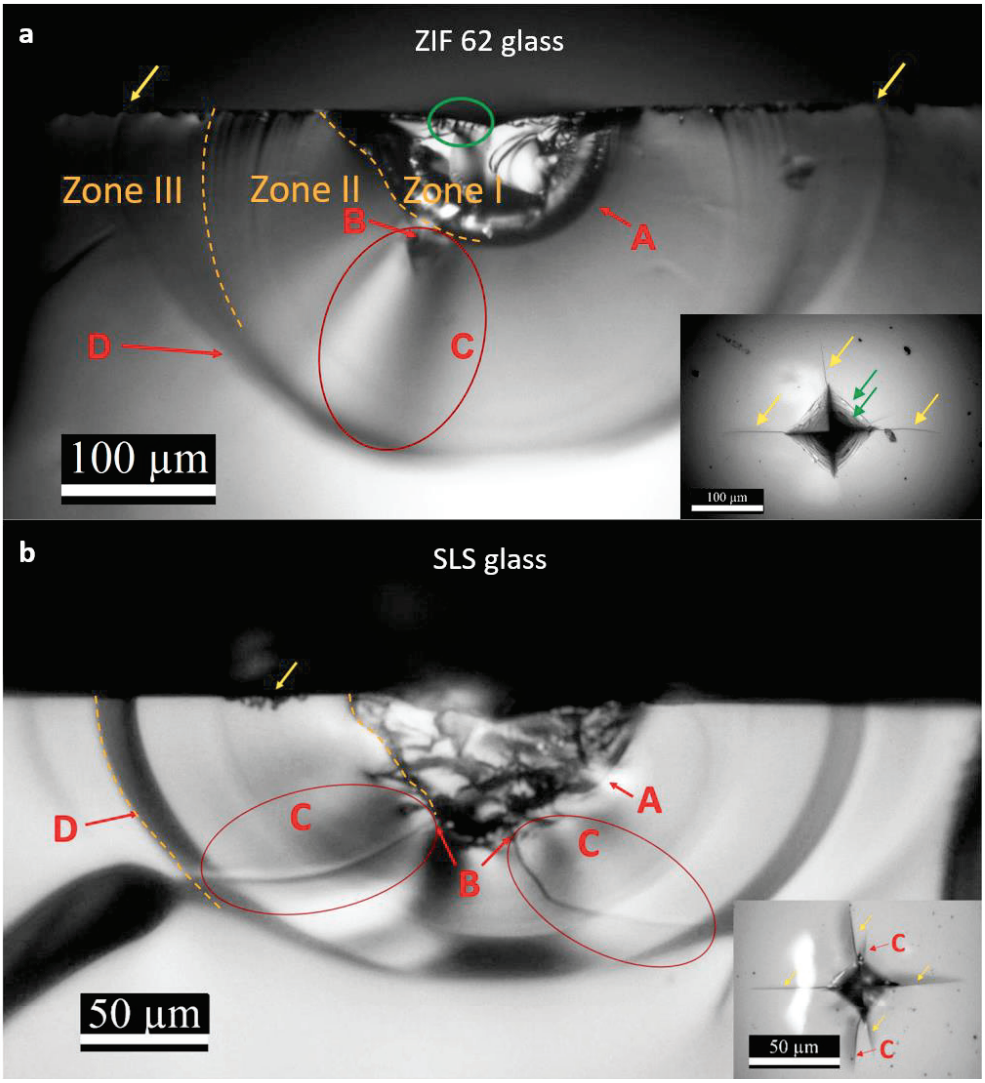

Figure 2. Cross-section view of an indentation deformed zone on (a) ZIF-62 glass and (b) soda-lime-silica (SLS) glass after loading with maximum force of 5 N. Different sub-surface features are observed: A – strongly deformed plastic zone; B – initiation point of the median crack; C – propagation zone of the median crack; D – radial crack; yellow arrows – points at which radial

cracks reach surface of the sample; green ellipse – examples of the lines visible inside indents, corresponding to shear bands and edge cracks. Inset: top view of an indent with radial cracks (yellow arrows) and lines visible inside the indent (examples shown with green arrows) and median cracks for SLS glass (red arrows, C). A more detailed top view image of indent on ZIF-62 can be found in Figure S2.

Figure 3a shows the optical top view image of an indent formed in the ZIF-62 glass under the load of 1.96 N, where we observe a layered indent pattern. In the domain marked by the red square frame, we recorded an atomic force microscopy (AFM) image, showing two distinct cracking features: shear band formation (designated as B) and edge cracking (designated as A), as shown in Figure 3b. Small, chipped domains on the sample surface are visible at the end of the radial cracks (yellow arrows in Figure 2). In Figure 3a, we also notice that the radial cracks do not originate from the corners of indents, but from the first-formed edge cracks.

The shear band formation at the nanoscale is herein verified by the sudden shift of the deformation curve, as measured by AFM (Figure 3c). Remarkably, we are here able to identify the scale of the shear band, i.e., a shear-induced dislocation. In other words, we discovered a stepwise structural sliding at the nano-scale (here about 35 nm in vertical direction) within the deformation zone in the ZIF-62 glass upon indentation, as indicated in Figure 3c. The scale of the shear band varies from one site to another, but is in the range of approximately 10-100 nm. The exact size distribution of the shear band still needs to be determined by collecting more indentation data. Here we focus on the shear band behavior and mechanism. The shear bands imply that the stepwise micro-crack is accompanied by a stepwise structural sliding upon indentation. More specifically, the formation of shear band must be caused by translational motion of structural units,[45] which in turn is due to the Zn-N bond breakage as these bonds in the

ZIF glass are much weaker than other types of bonds as mentioned above. It should be noted that both the Zn-N bond breakage and the reforming process take place dynamically during indentation, which are triggered by the external mechanical energy. The covalent bonds of the ligand molecules in ZIFs are not easily broken, i.e., they remain intact during melting as evidenced by solid-state ^{13}C-^{1}H coupling NMR results.[8,10] In addition, it should be pointed out that the observed shear band is not a result of melt inhomogeneity for the following reasons. Usually, one of the major types of inhomogeneous defects in bulk oxide glasses is striae due to an incomplete homogenization process.[46] However, the size (length and width in macro-scale) of the striae is significantly larger than the shear band (in nanoscale) shown in this work. Moreover, the similar optical transparency of the hot-pressed ZIF-62 glass to that of oxide glasses[16] is another indication for the high homogeneity of the sample studied in this work. Finally, the spatial fluctuations in the optical transparency of the hot-pressed ZIF-62 glass are rather low,[16] again implying the homogeneity of the present sample.

To the best of our knowledge, this behavior has never been observed in other network glasses with fully polymerized structure, i.e., completely corner-shared tetrahedral network, e.g., in pure silica glass. Shear bands or slip lines, which are narrow regions of excessive strain, are typically observed in metallic glasses,[26,47,48] but have also been reported in some modified oxide glasses.[40] However, not with a step height of several tens of nm as it is the case here. The latter type of shear bands has, however, been observed in some chalcogenide glasses.[49] Those typical glasses possess chain-like network structure, with van der Waal's bonding between the chains, effectively lowering the resistance to deformation upon indentation.[49] However, the microscopic origin of the shear band formation in the present ZIF glass is distinct from that in the chalcogenide glasses.

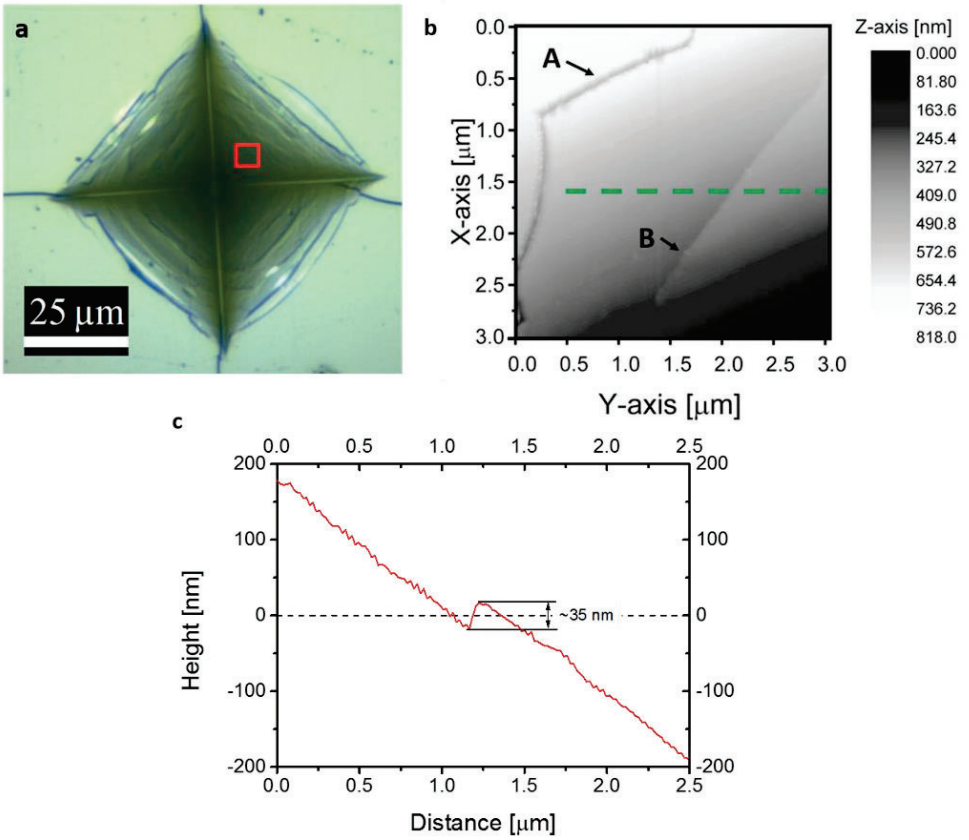

Figure 3. Atomic force microscopy (AFM) measurements on the indent walls (at 1.96 N) of the ZIF-62 glass. (a) Optical microscopy image of 1.96 N indent, with the red square showing the AFM scanned area. (b) Two-dimensional height profile of the AFM scanned area, showing a crack (designated as A) and a shear band (designated as B). Note the change of height in the vicinity of the observed shear band. (c) AFM height profile through a shear band (dashed green line is subfigure b), showing an increase in height of around 35 nm at the location of the shear band.

Figure 4 shows the nanoindentation data, from which we find a decreasing trend in both hardness and indentation modulus with increasing load, similar to that for Vickers microhardness (Figure 1b). The E_{ind}/H_{nano} ratio is about 8.2 at the load of 0.01 N, and then slightly increases to a constant value of 8.5 with increasing load (Figure 4a). Similarly to the microindentation impressions (Figure 1a), the nanoindentation impressions after unloading exhibit linearly aligned patterns parallel to the indent edges, being either edge cracks or nano-shear bands (Figure S3). The occurrence of cracks at those low loads implies relatively high brittleness of ZIF glass, whereas the presence of shear bands suggests a low threshold for initiation of localized shearing process. The load–displacement curves (Figure S4) have been analyzed to determine the relative elastic and plastic work (see method in Figure S5), as well as the relative elastic and plastic displacement during indentation (Table S1). An elastic deformation of about 50% is estimated for all the applied loads, implying rather high contribution of elastic deformation to the total deformation induced by indentation loading, compared to most oxide glasses.[50] Based on the AFM indent shape analysis (Figure 4b), only a slight pile-up contribution can be observed in the vicinity of the indents. Observation of pile-up around the indent edges would have been indicative of activated isochoric shear flow during indentation.[44] As such, this is an interesting observation, considering the pronounced presence of shear bands inside the indents, which implies a plastic deformation. The lack of pile-up, together with the occurrence of nano-shear bands, implies that the plastic deformation in ZIF glass is highly localized process at nano-scale.

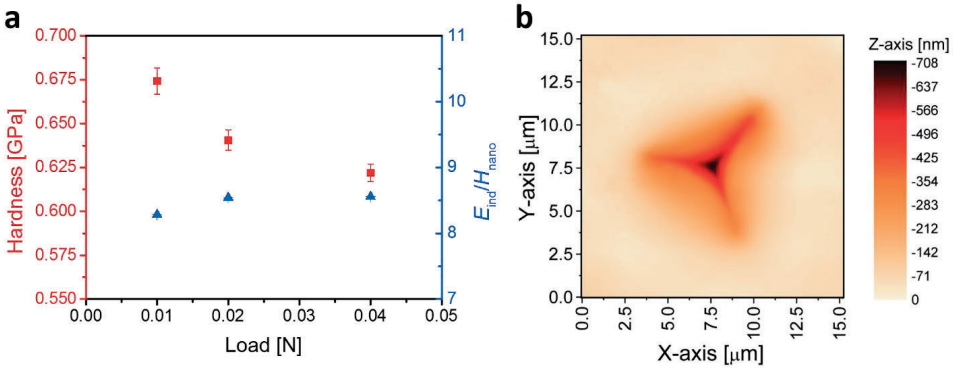

Figure 4. Mechanical properties of ZIF-62 glass as determined by nanoindentation and the nano-indent image obtained by AFM. (a) Hardness (red points) and indentation modulus normalized by nanohardness (E_{ind}/H_{nano}, blue points) as a function of applied load. (b) Topographical AFM image of the indent produced under the load of 0.01 N. Note the slight pile-up in the vicinity of the indent.

Finally, based on measurements of the longitudinal and transverse sound wave velocities, we calculated the Poisson's ratio of the ZIF-62 glass to be 0.35. This value is lower than that recently measured by Brillouin scattering (0.45).[10] The origin of this discrepancy still needs to be clarified in future work.

In summary, we investigated the sharp contact cracking and deformation behavior of ZIF-62 glass by performing micro- and nano-indentation measurements. By doing so, we have discovered the anomalous fracture, i.e., the indentation-induced stepwise cracking and ascribed this to the weak coordinative bonds. The presence of nano-shear bands, which is partially responsible for the creation of the cracking pattern, is consistent with the relatively high Poisson's ratio of ZIF-62 glass. This glass is also characterized by relatively low values for

hardness, indentation modulus, and elastoplastic ratio, compared to other types of 3D network glasses, e.g., oxide glasses. We have attributed the lower hardness of ZIF glasses to four distinct structural features. Moreover, the ZIF-62 glass exhibits a high degree of elastic deformation, and only a slight amount of pile-up is detected, implying a high degree of densification during indentation.

ASSOCIATED CONTENT

Supporting Information.

This material is available free of charge on the ACS Publications website:

- Experimental section, DSC upscan of ZIF-62 crystals, Close-up on top view of indent on ZIF-62 glass, Indent images obtained for nanoindentation measurements, Force-displacement curves for nanoindentation on ZIF glass, Structural characterization of ZIF-62 in crystalline and glassy states, Mechanical properties obtained from nanoindentation of the ZIF-62 glass (PDF)

AUTHOR INFORMATION

Corresponding Author

* E-mail (Y.Z.Y.): yy@bio.aau.dk

Author Contributions

Y.Z.Y. initiated the project. M.S. designed the experimental plan with advices from K.J., C.Z., Y.Z.Y., M.M.S. and A.Q. M.S. and Y.Z.Y. wrote the manuscript with inputs from M.M.S., K.J., C.Z., and A.Q. M.S. and C.Z. prepared the samples, and M.S. and A.Q. performed hot pressing. M.S. and C.Z. conducted DSC analysis. M.S. and K.J. performed ultrasonic measurements to

determine wave propagation velocities. M.S. carried out micro- and nano-indentation measurements. M.S. and K.J made indent cross-section optical images. M.S. and K.J. analyzed the images with inputs from M.M.S and Y.Z.Y. M.S. and K.J. conducted all the AFM measurements and analyzed the AFM data with inputs from Y.Z.Y.

Funding Sources

This work was supported by VILLUM FONDEN (No. 13253).

Notes

The authors declare no competing financial interest.

ACKNOWLEDGMENTS

The authors are grateful to Grethe Winther (Technical University of Denmark) for her help with nanoindentation and Haizheng Tao (Wuhan University of Technology) for facilitating sample production and valuable discussions.

REFERENCES

(1) Park, K. S.; Ni, Z.; Côté, A. P.; Choi, J. Y.; Huang, R.; Uribe-Romo, F. J.; Chae, H. K.; O'Keeffe, M.; Yaghi, O. M. Exceptional Chemical and Thermal Stability of Zeolitic Imidazolate Frameworks. *Proc. Natl. Acad. Sci. U. S. A.* **2006**, *103*, 10186–10191.

(2) Gustafsson, M.; Zou, X. Crystal Formation and Size Control of Zeolitic Imidazolate Frameworks with Mixed Imidazolate Linkers. *J. Porous Mater.* **2013**, *20*, 55–63.

(3) Liu, Y.; Kravtsov, C.; Larsen, R.; Eddaoudi, M. Molecular Building Blocks Approach to the Assembly of Zeolite-like Metal – Organic Frameworks (ZMOFs) with Extra-Large Cavities. *Chem. Commun.* **2006**, *14*, 1488–1490.

(4) Huang, X.; Lin, Y.; Zhang, J.; Cheng, X.-M. Ligand-Directed Strategy for Zeolite-Type

Metal– Organic Frameworks: Zinc (II) Imidazolates with Unusual Zeolitic Topologies. *Angew. Chemie* **2006**, *45*, 1557–1559.

(5) Zhang, J.; Chen, X. Crystal Engineering of Binary Metal Imidazolate and Triazolate Frameworks. *Chem. Commun.* **2006**, *16*, 1689–1699.

(6) Tan, J.; Bennett, T. D.; Cheetham, A. K. Chemical Structure, Network Topology, and Porosity Effects on the Mechanical Properties of Zeolitic Imidazolate Frameworks. *Proc. Natl. Acad. Sci. U. S. A.* **2010**, *107*, 9938–9943.

(7) Bennett, T. D.; Tan, J. C.; Yue, Y. Z.; Baxter, E.; Ducati, C.; Terrill, N. J.; Yeung, H. H. M.; Zhou, Z.; Chen, W.; Henke, S.; Cheetham, A. K.; Greaves, G. N. Hybrid Glasses from Strong and Fragile Metal-Organic Framework Liquids. *Nat. Commun.* **2015**, *6*, 8079.

(8) Bennett, T. D.; Yue, Y. Z.; Li, P.; Qiao, A.; Tao, H.; Greaves, N. G.; Richards, T.; Lampronti, G. I.; Redfern, S. A. T.; Blanc, F.; Farha, O.K.; Hupp, J. T.; Cheetham, A. K.; Keen, D. A. Melt-Quenched Glasses of Metal-Organic Frameworks. *J. Am. Chem. Soc.* **2016**, *138*, 3484–3492.

(9) Tao, H.; Bennett, T. D.; Yue, Y. Z. Melt-Quenched Hybrid Glasses from Metal–Organic Frameworks. *Adv. Mater.* **2017**, *29*, 1601705.

(10) Qiao, A.; Bennett, T. D.; Tao, H.; Krajnc, A.; Mali, G.; Doherty, C. M.; Thornton, A. W.; Mauro, J. C.; Greaves, G. N.; Yue, Y. Z. A Metal-Organic Framework with Ultrahigh Glass-Forming Ability. *Sci. Adv.* **2018**, *4*, eaao6827.

(11) Zhou, C.; Stepniewska, M.; Longley, L.; Ashling, C. W.; Chater, P. A.; Keen, D. A.; Bennett, T. D.; Yue, Y. Z. Thermodynamic Features and Enthalpy Relaxation in a Metal–organic Framework Glass. *Phys. Chem. Chem. Phys.* **2018**, *20*, 18291–18296.

(12) Longley, L.; Collins, S. M.; Zhou, C.; Smales, G. J.; Norman, S. E.; Brownbill, N. J.; Ashling, C. W.; Chater, P. A.; Tovey, R.; Schönlieb, C. B.; et al. Liquid Phase Blending of Metal-Organic Frameworks. *Nat. Commun.* **2018**, *9*, 2135.

(13) Zhou, C.; Longley, L.; Krajnc, A.; Smales, G. J.; Qiao, A.; Erucar, I.; Doherty, C. M.;

Thornton, A. W.; Hill, A. J.; Ashling, C. W.; et al. Metal-Organic Framework Glasses with Permanent Accessible Porosity. *Nat. Commun.* **2018**, *9*, 5042.

(14) Zhang, J.; Longley, L.; Liu, H.; Ashling, C. W.; Chater, P. A.; Beyer, K. A.; Chapman, K. W.; Tao, H.; Keen, D. A.; Bennett, T. D.; Yue, Y. Z. Structural Evolution in a Melt-Quenched Zeolitic Imidazolate Framework Glass during Heat-Treatment. *Chem. Commun.* **2019**, *55*, 2521–2524.

(15) Li, S.; Limbach, R.; Longley, L.; Shirzadi, A.; Walmsley, J. C.; Johnstone, D. N.; Midgley, P. A.; Wondraczek, L.; Bennett, T. D. Mechanical Properties and Processing Techniques of Bulk Metal-Organic Framework Glasses. *J. Am. Chem. Soc.* **2019**, *141*, 1027–1034.

(16) Qiao, A.; Tao, H.; Carson, M.; Aldrich, S.; Thirion, L.; Bennett, T.; Mauro, J.; Yue, Y. Z. Optical Properties of a Melt-Quenched Metal-Organic Framework Glass. *Opt. Lett.* **2019**, *44*, 1623–1625.

(17) Horike, S.; Nagarkar, S. S.; Tomohiro, O.; Kitagawa, S. New Dimension of Coordination Polymers and Metal–Organic Frameworks toward Functional Glasses and Liquids. *Angew. Chemie Int. Ed.,* DOI: 10.1002/anie.201911384, (Accepted manuscript).

(18) Banerjee, R.; Phan, A.; Wang, B.; Knobler, C.; Furukawa, H.; O'Keeffe, M.; Yaghi, O. M. High-Throughput Synthesis of Zeolitic Imidazolate Frameworks and Application to CO_2 Capture. *Science* **2008**, *319*, 939–943.

(19) Greaves, G. N.; Greer, A. L.; Lakes, R. S.; Rouxel, T. Poisson's Ratio and Modern Materials. *Nat. Mater.* **2011**, *10*, 823–837.

(20) Wada, M.; Furukawa, H.; Fujita, K. Crack Resistance of Glass on Vickers Indentation. *Proc. X Int. Congr. Glas.* **1974**, *11*, 39–46.

(21) Manika, I.; Maniks, J. Size Effects in Micro- and Nanoscale Indentation. *Acta Mater.* **2006**, *54*, 2049–2056.

(22) Farges, G.; Degout, D. Interpretation of the Indentation Size Effect in Vickers Microhardness Measurements-Absolute Hardness of Materials. *Thin Solid Films* **1989**, *181*,

365–374.

(23) Gong, J.; Wu, J.; Guan, Z. Examination of the Indentation Size Effect in Low-Load Vickers Hardness Testing of Ceramics. *J. Eur. Ceram. Soc.* **1999**, *19*, 2625–2631.

(24) Li, H.; Bradt, R. C. The Microhardness Indentation Load/Size Effect in Rutile and Cassiterite Single Crystals. *J. Mater. Sci.* **1993**, *28*, 917–926.

(25) Kavetskyy, T.; Borcc, J.; Sangwal, K.; Tsmots, V. Indentation Size Effect and Vickers Microhardness Measurement of Metal-Modified Arsenic Chalcogenide Glasses. *J. Optoelectron. Adv. Mater.* **2010**, *12*, 2082–2091.

(26) Lu, Y. M.; Sun, B. A.; Zhao, L. Z.; Wang, W. H.; Pan, M. X.; Liu, C. T.; Yang, Y. Shear-Banding Induced Indentation Size Effect in Metallic Glasses. *Sci. Rep.* **2016**, *6*, 28523.

(27) Januchta, K.; Youngman, R. E.; Goel, A.; Bauchy, M.; Logunov, S. L.; Rzoska, S. J.; Bockowski, M.; Jensen, L. R.; Smedskjaer, M. M. Discovery of Ultra-Crack-Resistant Oxide Glasses with Adaptive Networks. *Chem. Mater.* **2017**, *29*, 5865–5876.

(28) Gaillac, R.; Pullumbi, P.; Courdet, F.-X. Melting of Zeolitic Imidazolate Frameworks with Different Topologies: Insight from First-Principles Molecular Dynamics. *J. Phys. Chem. C* **2018**, *112*, 6730−6736.

(29) Clupper, D. C.; Hench, L. L. Crystallization Kinetics of Tape Cast Bioactive Glass 45S5. *J. Non. Cryst. Solids* **2003**, *318*, 43–48.

(30) Johnson, P. A. V.; Wright, A. C.; Sinclair, R. N. Neutron Scattering from Vitreous Silica II. Twin-Axis Diffraction Experiments. *J. Non. Cryst. Solids* **1983**, *58*, 109–130.

(31) Greaves, G. N.; Sen, S. Inorganic Glasses, Glass-Forming Liquids and Amorphizing Solids. *Adv. Phys.* **2007**, *56*, 1–166.

(32) Zheng, Q.; Yue, Y. Z.; Mauro, J. C. Density of Topological Constraints as a Metric for Predicting Glass Hardness. *Appl. Phys. Lett.* **2017**, *111*, 011907.

(33) Zhang, Y.; Huang, L.; Shi, Y. Silica Glass Toughened by Consolidation of Glassy

Nanoparticles. *Nano Lett.* **2019**, *19*, 5222–5228.

(34) Rouxel, T. Elastic Properties of Glasses: A Multiscale Approach. *Comptes Rendus - Mécanique* **2006**, *334*, 743–753.

(35) Wondraczek, L.; Mauro, J. C.; Eckert, J.; Kühn, U.; Horbach, J.; Deubener, J.; Rouxel, T. Towards Ultrastrong Glasses. *Adv. Mater.* **2011**, *23*, 4578–4586.

(36) Sellappan, P.; Rouxel, T.; Celarie, F.; Becker, E.; Houizot, P.; Conradt, R. Composition Dependence of Indentation Deformation and Indentation Cracking in Glass. *Acta Mater.* **2013**, *61*, 5949–5965.

(37) Park, K. W.; Jang, J. il; Wakeda, M.; Shibutani, Y.; Lee, J. C. Atomic Packing Density and Its Influence on the Properties of Cu-Zr Amorphous Alloys. *Scr. Mater.* **2007**, *57*, 805–808.

(38) Cheng, Y. Q.; Ma, E. Atomic-Level Structure and Structure-Property Relationship in Metallic Glasses. *Prog. Mater. Sci.* **2011**, *56*, 379–473.

(39) Atkinson, C.; Martínez-Esnaola, J. M.; Elizalde, M. R. Contact Mechanics: A Review and Some Applications. *Mater. Sci. Technol.* **2012**, *28*, 1079–1091.

(40) Gross, T. M.; Wu, J.; Baker, D. E.; Price, J. J.; Yongsunthon, R. Crack-Resistant Glass with High Shear Band Density. *J. Non. Cryst. Solids* **2018**, *494*, 13–20.

(41) Gross, T. M.; Tomozawa, M. Indentation-Induced Microhardness Changes in Glasses: Possible Fictive Temperature Increase Caused by Plastic Deformation. *J. Non. Cryst. Solids* **2008**, *354*, 4056–4062.

(42) Sglavo, V. M.; Green, D. J. Subcritical Growth of Indentation Median Cracks in Soda-Lime-Silica Glass. *J. Am. Ceram. Soc.* **1995**, *78*, 650–656.

(43) Rouxel, T. Driving Force for Indentation Cracking in Glass: Composition, Pressure and Temperature Dependence. *Philos. Trans. R. Soc. A Math. Phys. Eng. Sci.* **2015**, *373*, 20140140.

(44) Januchta, K.; Smedskjaer, M. M. Indentation Deformation in Oxide Glasses: Quantification,

Structural Changes, and Relation to Cracking. *J. Non. Cryst. Solids X* **2019**, *1*, 100007.

(45) Ernsberger, F. M. Mechanical Properties of Glass. *J. Non. Cryst. Solids* **1977**, *25* (1–3), 293–321.

(46) Bange, K.; Müller, H.; Strubel, C. Characterization of Defects in Glasses and Coatings on Glasses by Microanalytical Techniques. *Mikrochim. Acta* **2000**, *132*, 493–503.

(47) Greer, A. L.; Cheng, Y. Q.; Ma, E. Shear Bands in Metallic Glasses. *Mater. Sci. Eng. R Reports* **2013**, *74*, 71–132.

(48) Egami, T.; Iwashita, T.; Dmowski, W. Mechanical Properties of Metallic Glasses. *Metals (Basel).* **2013**, *3*, 77–113.

(49) Guin, J.; Rouxel, T.; Sanglebœuf, J.; Melscooet, I.; Lucas, J. Hardness, Toughness, and Scratchability of Germanium–Selenium Chalcogenide Glasses. *J. Am. Ceram. Soc.* **2002**, *85*, 1545–1552.

(50) Yamane, M.; Mackenzie, J. D. Vicker's Hardness of Glass. *J. Non. Cryst. Solids* **1974**, *15*, 153–164.

SYNOPSIS

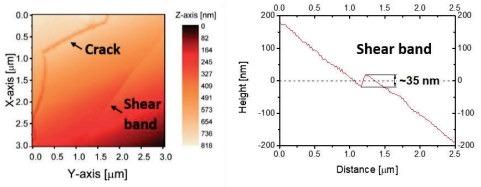

Supporting Information

Observation of Indentation Induced Nano-Shear Bands in a Metal-Organic Framework Glass

*Malwina Stepniewska,[†] Kacper Januchta,[†] Chao Zhou,[†] Ang Qiao,[†,§] Morten M. Smedskjaer[†] and Yuanzheng Yue [†,‡,§,]**

[†] Department of Chemistry and Bioscience, Aalborg University, DK-9220 Aalborg, Denmark

[‡] State Key Laboratory of Silicate Materials for Architectures, Wuhan University of Technology, Wuhan 430070, China

[§] School of Materials Science and Engineering, Qilu University of Technology, Jinan

Methods

Sample preparation and structural characterization. ZIF-62 was synthesized by using the solvothermal method with the Zn:Im:bIm molar ratio of 1:8.5:1.5, which gave the final composition of ZIF-62 crystal $Zn(Im)_{1.68}(bIm)_{0.32}$ based on the relation between the designed and measured Im/bIm ratio reported elsewhere.[1] To achieve this ratio, we mixed 17.453 ml of 0.6 molar zinc nitrate hexahydrate ($Zn(NO_3)_2 \cdot 6H_2O$) (Merck), 33.816 ml of 4 molar imidazole ($C_3H_4N_2$) (Merck), and 21.817 ml of 0.5 molar benzimidazole ($C_7H_6N_2$) (Merck) solutions in N,N-dimethylformamide (DMF) (VWR). This mixture was then magnetically stirred for 1 hour. Afterwards, the solution was moved to a sealed glass jar (100 ml) and placed in a furnace for 48 hours at 403 K. The derived crystals were washed three times in DMF and finally once in dichloromethane (DCM) (Merck). X-ray powder diffraction analysis confirmed that the obtained phase was indeed crystalline ZIF-62 (Figure S6a). PANalytical empyream XRD with Cu $K_{\alpha 1}$ radiation (λ = 1.54098 Å) machine was used to collect XRD data in the range of 5 to 50° (step size 0.013°). In order to prepare bulk ZIF-62 glass samples for the mechanical testing, we applied a novel processing method, i.e., hot-press method.[2] The as-prepared crystalline ZIF-62 powder was first put into a metal mould with 10 mm inner diameter. Subsequently, the mould was placed into the hot-press machine (Hefei Kejing Materials Technology Co., Ltd., China), in which the sample was compressed under the pressure of 50 MPa and afterwards heated under vacuum to 833 K at 5 K/min and held for 30 min. Then, the liquid was cooled down to room temperature, resulting in vitrification. During the hot-press process, the applied pressure and vacuum help, respectively, to remove the bubbles from ZIF-62 melt and prevent the sample from oxidation at high temperature. The glassy nature of the obtained sample was confirmed by X-ray powder diffraction (Figure S6a). In order to compare the hot pressed glass structure to those of both the starting crystalline material and the ambient-pressure melt-quenched

glass, additional infrared spectroscopy (FT-IR) measurements were performed (Figure S6c). FT-IR data was collected in absorbance mode on a Bruker Tensor II equipped with platinum ATR in range of 400-4000 cm^{-1} wavenumber. A difference in infrared spectra between the two samples cannot be identified, indicating that there is no difference in microstructure. Liquid-state nuclear magnetic resonance (NMR) measurement was carried out on Bruker DPX600 Advance (at 600 MHz frequency) spectrometer at 298 K to quantify the ligand ratio in both the crystalline sample and the hot pressed glass, and the results show that the ligand ratio remains nearly constant after quenching under pressure. Samples were digested in DCl/D_2O/DMSO-d6 solution. This confirms that the ligands do not decompose in a detectable level when the ZIF sample is hot-pressed (Figure S6b). Finally, we obtained a 10 mm bulk transparent homogeneous ZIF-62 glass sample without visible bubbles. Samples for indentation measurements were embedded in resin (Struers epofix), grinded using SiC paper of grit size 600, 800, 1200, 2400, and 4000, and finally polished using a suspension of diamond particles with decreasing size (3, 1, and 0.25 μm).

Mechanical characterization. Vickers microindentation was performed using Nanovea CB500 Hardness Tester with loads of 0.1, 0.2, 0.49, 0.98, and 1.96 N to observe the change of microhardness with load and to study the cracking mechanism. The Vickers diamond indenter is a square pyramid with opposite faces at an angle of 136°. For each load, a duration of 6 seconds was needed to obtain maximum load, while the time of unloading was 60 seconds. The maximum load was kept for 15 seconds. In addition to calculating Vickers hardness, we also calculated the probability of crack initiation under loads based on the obtained indent images, which was defined as the ratio between the number of observed cracks and that of indent corners (i.e., four corners per indent). The load corresponding to the crack initiation probability of 50% was considered to be the crack resistance (CR).[3]

We examined the crack pattern and shape of the sub-surface indent on both ZIF-62 glass and soda-lime-silica (SLS) window glass. The composition of SLS is $13Na_2O$-6MgO-10CaO-$71SiO_2$ in mol% and was obtained from Velux A/S. We compare the crack pattern of ZIF-62 glass to that of SLS glass, which is a typical oxide glass that exhibits long radial cracks from the indent corners.[4] To view the indent cross-sections of both glass samples, we generated a line of indents with a distance of 1.5 times the indent size between indents using the maximum load of 5 N. The samples were then broken to obtain fresh fracture surfaces passing through the indents.

To access the deformation patterns, hardness and apparent elastic modulus of ZIF-62 glass were measured under smaller load (<0.1 N). This was done using nanoindentation (CSM nanoindentation tester) with Berkovich tip under maximum loads of 10, 20, and 40 mN. The Berkovich diamond indenter is a three-sided pyramid with the same ratio of project area to depth as the Vickers indenter. The indenter was calibrated using a standard sample of fused silica. The obtained indentation data were analyzed based on the Oliver-Pharr method.[5]

Atomic force microscopy (AFM) measurements were performed using an Ntegra (NT MDT) instrument and silicon tip cantilevers (NSG10, NT-MDT) in semi-contact mode in order to explore the deformation mechanism of ZIF-62 glass under contact loading. Due to the large size of the Vickers microindents, only selected areas (~3×3 μm^2) were imaged, while 10 mN nanoindents were imaged in their entirety (~15×15 μm^2). The scanning frequency was adjusted according to the size of the topographical image, with the scanning velocity of 3 μm/s for ~15×15 μm^2 areas and 1 μm/s for the smaller areas. All AFM images have a resolution of 256×256 pixels.

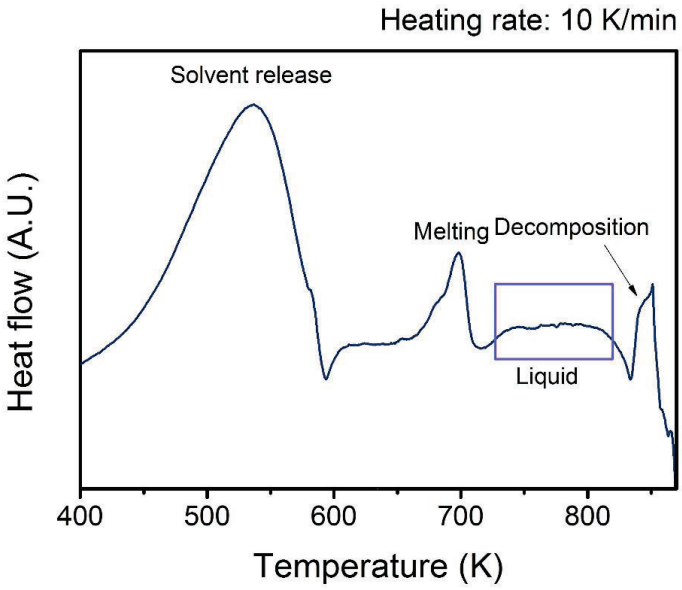

Figure S1. Differential scanning calorimetry (DSC) measurement of crystalline ZIF-62, showing heat flow dependence on temperature during heating at 10 K/min. With increasing temperature, we first observe the release of remaining solvent after the synthesis (from the pores in the framework), then melting of ZIF-62, and finally the beginning of its decomposition. The sample is thermally stable in the liquid state in the temperature range between melting and decomposition events.

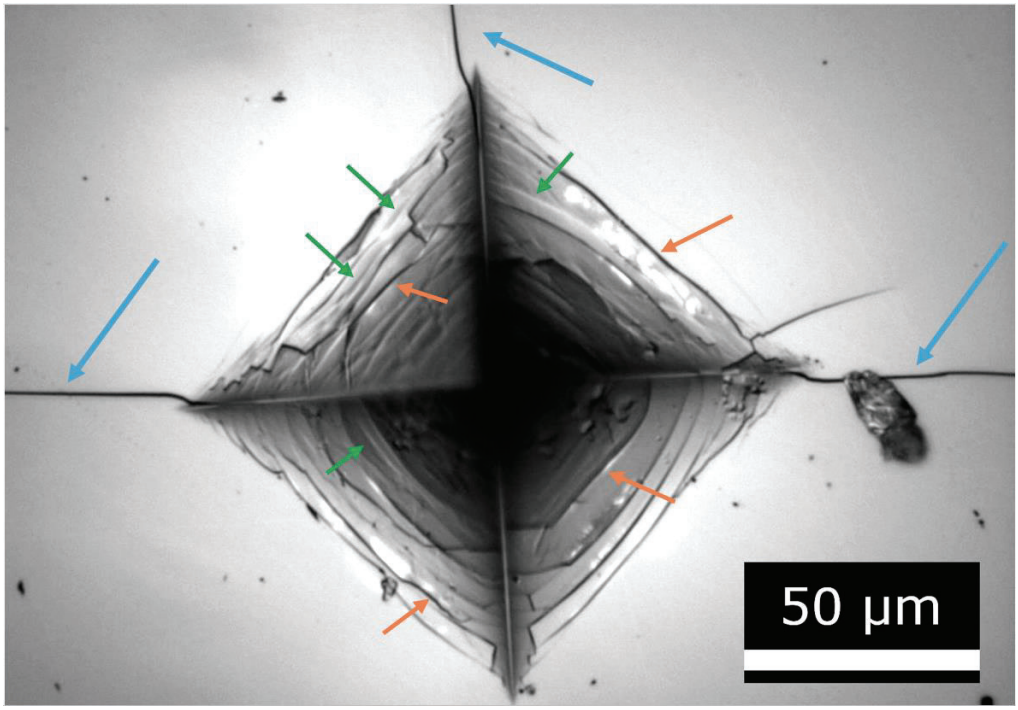

Figure S2. Close-up on top view of indent on ZIF-62 glass. Radial crack (blue arrows) and two types of cracking features: edge cracks (examples shown with orange arrows) and shear bands (examples shown with green arrows) are visible.

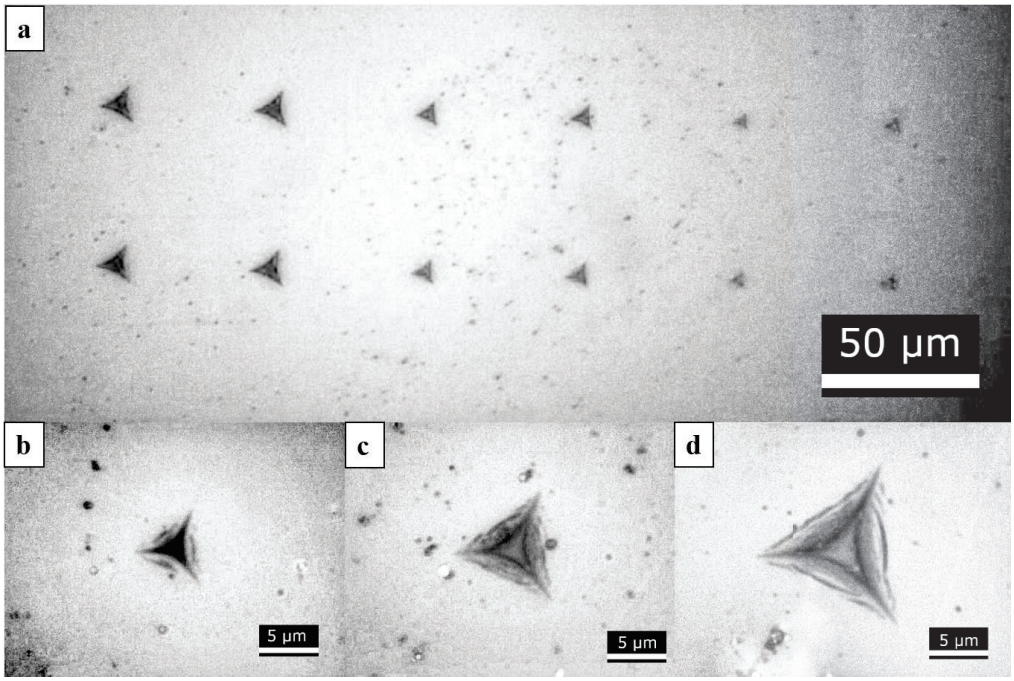

Figure S3. Indent images obtained for nanoindentation measurements: (a) an example of an area with indents created with 3 loads used, from the highest on the left (40 mN), the middle (20 mN) to the lowest (10 mN) on the right, (b – d) close-ups of examples of indent impressions after measurements with 3 loads: (b) 10 mN, (c) 20 mN, (d) 40mN.

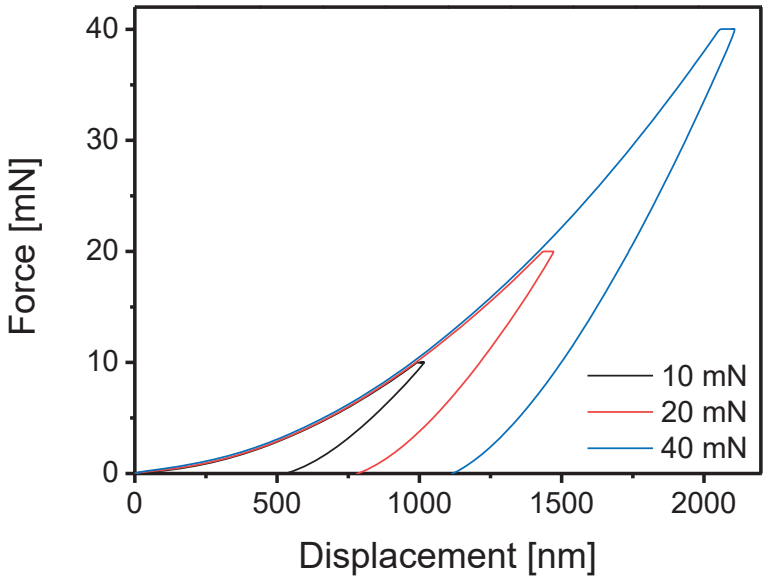

Figure S4. Force-displacement curves for nanoindentation on ZIF glass with changing maximum load. Black line represents the curve obtained for 10 mN maximum load; red curve – 20 mN, and blue curve – 40 mN respectively.

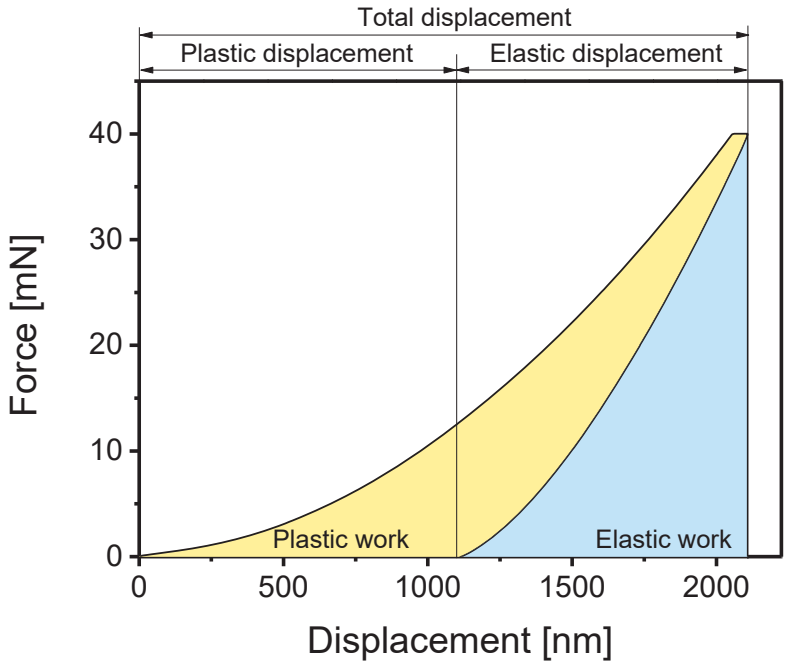

Figure S5. Schematic representation of calculation methodology for parameters presented in Table S1. On the top of the figure, the displacement is shown; yellow area shows the plastic work; blue area refers to the elastic work during indentation. The shown curve has been obtained with a maximum load of 40 mN.

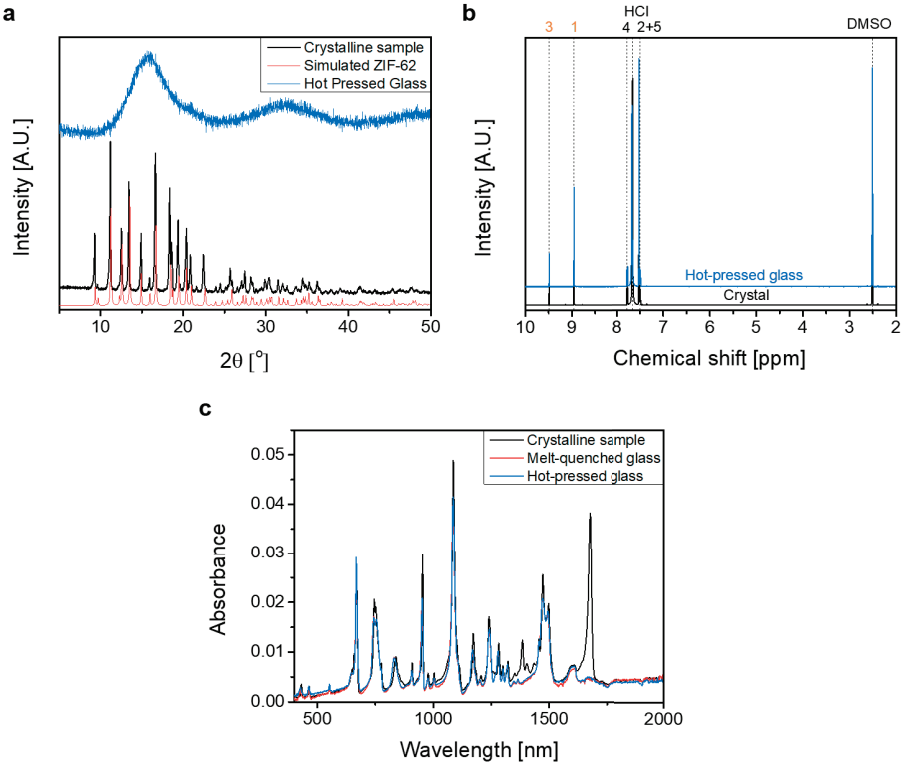

Figure S6. Structural characterization of ZIF-62 in crystalline and glassy states. (a) P-XRD patterns for obtained ZIF-62 crystals, simulated ZIF-62,[6] and the hot-pressed glass. It is confirmed that the obtained phase is ZIF-62 and that the sample after hot pressing has a pattern characteristic for glassy samples (visible amorphous bump). (b) ^{1}H-L-NMR spectra measured for both the crystalline and hot pressed sample. The two spectra are found to be analogous to that of the crystalline sample, suggesting the amorphization does not have a pronounced effect on the organic ligands. Peaks corresponding to hydrogen 1 (imidazole) and 3 (benzimidazole) have been integrated in order to assess the ratio of ligands in the structure. By calculating the percentage of benzimidazole (where 100% is Im+bIm

content), it was determined that benzimidazole accounts for around 15.1% of ligands in the crystalline sample and 15.4% of ligands in the hot-pressed glass. This suggests the ligand ratio stays nearly constant during melt-quenching under pressure. (c) FT-IR spectra obtained for the crystalline sample and both melt-quenched and hot-pressed glasses. Only some small differences are observed, as expected during amorphization. The additional peaks for the crystalline samples (around 1350-1440 cm^{-1} and at 1677 cm^{-1}) are due to the remaining solvent (DMF) in the crystals. Only small differences are seen between the two measured glasses, confirming the bonds are not changed significantly with the applied pressure during melting.

Table S1. Mechanical properties obtained from nanoindentation of the ZIF-62 glass as a function of the maximum load.

Maximum load (F_{max})	10 mN	20 mN	40 mN
Hardness [GPa]	0.674 ± 0.007	0.641 ± 0.006	0.622 ± 0.005
Indentation modulus [GPa]	5.59 ± 0.02	5.47 ± 0.02	5.32 ± 0.03
Elastic work (unloading) [a)] [pJ]	1960 ± 20	5620 ± 20	16050 ± 50
Total work [a)] [pJ]	3640 ±160	10610 ± 100	31152 ± 80
Elastic work [a)] [%]	53.8	53.0	51.5
Elastic displacement [a)] [nm]	496 ± 6	713 ± 5	1022 ± 6
Total displacement [a)] [nm]	1019 ± 6	1473 ± 4	2116 ± 8
Elastic displacement [a)] [%]	48.7	48.4	48.3

[a)] The method for determining these properties is illustrated in Figure S4 in Supporting Information.

REFERENCES

(1) Qiao, A.; Bennett, T. D.; Tao, H.; Krajnc, A.; Mali, G.; Doherty, C. M.; Thornton, A. W.; Mauro, J. C.; Greaves, G. N.; Yue, Y. Z. A Metal-Organic Framework with Ultrahigh Glass-Forming Ability. *Sci. Adv.* **2018**, *4*, eaao6827.

(2) Qiao, A.; Tao, H.; Carson, M.; Aldrich, S.; Thirion, L.; Bennett, T.; Mauro, J.; Yue, Y. Z. Optical Properties of a Melt-Quenched Metal-Organic Framework Glass. *Opt. Lett.* **2019**, *44*, 1623–1625.

(3) Wada, M.; Furukawa, H.; Fajita, K. Crack Resistance of Glass on Vickers Indentation. In *Proc. Int. Congr. Glass 10th*; 1974; 39–46.

(4) Arora, A.; Marshall, D. B.; Lawn, B. R.; Swain, M. V. Indentation Deformation/Fracture of Normal and Anomalous Glasses. *J. Non. Cryst. Solids* **1979**, *31*, 415–428.

(5) Oliver, W. C.; Pharr, G. M. An Improved Technique for Determining Hardness and Elastic Modulus Using Load and Displacement Sensing Indentation Experiments. *J. Mater. Res.* **1992**, *7*, 1564–1583.

(6) Banerjee, R.; Phan, A.; Wang, B.; Knobler, C.; Furukawa, H.; O'Keeffe, M.; Yaghi, O. M. High-Throughput Synthesis of Zeolitic Imidazolate Frameworks and Application to CO_2 Capture. *Science* **2008**, *319*, 939–943.

PAPER III

Towards Large-Size Bulk ZIF-62 Glasses via Optimizing the Melting Conditions

Malwina Stepniewska, Martin B. Østergaard, Chao Zhou, Yuanzheng Yue*

Department of Chemistry and Bioscience, Aalborg University, DK-9220 Aalborg East, Denmark

*Corresponding author. E-mail: Y.-Z.Y. yy@bio.aau.dk

Abstract

Production of large-size, bulk, and bubble-free melt-quenched Zeolitic Imidazolate Framework (ZIF) glasses is a challenge due to the difficulty in up-scaling of the synthesis of the initial ZIF crystals, to the extremely high viscosity at melting point and to their relatively high brittleness. In this work, we optimize the melt-quenching process to increase the size of ZIF-62 glass products and to increase their homogeneity and transparency. By finding the optimum melting time (i.e., <5 min), we succeeded in producing >10 mm large glass samples with a certain degree of transparency and low bubble content, which can be used for mechanical characterizations. We have found the condition (e.g., melting time > 30 min) for obtaining ZIF-62 glass foams, which result from partial decomposition during melting. This work provides some information for upscaling the ZIF glass production.

Keywords: Zeolitic Imidazolate Framework (ZIF); Melting; Bulk ZIF-62 Glass; ZIF-62 glass foam

1. Introduction

Metal organic frameworks (MOFs) are composed of two building units: metal nodes, usually being transition metals, and organic ligands [1]. A promising group of MOFs, based on imidazolate organic ligands, is zeolitic imidazolate frameworks (ZIFs). ZIFs have been widely studied in the recent years due to their high chemical and thermal stability, when compared to other subgroups of MOFs [2–4]. This makes them attractive candidates for potential use in fields such as catalysis, drug delivery, and gas separation [4]. ZIFs are characterized by a structure analogous to that of silica, with metal atoms (e.g. Zn [3,4], Co[4], Cd [5], Cu [6], or In [7]) coordinated by nitrogen atoms from imidazolate (Im) ligands or its derivative, e.g., 2-methylimidazolate (mIm) [8–10] or benzenimidazolate (bIm) [10–12], forming tetrahedra with Im-M-Im bond angle corresponding to that of O-Si-O [4,9]. Moreover, ZIFs with diverse topological structures and thus different properties can be produced by varying the chemical composition of precursors [11,13,14], by using different synthesis methods [8,15], by choosing solvent type or amount [16], and by controlling kinetic parameters [17,18].

Recently, it has been shown that a number of MOFs, especially some ZIFs, can be melt-quenched to glasses, which are a new family of glasses [19–21]. These glasses show a number of fascinating features, such as high viscosity (10^5 Pa s) at the melting point (T_m) [22], thermal stability against degradation, and glass stability against crystallization [23]. The melting and glass formation can occur only in some of ZIFs before decomposition of organic ligands. These processes require inert atmosphere and reliable temperature control, as presence of oxygen and even small temperature overshoot can lead to oxidation and decomposition of ZIFs, respectively. Furthermore, it is challenging to obtain glass samples with large sizes for measuring their mechanical properties and for potential optical and photonic applications. To enable production of large bulk samples, a detailed study of melt-quenching parameters has to be performed. Qiao et al. [22] have shown that the maximum melting temperature plays an important role in obtaining a bulk, transparent glass sample.

The standard ZIF-62 [$Zn(Im)_{1.75}(bIm)_{0.25}$] is a promising MOF candidate for producing a large-size glass, owing to its ultrahigh glass forming ability. ZIF-62 is built with the corner-shared tetrahedra, each of which is composed of one zinc nodes (Zn) and four ligands consisting of 3.5 imidazolate (Im, $C_3H_3N_2^-$) and 0.5 benzimidazolate (bIm, $C_7H_5N_2^-$) [22]. By optimization of the melting process, Qiao et al [22] obtained bulk glass samples. For this particular ZIF type, remelting of the melt-quenched sample has also allowed production of samples with a diameter of 13 mm for scratch tests [24]. Here we also chose ZIF-62 as a candidate to explore the possibility to produce the bulk sample. By variation in the melting duration above T_m in an inert atmosphere tube furnace, we discovered a significant influence of the prolonged melting time on the quality and properties of ZIF-62 glasses. Then, we found the optimum melting conditions to obtain centimeter-sized, relatively homogenous samples.

2. Experimental

1. Synthesis of ZIF-62 crystals

Crystalline ZIF-62 was obtained by the solvothermal synthesis method. 17.45 ml of 0.6 M zinc nitrate hexahydrate solution (Merck) in N,N-dimethylformamide (DMF, VWR) was mixed with two solutions of ligand sources: 33.82 ml of 0.5 M benzimidazole (Merck) and 21.82 ml 4 M imidazole solutions (Merck) in DMF. The mixture volume was adjusted to 75 ml by adding 1.914 ml DMF. The solution was stirred with a magnetic stirrer for 30 minutes, and subsequently placed in a furnace at 403 K for 48 hours. The obtained crystals were separated from the waste solution and washed three times with DMF and once with dichloromethane. The sample was left overnight for drying in a fumehood at room temperature. Finally, the synthesized crystals were placed in a furnace at 373 K for 72 hours to remove remaining solvents from the framework pores.

2. Bulk sample production

Around 200 mg of crystals were used to produce all the glass samples. The crystals were uniaxially pre-pressed into pellets with 40 MPa pressure, and subsequently placed in an electrical heated tube furnace. The furnace chamber was flushed with nitrogen to ensure an inert atmosphere. During heating, a continuous nitrogen flow was set at 5 mL/min to ascertain protective atmosphere during the process. The samples were heated to 733 K at 10 K/min, kept for melting for different duration t_m (0, 1, 2, 5, 10, 15, 20, 25, 30, and 60 min). Following the melting, the samples were cooled at 10 K/min to 593 K for a 30 min annealing of the glass to relieve internal thermal stress (the glass transition temperature, T_g, of melt-quenched ZIF-62 with 0 min melting duration is 605 K as shown in Table 2). Finally, the samples were cooled at 10 K/min to room temperature.

3. Characterizations

Crystal phases of the synthesized crystals were identified using powder X-ray diffraction (XRD). Samples were crushed in a mortar by pestle and diffraction patterns were obtained using an Empyrean XRD (PANalytical) with Cu $K_{\alpha 1}$ radiation (λ = 1.54098 Å) by scanning in the 2θ range of 5-50°, with a step size of 0.013°. The morphology and size of ZIF-62 crystals as well as size and number of bubbles in glasses were analyzed by scanning electron microscopy (SEM) (Zeiss EVO 60 S). The samples were coated with a gold layer of 10-15 nm thickness. A custom-made EM201x heating microscope (Hesse Instruments) was utilized to observe the sample size changes during heating on a pellet prepared in an analogous method to those molten in a tube furnace. 60 minutes melting step was included in the heating program at 733K, though argon inert atmosphere was used, instead of nitrogen. Results were analyzed based on observed sample silhouette area (A), in respect to the initial silhouette area (denoted as A_0). The density of the bulk glasses was calculated using Archimedes' Principle, by weighting the samples in air and ethanol. The glass transition temperature (T_g) was

determined by differential scanning calorimetry (DSC) (STA 404 C, Netzsch). Mass loss was obtained simultaneously to the DSC scan using thermogravimetry (TG). Two upscans were performed, both times heating the material to 733 K at 10 K/min and the same cooling rate. The T_g determined from the second upscan is within 3 K of the T_g determined by viscometry [25]. Structural measurements of the MOF glasses were conducted using ^{1}H liquid Nuclear Magnetic Resonance (NMR) spectroscopy (DPX600, Bruker) operating at 600 MHz. Samples were digested in DCl/D_2O/DMSO-d_6 solutions. The hardness was measured using a Vickers indentation (CB5000, Nanovea) with 0.98 N loading. The surface of the samples were polished (final size: 1 μm diamond suspension) for hardness measurements. Loading rate was set to ascertain 6 sec loading time (9.8 N/min), 15 sec creep at highest load was applied, and unloading was set to 60 sec.

3. Results and Discussion

The crystalline nature of the as-synthesized ZIF-62 sample is verified (Figure 1 a) by matching the experimental XRD patterns (peak positions and intensities) with the simulated ones, as taken from the Cambridge Crystallographic Database Centre, CCDC code GIZJOP [13]. The morphology of the synthesized crystals varies among the crystal particles (Figure 1b). Some crystal particles have irregular shape, while other are highly regular with well-defined, clear edges, consistent with the simulated crystal morphology [11]. The size of the crystals varies in the range of 100 μm for the largest to 5 μm for the smallest crystals from the SEM results. The bulk glasses produced in the gas-controlled tube furnace were confirmed to be X-ray amorphous, as shown in Figure 1 a.

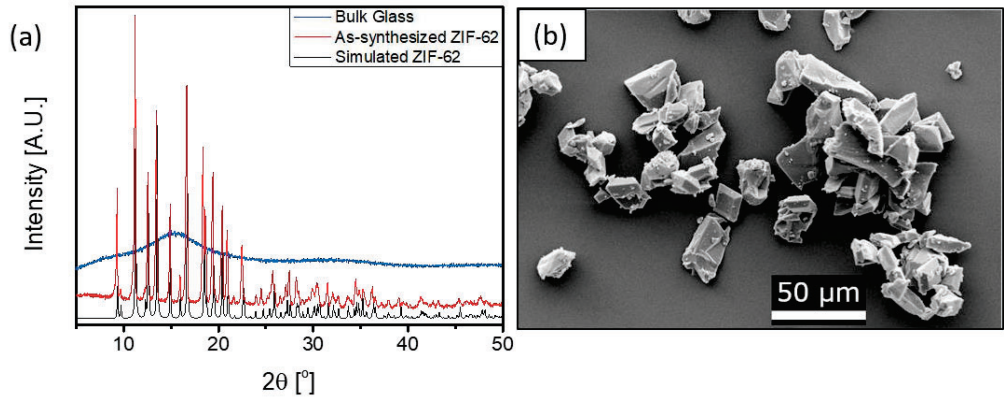

Figure 1. Characteristics of the as-synthesized crystalline ZIF-62 and the melt-quenched glass: (a) XRD patterns of as-synthesized ZIF-62 crystals (red line), simulated ZIF-62 crystals (black line), and the melt-quenched bulk glass (t_m = 5 min) (blue line); (b) SEM image of the as-synthesized crystalline ZIF-62. Note: Presence of both regularly and irregularly shaped crystal particles.

Heating microscope is a useful method to observe changes in sample size during heat treatment, and thus such processes as sintering, melting, and foaming can be observed [26–28]. In this work, this technique was utilized to observe the melting and foaming processes of the crystalline sample occurring during heating, melting time of 60 minutes (at 733 K) and cooling (Figure 2). The silhouette area (A/A_0) during the heating process is shown in red line. The expansion occurring in the range of about 350 K – 550 K is ascribed to the dissolution process as the synthesized crystals still contains solvent after the drying process, which is in agreement with the findings from DSC measurements (Figure 2b). The heating induces evaporation of the solvent leading to the expansion of the ZIF-62 crystals. The following shrinkage is caused by release of the solvent from the sample. The silhouette area increase at about 640 K indicates the expansion of the sample right before the

melting processes. Subsequently, a visible shrinkage in sample volume occurs, due to the sintering of the crystallites in the pellet followed by melting.

After reaching the maximum temperature of 733 K (23 K above T_m), the liquid stays isothermally for 60 minutes (purple curve). Further expansion of the sample is observed during this period, implying the decomposition of organic ligands.

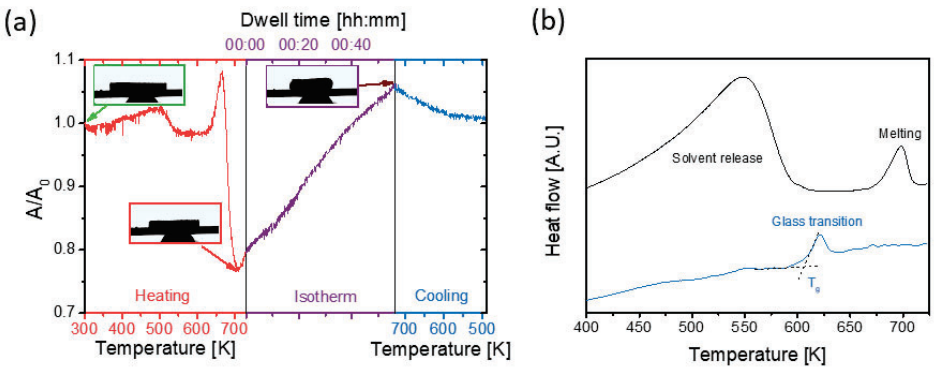

Figure 2. (a) Change in size (A/A_0) of ZIF-62 crystalline sample during heating at 10 K/min, measured using a heating microscope. Inserted images: the silhouette areas of the sample at 3 different time points. Green framed image: initial size (A_0) and shape of the sample; Red framed image: minimum silhoutte area; Purple framed image: Maximum A/A_0 ratio after foaming. Temperature uncertainity of the equipment is ± 4 K as shown in [26]; (b) DSC curves obtained during heating of crystalline ZIF-62 (solvent dissolution and melting) (black line) and during heating of the as-melt-quenched sample, showing the glass transition (blue line).

The obtained glass samples show different degree of transparency. This can be seen in Figure 3, where the samples are placed on top of a printed 'X'. The 'X' is only visible for samples melted at 733 K for < 5 min. At the same time, the density of the samples with t_m < 5 min shows a limited change (Figure 4). The samples are almost bubble–free in the cross-section (Figure 5), with only a minor number of small bubbles. However, we can observe some bubbles with a size of about 10-20 μm in the sample called 0min-2 (Fig. 5). The presence of the small bubbles implies that the samples are only partially melted, and the melting time was too short or the melting temperature was too low for the crystals to be fully melted. Short time sintering below T_m of compacted powder usually results in samples with small bubbles or pores [29]. The small bubbles are not visible for the glass melted for 1 min (Figure 5). Hence, 1 min melting seems to be sufficient for melting the green body. For longer durations ($t_m \geq 10$ min), the obtained glasses are no longer transparent and they are severely colored, and the density decreases significantly with increasing t_m. Extending t_m also causes an increase in bubble size, from approximately 20-50 μm for sample with t_m of 2 minutes, up to about 500 μm for sample with t_m of 60 minutes. The samples melted in the range 0 min $\leq t_m \leq$ 25 min all appear circular in shape. However, the two samples melted for t_m = 30 min and t_m = 60 min are much bigger (Fig. 3), a drastic decrease in density is found (Figure 4), and most of the sample volume is porous (Fig. 5), with only thin walls separating the pores, and thus, ZIF foams are produced. The changes in transparency, the decrease of density, and the increase of porosity are most likely caused by decomposition of the liquid samples. As MOFs consist of both inorganic and organic parts, the oxygen remaining in protecting atmosphere might react with the organic ligands, leading to the bond breakage and consequent partial decomposition of organic linkers [30]. As the organic ligands are decomposed, gas molecules (such as H_2, CO_2, NH_3) are most likely generated. Due to the high viscosity and surface tension of the ZIF-62 melt [22], the sample surface remains bubble-free. When the gas pressure inside the framework reaches a critical value, a foaming process takes place, leading

to ZIF glass foams. This is comparable with the sintering-foaming process during production of traditional glass foams [27,31].

Figure 3. Photographs of the as-prepared MOF glasses for different melting durations. The samples with "X" were used to assess the variation in the transparency by using naked eyes.

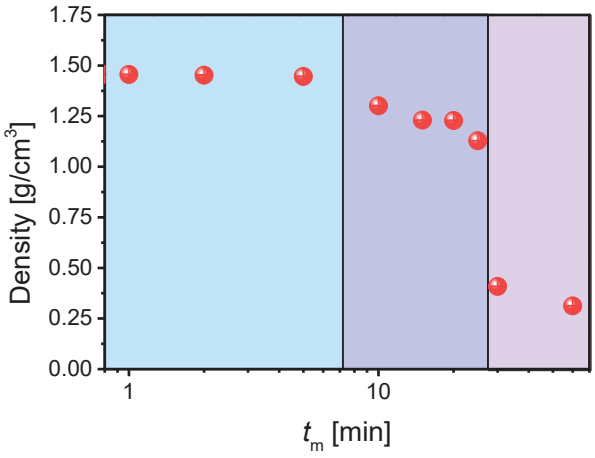

Figure 4. Density of MOF glasses prepared as a function of melting time (t_m). Three colors of the background in the figure refer to three stages of the density change. The error of the densities are smaller than the size of the symbols.

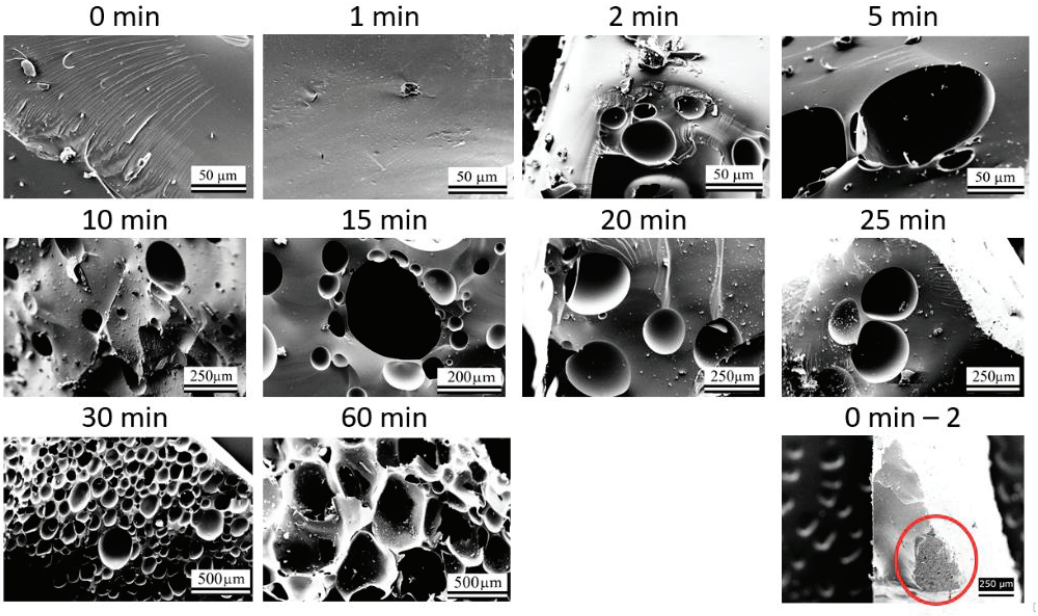

Figure 5. SEM images of the samples melted for different melting durations t_m (denoted over images). Note the increase of bubble size and number with increasing melting time, up to the 60 minutes melting time, when bubbles coalesce. Image denoted as 0 min – 2 shows the area of partially sintered crystals observed for sample with melting time of 0 minutes.

In order to assess the degradation mechanism during the melting process, the ratio between imidazole and benzimidazole in the glasses with varying melting duration t_m is quantified by liquid ^{1}H-NMR. Both imidazole and benzimidazole have an isolated proton that is useful for calculation of the ligand ratio (Figure 6). To obtain the ratio, the integrals of the peaks caused by protons marked as '1' and '3' on figure 6 are compared. The bIm/Im ratios are shown in Table 1. These ratios indicate that both

ligands are intact after glass formation. The degradation of ZIF-62 during melting does not affect the bIm/Im ratio, considering that the foamed glass has a similar ratio to that of other glass samples.

Table 1. Ligand ratios calculated from the ^{1}H L-NMR results

Sample	Benzimidazole:Imidazole ratio
As-evacuated Crystal	1:7.34
Glass, t_m = 1 min	1:7.24
Glass, t_m = 10 min	1:7.24
Glass, t_m = 25 min	1:7.24
Glass (foam), t_m = 60 min	1:7.34

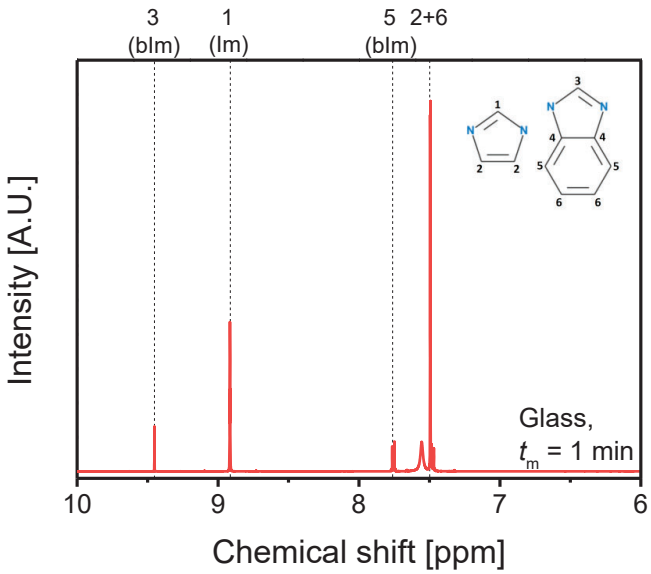

Figure 6. ^{1}H-NMR spectrum of the ZIF-62 glass with an melting time of 1 min. Inset: imidazole and benzimidazole configurations. The areas of peaks 3 and 1 were determined to compare the molar ratio of imidazolate and benzimidazolate ligands.

Measured glass transition temperature (T_g) (Table 2) varies slightly between the samples, yet no detectable trend can be observed. Together with the unchanged bIm/Im ratio with t_m, the not-detectable T_g trend with t_m confirms that the chemical composition of the glasses obtained for various t_m remains similar, and the two ligands decompose at a similar rate. Thus, the coordination bond strength of both ligands to the metal node is similar. It is worth mentioning that after reheating above T_g the foamed samples produced for t_m of 30 and 60 min regain a bulk form without bubbles. This suggests that the foaming process observed for the longest t_m does not affect the bulk glass forming ability of the reheated melt.

Table 2. Glass transition temperatures (T_g) measured for samples produced for various melting time (t_m). Measurement uncertainty is 2 K.

t_m [min]	T_g [K]
0	606
1	604
2	605
5	602
10	606
15	599
20	597
25	597
30	598
60	603

The hardness of the obtained samples (Fig. 7) is characterized by Vicker's indentation with 0.98 N loading. The results show that the hardness of the samples lies in the range between 0.45 and 0.5 GPa, not giving a conclusive trend considering the large error range of the data. The hardness value is lower than those (0.66-1 GPa) obtained by nanoindentation [21,24]. The lower hardness value in current work could be attributed to the indentation size effect [32,33,34] since we used the higher

load. Vicker's hardness of hot-pressed ZIF-62 glass was measured to be 0.51 GPa at 0.96 N load [34], which is higher than that shown in the present study. For the hot-pressing method [34], a pressure (50 MPa) was applied during the melting of the crystalline pellet, whereas for the tube furnace method the ambient pressure (0.1 MPa) was utilized. In the latter case, the high viscosity of the melt could hinder escape of the small bubbles, leading to a slight decrease of the density of the sample, and hence, to the reduced resistance to permanent deformation, consequently, to lower hardness.

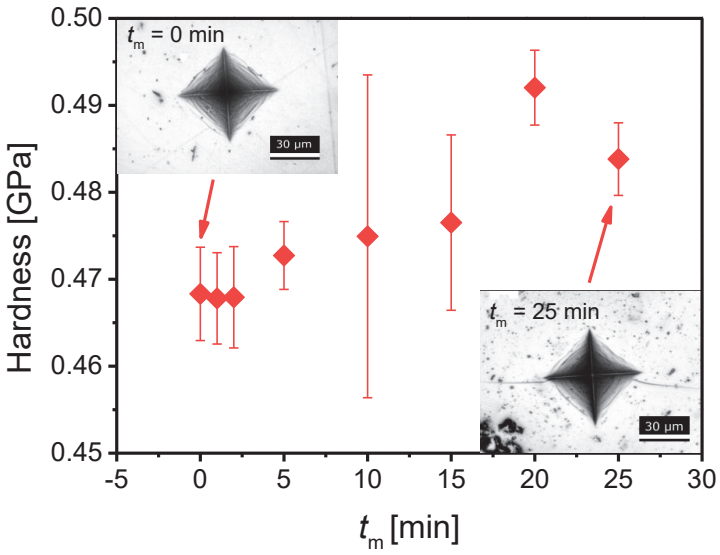

Figure 7. Hardness of ZIF-62 glasses versus t_m, which was measured using Vicker's indenter with maximum load of 0.98 N.

4. Conclusions

This work gives insight into impacts of the melting process on the quality, chemical composition, and properties of melt-quenched ZIF-62 glass. With extension of melting time, decomposition processes

of the glass were observed. The glass samples produced by melting for up to 5 minutes are more transparent and contain less bubbles than other samples. The density of the glass decreases significantly with increasing melting time over 10 minutes, and glass foams can be obtained if melting lasts > 30 minutes. T_g does not vary with melting time. Microstructural changes are not observed in the ZIF-62 glass with extending melting time, being confirmed by the unchanged benzimidazole:imidazole ratio within the error range.

Acknowledgments

We would like to thank VILLUM FONDEN for the financial support of this work under research grant no. 13253.

References

[1] O.M. Yaghi, M. O'Keeffe, N.W. Ockwig, H.K. Chae, M. Eddaoudi, J. Kim, Reticular synthesis and the design of new materials, Nature. 423 (2003) 705–714. doi:10.1038/nature01650.

[2] K.S. Park, Z. Ni, A.P. Côté, J.Y. Choi, R. Huang, F.J. Uribe-Romo, H.K. Chae, M. O'Keeffe, O.M. Yaghi, Exceptional chemical and thermal stability of zeolitic imidazolate frameworks., Proc. Natl. Acad. Sci. U. S. A. 103 (2006) 10186–10191. doi:10.1073/pnas.0602439103.

[3] J. Tan, T.D. Bennett, A.K. Cheetham, Chemical structure, network topology, and porosity effects on the mechanical properties of Zeolitic Imidazolate Frameworks, Proc. Natl. Acad. Sci. U. S. A. 107 (2010) 9938–9943. doi:10.1073/pnas.1003205107.

[4] B. Chen, Z. Yang, Y. Zhu, Y. Xia, Zeolitic imidazolate framework materials: recent progress in synthesis and applications, J. Mater. Chem. A. 2 (2014) 16811–16831. doi:10.1039/C4TA02984D.

[5] Y.Q. Tian, S.Y. Yao, D. Gu, K.H. Cui, D.W. Guo, G. Zhang, Z.X. Chen, D.Y. Zhao, Cadmium imidazolate frameworks with polymorphism, high thermal stability, and a large surface area, Chem. - A Eur. J. 16 (2010) 1137–1141. doi:10.1002/chem.200902729.

[6] N. Masciocchi, S. Bruni, E. Cariati, F. Cariati, S. Galli, A. Sironi, Extended polymorphism in copper(II) imidazolate polymers: A spectroscopic and XRPD structural study, Inorg. Chem. 40 (2001) 5897–5905. doi:10.1021/ic010384+.

[7] M.E. Schweinefuß, I.A. Baburin, C.A. Schröder, C. Näther, S. Leoni, M. Wiebcke, Indium

imidazolate frameworks with differently distorted ReO3-type structures: Syntheses, structures, phase transitions, and crystallization studies, Cryst. Growth Des. 14 (2014) 4664–4673. doi:10.1021/cg5007499.

[8] Y.R. Lee, M.S. Jang, H.Y. Cho, H.J. Kwon, S. Kim, W.S. Ahn, ZIF-8: A comparison of synthesis methods, Chem. Eng. J. 271 (2015) 276–280. doi:10.1016/j.cej.2015.02.094.

[9] S.A. Moggach, T.D. Bennett, A.K. Cheetham, The effect of pressure on ZIF-8: Increasing pore size with pressure and the formation of a high-pressure phase at 1.47 GPa, Angew. Chemie - Int. Ed. 48 (2009) 7087–7089. doi:10.1002/anie.200902643.

[10] A. Phan, C.J. Doonan, F.J. Uribe-Romo, C.B. Knobler, M. O'Keeffe, O.M. Yaghi, Synthesis, structure, and carbon dioxide capture properties of zeolitic imidazolate frameworks, Acc Chem Res. 43 (2010) 58–67. doi:10.1021/ar900116g.

[11] M. Gustafsson, X. Zou, Crystal formation and size control of zeolitic imidazolate frameworks with mixed imidazolate linkers, J. Porous Mater. 20 (2013) 55–63. doi:10.1007/s10934-012-9574-1.

[12] J.A. Thompson, C.R. Blad, N.A. Brunelli, M.E. Lydon, R.P. Lively, C.W. Jones, S. Nair, Hybrid Zeolitic Imidazolate Frameworks: Controlling Framework Porosity and Functionality by Mixed-Linker Synthesis, Chem. Mater. 24 (2012) 1930–1936. doi:10.1021/cm3006953.

[13] R. Banerjee, A. Phan, B. Wang, C. Knobler, H. Furukawa, M. O'Keeffe, O.M. Yaghi, High-throughput synthesis of zeolitic imidazolate frameworks and application to CO2 capture, Science (80-.). 319 (2008) 939–943. doi:10.1126/science.1152516.

[14] B.R. Pimentel, A. Parulkar, E. Zhou, N.A. Brunelli, R.P. Lively, Zeolitic Imidazolate Frameworks: Next-Generation Materials for Energy-Efficient Gas Separations, ChemSusChem. 7 (2014) 3202–3240. doi:10.1002/cssc.201402647.

[15] H.Y. Cho, J. Kim, S.N. Kim, W.S. Ahn, High yield 1-L scale synthesis of ZIF-8 via a sonochemical route, Microporous Mesoporous Mater. 169 (2013) 180–184. doi:10.1016/j.micromeso.2012.11.012.

[16] E.L. Bustamante, J.L. Fernández, J.M. Zamaro, Influence of the solvent in the synthesis of zeolitic imidazolate framework-8 (ZIF-8) nanocrystals at room temperature, J. Colloid Interface Sci. 424 (2014) 37–43. doi:10.1016/j.jcis.2014.03.014.

[17] C. Zhou, M. Stepniewska, J.M. Sørenses, L. Scarpa, G. Magnacca, V. Boffa, T.D. Bennett, Y.Z. Yue, Polymorph formation for a zeolitic imidazolate framework composition - Zn(Im)2, Microporous Mesoporous Mater. 265 (2018) 57–62. doi:10.1016/j.micromeso.2018.01.038.

[18] L.S. Lai, Y.F. Yeong, K.K. Lau, A.M. Shariff, Effect of Synthesis Parameters on the Formation of ZIF-8 under Microwave-assisted Solvothermal, Procedia Eng. 148 (2016) 35–42. doi:10.1016/j.proeng.2016.06.481.

[19] T.D. Bennett, J.C. Tan, Y.Z. Yue, E. Baxter, C. Ducati, N.J. Terrill, H.H.M. Yeung, Z. Zhou, W. Chen, S. Henke, A.K. Cheetham, G.N. Greaves, Hybrid glasses from strong and fragile metal-organic framework liquids, Nat. Commun. 6 (2015) 8079. doi:10.1038/ncomms9079.

[20] H. Tao, T.D. Bennett, Y. Z.Yue, Melt-Quenched Hybrid Glasses from Metal–Organic

Frameworks, Adv. Mater. 29 (2017) 1601705. doi:10.1002/adma.201601705.

[21] T.D. Bennett, Y.Z. Yue, P. Li, A. Qiao, H. Tao, N.G. Greaves, T. Richards, G.I. Lampronti, S.A.T. Redfern, F. Blanc, O.K. Farha, J.T. Hupp, A.K. Cheetham, D.A. Keen, Melt-Quenched Glasses of Metal-Organic Frameworks, J. Am. Chem. Soc. 138 (2016) 3484–3492. doi:10.1021/jacs.5b13220.

[22] A. Qiao, T.D. Bennett, H. Tao, A. Krajnc, G. Mali, C.M. Doherty, A.W. Thornton, J.C. Mauro, G.N. Greaves, Y.Z. Yue, A metal-organic framework with ultrahigh glass-forming ability, Sci. Adv. 4 (2018) eaao6827. doi:10.1126/sciadv.aao6827.

[23] C. Zhou, M. Stepniewska, L. Longley, C.W. Ashling, P.A. Chater, D.A. Keen, T.D. Bennett, Y.Z. Yue, Thermodynamic features and enthalpy relaxation in a metal–organic framework glass, Phys. Chem. Chem. Phys. 20 (2018) 18291–18296. doi:10.1039/C8CP02340A.

[24] S. Li, R. Limbach, L. Longley, A. Shirzadi, J.C. Walmsley, D.N. Johnstone, P.A. Midgley, L. Wondraczek, T.D. Bennett, Mechanical Properties and Processing Techniques of Bulk Metal-Organic Framework Glasses, J. Am. Chem. Soc. 141 (2019) 1027–1034. doi:10.1021/jacs.8b11357.

[25] Y.Z. Yue, Characteristic temperatures of enthalpy relaxation in glass, J. Non. Cryst. Solids. 354 (2008) 1112–1118. doi:10.1016/j.jnoncrysol.2006.11.027.

[26] R.R. Petersen, J. König, Y.Z. Yue, Evaluation of Foaming Behavior of Glass Melts by High-Temperature Microscopy, Int. J. Appl. Glas. Sci. 7 (2016) 524–531. doi:10.1111/ijag.12185.

[27] M.B. Østergaard, R.R. Petersen, J. König, M. Bockowski, Y.Z. Yue, Foam glass obtained through high-pressure sintering, J. Am. Ceram. Soc. 101 (2018) 3917–3923. doi:10.1111/jace.15574.

[28] M.B. Østergaard, R.R. Petersen, J. König, Y.Z. Yue, Effect of alkali phosphate content on foaming of CRT panel glass using Mn3O4 and carbon as foaming agents, J. Non. Cryst. Solids. 482 (2018) 217–222. doi:10.1016/j.jnoncrysol.2017.12.041.

[29] S.-J.K. Kang, Initial stage sintering, in: Sinter. Densif. Grain Growth, Microstruct., 1st ed., Elsevier Butterworth-Heinemann, 2005: pp. 39–55. doi:https://doi.org/10.1016/B978-0-7506-6385-4.X5000-6.

[30] B. Xu, Y. Mei, Z. Xiao, Z. Kang, R. Wang, D. Sun, Monitoring thermally induced structural deformation and framework decomposition of ZIF-8 through in situ temperature dependent measurements, Phys. Chem. Chem. Phys. 19 (2017) 27178–27183. doi:10.1039/c7cp04694d.

[31] R.R. Petersen, J. König, Y.Z. Yue, The mechanism of foaming and thermal conductivity of glasses foamed with MnO2, J. Non. Cryst. Solids. 425 (2015) 74–82. doi:10.1016/j.jnoncrysol.2015.05.030.

[32] H. Li, R.C. Bradt, The microhardness indentation load/size effect in rutile and cassiterite single crystals, J. Mater. Sci. 28 (1993) 917–926. doi:10.1007/BF00400874.

[33] T. Kavetskyy, J. Borcc, K. Sangwal, V. Tsmots, Indentation size effect and Vickers microhardness measurement of metal-modified arsenic chalcogenide glasses, J. Optoelectron. Adv. Mater. 12 (2010) 2082–2091.

[34] M. Stepniewska, K. Januchta, C. Zhou, A. Qiao, M.M. Smedskjaer, Y.Z. Yue, Anomalous Cracking in a Metal-Organic Framework Glass, ChemRxiv Prepr. (2019). doi:10.26434/chemrxiv.7844720.v1.

ISSN (online): 2446-1636
ISBN (online): 978-87-7210-543-7 AALBORG UNIVERSITY PRESS